1-23-2017

Numerical and Analytical Investigation of Satellite Precipitation Error Propagation in Hydrologic Simulations

Yiwen Mei
University of Connecticut - Storrs, yiwen.mei@uconn.edu

Numerical and Analytical Investigation of Satellite Precipitation Error Propagation in Hydrologic Simulations

Yiwen Mei Ph. D.

University of Connecticut, 2017

The overarching goal of the research described in this dissertation is to understand the hydrologic implications of error propagation from satellite precipitation products to hydrologic simulations. The complex interaction between precipitation error and corresponding hydrologic response is examined following a numerical- and an analytical-based approach. The application of a hydrologic model forced by various satellite precipitation products is adopted as the numerical-based framework that is used to identify the properties of error propagation with respect to a number of factors (e.g. basin scale, seasonality, severity of rainfall and flow). The investigation is conducted in complex terrain basins of the Eastern Italian Alps. Results show better consistency between gauges for events occurred over larger scale basins during warm season months that are associated with moderate intensity of rain and flow rate. Furthermore, an event-based error analysis is conducted focusing on the evaluation of satellite-simulated flood event characteristics for different flood types. Results revealed that on average systematic rainfall error is reduced in simulated runoff, highlighting the dampening effect on error during the rainfall-runoff transformation. The dampening effect on random error was decreasing with increasing runoff coefficient. In addition to the numerical investigation, an analytical framework is developed to decompose the error propagation into space and time components. This essentially allows to assess the relative contribution of the different processes of catchment flood response on error propagation. Demonstration of the analytical framework is conducted based on 180 rainfall-runoff

Yiwen Mei Ph. D.

University of Connecticut, 2017

events that occurred over the Tar River basin in North Carolina. It is shown that error in timing of flood event is attributed equally to error in runoff generation and routing time. Error in hydrograph shape is mainly controlled by the error in the variability of runoff generation time while error in flood volume is predominantly controlled by the error in rainfall volume. Overall, these investigations provide important information for the hydrologic modelers to choose the appropriate precipitation products for the hydrologic-related practice. It also serves as guidance for the satellite precipitation-product developers on the designs of more advance retrieval algorithms.

Numerical and Analytical Investigation of Satellite Precipitation Error Propagation in Hydrologic Simulations

Yiwen Mei

B.Eng., Guangdong University of Technology, 2010

M.Sc., University of Connecticut, 2012

A Dissertation

Submitted in Partial Fulfillment of the

Requirements for the Degree of

Doctor of Philosophy at the

University of Connecticut

2017

Approval Page

Doctor of Philosophy Dissertation

Numerical and Analytical Investigation of Satellite Precipitation Error Propagation in Hydrologic Simulations

Presented by

Yiwen Mei, B.Eng., M.Sc.

Major Advisor_____

Emmanouil N. Anagnostou

Associate Advisor_____

Efthymios I. Nikolopoulos

Associate Advisor_____

Guiling Wang

Associate Advisor_____

Amvrossios C. Bagtzoglou

Associate Advisor_____

Marina Astitha

University of Connecticut

2017

Acknowledgements

Six years and a half, to climatologist, could be too short to determine the trend of precipitation changes, while it could be long enough to observe the seasonal variability of catchment response for hydrologist. It, to me, is the length of my Ph.D. career at the University of Connecticut. I am finally at the destination of my Ph.D. degree and the entrance of my professional career. I hold my sincere thanks to many people who provides me supports during this Six years and a half.

First of all, I would like to express my sincere thanks to my major advisor, Prof. Emmanouil N. Anagnostou (Manos), for his limitless patience, continuous encouragement and professional support during for my grad student career. My undergrad background is not related to hydrology and the only data processing tool I know when I first arrived in this glade is Excel. It is Manos, who shared with me the expertise from the fundamental concept to the frontier of hydrology, who provided me the opportunity to join this group, working with great researchers worldwide, and more importantly, who made me evolved to a more advance status as you seen now. I greatly appreciate his faith in me as well as the fact that we have been teammates and competitors at the basketball court.

I am also extremely grateful to my committee members: Dr. Efthymios I. Nikolopoulos, Prof. Guiling Wang, Prof. Amvrossios C. Bagtzoglou and Prof. Marina Astitha for their comments and suggestions on my dissertation research, their great support and help at different stages of my graduate study whenever I need them. A special thank goes to Dr. Efthymios I. Nikolopoulos (who is also a teammate and competitor of me at the basketball court) for his patience and supports since the very beginning of my grad student career to now and to the future. Without him, I will not be able to learn Matlab in a short time; I will not be able to be as productive as I am; and I will not be able to have my current horizon of knowledge.

I would like to extend my gratitude and appreciation to Dr. Xinyi Shen for constantly sharing with me the advance knowledge of the remote sensing field and for helping me to learn CREST. In addition, I would like to thank Dr. Rui Mei for teaching me the basic of computer coding at the very beginning of my UConn journey.

My graduate student colleagues were very important to me during these past six and a half years. Without you, my graduate life would have been far less enjoyable and memorable. Special thanks go to Ehsan, Xinxuan, Jaemo, Dave and Diego for organizing the bowling night, inviting me for dinner and drinks, helping me with issues such as health insurance, visa status, car problem and many other things that I encountered.

Last, but not the least, I would like to thank my family members: my wife Rose, my parents Rongjin and Qiaoyu for their unwavering love and support, which has always been the source of strength in my life.

Table of Contents

List of Figures

List of Tables

Chapter 1 Introduction

1.1 Background and Motivation

Accurate measurement of surface precipitation is of great importance for the monitoring, forecasting and early warning of flood hazards, often triggered by heavy precipitation events (HPEs) occurring over mountainous regions (Borga, et al., 2010; Creutin & Borga, 2003). Conventional ground-based measurements for quantifying precipitation include observations from rain gauge and weather radar networks (Michaelides, et al., 2009). Rain gauge networks represent direct measurements of precipitation but due to the point-wise characteristics of gauge measurements, they exhibit significant uncertainty on the space-time representativeness of rainfall variability over some critical areas such as the tropics and high mountain regions (Nikolopoulos, et al., 2015; Berne & Krajewski, 2013). Weather radar networks, on the other hand, provide precipitation estimates with high spatiotemporal resolutions (i.e., 1–4 km and 5–15 min) but are subjected to uncertainties arising from variations in rainfall drop size distribution, beam blockage, beam overshooting, beam filling, hardware calibration, and random sampling error (Kirstetter, et al., 2015; Delrieu, et al., 2014; Berne & Krajewski, 2013). A combination of rain gauges and weather radar can increase the accuracy in precipitation estimations but this cannot apply for mountainous areas, characterized by large radar beam blockages due to the orographic effect (Kirstetter, et al., 2015; Prat & Nelson, 2015).

The quasi-global availability of satellite rainfall estimates in TRMM- and currently GPM-era provide a potentially feasible solution to this observational shortage from ground-based sensors. Precipitation estimation from satellite remote sensors is uninhibited by topography, thus can provide coherent global-scale estimates at high spatiotemporal resolution (as fine as 4 km/15 min). High space and time resolution satellite precipitation retrievals are based on observations from the visible–infrared (VIS–IR) spectrum, the passive microwave (PMW) sensors and a combination of these observations. The advantages of the IR sensors onboard geostationary (GEO) satellites is its high sampling frequency; but the estimates of precipitation rate are indirectly retrieved from the cloud-top temperature observations. The PMW sensors onboard low-Earth-orbiting (LEO) of polar-orbiting satellites, on the other hand, observe directly the

hydrometeor content present within the atmospheric column, but have low sampling frequency. In addition to the VIS-IR and PMW measurements, the ground gauge observations are commonly incorporated with the space-based measurements to improve the accuracy of precipitation retrievals. The ground gauge adjustments are often implemented on a monthly basis to reduce the systematic error in remote sensing precipitation estimations.

The integration of satellite precipitation products (as well as other remote sensing observations) with land surface and distributed hydrologic models provide an opportunity to study the space-time variability of hydro-meteorological extremes (e.g. flash flood, debris flow, drought) in sparsely gauged or even ungauged areas. However, satellite-based estimation of precipitation is associated with significant systematic and random errors that propagate through hydrologic modeling in varying ways. This lack of predictive understanding of error propagation characteristics imposes severe limitations on the use of these products in flood forecasting and water resource management (Mei, et al., 2016b; Seyyedi, et al., 2015; Siddique-E-Akbor, et al., 2014; Xue, et al., 2013). Therefore, assessing the accuracy of satellite precipitation estimates and their corresponding use in simulating hydrologic variables is critical for advancing satellite-based hydrologic applications.

Current frameworks to assess the hydrologic potential of satellite precipitation estimates are divided into two types: those that involve direct comparison of the products to ground-truth precipitation measurement (Guo, et al., 2016; Prakash, et al., 2016; Zhang, et al., 2015; Yong, et al., 2014); and those that compare hydrologic simulations driven by satellite precipitation forcing to simulations driven by reference precipitation (Tang, et al., 2016; Nikolopoulos, et al., 2013; Bitew, et al., 2011; Su, et al., 2008). Common results from these studies include that the errors in satellite precipitation retrievals and its propagation in hydrologic simulations depend on a variety of factors, including the product type, scale of analysis, seasonality, precipitation severity, precipitation type and geomorphology. For instance, larger basins and coarser temporal aggregation scales can buffer higher degree of error in precipitation (Mei, et al., 2016a; Vergara, et al., 2013; Beighley, et al., 2011; Pan, et al., 2010); underestimation is more severe

for heavy precipitation and high flow rates (Mei, et al., 2016a; 2014b; Zhang, et al., 2016; Seyyedi, et al., 2015); the bias in precipitation tends to be directly translated in terms of runoff simulation for events with higher initial conditions (Mei, et al., 2016b; Shah & Mishra, 2016; Nikolopoulos, et al., 2013); the inclusions of additional precipitation information (ground-based sources, atmospheric models and other auxiliary atmospheric and land surface variables) can improve the hydrologic performance (Zhang, et al., 2016; Falck, et al., 2015; Habib, et al., 2014). These studies have provided insights regarding the controls on error propagation of satellite precipitation from a statistical standpoint, which provides guidance to end-users in choosing products and adjustment methods that are suitable for their applications.

Aiming at facilitating a more physically based explanations on the error propagation process of satellite precipitation products, a hydrologic analytical framework is proposed in this study (Mei, et al., 2016c) that builds upon previous works on this topic (Viglione, et al., 2010a; Woods & Sivapalan, 1999). The framework estimates three flood event properties (that is, cumulative volume, centroid, and dispersion) by the generation of rainfall excess and the expectation and variance, respectively, of catchment response time. The framework has been used to assess the relative importance among different processes quantifying the space and time interactions of rainfall, runoff generation, and routing to catchment response (Mei, et al., 2016c; Mejía, et al., 2015; Viglione, et al., 2010b; Sangati, et al., 2009). Besides, this framework provides an analytical way to study the effects of neglecting the spatiotemporal information on rainfall in runoff generation (Zoccatelli, et al., 2015; 2011; Mei, et al., 2014a; Nikolopoulos, et al., 2014). In this study, we apply this hydrological analytical framework to link the error in different precipitation sources (e.g. satellite precipitation vs. ground-based precipitation, reanalysis precipitation vs. observation) with the error in flow simulations driven by these precipitation sources. This provides us a novel angle to investigate the error propagation process since the framework allows decomposing the precipitation error into different levels of space and time complexity, and then formulating in terms of error in flow simulation. For the satellite product developers, this framework could guide the selection of optimal spatiotemporal resolutions for the

different satellite precipitation products. In addition, it helps the end users to choose the optimal space and time complexity of hydrological modeling with minimal loss in accuracy for particular basins and events.

1.2 Objectives

The primary focus of this dissertation is to analyze the potential of satellite precipitation products in flow simulations through the numerical models and the hydrologic analytical framework. Specifically, in the first part, I render statistical evaluations for the satellite precipitation products and their flow simulations derived from numerical hydrologic models. In the second part, I develop the analytical framework for catchment flood response and implement it in the error propagation study to give new insights on the topic. These two tasks are summarized as follows:

1) *Hydrologic evaluation of satellite precipitation products over mountainous areas*:

   Chapter 2 Error Analysis of Satellite Rainfall Products in Mountainous Basins.

   Chapter 3 Evaluating Satellite Precipitation Error Propagation in Runoff Simulations of Mountainous Basins.

   Chapter 4 Error Analysis of Satellite Precipitation-Driven Modeling of Flood Events in Complex Alpine Terrain.

2) *Development of an analytical framework for satellite precipitation error propagation in catchment flood response*.

   Chapter 5 A Synthesis of Space-time Variability in Multi-Component Flood Response.

   Chapter 6 Quantifying the Error Propagation of Satellite Precipitation by a Hydrologic Analytical Framework.

For the numerical investigation, statistical evaluations based on continuous rainfall and flow simulations are provided in Chapter 2 and Chapter 3; a flood event based evaluation of the satellite products

is provided in Chapter 4. The aim of these studies is to understand the error structures in properties of satellite precipitation products and their driven flow simulations and interaction (error propagation from rainfall to runoff) as a function of a wide variety of factors (i.e. basin scales, elevation, storm type, rainfall and flow severity) at both long-term simulations and event basis. For the other research track, a hydrologic analytical framework is developed and used in Chapter 5 and Chapter 6 to analyze the error propagation of satellite precipitation in the context of flood events. The goal here is to understand what the dominant processes in catchment flood response are, and how much complexity is needed to model the error propagation in flood simulations. Lastly, I summarize the main findings from these varied research topics and provide vista on the integration of satellite precipitation product in hydrologic simulation in Chapter 7.

Chapter 2 Error Analysis of Satellite Rainfall Products in Mountainous Basins

2.1 Introduction

Measuring surface rainfall is of great importance particularly for the heavy precipitation events (HPEs) occurring over mountainous regions often acting as flash flood-triggering storms (Borga, et al., 2010). Methods for quantifying precipitation include ground observations from rain gauge and weather radar networks, estimates inferred from satellite observations, outputs from numerical weather prediction models and estimates produced by a combination of all these different products (Michaelides, et al., 2009). Each of these is associated with specific rainfall estimation uncertainties. Rain gauge networks are the most common estimation method. These networks can provide accurate point-wise precipitation measurements, but the spatial representativeness is limited (Anagnostou, et al., 2010; Sapiano & Arkin, 2009). Weather radar networks provide precipitation estimates with high spatial and temporal resolutions (i.e. 1-4 km and 5-15 min) but with variable accuracy. Moreover, mountainous terrain tends to degrade the accuracy of radar-derived rainfall estimates, due to observational limitations (beam blockages, ground clutter) and their interaction with precipitation vertical structure (Ciach, et al., 2007; Germann, et al., 2006; Piccolo & Chirico, 2005; Anagnostou, 2004; Sharif, et al., 2002). In addition, radar observations have limited utility in cold weather, when the beam detects primarily snow, which complicates the assessment of surface precipitation (Schneebeli, et al., 2013). Combining rain gauges with weather radar gives partial solution to the accuracy issues, but it is not a viable solution for cases with large radar beam blockages due to orography or in areas where those systems are not widely available.

Satellite-based estimates of precipitation can potentially provide a solution to the spatial sampling limitations of ground-based sensors. Satellite sensors are uninhibited by mountains and provide global coverage without spatial inconsistencies (Sapiano & Arkin, 2009; Kidd, et al., 2003; Scofield & Kuligowski, 2003; Arkin & Ardanuy, 1989). Several of the current global-scale satellite precipitation retrieval

algorithms are based on the combination of high spatiotemporal resolution observations in the visible-infrared (VIS-IR) spectrum from geostationary satellites (GEO) and the less frequent but more direct precipitation observations from active and passive microwave (MW) sensors deployed on low earth-orbiting satellites (LEO). The VIS-IR techniques relate surface precipitation to cloud-top information (brightness temperatures) with a high sampling frequency (15-min/3–4-km resolution, 1-km VIS). However, these measurements cannot directly retrieve surface precipitation from the inferred cloud-top properties, implying a weak link between cloud-top information to surface precipitation estimation (Sapiano & Arkin, 2009). On the other hand, MW techniques are more accurate than the VIS-IR because they physically link the signal received by the satellite sensors to the size and phase of the hydrometeors present within the observed atmospheric column. Nonetheless, MW observations are associated with large degree of sampling error particularly in dealing with short rain events due to their low observational frequency and large sensor field of view areas (Ebert, et al., 2007; Kidd, et al., 2003).

It is deemed by many studies that rainfall retrieved based on either VIS-IR or MW sensors, or the combination of both sensor observations, suffers from noticeable deficiencies compared to ground-based measurements (Stampoulis & Anagnostou, 2011; AghaKouchak, et al., 2011; Fleming, et al., 2011; Yong, et al., 2010; Su, et al., 2008; Dinku, et al., 2007; Ali, et al., 2005). Stampoulis & Anagnostou (2011) conducted an analysis for 3B42-V6 and CMORPH over the continental Europe and found that correlations of the two rainfall products to the gauge interpolated rainfall are magnitude dependent in terms of daily rainfall accumulation; moreover, the products exhibited more pronounced seasonal dependency over high elevation regions compared to the low elevation areas. Anagnostou et al. (2010) evaluated two satellite products (CMORPH and 3B42-V6) over the Oklahoma region in the Midwestern U.S. The study pointed out that CMORPH tend to overestimate the precipitation volume more prominent than 3B42-V6 during the warm season while the bias of both satellite products are lower than 20% during the cold season. Yong et al. (2010) highlighted the geography-dependent (latitude- and elevation-dependent) roles of 3B42-RT and 3B42-V6 over Laohahe Basin in the Northeast China. Meanwhile, better agreement with gauge

observations was found for 3B42-V6 at both daily and monthly scales. Su et al. (2008) focused on the performances of 3B42-V6 over La Plata Basin in Amazon. They concluded that the satellite estimates are slightly higher than the gridded gauge data at both monthly and daily time scales with higher degree of agreement for the monthly time scales. Other satellite error studies are those of Ali et al. (2005) and Dinku et al. (2007) who investigated the error structures of four satellite products over the Sahara and nine satellite products over the complex terrain on the East Africa respectively. They showed that the products are consistent with rainfall estimated from the ground based gauge networks at a coarse resolution (i.e. 2.5°×2.5° grid cell at monthly interval).

Although the topic of satellite rainfall error analysis has been investigated globally for more than two decades (Anagnostou, 2004; Petty & Krajewski, 1996; Arkin & Ardanuy, 1989), only a small portion of these studies have focused on the error structure of satellite products on the event basis (Nikolopoulos, et al., 2013; Mishra, 2012; AghaKouchak, et al., 2011); even fewer of them have attempted to decipher the error structure based on a large number of storm events (Stampoulis & Anagnostou, 2011). Furthermore, the majority of the satellite rainfall error literature is generally focused on the error analysis at the satellite products' spatial (typically ranging between 0.04-0.5 deg) and temporal scales (ranging between 15 minutes and 3-hours). While using a regular space-time scale has allowed consistency in the evaluation of results from different error studies, it does not allow a direct interpretation of the satellite rainfall error in terms of hydrologic applications. In hydrologic modeling, particularly the basin flood response to precipitation, spatial and temporal scales are dictated by the basin's drainage area and duration of storm causing the flood event. Therefore, the current literature lacks comprehensive hydrologic-driven satellite rainfall error studies that depict the error structure of basin-average satellite rainfall on the basis of long-term records of storm events. Understanding and improving satellite rainfall error characteristics at the basin scale, and on an event basis, will improve uses of satellite rainfall data in regional water budget analyses and for monitoring or forecasting of hydrologic extremes (flash floods and droughts).

This study attempts to evaluate the error characteristics of four quasi-global satellite-precipitation algorithms (3B42-RT, 3B42-V7, CMORPH and PERSIANN) over a mountainous area in the Eastern Italian Alps. The surface rainfall data are derived from a dense rain gauge network over the study area. This error analysis is expected to give supplementary information and guidance to relevant studies regarding the uncertainties of satellite-derived precipitation estimates over complex mountainous region and for heavy precipitation events. It is noted that given the mountainous setting of the study domain precipitation particularly during cold season months could be in the form of snow or mixed phase, which is not discriminated in this study. In the next section we describe the study area and data used. Section 2.3 introduces the error metrics and the score system. Results are reviewed in section 2.4 and conclusions are drawn in section 2.5.

2.2 Study area and Data

2.2.1 Study area

This study focuses over the eastern part of the Upper Adige river basin, a mountainous region located in the Eastern Italian Alps (Figure 2.1), and particularly the Isarco basin (4166 km^2) and the upper Passirio basin (427 km^2). The basins have mean elevation of 1736 meter above sea level (m a.s.l.) with the highest/lowest elevation at about 3700/220 m a.s.l. The region is influenced by western Atlantic airflows and meridional circulation patterns (Frei & Schär, 1998) causing heavy precipitation events and associated flash floods and debris flows in the summer and fall seasons. The dominant climate pattern in the region is continental, with the precipitation monthly distribution exhibiting two maxima, during August and October. The mean (max/min) annual precipitation accumulations in the 2003 to 2010 period for the Isarco and Passirio basins were 651 mm (987 mm/480 mm) and 637 mm (865 mm/482 mm), respectively. October to April period are typically dominated by snow and widespread type precipitation, while in May to September

period precipitation is mainly characterized by mesoscale convective systems and localized thunderstorms (Norbiato, et al., 2009a).

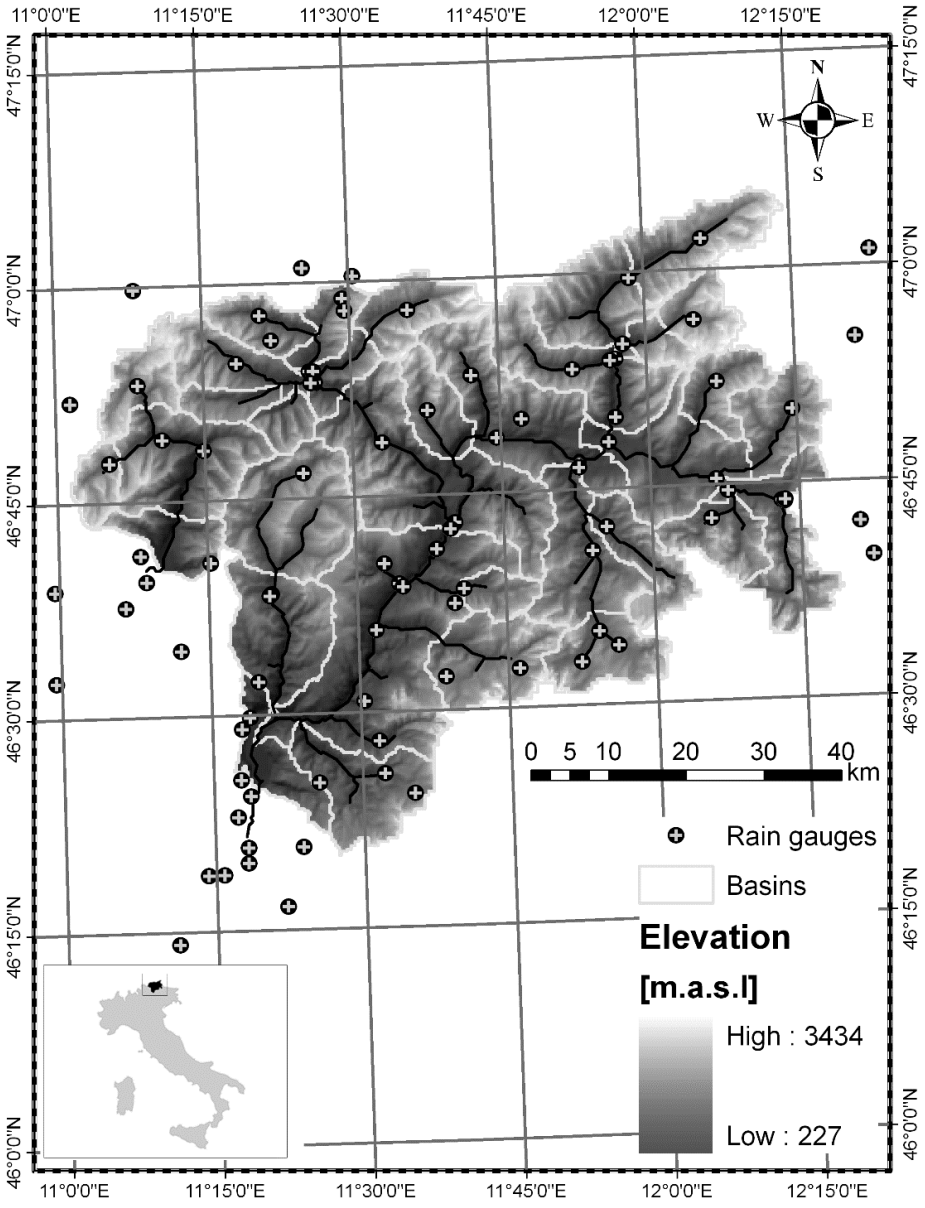

Figure 2.1 Elevation map of the study area (eastern part of Upper Adige river basin) and locations of available rain gauges. Inset map shows the location of study area over Italy and the overlaid grid corresponds to the satellite grid (0.25×0.25 degrees). The figure also shows boundaries of the sub-basins used in the study.

2.2.2 Rainfall data

The study area is covered by a dense rain gauge network (87 gauges) with densities of contributing gauges per basin ranging between one station per 16 km^2 (for the various analyzed sub-basins) to 53 km^2 (average gauge density for the entire area). The gauge rainfall record is hourly with an eight-year temporal coverage span (2003 to 2010). Hourly gauge precipitation time series averaged over the study basins were generated using the nearest neighbor interpolation technique.

Five near-global satellite products are used in this study. Three of these products are from the National Aeronautics and Space Administration (NASA) Tropical Rainfall Measuring Mission (TRMM) Multi-satellite Precipitation Analysis (TMPA) (Huffman, et al., 2007). The TMPA is available with a near-real-time, a climatological bias-adjusted and a gauge-adjusted version (hereafter 3B42-RT, 3B42-CCA and 3B42 respectively) (Huffman, et al., 2010). Another IR based precipitation product is the Precipitation Estimation from Remotely Sensed Information using Artificial Neural Networks (PERSIANN), which uses a coincident MW calibrated neural network technique to relate IR observations to rainfall estimates (Hsu, et al., 1997). The fifth product is the National Oceanic and Atmospheric Administration (NOAA) Climate Prediction Center morphing technique (CMORPH), which uses multi-satellite based MW rain estimates integrated in space and time using motion vectors derived from IR images (Joyce, et al., 2004). The spatial and temporal resolutions of the satellite rainfall products used in this study are 0.25 degree at 3 hourly time intervals covering the same period as the gauge rainfall product. As with the rain gauges, all four satellite products were spatially interpolated to derive basin-average precipitation, using the nearest neighbor approach (taken the center of satellite pixel as the equivalent station location).

Since satellite products represent 3-hourly rainfall values, hourly rain gauge basin-average rainfall time series were averaged every three consecutive time steps (i.e. 00, 03, 06, etc., synoptic hours) so as to match the CMORPH and PERSIANN products. Since the 3B42 post-real-time product represents MW or IR rainfall estimates within ±1.5 hours of the synoptic hours, we have taken a different approach of matching

gauges to this product. Namely, hourly basin-average rain gauge rainfall values were temporally averaged within ±2 hours around each synoptic hour to represent the 3-hourly temporal intervals of the product.

2.3 Methodology

A large number of precipitation events (3,249) based on the 8-year (2003-2010) rain gauge record was grouped into warm (May-Aug) and cold (Sep-Dec) season months (the terms warm season months and May-Aug, as well as cold season months and Sep-Dec are used interchangeably in the text). These events were used to evaluate systematic and random error metrics of the three satellite products and their dependency on seasonal characteristics of storms, basin scale and event severity. Analysis was based on basin-average precipitation rather than the usual pixel-based comparison. This approach allows us a more direct inference on the hydrological impact of the satellite precipitation estimation error. Thirteen basins with area greater than 200 km^2 were considered in this study and summarized in Table **2.1**. Basins with area less than 530 km^2 (namely the approximate mean area of satellite pixels over the study area) are classified here as small-size basins, while basins with area greater than this threshold are classified as medium size.

Table 2.1. Summary of basin information

Scale Class	Area (km^2)	Elevation (m.a.s.l)		Gauges	
		mean	STD	number	mean elevation
S1[1]	208	2040	606	13	1163
S2	236	1859	401	9	1076
S3	255	1894	448	12	1304
S4	345	1884	691	13	1388
S5	391	1892	516	10	1268
S6	417	1598	557	13	935
S7	427	1770	744	14	1258
S8	505	2008	618	16	1308
M1[1]	1262	1979	673	26	1206
M2	1906	1958	687	44	1255
M3	1992	1951	690	46	1231
M4	2863	1904	758	68	1230
M5	4166	1770	838	85	1185

[1] S and M stand for small and medium

2.3.1 Event identification and matching

Basin precipitation events were extracted from the rain gauge and satellite rainfall records for two distinct periods (May-August and September-December) using an ad hoc 9-hour zero-rainfall time window to represent inter-storm periods. The sensitivity of the results on the selected time window was investigated (not shown here) and found to be low for values in the range of 9-16 hrs. Our choice to use the lower value was to allow capturing the smaller duration storms in our database. Precipitation events identified on the basis of the rain gauge (i.e. reference) and satellite basin-average precipitation time series were matched according to their centroid differences as following:

$$\left|t_{c,s} - t_{c,g}\right| \leq R \tag{2.1}$$

where $t_{c,s}$ and $t_{c,g}$ are the centroids of the satellite and gauge precipitation events defined as:

$$t_c = \frac{\sum_{t=1}^{T_s} t \cdot p(t)}{\sum_{t=1}^{T_s} p(t)} \tag{2.2}$$

where $p(t)$ is the basin-average precipitation rate (mm·h^{-1}) at each time step t (3-hourly) of the event duration T_S. R is defined based on the reference data as:

$$R = \max(t_c - t_b, t_e - t_c) \tag{2.3}$$

where t_b and t_e are the beginning and ending time of the gauge-defined precipitation events, respectively. It is possible that for a given gauge-defined precipitation event with $t_{c,g}$ there are more than one eligible satellite-defined precipitation events. In those cases, the satellite precipitation events were merged into one event. Precipitation events with cumulative basin-average reference precipitation greater than 3 mm were considered in this study to eliminate minor events with negligible hydrologic response.

Table 2.2 lists the properties of the selected events. As noted from the table the May-August period has larger number of precipitation events (nearly twice as much as the Sep-Dec period) but events in the Sep-Dec period have longer duration and higher rainfall accumulations, due to the distinct meteorological patterns in these two periods. It is also noted that the basin-average precipitation accumulations (R_V) for the May-Aug period events are lower than those of the Sep-Dec period events for the small scale basins, while

for the medium scale basins the R_V values tend to be similar in the two periods. Figure 2.2 shows the empirical cumulative density functions (CDFs) of the precipitation event durations, basin-average precipitation accumulation and maximum event precipitation rates derived from the reference data. As shown in Table 2.2, small basin scale precipitation events in Sep-Dec period exhibit longer durations when compared to the May-Aug period events, and this parallels with higher rainfall accumulations during the Sep-Dec period relative to the May-Aug. It is also noted that in the Sep-Dec period, small size basin events have larger population in low quantiles (less than 12mm R_V) yet the population in high quantiles is smaller relative to the R_V values from the medium size basin scale events. Moreover, it is noted that small basin warm season precipitation accumulation CDFs exhibit lower precipitation accumulations than those in cold season months, while the distributions of maximum precipitation rates for events in both medium and small basins during warm season months exhibit slightly higher values than those in cold months.

Table 2.2. Summary of event properties

Scales	Num. of Events		Duration (h)		Rainfall Accumulation (mm)	
	Warm	Cold	Warm	Cold	Warm	Cold
S1	181	90	36	52	17	25
S2	153	80	46	59	15	20
S3	161	98	58	56	18	19
S4	180	92	41	58	15	22
S5	199	107	44	49	19	21
S6	117	75	53	61	16	18
S7	170	86	42	61	14	20
S8	156	87	66	72	21	26
M1	159	90	67	67	18	18
M2	157	93	74	71	20	19
M3	156	92	74	71	20	19
M4	153	88	82	84	21	21
M5	147	82	86	90	18	20

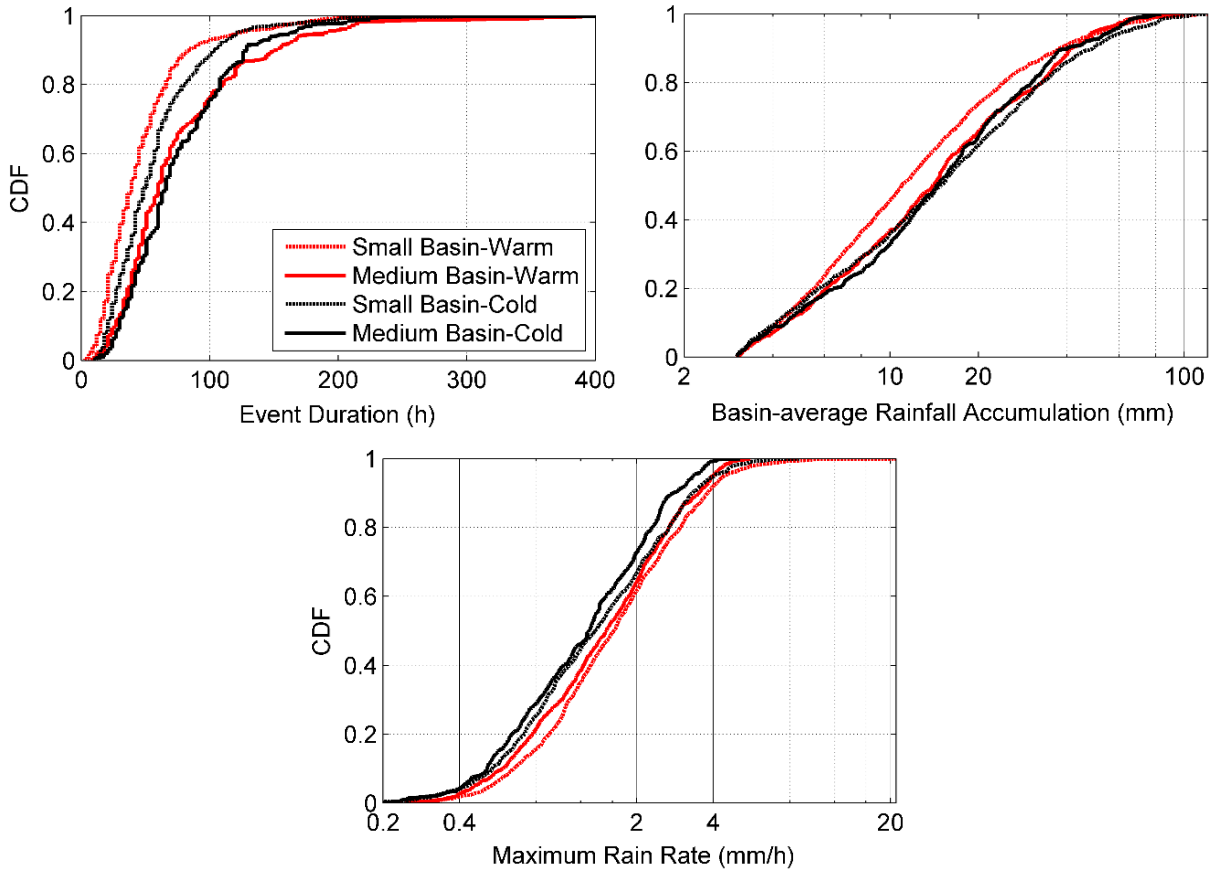

Figure 2.2. Event-based empirical cumulative density functions (CDFs) of event duration, *D* (upper left panel), basin-average rainfall accumulation, R_V (upper right panel), and maximum rain rate, R_M (lower panel), derived from reference rainfall.

The precipitation events were grouped according to values of basin-averaged precipitation accumulation associated with the 50th, 80th, 90th and 95th percentiles. Values below the 50th percentile were associated with low rainfall accumulation (smaller than 10mm see Table 3) and are excluded from this analysis since our interest is towards moderate to heavy precipitation events. The quantile values for the different basin scales and periods are summarized in Table 2.3. It is noted that the quantile values are greater in the Sep-Dec months than those for the May-Aug months, which is consistent with the cumulative distributions shown in Figure 2.2 and points to the contrasting precipitation properties in these two periods.

Table 2.3. Thresholds according to the selected quantiles

Scales	Q50		Q80		Q90		Q95	
	Warm	Cold	Warm	Cold	Warm	Cold	Warm	Cold
S1	11	14	22	38	31	53	44	62
S2	9	13	19	33	33	43	37	54
S3	8	15	20	28	38	36	49	49
S4	8	13	23	23	42	39	59	46
S5	13	14	29	28	39	40	48	61
S6	14	16	33	32	45	44	58	63
S7	12	17	24	39	33	60	57	77
S8	14	16	30	38	52	63	56	79
M1	12	14	27	28	37	37	48	55
M2	13	13	30	27	37	37	42	47
M3	13	16	28	32	40	45	51	59
M4	14	14	33	30	43	37	50	52
M5	15	14	34	31	43	37	50	53

2.3.2 Evaluating Metrics

Three evaluation metrics termed as relative centroid displacement (d_c), multiplicative error (ε) and a herein established accuracy index (AI) are selected for describing the degree of disagreement between reference (i.e. gauge precipitation) data and the four satellite-derived precipitation products.

A number of studies have shown that temporal error characteristics in precipitation estimates may propagate to the simulated hydrograph producing timing errors (Mei, et al., 2014a; Nikolopoulos, et al., 2013; Zoccatelli, et al., 2011; Yong, et al., 2010; Su, et al., 2008; Sharif, et al., 2002). However, to the best of our knowledge, these error characteristics have not been exploited to develop a metric for the evaluation of satellite precipitation estimates. The relative centroid displacement, Eq.(2.4), is therefore proposed herein as a metric to depict the error in estimating from satellite observations the time-of-arrival of the event temporal center of mass:

$$d_c = \frac{t_{c,s} - t_{c,g}}{D_g} \tag{2.4}$$

where D_g stands for the duration of gauge precipitation event. The numerator in Eq.(2.4) represents the centroid displacement. Since we have shown that the durations of events in Sep-Dec are in general shorter

than those in May-Aug months, we normalized the absolute displacements to the corresponding gauge-derived event durations. By the definition of t_c from Eq.(2.2), $t_{c,s}/t_{c,g}$ represents the temporal centroid location in terms of satellite- or gauge-retrieved basin-averaged precipitation rate for a matching event pairs; thus, positive and negative d_c values represent delay and advance in arrivals of storm center of mass, correspondingly. In practice, d_c reflects the situation of either early or delayed detection of storm events, which could be an important property when dealing with prediction of basin's hydrologic response.

The multiplicative error, ε, defined as the ratio between gauge-event properties to the corresponding satellite-event property is one of the classical error metrics used in satellite precipitation error studies, e.g. Hossain & Anagnostou (2006):

$$\varepsilon = \frac{I_S}{I_G} \tag{2.5}$$

where I_S and I_G are the basin-average rainfall properties derived from satellite products and gauges. The event properties are defined as:

$$\text{Event Duration: } D = t_e - t_b \tag{2.6}$$

$$\text{Event Rainfall Accumulation: } R_V = \sum_{t=1}^{T_s} p(t) \tag{2.7}$$

$$\text{Event Maximum Rainfall Rate: } R_M = \max_{t \in T_s}[p(t)] \tag{2.8}$$

Values of ε greater or smaller than one correspond to overestimation or underestimation, respectively, of the satellite product related to the reference for a given event property.

We introduce in this study an error metric (called Accuracy Index, *AI*) that is based on the ratio of the geometric to the arithmetic means of the satellite product and gauge based event properties (I_S and I_G):

$$AI = \frac{2\sqrt{I_S I_G}}{I_S + I_G} \tag{2.9}$$

AI is bounded between 0 and 1 given that the geometric mean would be always less or equal to the arithmetic mean (Steele, 2004). *AI* is more comprehensive than ε in that it incorporates both magnitude and rain detection discrepancies in the satellite derived products. Specifically, when either I_S or I_G is 0, *AI* would

equal to 0 denoting either missing or false alarm of satellite estimate; on the other hand, if I_S is equal to I_G, *AI* is 1, which implies perfect match between the two datasets. We attempt to visualize this index by relating it to the multiplicative error metric ε as following:

$$AI = \frac{2\sqrt{\varepsilon}}{\varepsilon + 1} \tag{2.10}$$

Figure 2.3 (panel a) shows the above relationship. As noted, *AI* is symmetric with respect to ε=1 (unbiased estimator), which divides the error into underestimation (left side) and overestimation (right side). As an example, if ε equals to 0.2, 0.1 or 0.02 (5, 10 and 50) the corresponding *AI* values are 0.75, 0.57 or 0.28, respectively, which indicates a non-linear relationship between the two metrics.

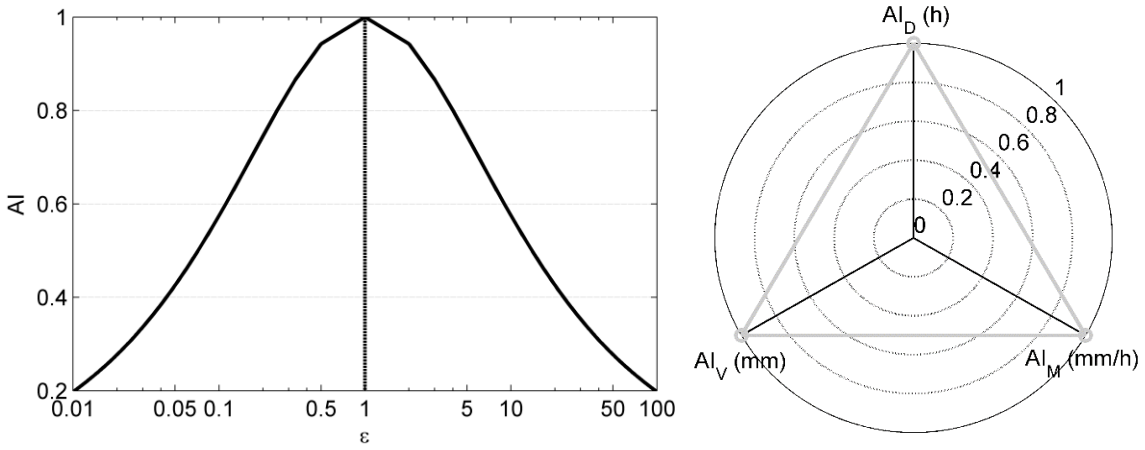

Figure 2.3. Left panel: the relationship between *AI* and ε; Right panel: schematic depicting the way score *S* is calculated.

AI and ε will be used in the herein analysis to provide complementary evaluations of the different satellite products. Specifically, ε will define the degree of overestimation (underestimation) of the satellite products for each event property separately, while *AI* will enable a combined evaluation of the three event properties (D, R_V and R_M) using a score system defined by a triangle with area (A) determined as:

$$A = \frac{\sin\alpha}{2} AI_D AI_V + \frac{\sin\alpha}{2} AI_V AI_M + \frac{\sin\alpha}{2} AI_M AI_D \tag{2.11}$$

where AI_D, AI_V and AI_M represent the AI values for D, R_V and R_M, and α is the angle between the different axes (120°). This triangle area is normalized with respect to the maximum triangle area to derive a score index (S) ranging between 0 (missing or false alarm) and 1 (accurate matching):

$$S = \frac{AI_D AI_V + AI_V AI_M + AI_M AI_D}{3} \tag{2.12}$$

S is employed in this study as an indicator of satellite skill determined for each event separately or on the basis of all events combined. One of the main assumptions of our formulation is that the three event properties are considered having equal weight in evaluating the score index for the satellite rainfall products. The weighting of the different event properties in the score index is an aspect that could be evaluated in future research on the basis of the relative significance of these properties on the flood hydrograph.

2.4 Results

2.4.1 Displacement of Centroid

As discussed in section 2.3.2 the displacement of basin-average precipitation centroid is an important error property that relates to the application of satellite precipitation data for simulating basin flood response. In Figure 2.4 we show the displacement between event centroid locations defined in Eq.(2.4). Results suggest that the displacement in event centroid is random implying no preference on either advance or delay of detection, because values of d_c display neither scale nor quantile dependency and distribute around zero (refer to the median location). However, as quantile range increases in value the range of d_c becomes narrower in most of the cases, pointing to the fact that satellite precipitation events from high quantile ranges have better consistency in terms of matching the timing of storms centroid. Apparently, high-quantile events are associatted with long duration, which result overall in a reduced relative displacement. It could thus be stated that the effect introduced by the shift in centroid is more significant for shorter duration events. Besides, events from medium basin scale tend to have smaller d_c values ranges

due to again the longer event duration of this event class which reduce the d_c. A product-wide comparison indicates that none of the product has distinctly good or bad performance by means of arrival of the centroids compared to the others, but the three 3B42 products show better convergence trend as quantile ranges increase. Consequently, the timing error being propagated to the hydrograph is more pronounced for shorter duration events (events typically from small basin and convective rainfall system).

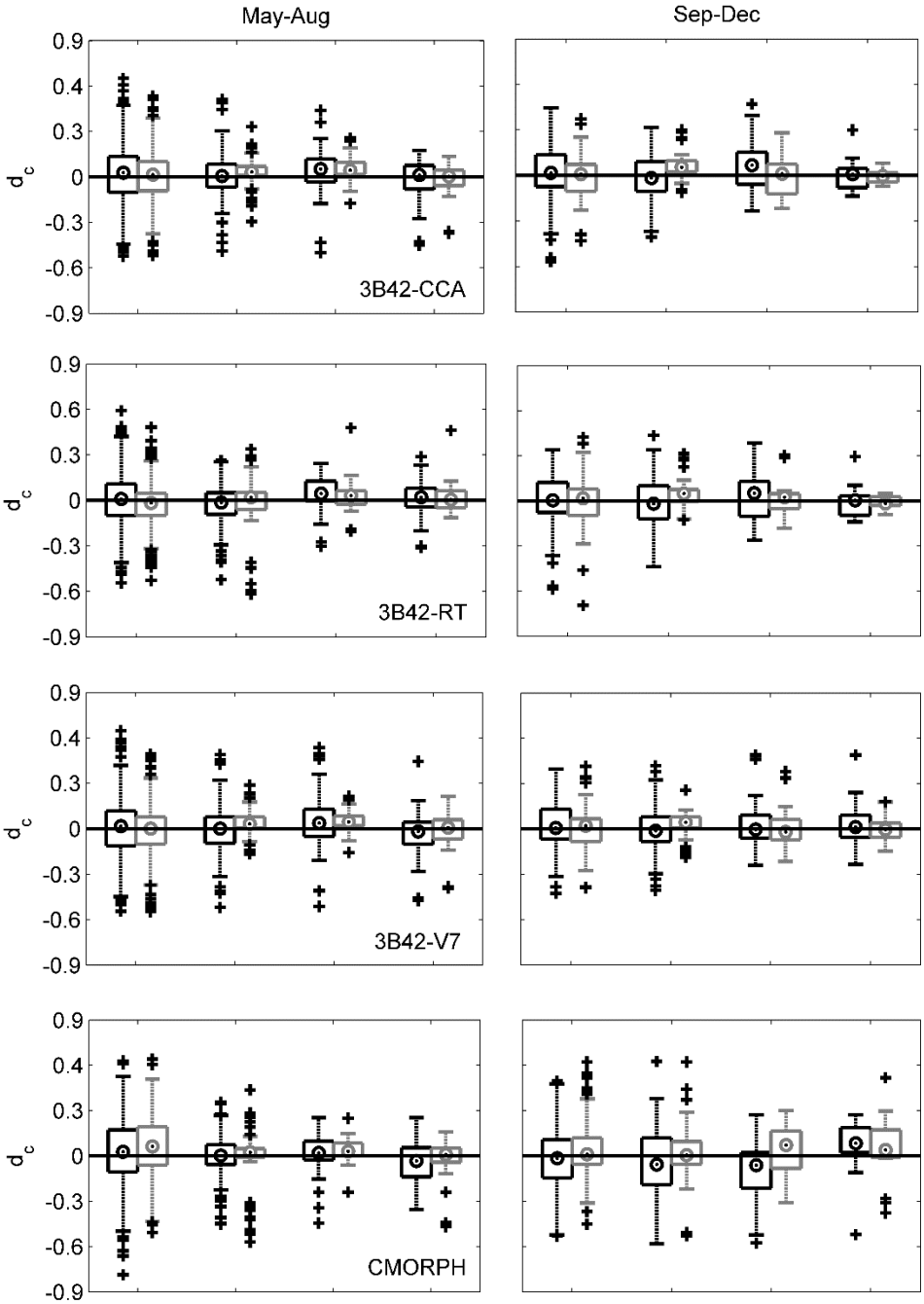

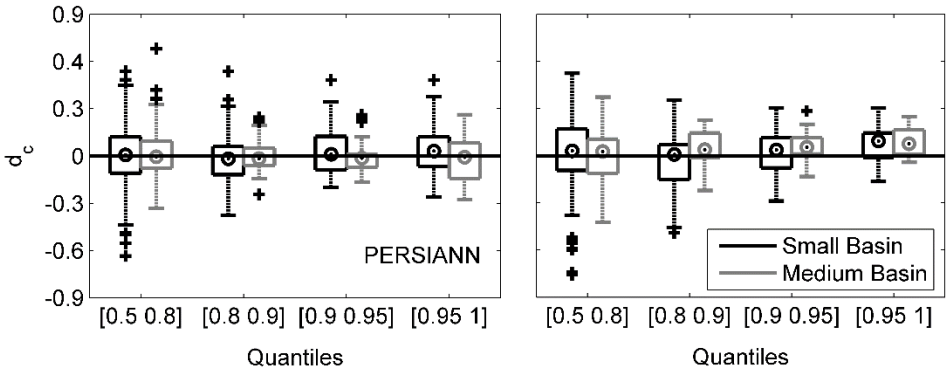

Figure 2.4. Box plots of event centroids displacement between the various satellite products and gauge-derived basin-average rainfall.

2.4.2 Multiplicative Error Analysis

Figure 2.5 shows the box plots of the event-based multiplicative error (ε) for different satellite products, i.e. quantile ranges, and the two basin scales over the May-Aug and Sep-Dec months. A first observation from Figure 2.5 is that the satellite estimates, especially CMORPH and PERSIANN, during Sep-Dec period, tend to underestimate the gauge rainfall in all quantile ranges and at both basin scales. These results are in general agreement with other studies that has shown significant underestimation from CMORPH and PERSIANN techniques over complex terrain and during cold season months due to snow contamination and low level orographic enhancement (AghaKouchak, et al., 2011; Tian, et al., 2009; Dinku, et al., 2007). On the other hand, the three 3B42 products (CCA, RT and V7) exhibit better consistency with the gauge-based reference data in both periods and basin scales. A reason behind this could be that the 3B42 products are retrievals based on combined IR and MW information while CMORPH or PERSIANN is solely MW- or IR-based.

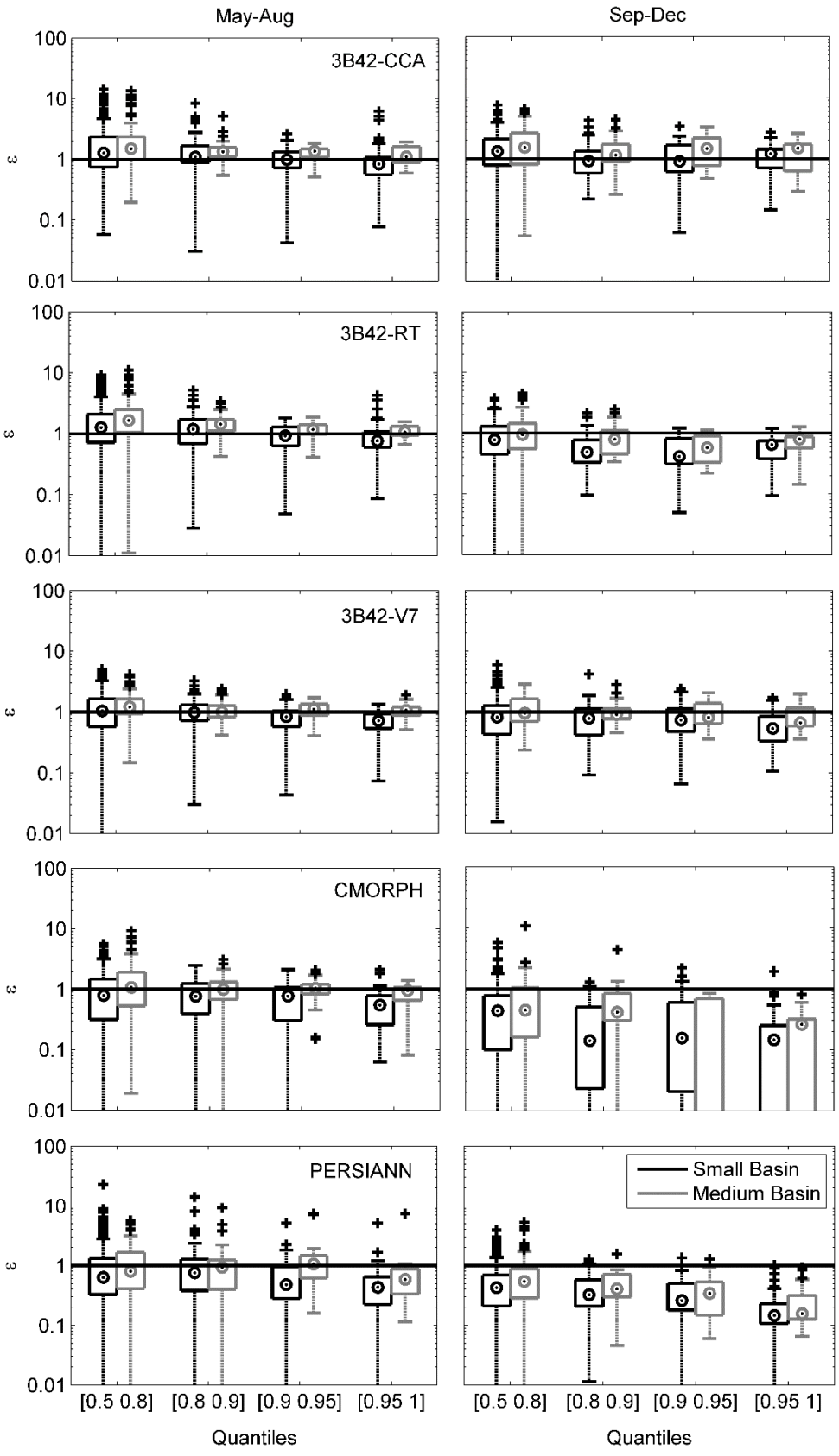
May-Aug
Sep-Dec
3B42-CCA
3B42-RT
3B42-V7
CMORPH
PERSIANN
Small Basin
Medium Basin
100
10
1
0.1
0.01
[0.5 0.8]
[0.8 0.9]
[0.9 0.95]
[0.95 1]
Quantiles

Figure 2.5. Box plots of event multiplicative error between the various satellite products and gauge-derived basin-average rainfall.

Furthermore, from these results a magnitude dependent error structure is noted ranging from overestimation to underestimation as the quantile range increases. In addition, results for 3B42 products indicate a convergence trend (namely, shorter 25^{th}-75^{th} interquartile range, shorter tails and decreasing number of outliers) in the ε values towards the higher quantiles of reference precipitation accumulation and for the medium size basins. This trend is not apparent for the other two products (only PERSIANN during cold months is showing a convergence and for only the medium size basins). It is also noted from the box plots that the median of ε values for the small scale basins is more skewed relative to the medium size basins for CMORPH and PERSIANN, pointing to the fact that the satellite precipitation error for the medium size basins is better represented by the mean value. It is briefly summarized here that satellite-precipitation estimates for smaller basins, higher quantile ranges or months with colder temperatures have lower values of multiplicative error (namely satellite underestimation), while for lower quantile ranges and larger size basins they exhibit overestimation.

A more focused analysis on the most severe events (precipitation accumulations greater than the 90^{th} quantile) was conducted with results reported in Figure 2.6 scatter plots and corresponding statistics reported in Table 2.4. Significant scatter is noted in all comparisons of satellite versus reference basin average precipitation accumulations. It is noted that underestimation is the most dominant scenario, particularly for CMORPH and PERSIANN products during cold months, which matches the multiplicative error distributions shown in Figure 2.5. Visually, 3B42-V7 has better correlation to gauge-based basin-average precipitation accumulation, which is also statistically supported by the correlation coefficients (*CC*) reported in Table 2.4 (*CC* for 3B42-V7 warm period is 0.51 the highest). This is expected since 3B42-V7 is adjusted to the actual monthly gauge. However, 3B42-V7 is ambiguously correlated to gauge during Sep-Dec months even with its gauge-adjusted feature. A possible explanation of this could be due to the uncertainties in gauge estimation of precipitation during cold period of the study region. Surprisingly, the

cold period scatter plot for 3B42-RT exhibits better linearity compared to its post-real-time counterpart in Figure 2.6 with the highest *CC* value (0.39) and relatively higher (but in absolute terms low) *CC* value in the May-Aug period (0.44), displayed in Table 2.4. Besides *CC*, the root mean square error (*RMSE*) statistic is also rendered for the comparison purpose. It is seen that the *RMSE* values for 3B42-V7/-RT is the lowest for the May-Aug/Sep-Dec period. CMORPH and PERSIANN are marked by low correlation and high magnitude discrepancies. Finally, all satellite rainfall products have nearly null Nash-Sutcliffe index values, meaning that these estimates perform merely as the mean of reference data in terms of predicting small to medium basin-scale event rainfall accumulations.

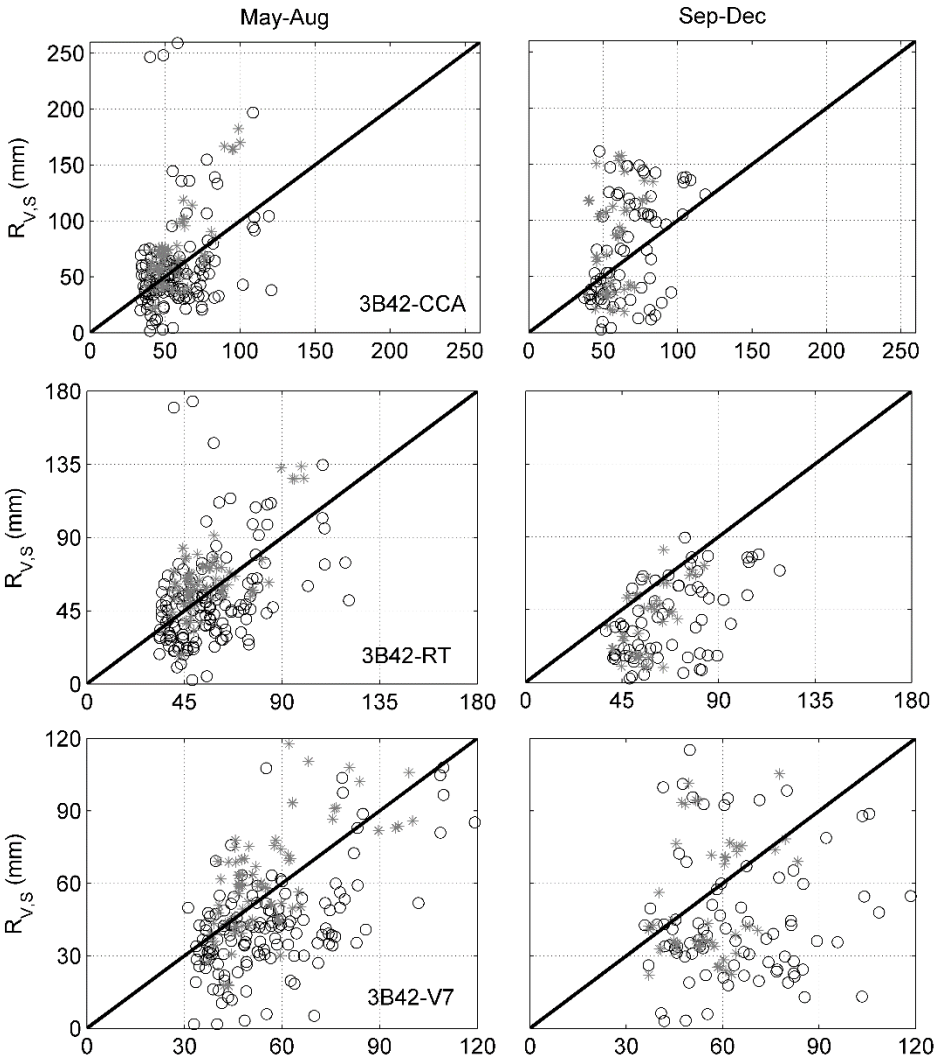

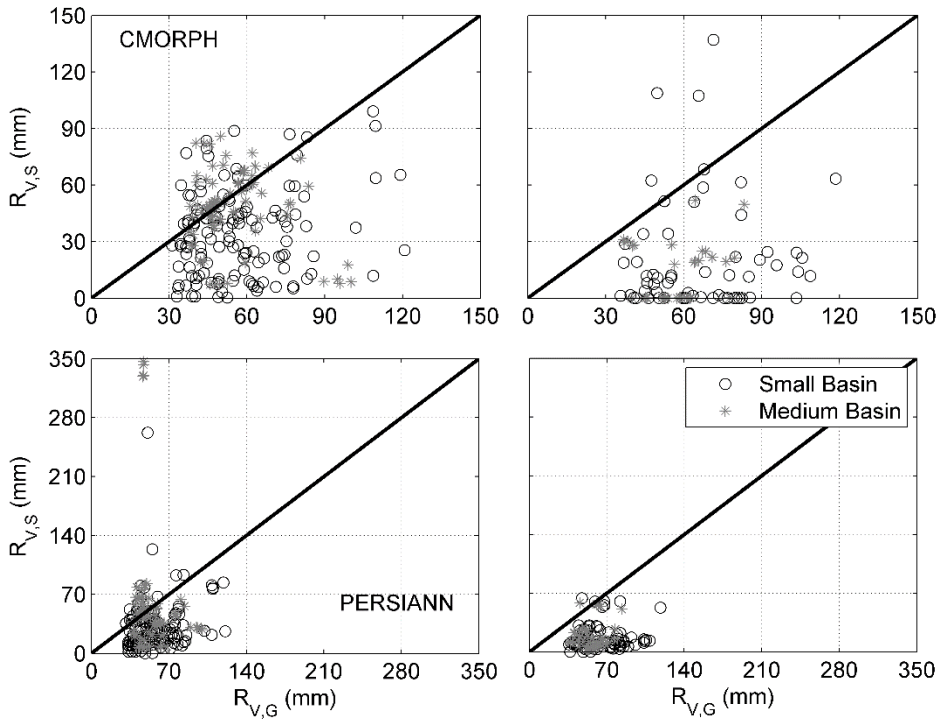

Figure 2.6. Scatter plot of satellite product vs. gauge-derived basin-average rainfall accumulation for events above Q90.

Table 2.4. Satellite product evaluation statistics for Q90 storm events

Periods	Statistics	3B42-RT	3B42-CCA	3B42-V7	CMORPH	PERSIANN
Warm	CC	0.44	0.38	***0.51***[1]	0.06	0.00
	RMSE	0.45	0.66	***0.38***	0.57	0.98
Cold	CC	***0.39***	0.34	0.04	0.11	0.06
	RMSE	***0.50***	0.72	0.54	0.86	0.80

[1] Bold italic fonts indicate best results among products

2.4.3 Score System Analysis

The score system, defined in section 2.3.2, was applied on the five satellite products by averaging the *AI* values over events belonging in the Q80 to Q100 quantile range for the two seasons and basin sizes with results demonstrated in Figure 2.7. The figure shows that *AI* values of duration for the products are all above 0.9 with negligible distinction (except for CMORPH with identifiably weaker performance in predicting the event durations), implying reasonable and similar performances in capturing the duration of the

reference precipitation. This is anticipated since the analyzed event population is for the most significant events (above the 80th quantile), which in general are associated with long durations and high rainfall accumulations, thus, the detection error by satellite is expected to be low. Although the rainfall duration is captured well, satellite estimates of basin-average storm total and maximum precipitation rate exhibit considerable uncertainty. As shown in Figure 2.7, the AI_V and AI_M values are high for the May-Aug months (around 0.9) but considerably low for the Sep-Dec months except for the three 3B42 products, which have both values still above 0.9. This finding confirms the results from Figure 2.5 that the error is quite close to 1 for the warm period but notably distant from 1 for cold months particularly for the CMORPH and PERSIANN. It is specifically shown that *AI* index for precipitation accumulation and max rain rate of CMOPRH are exceptionally low, ranging between 0.5 and 0.7 (0.7 to 0.9 for PERSIANN). Based on the evaluations on duration and magnitude in terms of *AI*, we can state that the snow contamination effect has a much stronger impact on the estimation of precipitation magnitude than that on duration in the event basis. Consequently, it appears that the CMORPH and PERSIANN algorithms lack the accuracy in those complex terrain heavy precipitation events, while 3B42 products can provide a more accurate estimation of the three storm parameters (rainfall accumulation, maximum rainfall rate and duration).

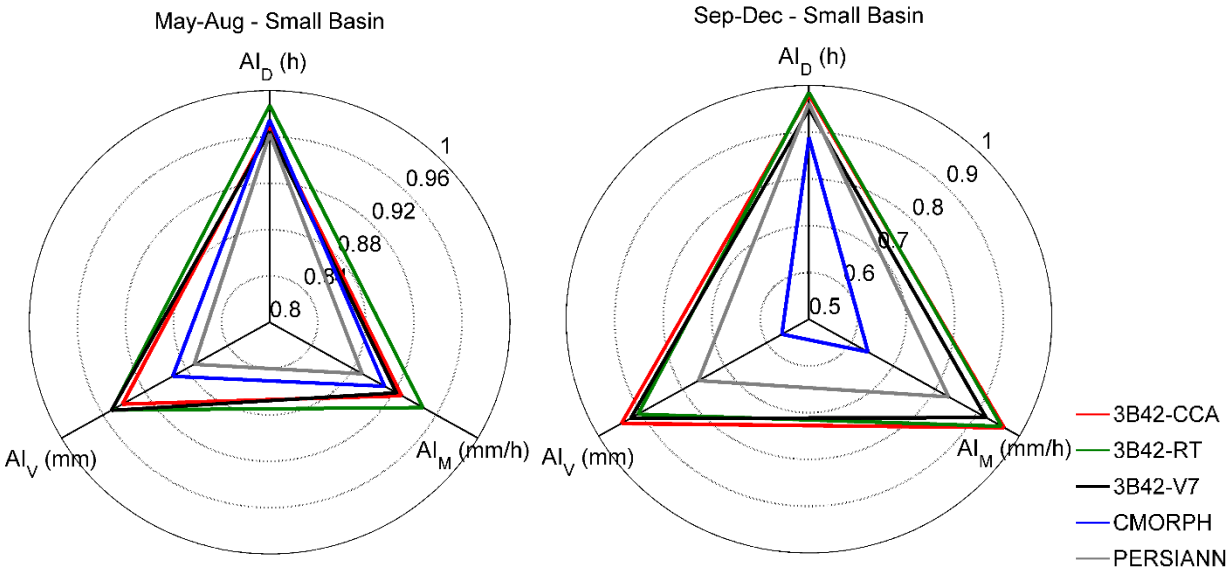

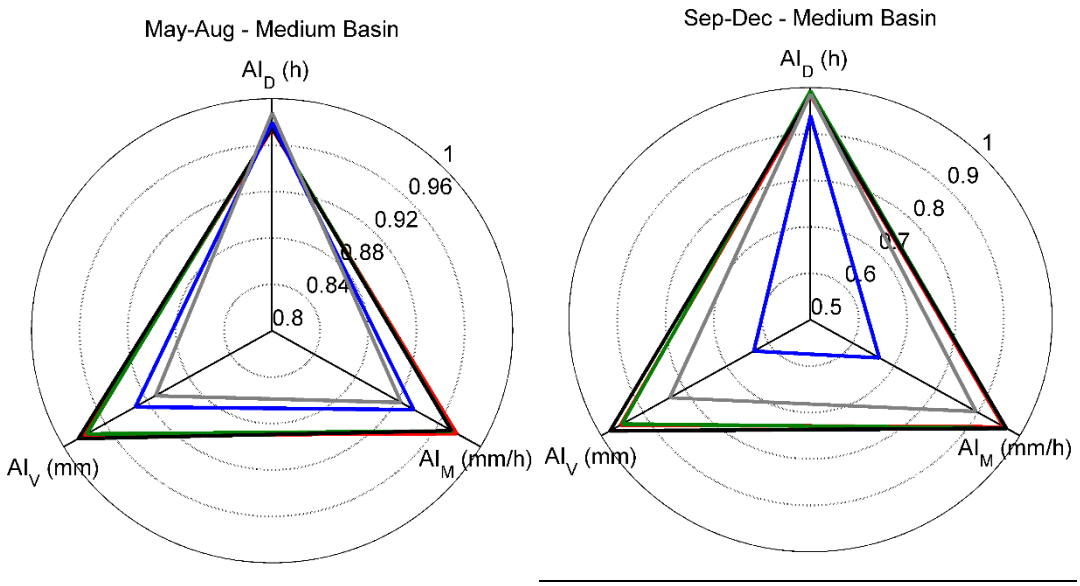

Figure 2.7. Polar plots of *AI* for the three event properties determined for the different seasons and basin scales.

A consecutive investigation on the Score (*S*) for the storm events exceeding the 80th percentile is shown in Table 2.5 and Figure 2.8. Table 2.5 lists the *S* values from Figure 2.7 (numbers in italic represent the best estimates based on seasons and basin sizes). The three 3B42 products surpass the other two satellite products to a great extent with *S* being over 0.9. The 3B42-RT scores no worse than 3B42-V7 and 3B42-CCA with a few obscure differences. Meanwhile, the values of standard deviation (STD) of *S* for 3B42-V7 are the smallest except for the small scale cases. It can be inferred that smaller STD could indicate better performance given the median of S is close to 1, namely *S* values tend to locate towards 1. The box plots of *S* determined for each product for the two seasons and basin scales are juxtaposed in Figure 2.8. The results reveal our findings according to Figure 2.7. Again, the 3B42 products show better consistency to gauge data with median locations fairly close to unity and low variability of *S*. In addition, the median locations for the other two products are apart from 1 with considerable large variability in *S* values (no outliers for CMORPH and PERSIANN in cold season) demonstrating worse performances compared to the three 3B42 products. In terms of seasonality, May-Aug months, exhibit smaller quantile range compared to the Sep-Dec months. To summarize, 3B42-V7 could be an eligible algorithm in retrieving rainfall over

medium scale basins while its unadjusted and CCA-adjusted version (3B42-RT and 3B42-CCA) provides sensible precipitation estimates for small scale basins in warm and cold season months. Overall, the 3B42 precipitation products are shown to outperform CMORPH and PERSIANN algorithms in terms of the *S* score examined; the algorithms of CMORPH and PERSIANN should be improved for cold season precipitation.

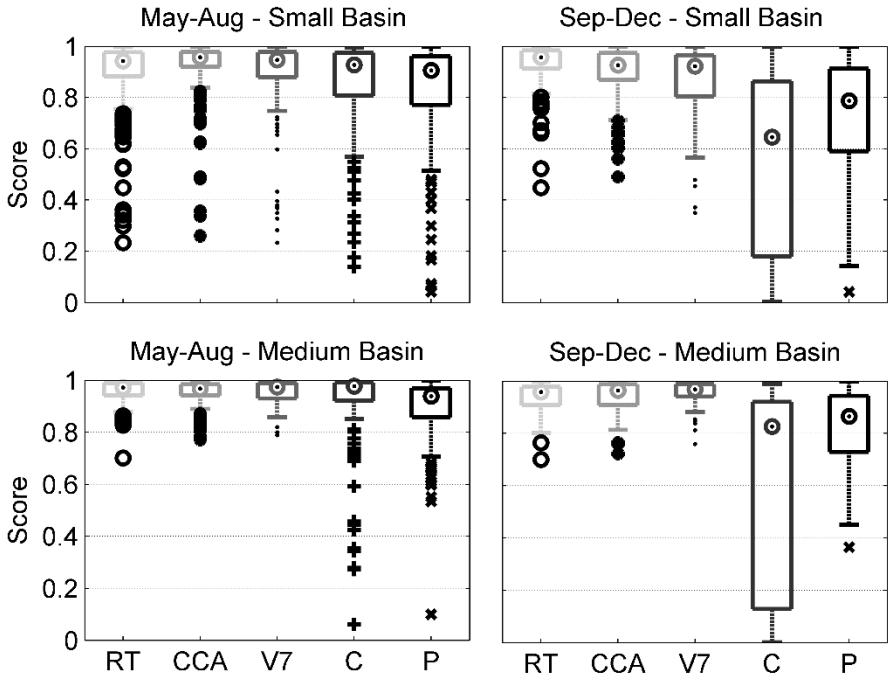

Figure 2.8. Box plots of score for the four satellite rainfall products based on events above Q80 (RT, CCA, V7, C and P stand for 3B42-RT, 3B42-CCA, 3B42-V7, CMORPH and PERSIANN).

Table 2.5. Comparison of products scores for different periods and scales

Periods	Scales	Stats	3B42-RT	3B42-CCA	3B42-V7	CMORPH	PERSIANN
Warm	Small	Mean	***0.93***[1]	0.90	0.90	0.86	0.84
		STD	***0.10***	0.14	0.13	0.17	0.18
	Medium	Mean	0.95	0.96	***0.96***	0.91	0.89
		STD	0.05	0.05	***0.04***	0.16	0.13
Cold	Small	Mean	0.90	***0.93***	0.88	0.55	0.74
		STD	0.10	***0.09***	0.13	0.35	0.21
	Medium	Mean	0.94	0.93	***0.95***	0.58	0.82
		STD	0.06	0.06	***0.05***	0.39	0.16

[1] Bold italic fonts indicate best results among products

[2] STD stands for standard deviation

2.5 Conclusions

In this study we review and evaluate the performance of five widely used global-scale satellite products over a mountainous area using variable spatiotemporal scales for comparison. Specifically, satellite products are evaluated for separate storm events and different basin areas. Three evaluating metrics, namely relative centroid displacement (d_c), multiplicative error (ε) and a score index (S) are used to quantify the satellite precipitation estimation performance. The d_c is a metric for depicting the timing error of the precipitation event; ε represents the multiplicative error (i.e. bias ratio) in the event basin-average precipitation accumulation; S accounts for the errors in three different properties of the storm events: the event duration, basin-average precipitation accumulation and event maximum rainfall rate. S is an error metric newly defined in this study, based on an accuracy index (AI) metric that was shown to be nonlinearly related to ε. Although AI cannot display the direction of error, it has the virtue of value unity (possible value space is bounded between 0 and 1), which allows a universal comparison of different precipitation, or hydrologic properties, of storm events.

It was shown that there is no clear trend in either the delay, or advance, in detection over different event precipitation accumulation quantiles, seasons (summer vs. fall) or basin scales for the different satellite products. The variability of disagreement in the event-based basin average precipitation centroid was shown to be more prominent for short duration events over small scale basins and low event-precipitation accumulations regardless of the satellite precipitation product. This implies that we cannot discriminate between satellite products in terms of timing error for hydrologic simulations.

On the other hand, all satellite products were shown to exhibit significant uncertainty in the estimation of basin-average precipitation accumulation at the event basis as indicated by ε. The degree of discrepancy is shown to vary between summer and fall months, basin scale and event severity (surrogated by basin-

average precipitation accumulation in this paper). A trend of overestimation to underestimation with increasing the quantile ranges of basin-average precipitation accumulation was shown, and was particularly apparent for the CMORPH and PERSIANN products. The uncertainty of this trend, visualized as the value range of ε, is in general decreasing with increasing precipitation accumulation quantile values and basin scale (CMORPH in cold season was an exception). For heavy precipitation events, the results demonstrated that the three 3B42 products exhibit better correlation as well as lower degree of disagreement (quantified by *RMSE*) to the gauges, while CMORPH and PERSIANN significantly underestimated the reference data (particularly in the fall-early winter months period).

Similar results are established from the *AI*-based score index. The predictive accuracy of satellite products for the selected event properties (event duration, basin-average storm total and maximum precipitation rate) in heavy precipitation events during the summer months is acceptable (*S* greater than 0.9), especially in estimating the storm duration. A reasonable prediction (*AI* for duration above 0.9) for the duration is also shown during the fall-early winter months. However, the retrieved basin storm accumulation and maximum precipitation rates are inaccurate for CMORPH and PERSIANN for the Sep-Dec months. A slight decrease of the *AI* for basin-average precipitation accumulation and max rate is also observed for the 3B42 products. Overall, the *score* index for 3B42 products are concentrated near unity with higher degree of centralization for the medium size basins during summer months. 3B42-V7 is shown to be the best product in predicting event precipitation occurring over medium scale basins, while 3B42-RT and 3B42-CCA outperformed 3B42-V7 in estimation for the small scale basins over warm and cold period, respectively. The evaluation of cold period precipitation events by CMORPH or PERSIANN estimates exhibited low *score* indices.

Although the study is based on a long data record (8 years), it represents a limited hydro-climatic and geomorphologic regime, and results can only be generalized for similar mountainous regions and orographic-driven precipitation events. Furthermore, given the mountainous setting and the early winter cold months considered in the study, we note the varying effects that snow covered surfaces and mixed-

phase precipitation can have on the satellite retrievals examined herein. Specifically, CMORPH is particularly prone to the effect of snow-screening on MW rainfall estimates, typically assigned zero rainfall values, which are propagated through the morphing technique, thus introducing strong underestimations of precipitation accumulations. Future, extensions of this study should focus on evaluating these surface effects using in situ meteorological and snow cover datasets. Furthermore, the value of higher spatial resolution satellite rainfall products (e.g. PERSIANN at ~0.04^{o} and CMORPH at ~0.07^{o}) should be examined, particularly during the warm season convective events, and evaluated in terms of their error propagation in simulating the hydrologic response of mountainous basins.

Chapter 3 Evaluating Satellite Precipitation Error Propagation in Runoff Simulations of Mountainous Basins

3.1 Introduction

Integration of satellite precipitation products with hydrologic models constitutes a potential solution for simulating hydrological processes at global scale. Such an approach is particularly important for mountainous areas where spatial coverage of precipitation observations is limited because of the generally low number of in-situ sensors and the blockage of ground remote sensors due to complex terrain. In this context, satellite sensors offer unique advantages relative to ground sensors since they can provide fine resolution observations of precipitation at quasi-global scale, uninhibited by mountains or spatial inconsistencies (Anagnostou, et al., 2010; Kidd, et al., 2003; Arkin & Ardanuy, 1989). The significance of these advantages has been recognized by the hydrologic community and numerous studies have focused on the use of satellite precipitation retrievals in hydrologic applications in the past two decades (Nikolopoulos, et al., 2013; Bitew & Gebremichael, 2011; Su, et al., 2008; Yilmaz, et al., 2005; Grimes & Diop, 2003; Tsintikidis, et al., 1999; Guetter, et al., 1996; among others). Focusing specifically on the satellite-based hydrologic applications over complex terrain, Table 3.1 provides a representative list of past studies focused on evaluating the error propagation of satellite products over mountainous areas. It can be seen that before 2010, few studies exist on the topic, while the majority of these studies were designated for coarse temporal resolution (mostly daily or monthly) over medium to large-scale basins (sizes greater than 1000 km^2).

Table 3.1. List of satellite hydrologic error propagation studies in the literature focusing on complex terrain.

Study	Watersheds Characteristics		Hydrologic Simulation	
	Area (km^2)	Elevation (m)	Resolution	Length
Hossain & Anagnostou (2004)	116	390 - 2230	Hourly	15 HPEs
Li et al. (2009)	12696	1134 - 2700	Daily	6 years
Yong et al. (2010)	18112	427 - 2017	Daily & monthly	6 years
Nikolopoulos et al. (2010)	108 - 1200	100 - 2000	Hourly	1 HPE

Bitew et al. (2011)	299	1890 - 3130	Daily & monthly	5 years
Bitew & Gebremichael (2011)	299 & 1656	1880 - 3530	Daily	2 years
Li et al. (2012)	15500	50 - 2138	Daily & monthly	7 years
Jiang et al. (2012)	9972	49 - 2093	Daily & monthly	6 years
Yong et al. (2012)	18112	427 - 2017	Daily & monthly	9 years
Thiemig et al. (2013)	53000 - 130000 & 76000	40 - 287 & 400 - 3100	Daily	6 years
Nikolopoulos et al. (2013)	623	1140 (mean)	Hourly	1 HPE
Tong et al. (2014)	121972 & 137704	2728 - 5969 3804 - 5959	Daily & monthly	14 years
Zulkafli et al. (2014)	4640 - 363848	1300	Daily & monthly	12 years

Some of these studies have examined the hydrologic response of heavy precipitation in small scale complex terrain basins (Nikolopoulos, et al., 2013; 2010; Bitew & Gebremichael, 2011; Bitew, et al., 2011; Hossain & Anagnostou, 2004). Bitew et al. (2011) and Bitew and Gebremichael (2011) conducted studies for basins in the Ethiopia highlands; Hossain & Anagnostou (2004) and Nikolopoulos et al. (2013; 2010) examined storm events over the northeast Italian Alps that had caused flash floods. Two common observations have resulted from the above studies. Firstly, the accuracy of the satellite precipitation-driven simulations is affected by the storm event severity, the precipitation product resolution and basin scale (Maggioni, et al., 2013; Vergara, et al., 2013; Gourley, et al., 2011). Specifically, moderate precipitation magnitudes, finer product resolutions and larger basin scales are associated with the most accurate hydrological applications. Secondly, notable improvements in satellite-based streamflow simulations can be obtained after recalibration of the hydrologic model with corresponding satellite precipitation estimates. However, values of the recalibrated model parameters typically lie outside the physical range, indicating the lack of hydrologic representativeness of the parameters themselves (Nikolopoulos, et al., 2013; Yong, et al., 2012; Tobin & Bennett, 2009).

Two questions specific to satellite precipitation applications in mountainous basins arise from the above studies: Does gauge adjustment of satellite products yield consistently lower uncertainty in hydrologic simulations? And, how does the precipitation error translate through the hydrologic model simulation? For

the first question, Hossain and Anagnostou (2004), Nikolopoulos et al. (2013) and most of the recent literature argues that the gauge adjusted satellite products are more promising than the unadjusted counterparts. Yet, the investigation on the Ethiopia highland done by Bitew et al. (2011) and Bitew and Gebremichael (2011) showed that this is not always the case; critical factors to the improvements resulting from gauge adjustment is the number and representativeness of included gauges (Gourley, et al., 2011; Wilk, et al., 2006). Gauge adjustment can be considered as qualified over densely gauged areas (e.g. Continental US or parts of Western Europe). On the other hand, this adjustment may introduce unnatural features in the precipitation products particularly in areas exhibiting strong precipitation gradients. Regarding the patterns of error propagation, a nonlinear error transformation process is prevailing among the hydrologic studies; that is the hydrologic models can tolerate a relatively small amount of error by the integrated basin processes, but may amplify this error in high precipitation magnitudes (Yong, et al., 2012; 2010; Artan, et al., 2007; Guetter, et al., 1996). It has also been shown that the properties of error propagation (magnification/dampening, linear/nonlinear) depend on several factors such as antecedent moisture conditions (Nikolopoulos, et al., 2013; 2011; Bitew, et al., 2011) basin scale (Cunha, et al., 2012; Nikolopoulos, et al., 2010) and the choice of hydrologic model or modeling complexity (Zhu, et al., 2013; Carpenter & Georgakakos, 2006).

This study build upon the above works providing a comprehensive evaluation of three different satellite products and their gauge-adjusted counterparts comparing them against a reference precipitation dataset derived from a dense gauge network over the upper Adige river basin of the Eastern Italian Alps characterized by strong mountainous relief (200-3900 m a.s.l.). We acknowledge the fact that due to significant spatial variability in precipitation over the study complex terrain environment, the representativeness of gauge measurements should be noted as demonstrated in Nikolopoulos et al. (2015). To evaluate the error propagation in flood simulations satellite precipitation datasets were used to force a gauge-calibrated hydrologic model to simulate runoff for 16 cascade basins (areas ranging from 255 to 6967 km^2), and comparing them to the gauge-driven simulated hydrographs for a range of moderate to high

flood events spanning a nine-year period. Our study brings a more holistic investigation of the questions posed above relative to previous studies, by capturing the dependency of satellite-driven flow simulation error on basin scale, basin altitude, seasonality and product type for different event severities.

In the next section we introduce the study area and precipitation datasets used, while section 3.3 describes the data processing procedure and details on the hydrologic model. Section 3.4 presents the categorization method for the time series and the error metrics applied in the following analysis. Results are reviewed in section 3.5 and conclusions are drawn in section 3.6.

3.2 Study Area and Data

3.2.1 Study Area

The study area is the Upper Adige river basin closed at Bronzolo (~7000 km^2), a mountainous region covered by broad-leaf and conifer forests located in the Eastern Italian Alps (Figure 3.1). This region is characterized by steep topographic gradients with elevation ranging from 200 to approximately 3900 m a.s.l., which mean elevation at about 1800 m a.s.l.. There are sixteen cascade basins involved in our study with areas ranging from 255 km^2 to 6967 km^2 and mean elevation above almost 1700 m a.s.l. (see Table 3.2 for a summary). Precipitation in the region is primarily attributed to mesoscale convective systems during summer to early fall and frontal or organized convective systems during fall and early winter (Norbiato, et al., 2009a; Frei & Schär, 1998). The mean annual precipitation for the period of this study (2002 to 2010) over the region is 788 mm with maximum/minimum annual values of 692 mm and 912 mm, respectively. The corresponding mean annual and maximum/minimum normalized runoff values measured at the outlet of Adige at Bronzolo (representing the entire drainage area of the study basin) for the same period are 603 mm and 747/482 mm, respectively.

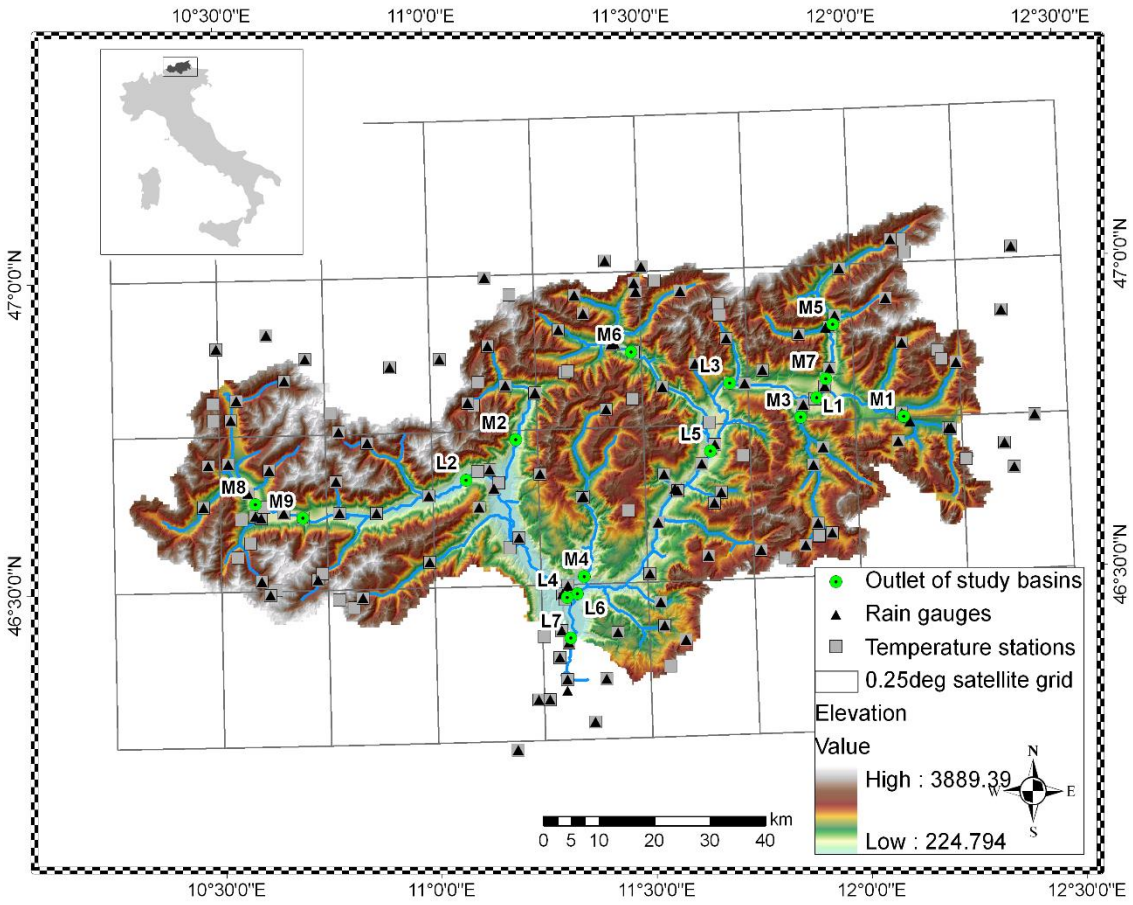

Figure 3.1. Map showing the terrain elevation of the Upper Adige river basin and the location of available rain gauges and temperature stations. The satellite spatial grid at 0.25° resolution is superimposed and the locations of outlets of study basins are shown and labeled according to basin id reported in Table 3.2.

Table 3.2. Summary of evaluated basins and hydrologic characteristics.

Basin ID	Basin		Rain gauge		Mean Accumulation (mm)			
	Area (km^2)	Elevation (m a.s.l)	Number	Height (m a.s.l)	Rainfall		Simulated Flow	
					May-Aug	Sep-Nov	May-Aug	Sep-Nov
M1[1]	255	1858	10	1302	449	239	295	205
M2	345	1952	11	1402	469	325	639	235
M3	391	1846	9	1287	421	231	232	155
M4	417	1684	12	926	414	230	279	165
M5	417	2113	8	1142	459	228	689	243
M6	505	1910	18	1295	476	266	522	224
M7	613	2035	12	1108	456	229	575	229

M8	653	2181	13	1600	307	169	261	152
M9	892	2162	17	1546	303	171	260	148
L1	1262	1908	23	1180	461	227	416	201
L2	1673	2109	29	1384	309	194	257	140
L3	1906	1857	32	1221	449	227	346	182
L4	2712	1900	44	1296	343	231	303	153
L5	2863	1830	53	1198	447	230	355	184
L6	4166	1743	71	1155	436	225	309	170
L7[1]	6967	1793	104	1216	398	227	305	163

[1] M and L stands for medium and large scale basins; L7 is the entire basin

3.2.2 Precipitation Data

Three quasi-global satellite products and their gauge-adjusted counterparts are used in this study. The Tropical Rainfall Measuring Mission (TRMM) Multi-satellite Precipitation Analysis (TMPA) is a combined IR and MW product from the National Aeronautics and Space Administration (NASA). The TMPA (Huffman, et al., 2007) is available with a near-real-time version adjusted according to a climatological correction algorithm (CCA) (3B42-CCA, hereafter named TR) (Huffman, et al., 2010). In addition to the near-real-time product, the post-processing gauge-adjusted equivalent product (3B42-V7, hereafter named aTR) is used. The second product is the National Oceanic and Atmospheric Administration (NOAA) Climate Prediction Center morphing (CMORPH, abbreviated as CM) technique, which utilizes multi-satellite based MW rain estimates propagated spatiotemporally by IR-derived motion vectors (Joyce, et al., 2004). Recently a bias adjustment procedure has been developed based on daily gauge estimates (30000 gauges worldwide) (Xie, et al., 2011) and has been applied on the entire CMORPH record to provide the gauge-adjusted equivalent of CMORPH product (named hereafter as aCM). The third product evaluated in this work is the Precipitation Estimation from Remotely Sensed Information using Artificial Neural Networks (PERSIANN, hereafter named PE). This algorithm (Sorooshian, et al., 2000) uses a neural network approach calibrated by MW data to derive relationships between IR data and rainfall estimates (Sorooshian, et al., 2000). The bias-adjusted version of PERSIANN (hereafter named aPE) is computed based on a correction factor that represents the ratio of GPCP (Global Precipitation Climatology Project) product and PERSIANN estimates at 2.5° and monthly space-time windows (Huffman, et al., 2009; Adler,

et al., 2003). Spatial and temporal resolutions of the satellite rainfall products evaluated in this study are 0.25° and 3 hourly time intervals covering a period from 2002 to 2010.

A total of 104 rain gauges are distributed over the study area (Figure 3.1) providing a gauge density of approximately 1/67 (1 gauge station / area in km^2) over the whole area. Note that gauge density over the sixteen selected cascade basins varied between 1/25 (M1) to 1/67 (the entire basin, Table 3.2 reports the number of contributing gauges for each basin). The rain gauge rainfall record used in this study covers a nine-year period (2002 to 2010) at hourly temporal resolution. These rain gauge data have gone through a quality control (QC) process according to the guidelines of the World Meteorological Organization (Zahumenský, 2010). Values that did not pass the QC were discarded. An average of 14.5% of hourly rainfall record from each of the gauge locations have been disregarded according to the QC for the study years. The hourly temperature records are also provided by a dense station network (143 stations) over the study area (Figure 3.1).

3.3 Data Processing and Hydrologic Simulations

3.3.1 Precipitation Data Processing

All satellite products were spatiotemporally interpolated, using the nearest neighbor method, to derive hourly areal weighted basin-average precipitation for each of the cascade basins analyzed. Additionally, since the TMPA (3B42-V7) represents MW and IR rainfall estimates within ±1.5 hours of the synoptic hours a temporal matching was applied for this product. Specifically, the 3B42-V7 time series were interpolated to half-hourly by the nearest neighbor method, then each two consecutive time steps were aggregated so as to get the hourly records. Hourly gauge precipitation and temperature time series averaged over the sixteen cascade study basins were also generated using the nearest neighbor interpolation technique.

3.3.2 Hydrologic Model

The Integrated Catchment Hydrological Model (ICHYMOD) is used in this study. This is an off-line version of the modeling scheme run operationally by the Hydrologic Office of the Autonomous Province of Bolzano as part of the Adige River Flood Forecasting System. ICHYMOD involves a semi-distributed conceptual rainfall-runoff model that consists of a snow routine, a soil moisture routine and a flow routine. This model has been successfully applied in several studies in the greater area of northern Italy (Norbiato, et al., 2009b; 2008). A summary of the modeling framework is provided below, while for a detailed description of the modeling structure, the interested reader is referred to Norbiato, et al. (2008). Snow accumulation and melting is calculated using a distribution function approach based on a combined radiation index degree-day concept (Cazorzi & Dalla Fontana, 1996). Potential evapotranspiration is estimated with the Hargreaves method (Hargreaves & Samani, 1982). A probability distribution function (Moore, 1985) is used to describe the spatial variation of water storage capacity across the basin. Surface runoff is generated via saturation excess at any point in the basin and is integrated over the basin to derive the total direct runoff entering the fast response pathways to the basin outlet. Drainage from the soil enters slow response pathways and is represented by a function of basin moisture storage (Moore, 2007). Total flow at the outlet of the basin results from the summation of storage representations of the fast and slow response pathways. Direct runoff routing is based on the Muskingum-Cunge method (Cunge, 1969) while slow or base flow component of the total runoff is routed through an exponential store.

The model runs at hourly time-step using hourly input of temperature and precipitation. The semi-distribute structure of the model allows dividing the modeling area into different sub-areas (e.g. areas with different hydrological properties), which comprise the computational elements of the model. This permits spatial variability in the model parameterization and allows simulating hydrologic response at several points within a greater basin. Application of the model requires specification of 14 parameters: three for the snow routine, eight for the runoff generation module and three for the runoff propagation module (Norbiato, et al., 2008). The operational version of ICHYMOD, which is an already calibrated version of the model,

includes the area of study. The calibration procedure for determining the model parameters is detailed in Borga et al. (2014), and in general involved the minimization of error in runoff simulations. In the current work, we adopted the same modeling parameters for our simulations to allow results to be directly related to an existing flood forecasting application. We avoided further calibration of the model because improving the model performance (relative to its current status) is not within the scope of this study.

3.3.3 Setup of Hydrologic Simulations

Within ICHYMOD, our study area was discretized into 51 sub-basins (i.e. computational elements) that range in area between 30 and 500 km^2. Discretization of the area into corresponding sub-basins was based on a combination of criteria involving mainly: data availability (most outlets coincide with the existence of stream gauge) and hydrologic interest (i.e. areas that are highly prone to floods/flash floods were discretized at a higher detail i.e. number of sub-basins to allow modeling of the hydrologic response at finer spatial scales). For each of these sub-basins, precipitation was provided as sub-basin-average hourly time series following the procedure described in section 3.3.1. Model simulations were then carried out and the simulated discharge was extracted from model output for the sixteen study cascade basins selected for analysis (Figure 3.1). This procedure was repeated for all precipitation products (gauge and satellite based) to obtain simulated discharge for each precipitation forcing. An important note is that due to the fact that precipitation in the region during winter and early spring (i.e. Dec-Apr) is dominated by snow, we restricted the simulation period between May and November to avoid, to a large extent, mixing in our analysis satellite estimation errors for both rainfall and snowfall. However, recognizing that snowfall plays an important role in the hydrologic response of the region during the melting period, we were initializing each simulation cycle (i.e. May-Nov per year) using the state variables (snow and soil moisture storage) obtained from continuous gauge-based simulations. Note that the continuous gauge-based simulations were performed for the period 2000-2010 (i.e. starting 2 years earlier than analysis period) allowing the first 2 years of simulation to be used for model spin up, which according to our previous experience with ICHYMOD has shown to be adequate. This was important for two main reasons. First, runoff generated from snow-melting

process was included (due to available snow storage) thus making simulations realistic for the region. Second, simulations for all precipitation products were performed using the same initial conditions allowing decoupling observed differences (among products) from the effect of initial conditions and focusing only on rainfall-runoff dynamics.

Throughout the analysis the gauge-based simulations are used as reference for comparison with the satellite-based simulations. Given that gauge-based precipitation is also used as reference for evaluating satellite-rainfall error metrics, using the gauge-based runoff simulations as reference (instead of observed discharge) permit us to directly analyze the characteristics of error propagation from rainfall to runoff. Although, as previously stated, a rigorous evaluation of the efficiency of the model is not within the scope of this study, a comparison with observed discharge was carried out to gain a basic understanding on the efficiency of gauge-based simulations (used as our reference) to represent actual streamflow. The Nash-Sutcliffe (NS) model efficiency coefficient (Nash & Sutcliffe, 1970) between reference flow simulations and streamflow observations for the entire basin is 0.80 while the mean NS values for all the study basins is 0.60 (Borga, et al., 2014). While these results indicate considerable variability in model performance for the different cascade basins analyzed, they show that representation of hydrologic response by the reference simulations holds a certain degree of realism. An example of the various flow simulations is shown in Figure 3.2 where hydrographs from satellite and reference simulations are shown for the largest and smallest basin (denoted as L7 and M1, see section 3.4.1 for the implications) examined and for their corresponding wettest and driest years. Variability in the performance of different products is clearly shown in the figure and one can immediately recognize distinct product-related behaviors. For example, the CCA-corrected 3B42 product is overestimating in all four cases, particularly for the dry year, while the unadjusted PERSIANN and CMORPH are underestimating. A detailed analysis on this is provided in section 3.5.

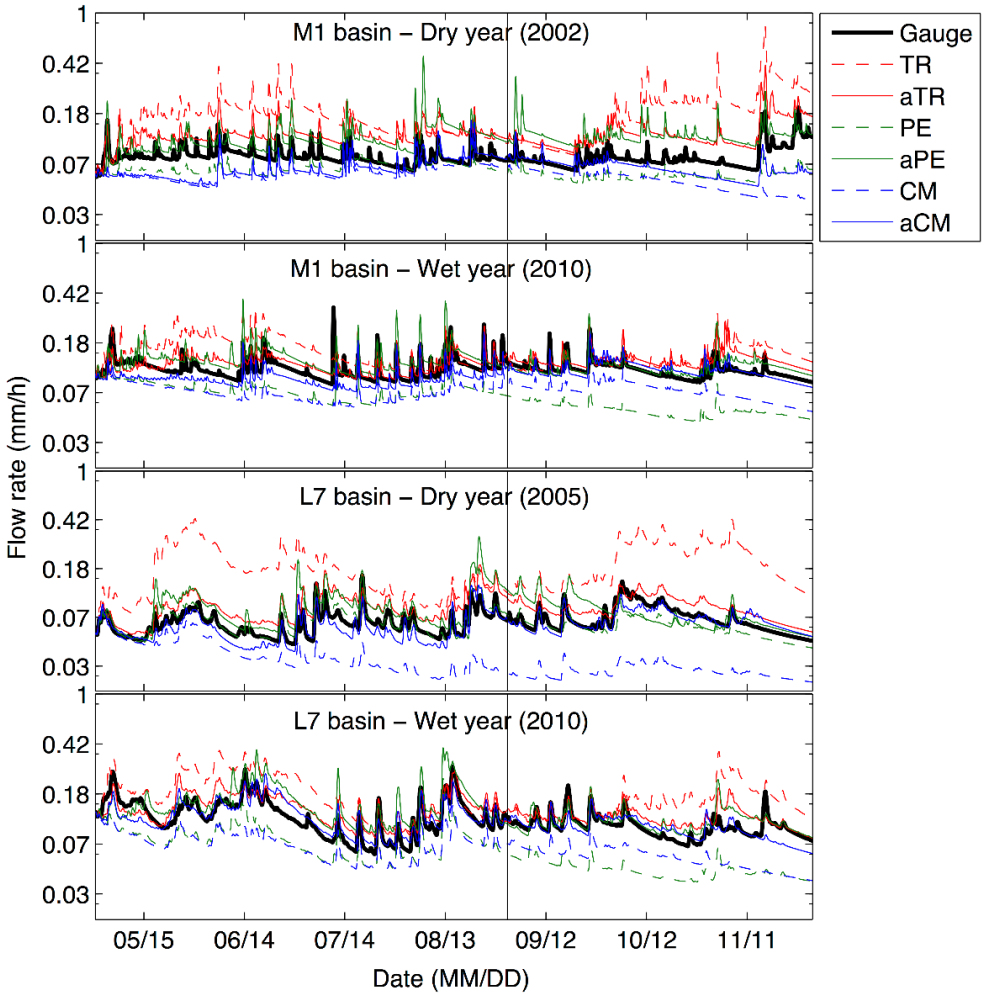

Figure 3.2. Sample hydrographs for M1 and L7 basins over the wettest and driest years; the vertical line separates the two seasonal periods defined in this study as warm and cold.

3.4 Methodology

The methodology in this study devises error metrics that evaluate the error structure of satellite products and their driven runoff-simulations according to basin scale, basin elevation, seasonality and event severity. Description of the metrics is provided in section 3.4.2. Next we describe the classification approach followed to separate the simulated flow data to different cases.

3.4.1 Classification

The sixteen study basins considered in this study were grouped into two classes according to their area (see summary in Table 3.2), where basins with area greater (less) than 1000 km^2 were considered as large (medium) scale basins indicated by letter L (M). Nine years (2002-2010) of precipitation time series and the corresponding simulated discharges from the six satellite precipitation products and the rain gauge network measurements were analyzed for each of the selected basins. Analysis was carried out for two different periods corresponding to warm (May-Aug) and cold (Sep-Nov) season months according to the regional climatologic patterns (note that the terms warm season months and May-Aug, as well as cold season months and Sep-Nov are used interchangeably in the text). Table 3.2 lists the mean annual precipitation and runoff accumulations for the selected basins in the two seasons. It is seen that the warm season months' precipitation/runoff accumulations are almost twice as much those in the cold season months. A point to note from the table is that in some basins the runoff accumulation is higher than the corresponding basin-average precipitation due to the significant contribution from snow storage.

The hourly runoff values were also grouped according to different percentiles to investigate the error structure in flow simulation for different magnitude levels. The thresholds were defined based on the 90^{th} percentile values determined from reference (i.e. gauge-based streamflow simulations) runoff time series. The determined threshold values for different basin scales and seasons are summarized in Table 3.3. It is noted that the runoff threshold values are greater in the May-Aug months than those in the Sep-Nov months for most of the study basins, indicating (as expected) that the high runoff regime in this region is higher in the warm than the cold period considered. This is expected given that most of the flash floods (i.e. high peak runoff events) in the region occur during the summer (Marchi, et al., 2010).

Table 3.3. The 90^{th} percentile reference runoff threshold for the different sub-basins and two periods.

Basin ID	Runoff Threshold (mm)	
	May- Aug	Sep-Nov
M1	0.28	0.16
M2	0.29	0.16

M3	0.33	0.17
M4	1.73	2.37
M5	0.46	0.52
M6	0.40	0.56
M7	0.34	0.31
M8	0.30	0.37
M9	0.46	0.39
L1	1.27	1.28
L2	1.68	1.31
L3	0.39	0.39
L4	1.30	1.11
L5	0.70	0.61
L6	0.36	0.33
L7	0.50	0.46

3.4.2 Error metrics

Three evaluation metrics are used to describe the properties of error in basin-average precipitation and simulated runoff. They are the mean relative error (*MRE*), centered relative root mean square error (*CRMSE*) and correlation coefficient (*CC*) with the listed forms:

$$MRE = \frac{\sum[S(G \in T_G) - G(G \in T_G)]}{\sum G(G \in T_G)} \tag{3.1}$$

$$CRMSE = \frac{\sqrt{\frac{1}{M}\sum\left\{S(G \in T_G) - G(G \in T_G) - \frac{1}{M}\sum[S(G \in T_G) - G(G \in T_G)]\right\}^2}}{\frac{1}{M}\sum G(G \in T_G)} \tag{3.2}$$

$$CC = \frac{\sum\left[S(G \in T_G) - \frac{1}{M}\sum S(G \in T_G)\right]\left[G(G \in T_G) - \frac{1}{M}\sum G(G \in T_G)\right]}{\sqrt{\sum\left[S(G \in T_G) - \frac{1}{M}\sum S(G \in T_G)\right]^2 \sum\left[G(G \in T_G) - \frac{1}{M}\sum G(G \in T_G)\right]^2}} \tag{3.3}$$

G and *S* are symbols representing gauge and satellite precipitation time series. T_G defines the space of values satisfying a given condition (i.e. above or below the threshold value defined from the reference data). *M* is the total number of values belonging to T_G from the gauge time series. Note that the corresponding error metrics for runoff can be obtained by replacing the precipitation series (*G* and *S*) and the thresholds (T_G) with the runoff series and thresholds calculated from the gauge-based simulated runoff time series. The

MRE is an error metric measuring the systematic error component with values greater or smaller than zero indicating over- or underestimation, respectively. This is complementary to the *CRMSE*, which is a metric measuring the random component of error, as bias has been removed. *CC* is an indicator of the temporal similarity between reference and satellite-derived basin-average precipitation and simulated runoff.

Aiming to demonstrate how error translates from basin-average precipitation to simulated runoff, the error metric ratio (denoted as γ) is used as following:

$$\gamma = \left| \frac{EM_r}{EM_p} \right| \tag{3.4}$$

where EM_p and EM_r are the error metrics (i.e. *MRE*, *CRMSE* and *CC*) determined in our analysis for basin-average precipitation and runoff simulations, respectively, for the different basins and seasons. The values of γ for different error metrics will have different implications. γ for *MRE* or *CRMSE* that is smaller (greater) than one indicates dampening (amplification) of error through its transformation from rainfall to runoff simulations. By taking the absolute value we neglect the direction of the systematic error so as to focus purely on the error magnitude propagation from precipitation to runoff. The indication of γ values reverses for *CC*, namely, γ above/below one stands for increase/deterioration of temporal co-variation.

3.5 Results

An overview of the precipitation and simulated flow accumulations for different products and seasons over the entire study region are shown in Figure 3.3. The most striking features from these results are the strong overestimation from the climatologically adjusted 3B42-CCA and the relatively significant underestimation from the unadjusted CMORPH product; the CCA-adjusted 3B42 is 90% (for warm period) and 143% (for cold period) higher than the reference precipitation, while unadjusted CMORPH underestimates by 34% (warm) and 62% (cold). Similarly, 3B42-CCA forced hydrologic simulations exhibit 106% and 125% overestimation of the reference flow, while the unadjusted CMORPH driven simulations underestimated the reference flows by 27% and 37% for the warm and cold periods,

respectively. The magnitude of error for the gauge-adjusted 3B42 and CMORPH precipitation products is significantly lower than their unadjusted (or climatologically adjusted) counterparts. Specifically, the overestimation in the adjusted 3B42 product reduced to 22% and 18% (18% and 26%) for basin-average precipitation (simulated runoff) for the warm and cold periods, respectively. Performance of the adjusted CMORPH was also greatly improved relative to the unadjusted product with 2% and 28% underestimation for basin-average precipitation in the warm and cold periods, and nearly unbiased results (0.4% and 3%) for the flow simulations. For PERSIANN, the gauge-adjustment shifts both precipitation and runoff simulations from underestimation to overestimation. Specifically, the unadjusted PERSIANN exhibits 3% and 32% (4% and 14%) underestimation of the warm and cold period basin-average precipitation (simulated flow); the adjusted version gives 19% and 17% (15% and 27%) overestimation for basin-average precipitation (simulated flow) over the two periods. Figure 3.3 also suggests that the mean annual accumulations of precipitation and runoff simulation for the gauge-adjusted 3B42 and PERSIANN are almost identical over the study area. This is expected given that both products are adjusted to the global precipitation-gauge analyses from the GPCP (Huffman, et al., 2009).

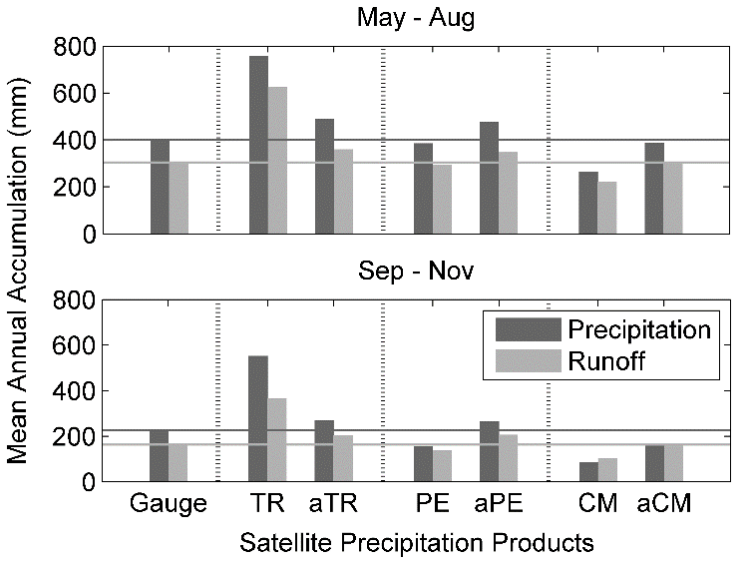

Figure 3.3. Mean annual values of basin-average precipitation and runoff for the entire basin (L7) derived from gauges and the different satellite products.

The following sub-sections provide more in depth error analysis of satellite precipitation retrievals, the satellite-based flow simulations and the characteristics of error propagation from basin-average precipitation to simulated runoff. The analysis was carried out with respect to four main aspects including: a) dependence of systematic error on elevation, b) systematic, random error and temporal correlation of the flow simulations and c) dependence of error metrics ratios on basin elevation.

3.5.1 Role of elevation on systematic error

Given the focus of this study on complex terrain this section evaluates the role of elevation on the precipitation and runoff simulation error magnitudes. Figure 3.4 and Figure 3.5 show scatter plots of biases in precipitation and the corresponding runoff simulations against mean basin elevation values for the two seasons. Positive linear relationship can be seen from most of the scatter plots, pointing to the fact that the systematic error in satellite-derived basin-average precipitation and the corresponding runoff simulations change from underestimation to overestimation with increase in basin altitude. The linearity is stronger for the climatologically-adjusted 3B42 precipitation product and the adjusted CMORPH driven runoff simulations (the r^2 values for the two scenarios are 0.71 and 0.72, respectively). This correlation is not as strong for PERSIANN (r^2 is generally below 0.3), which may be explained by that this is an IR-only satellite product. It is noted that the increase shown in the 3B42 (both adjusted and climatologically adjusted) product overestimation with elevation is consistent to results presented in Yong et al. (2010).

From the perspective of error magnitude, we observe overestimation in the two 3B42 products and adjusted PERSIANN products and underestimation in both CMORPH products and the unadjusted PERSIANN products (most of the cases). The strongest over- and under-estimations in basin-average precipitation and flow simulations are from the 3B42-CCA and unadjusted CMORPH products, which represent combined IR-MW and sole MW retrievals, respectively. Besides, improvements from unadjusted (or climatologically adjusted) to adjusted products are noted as the adjusted products have bias values generally closer to zero (not clear for the PERSIANN product, which is an IR-alone based technique),

indicating the importance in improving accuracy by incorporating gauge-adjustment to the satellite rainfall estimates (Gourley, et al., 2011; Wilk, et al., 2006).

From the seasonal perspective, we found higher degree of consistency in warm season precipitation estimations and flow simulations than in the cold season counterparts, especially for the unadjusted precipitation products (with the exception of PERSIANN product where biases of the warm and cold season precipitation and flow simulation are similar; which again could attribute to the fact that PERSIANN is an IR-alone technique). A possible explanation for this seasonal difference is the effect of snow screening applied in the passive microwave satellite retrievals used by CMORPH and 3B42 techniques (Mei, et al., 2014b). In addition, the study reflects the effectiveness of gauge-adjustment in eliminating the high bias in cold season precipitation retrievals.

Based on the trend of the scatter plots in Figure 3.4 and Figure 3.5, it is noted that slopes of the 3B42 products drop considerably from the CCA to the adjusted versions for both the precipitation and simulated flow over the two seasons (3.7 and 4.5 times as CCA over adjusted for warm and cold season basin-average precipitation values while 6.7 and 3.1 times for the simulated flows). This decreasing trend in slopes yields lower magnitudes of systematic error in the basin-average precipitation estimation and corresponding flow simulations for higher altitude basins. The slope values remain similar for the unadjusted and adjusted versions of the other products. Therefore, gauge adjustment in 3B42 greatly mitigates the strong systematic error over high altitude basins.

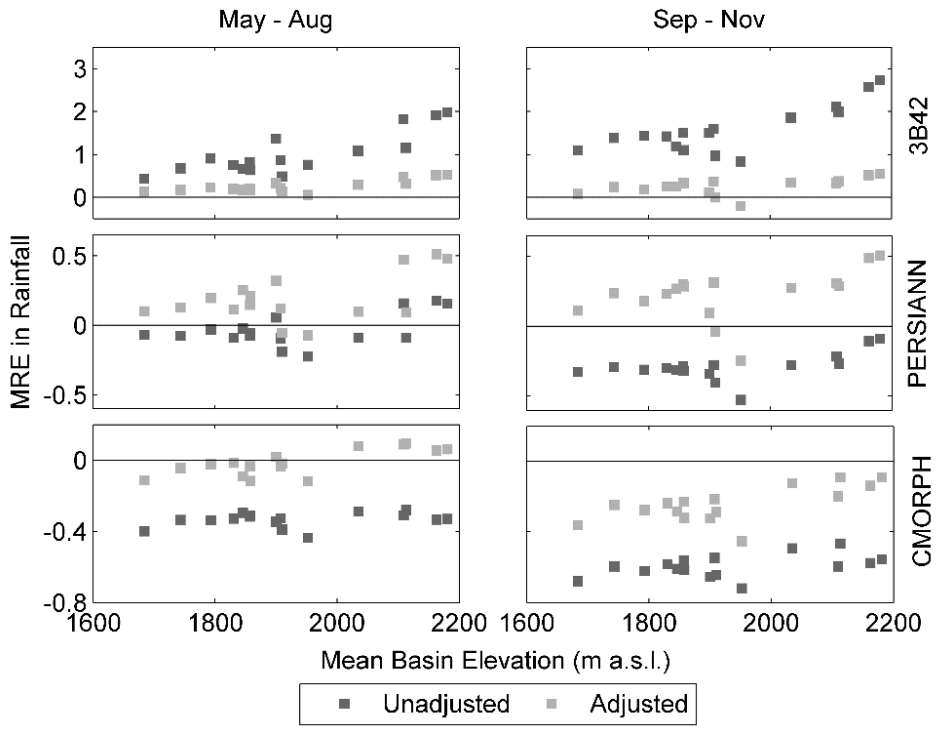

Figure 3.4. Bias in basin-average satellite precipitation products versus mean basin elevation for the different basins and two periods.

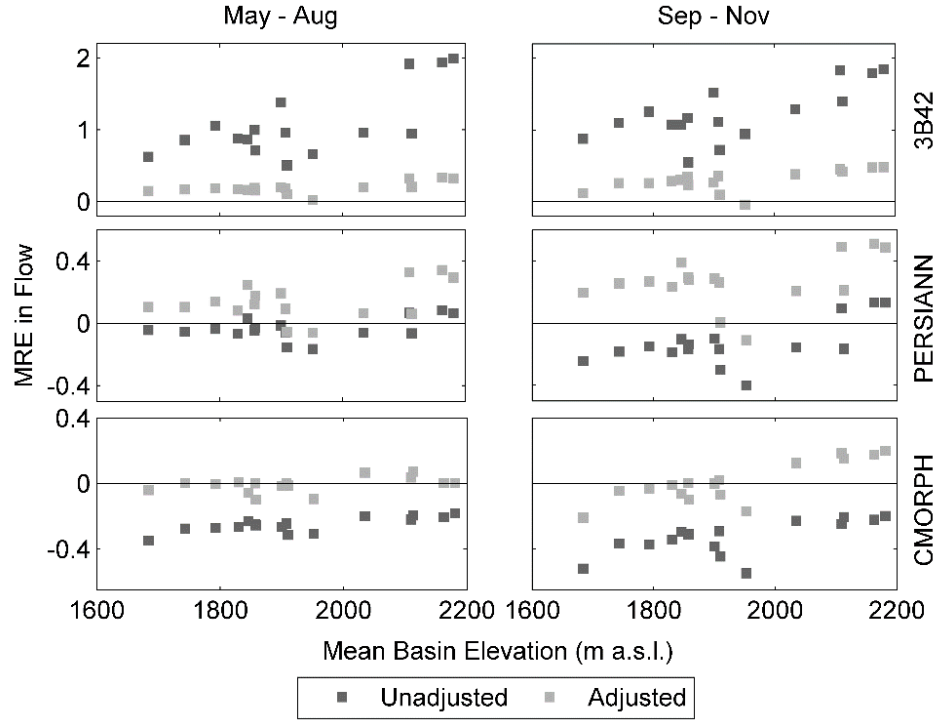

Figure 3.5. Same as in Figure 3.4, but for the precipitation-driven simulations.

3.5.2 Effects of basin scale, seasonality and flow severity

As mentioned above, goal of this study is to quantify the performance of satellite-precipitation products driven hydrologic simulations by rendering the mean relative error (Figure 3.6), centered root mean square error (Figure 3.7) and correlation coefficient (Figure 3.8) as a function of basin scale, streamflow magnitude and seasonal period. Figure 3.6 demonstrates that there exists strong overestimation from the CCA-corrected 3B42 and relatively strong underestimation from the unadjusted CMORPH, which is consistent with the results from Figure 3.5. It is seen that the flow simulations tend to be more underestimated in higher flow threshold (above the 90th percentile) with wider *MRE* variability (longer value range). On average *MRE* values are relatively stable among basin scales examined and for a given product; however, the medium scale basins exhibit considerably higher variability in *MRE* values than the larger size basins of this study. These aspects are especially noted for the extreme flow values (>90th percentile). In terms of seasonality effects, results show stronger underestimation for the two PERSIANN and CMORPH precipitation products and higher degree of variability in *MRE* values during cold period months for stream flows above the 90th percentile threshold; the 3B42-CCA is an exception.

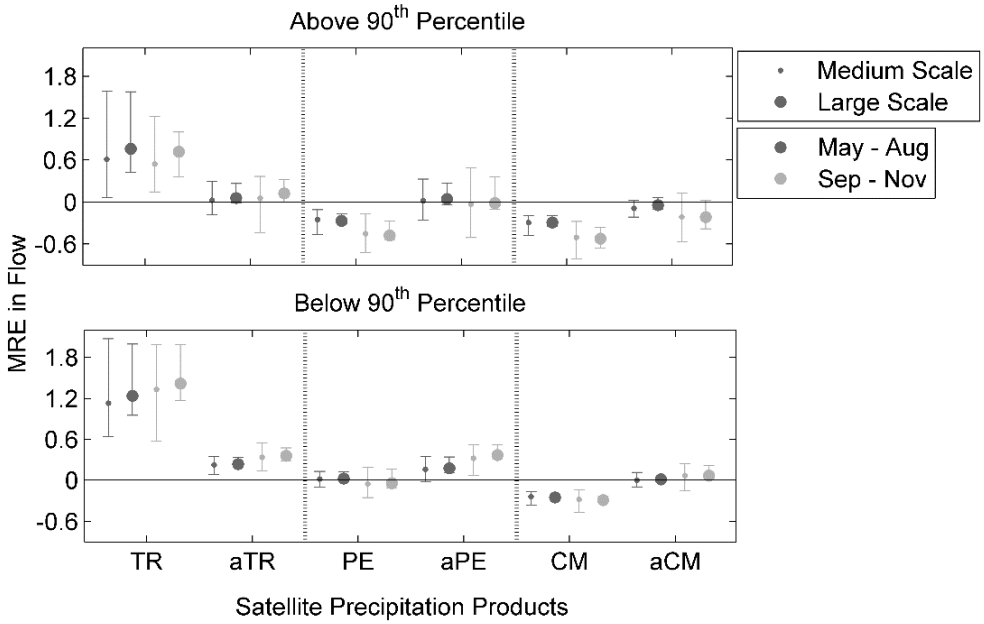

Figure 3.6. Mean (circles) and max/min values (vertical bars) of the mean relative error of stream flows simulated based on the different satellite precipitation products. Results are shown for two value ranges, two basin scale categories and the two periods.

The random component of error in the flow simulation is quantified by the centered root mean square error (*CRMSE* shown in Figure 3.7). As a first glance, the CCA-adjusted 3B42 and PERSIANN (below the 90th percentile group and warm season) products are characterized with high *CRMSE*, while those for CMORPH products are mostly below 0.4. High *CRMSE* values for the 3B42-CCA are expected since this product is corrected by the CCA (climatological corrected algorithm), which has been found to be introducing random error on the precipitation estimates (Mei, et al., 2015; Yong, et al., 2013). In addition, the random component of error is slightly higher for the high flows (above the 90th percentile) relative to those below the 90th percentile; 3B42-CCA and PERSIANN are two exceptions. Lower *CRMSE* values with narrower value ranges are found for the larger basin scale for all the adjusted products (and most of the unadjusted ones) regardless of flow threshold pointing to the more significant smoothing effect on random error from larger basin scales. Similar findings were revealed in Maggioni et al. (2013) and Vergara et al. (2013) studies. Besides, cold season is characterized with higher *CRMSE* values as anticipated ascribing to the issue of satellite detection of solid- and mix-phase precipitation during the cold season. A comparison between adjusted and unadjusted products shows that the gauge adjustments are able to reduce the random error in precipitation estimation in most of the cases (this improvement is not apparent for CMORPH), particularly pronounced for the flow simulations below the 90th percentile threshold.

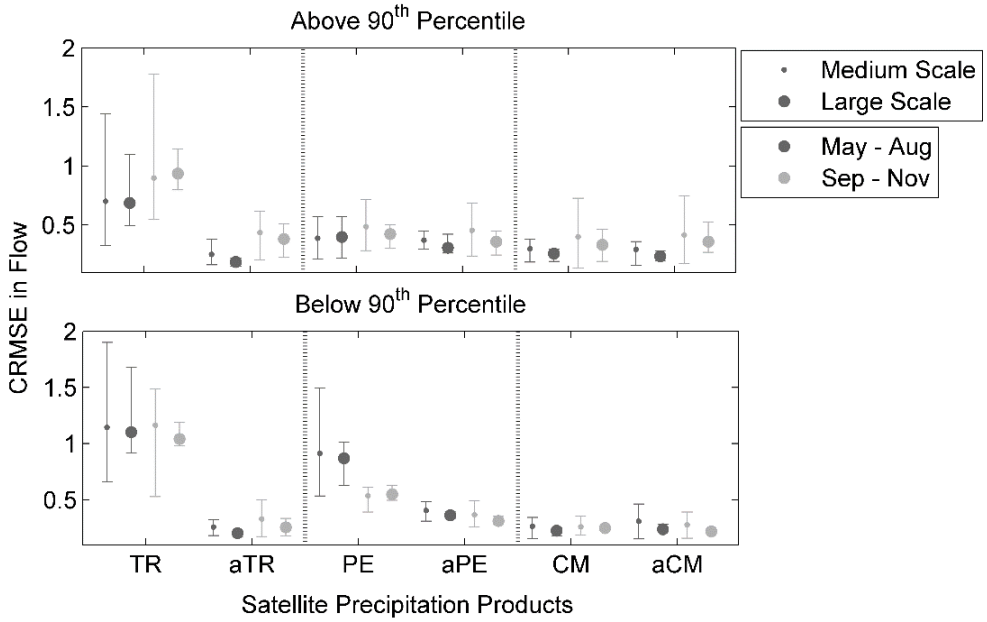

Figure 3.7. Same as in Figure 3.6, but for the centered root mean square error.

The correlation coefficient was used to quantify the temporal similarity of the hydrologic simulations; the mean and range for *CC* values are shown in Figure 3.8. The figure reveals different behaviors of *CC* for the two flow threshold groups where lower *CC* values are observed for the above 90th percentile group. Additionally, cold season is characterized by lower *CC* values and longer value ranges, implying the influence on temporal dynamics of the solid- and mix-phase precipitation effect on passive microwave retrieval. Investigation on the scale dependency of *CC* value demonstrates that there is a convergence trend in value variability from medium to larger scale basins. This means that the performance of satellite-based flow simulation is more consistent, in terms of correlation, for the larger (>1000 km^2) basins. Moreover, similar to the improvements found over *MRE* and *CRMSE* statistics, the adjusted products give higher *CC* values in flow simulations. A product-wise comparison indicates that the adjusted 3B42 outperformed the other products over the various error metrics determined for the flow simulations. The two CMORPH products gave acceptable temporal correlations during the warm season, but the *CC* value ranges dropped below zero during the Sep-Nov period for the extreme flow threshold group, which indicated the limitation of this technique for cold season precipitation events.

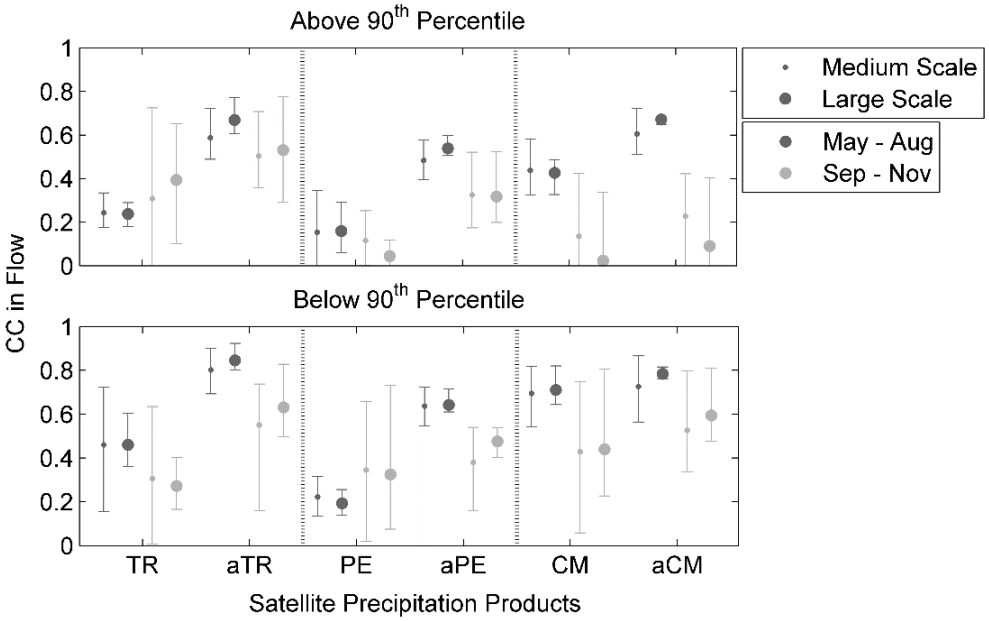

Figure 3.8. Same as in Figure 3.6, but for the correlation coefficient.

3.5.3 Error propagation

Investigation of the basin scale precipitation-to-runoff simulation error propagation is conducted by rendering the ratio between the three error metrics following Eq.(3.4). The top panel of Figure 3.9 shows the ratio of *MRE* indicating how the basin-average precipitation error translates to systematic error through the flow simulations (note that this ratio is defined as the absolute value of the error metrics). As noted from the figures, values of the γ_{MRE} for the two 3B42 products are distributed between 0.5 and 2, which means there is no well definition of the direction to either dampening or magnification of the systematic error of precipitation by the model. On the other hand, as most of the ratios for the PERSIANN and CMORPH products are less than one, suggests that systematic error is mostly dampened through the rainfall-to-runoff transformation; this is especially noted for the adjusted CMORPH precipitation product. In addition, the values of precipitation-to-simulated-runoff error metric ratios show dependency on basin scale and seasons. Specifically, the mid-size basins and cold period month events are characterized with wider γ_{MRE} value ranges. This could be expected since storm systems occurring in the cold period over this area are characterized with higher degree of heterogeneity (mix of frontal and mesoscale convective systems).

Furthermore, the gauge-adjustment for CMORPH is shown to give higher degree of error dampening compared to the other two algorithms.

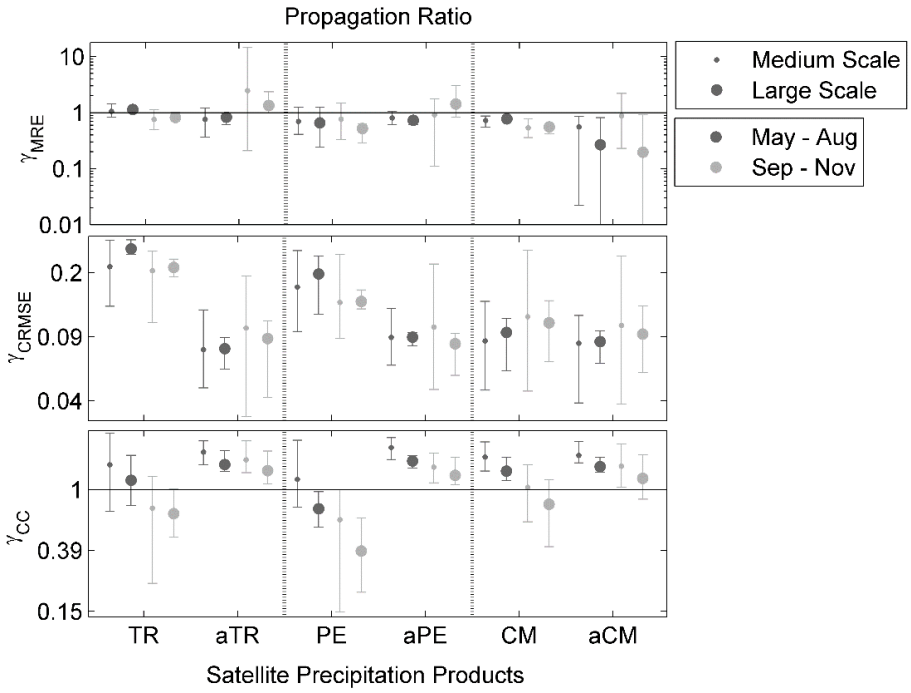

Figure 3.9. Mean (circles) and max/min values (vertical bars) of the error metrics ratios presented for the different satellite precipitation products, two basin scale categories and the two periods.

The error propagation of the random component is quantified by γ_{CRMSE} with results demonstrated in the middle panel of Figure 3.9. Compared to the pattern of γ_{MRE}, which show no obvious tendency in terms of either under/over-estimation, the γ_{CRMSE} values are all below one, highlighting the dampening effect on the random error of basin-average precipitation in simulated flows. Based on the magnitude of γ_{CRMSE}, the random component of error in basin-average precipitation is at least 3 times that in simulated runoff values. Also, we observed similar seasonal and basin scale dependencies in the value ranges of γ_{CRMSE} compared to the behavior of γ_{MRE} (longer value range found over the medium scale and cold season cases), attributed again to the more heterogonous storm system characteristics over the cold period for this region. No clear basin scale or seasonal dependency is revealed for the mean values of *CRMSE* ratio. Besides, the figures show that gauge adjusted products have lower γ_{CRMSE} ratio with similar magnitudes compared to the

unadjusted products (not very clear for CMORPH). Specifically, for the unadjusted (and the climatological adjusted 3B42-CCA) products, the most significant (insignificant) error dampening effect is observed for the CMORPH (3B42) over the two periods.

The error propagation is also quantified in terms of the ratio between temporal correlations of simulated runoff over those of basin-average precipitation (γ_{CC}, bottom panel of Figure 3.9). A first observation is that most of the γ_{CC} values are greater than one, pointing to improvement from rainfall to runoff. Besides, we can see that the values and value ranges of γ_{CC} are dropping from the medium to the large scale basins, ascribing to possibly the increase in runoff routing timing error as basin scale increases. A season based comparison reveals that the cold season γ_{CC} values are typically with smaller mean values and longer variability. This observation reflects on the one hand, the degree of model error dampening effect for the cold period months is not as effective as that for the warm months; on the other hand, error patterns of the winter storm estimation are more complex introducing higher variability in streamflow simulation error. Moreover, adjusted products are characterized with higher γ_{CC} values (always greater than one), which demonstrates the positive aspect of the correction algorithm. A product-wise comparison indicates that warm season gauge-adjusted CMORPH and cold season gauge-adjusted PERSIANN products have more significant error dampening effects in terms of the temporal similarity contrasting to the other cases.

To summarize, higher degree of variability in terms of the three error metrics ratios is observed for the smaller-size basins. The cold period months' propagation ratio for the random error and temporal similarity are characterized with wider value ranges. The propagation ratio of temporal correlation is higher for the mid-size basins of this study for the warm period. It is noted that the random error is dampened by the rainfall-runoff translation in all cases while the systematic error showed no significant sensitivity to model effect.

3.6 Conclusions

This paper provides a rigorous hydrologic assessment of the error propagation of three widely-used satellite precipitation products and their corresponding gauge-adjusted versions over a cascade of mountainous basins in the Upper Adige basin of northeast Italian Alps. Results reported in this study evaluate the error properties of both basin-average precipitation and the simulated flows derived from a semi-distributed hydrologic model, and the links between them, for different basin characteristics (size, elevation) and storm types. Error characteristics were defined in terms of basin-average precipitation and simulated runoff error statistics (mean relative error, centered root mean square error and correlation coefficient) and error metrics ratios (γ ratios). The principal conclusions of this study are summarized below.

The systematic error of products and their corresponding simulations ranged from underestimation to overestimation as the mean basin elevation increased. Values of the systematic error are closer to zero after the gauge adjustments highlighting the necessity of incorporating the ground-based gauge measurements in satellite precipitation retrievals. This is of particular importance for the cold season precipitation retrievals and for the flow simulations as the performance of all products in the cold months period are shown to be worse than in the warm month period. The two 3B42 products (CCA-adjusted and V7) are characterized with overestimation, while the unadjusted CMORPH is consistently underestimating both basin-average precipitation and flow simulations.

The magnitude of error metrics for flow simulations show that the low to moderate flow rates (below the 90^{th} percentile threshold) are predicted with lower systematic and random error and higher degree of temporal similarity compared to the extreme flow rates. Also, the random errors are reducing with converging trends as basin scale increases and from cold to warm season months. Gauge adjustment was able to moderate the random error and increase the degree of temporal similarity in the simulated flows. The CCA-corrected 3B42 is characterized with the highest random error, while the estimates from the two

CMORPH products exhibited the lowest random error; the adjusted 3B42-driven flow simulations exhibited the highest degree of temporal similarity with the gauge-driven flow simulations.

We evaluated the basin scale precipitation-to-runoff error propagation by taking the error metric ratios of simulated flow to basin-average precipitation. Overall, the ratios show dependencies on basin scale and seasonality. Ratios from larger basins are characterized with lower degree of variability. The cold period cases are characterized with higher degree of heterogeneity exhibited by the wider value ranges of the error metric ratios of the random error and temporal similarity metrics. Furthermore, we showed that the flow simulations dampening effect in terms of temporal similarity is more significant for the cold period that is associated with more widespread precipitation systems. Finally, it was shown that gauge adjustment is meaningful in terms of error dampening for nearly all of the cases (seasons and basin scales).

We recognize that our analysis gives particular focus on a limited hydroclimatic and geomorphologic regime; therefore, results are directly relevant only for mountainous regions where precipitation processes are driven by orographic enhancement. However, the study rendered error propagation based on long-term data, accounting for both warm and cold season weather patterns, which represents a wide variety of precipitation events and basin responses (i.e. runoff generation). The potential effect of the physical mechanism of runoff processes (antecedent basin conditions, spatial and dynamic aspects of runoff generation) in the precipitation-to-runoff error propagation is not addressed in this study. This error analysis would require detailed event classification and distributed modeling of the rainfall-runoff transformation. Furthermore, use of satellite precipitation products with higher spatiotemporal resolution (e.g., PERSIANN-CCS available at 0.04°/hourly; and GSMaP and IMERG available at 0.1°/hourly) should be examined to tradeoff between product resolution and retrieval uncertainty in terms of flow simulations.

Chapter 4 Error Analysis of Satellite Precipitation-Driven Modeling of Flood Events in Complex Alpine Terrain

4.1 Introduction

The potential of high-resolution satellite precipitation estimation in hydrological applications has been investigated for more than two decades (Seyyedi, et al., 2015; Siddique-E-Akbor, et al., 2014; Nikolopoulos, et al., 2010; Hossain & Anagnostou, 2004; Guetter, et al., 1996). The main advantage to the conventional ground based measurements is that precipitation estimation from space-born sensors is uninhibited by topography, thus can provide coherent global scale estimates at high space (0.25^o) and time (3h) resolution (Anagnostou, et al., 2010; Kidd, et al., 2003; Arkin & Ardanuy, 1989). This provides a potential solution of measuring precipitation over complex terrain basins where ground based measurement networks are sparsely distributed or unavailable. However, precipitation estimates from satellite sensors are associated with errors that propagate to the prediction of hydrologic variables through the rainfall-runoff modeling (Mei, et al., 2016a; Seyyedi, et al., 2015; Maggioni, et al., 2013; Vergara, et al., 2013; Nikolopoulos, et al., 2010). It has been argued that the performance of satellite precipitation estimates and its driven simulation largely depend on the regional rainfall properties (e.g. types, magnitudes, space-time pattern, etc.), the geomorphology of the area (e.g. surface inclination, basin scales, etc.), the basin conditions (e.g. soil moisture, existence of snow cover, etc.), the choice of modeling complexity and finally the interactions between all of these factors (Mei, et al., 2016a; Nikolopoulos, et al., 2013; Vergara, et al., 2013; Wu, et al., 2012; Yong, et al., 2012; 2010).

Mei et al. (2014b) classified 3249 storm events from 13 varying size basins (200 km^2 to 4200 km^2) according to their rain volume and storm type (i.e. convective vs. organized frontal systems). Their results showed that satellite precipitation estimates are more biased in frontal precipitation events. On the other hand, it was shown that error has higher degree of variability for short duration events, which were associated with low rain accumulations over small basin scales. Similar results were exhibited for satellite

driven hydrologic simulations by Wu et al. (2012) who showed that the performance of hydrologic simulations improved with flood duration. Vergara et al. (2013) and Maggioni et al. (2013) conducted separate satellite precipitation error propagation analyses over mild-slope terrain basins with results revealing that the satellite-precipitation error variance is buffered by the rainfall-runoff process and that this dampening effect exhibits basin-scale dependence. Another two hydrologic evaluation studies of satellite products have shown terrain elevation dependence on the performance of satellite precipitation estimation (Mei, et al., 2016a; Yong, et al., 2012). Furthermore, Yong et al. (2014; 2012) have shown that the existence of snow cover and mixed phase precipitation over complex terrain basins can significantly affect satellite precipitation uncertainty and the satellite-precipitation driven simulations.

The majority of studies on satellite precipitation error propagation presented in the literature rely on pixel-based evaluation or long-term basin averaged time series. Few studies have focused on storm events at catchment scale, which represents the physical aspect of the rainfall-runoff transformation process (Seyyedi, et al., 2015; Nikolopoulos, et al., 2010; Hossain & Anagnostou, 2004). Nikolopoulos et al. (2010) showed that the volumetric error in rainfall is linearly translated to the error in the simulated runoff for the steep slope topography of their study region. Furthermore, Nikolopoulos et al. (2013) for a major flash flood event in the same region showed that linearity in error translation appears for wet soil moisture condition while for dry antecedent conditions error propagation was nonlinear. Several of the studies also revealed that the magnitude of error in rainfall and runoff are reduced with increasing the satellite product resolution and basin scale (Seyyedi, et al., 2015; Nikolopoulos, et al., 2013; Yilmaz, et al., 2010; Hossain & Anagnostou, 2004); these dependencies of error vary seasonally and across climate regions (Seyyedi, et al., 2015; Yilmaz, et al., 2010). Apart from the magnitude of error in hydrologic response, the timing-error is another important source of error with particular significance in satellite-based flood predictions. Hossain & Anagnostou (2004) showed that the time-to-peak error depends on various factors (e.g. duration of event, magnitude of rainfall rate, etc.).

The event-based error analysis studies discussed above relied on small number of flood events and were focused on the error magnitude in rainfall or simulated runoff missing other important event properties (e.g. overall shape of hydrograph or hyetograph). Accurate representation of the hydrographs is important for a number of flood risk operations such as reservoirs operation and timely emergency response. This study focuses on the analysis of satellite precipitation error propagation in flood simulations expanding in two main aspects: (i) evaluate a relatively large number of flood events that occurred over mountainous basins; (ii) examine error propagation for different flood types and with respect to several characteristics of flood response (i.e. timing and magnitude). Thus, we believe this study will provide new insights on the hydrologic implications of satellite precipitation error propagation.

Previous studies over the Upper Adige region have investigated the uncertainty of satellite precipitation products and its propagation in hydrologic simulations (Mei, et al., 2016a; 2014b). This study renders focus on the assessment of satellite precipitation for the prediction of flood events. Eight satellite precipitation products and 128 flood events that occurred in the period of May to November between 2002 and 2010 over nine sub-basins of the region are used to support this study. The satellite precipitation retrieval and flood modeling errors are defined with respect to reference rainfall and reference rainfall based simulations to directly make a connection between the error in quantifying the basin-average rainfall and as the corresponding error in satellite-driven runoff prediction. Events from the cold season months (December to April) where precipitation in the region is dominated by snow and the satellite products are significantly subjected to detection issues (typically non-detecting light precipitation) were not considered (Mei, et al., 2016a). It is noted that flood events occurring during the cold period in the study area are typically triggered by rain falling on snow covered areas or snowmelt processes (Zoccatelli, et al., 2017). The study is organized as follows: section 4.2 provides a description of the study area, the hydrologic model used for flood simulations, the satellite and reference precipitation data and the flood events database. Section 4.3 introduces the method used to identify and match satellite events with reference events and the error metrics

used to quantify the event-based satellite product and flood simulation error at the basin scale. Results and discussions are presented in section 4.4 and 804.5. Conclusions are summarized in section 4.6.

4.2 Study area, data and hydrologic model

4.2.1 Study area

The study focuses on nine catchments of the Upper Adige river basin closed at Bronzolo (6,967 km^2) and located in the Eastern Italian Alps (Figure 4.1). This is a mountainous area characterized with high elevation from 200 to 3900 meter above sea level (m a.s.l.), steep slopes and sharp hydro-climatic gradient (Parajka, et al., 2010). The nine selected study sub-basins (located on the west and north part of the Upper Adige basin) have mean basin elevations above 1,800 m a.s.l. and small drainage areas (50 to 600 km^2) (Table 4.1). This region is influenced by the Meridional South and Southeast circulation patterns and western Atlantic airflows causing heavy precipitation events and associated flash floods and debris flows in August to November period. The late October to April period is typically dominated by snow and widespread type precipitation, which increase the cumulative snow depth. The following late spring snow melting increases the soil moisture; precipitation and large snow melt episodes may cause floods from June to early August (Parajka, et al., 2010; Norbiato, et al., 2009a; Frei & Schär, 1998).

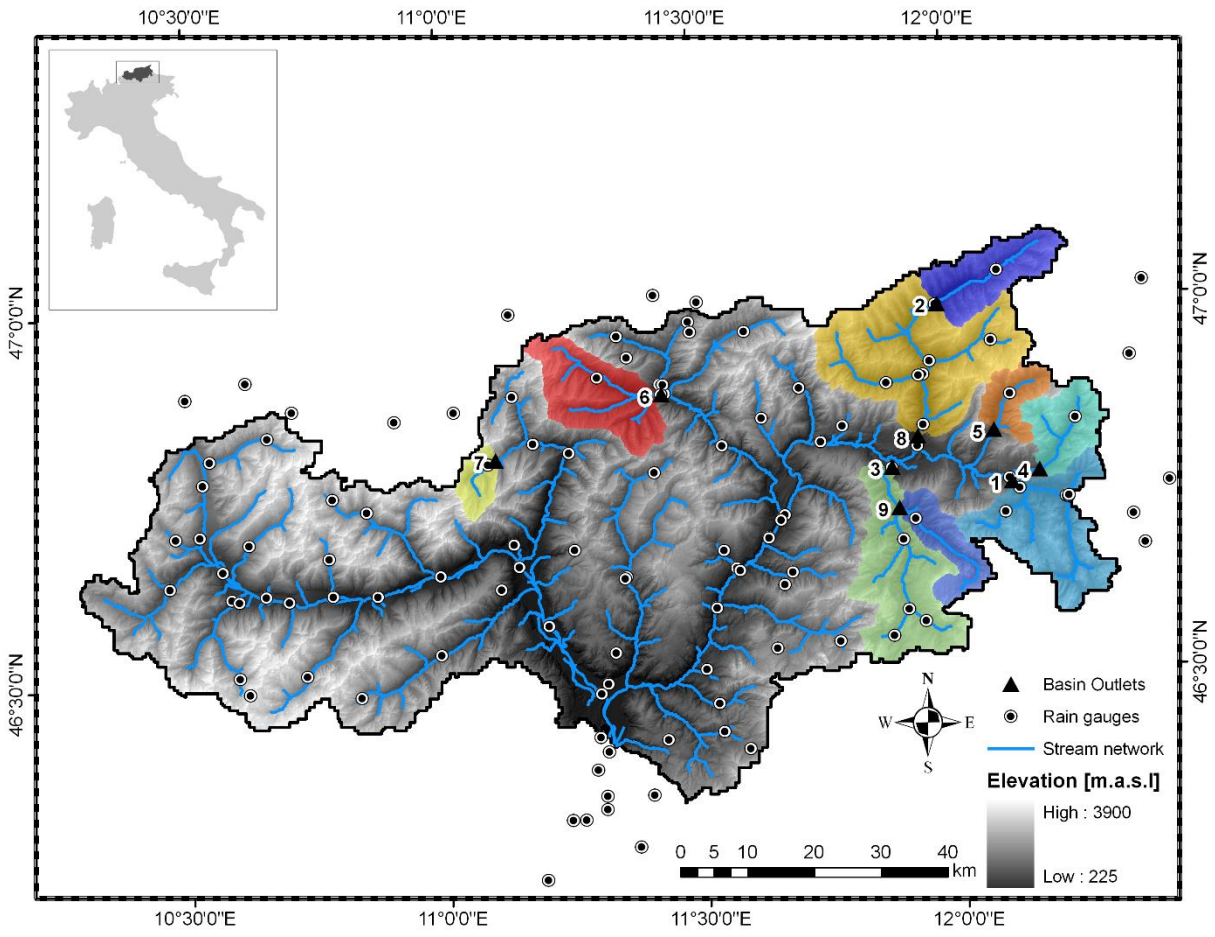

Figure 4.1. Location and topography of the sub-basins.

Table 4.1. Information of the study sub-basins.

ID	Sub-basin Name	Area (km^2)	Mean of Elevation (m a.s.l.)	NSI[1]
1	Rienza at Monguelfo	269	2401	0.61
2	Aurino at Cadipietra	150	2165	0.78
3	Gadera at Mantana	397	1956	0.42
4	Rio Casies at Colle	117	2038	0.70
5	Anterselva at Bagni di Salomone	82	1899	0.75
6	Ridanna at Vipiteno	210	1852	0.81
7	Plan at Plan	49	1858	0.66
8	Aurino at San Giorgio	608	2035	0.86
9	San Vigilio at Longega	105	1846	0.37

[1] Nash-Sutcliffe Index

4.2.2 Precipitation data

Eight quasi-global satellite precipitation products are evaluated. The first two products, named 3B42-CCA and 3B42-V7 (hereafter named TR and aTR), are from the National Aeronautics and Space Administration Tropical Rainfall Measuring Mission Multi-satellite Precipitation Analysis (TMPA). The 3B42-CCA and 3B42-V7 product are corrected versions of the near-real-time 3B42 where the 3B42-CCA is adjusted according to the climatological correction algorithm (CCA) and the other is the post-processing gauge-adjusted product (Huffman, et al., 2010; 2007). The next two products are the Precipitation Estimation from Remotely Sensed Information using Artificial Neural Networks (PERSIANN, hereafter named PE) (Sorooshian, et al., 2000) and its bias adjusted version based on the GPCP (Global Precipitation Climatology Project) product and the 2.5°/monthly PERSIANN estimates (hereafter named aPE) (Huffman, et al., 2009; Adler, et al., 2003). The National Oceanic and Atmospheric Administration Climate Prediction Center morphing (CMORPH, abbreviated as CM) technique (Joyce, et al., 2004) and a recently available gauge-adjusted version (named hereafter as aCM) based on daily gauge estimates from 30,000 gauges worldwide are also investigated (Xie, et al., 2011). These six products are 0.25°/3-hourly. We also included two high-resolution products available at 0.073° and hourly space-time scale. These two products are the Kalman Filter-based CMORPH and similarly its gauge-corrected counterpart (named as hC and ahC hereafter). The Kalman Filter-based CMORPH incorporates additional IR-based information and the integration of all PMW- and IR-based information from the original CMORPH to produce accurate estimations of precipitation (Joyce & Xie, 2011).

A network of 108 rain gauges distributed across the entire Upper Adige river basin represent an untypically high density network (~1 gauge per 65 km^2) for a mountainous area. The hourly rain gauge record used in this study spans a nine-year period from 2002 to 2010. Rain gauge data were interpolated, using the nearest neighbor method, which is the procedure used by the hydrologic model to convert rain gauge data to basin-averages; this interpolation method is consistent to previous satellite precipitation error studies in the area (Mei, et al., 2016a; 2014b). Gauge and satellite precipitation fields are then averaged at

the sub-basin scale using areal weighting, to produce the basin-average precipitation time series for the nine study catchments. These time series were used to force the hydrologic model, which is discussed next.

4.2.3 Hydrologic simulations

In this study we applied the Integrated Catchment Hydrological Model (ICHYMOD), which is an off-line version of the operational modeling scheme of the Adige River Flood Forecasting System. ICHYMOD involves a semi-distributed conceptual rainfall-runoff model that consists of a snow routine, a soil moisture routine and a flow routine model. The soil moisture component of the ICHYMOD follows the structure of the probability distributed moisture model (Moore, 2007; 1985). Snow accumulation and melting is modeled based on temporally variable distribution functions which exploit a combined radiation index degree-day concept originally developed by Cazorzi & Dalla Fontana (1996); potential evapotranspiration is estimated by the Hargreaves method (Hargreaves & Samani, 1982). The model is applied in a semi-distributed way by dividing the study area into sub-basins. At the sub-basin scale, runoff is routed by using a cascade of two linear conceptual reservoirs. Hydrographs are routed through the river network by means of the Muskingum-Cunge method (Cunge, 1969). Application of the model requires specification of 14 parameters for the snow routine, the runoff generation module and the runoff propagation module (Norbiato, et al., 2008). The calibration procedure for determining the model parameters is detailed in Borga et al. (2014). In our analysis, we adopt the same modeling parameters for our simulations to allow results to be directly related to an existing flood forecasting application. This also helps to exclude the effect of model uncertainty isolating the effect of precipitation error propagation, which is the focus of our study.

The input precipitation forcing is aggregated at the sub-basin scale, accordingly with the procedure reported in the previous section. Given the dense rain gauge coverage, sub-basin scale rainfall estimates obtained by using the ground stations are considered as the ground reference for inter-comparison in this work. Analogously, the gauge-precipitation driven hydrological simulations are used as reference for comparison with the satellite-precipitation driven hydrological simulations. Hydrological simulations are carried out by using rain gauge-derived precipitation for the nine study basins from 2002 to 2010, thus

providing the reference discharge time series. The accuracy of the simulations was qualified by using the Nash-Sutcliffe Index (NSI) (Nash & Sutcliffe, 1970). The mean of NSI determined between the gauge-driven simulated stream flows and measured stream flows for the selected basins and period of simulation is 0.66 (Table 4.1). We notice low model efficiency for basin 3 and 9, which is partially attributed to the difficulties in simulating responses from a karst aquifer-dominated catchment. The flood periods in the observed streamflow data are well captured by the model, whereas recession periods are less reliably represented. The hourly runoff simulations for all satellite products were run for the May to November period of each study year to avoid mixing satellite estimation errors for rainfall and snowfall (snowfall dominate from December to April of the study area). Each simulation cycle (i.e. May-Nov per year) was initialized by the state variables (snow and soil moisture storage) obtained from the continuous gauge-based simulations.

4.2.4 Flood events: archive and flood types

The archive of observed flood events used in this study has been established based on the work of Zoccatelli et al. (2017). In this work, the archive of the three most intense floods observed over each year and over each study basin has been used to establish a flood type classification based on a combination of a number of process indicators, including the timing of the floods, storm duration, rainfall depths, snowmelt, catchment state, runoff response dynamics, and spatial coherence (Merz & Blöschl, 2003). In Zoccatelli et al. (2017) the flood type classification scheme is based on data from 33 basins distributed along a North-South Alpine transect (including the 9 basins used in the current study), with a focus which permits to analyze the changes in flood types along an altitudinal and climatic gradient. The application of the ICHYMOD model over each basin allows retrieving variables such as catchment soil moisture conditions, solid precipitation/snowmelt contribution to flood formation.

The analysis, carried out based on a cluster analysis, helped to determine three flood types:

1. Snow-dominated floods: events in which the input from snowmelt dominates over liquid precipitation.

2. Rain dominated events: floods with time to flow peak exceeding 24 hours and moderately intense rainfall uniformly distributed over the area.

3. Flash flood events: events developing in smaller basins (mostly smaller than 200 km^2) triggered by intense rainfall and with time to flow peak less than 24 hours.

In the current work, we limited the analysis only to the warm season floods (May to November), which lead to the exclusion of the snow-dominated events. Thus, only two types of floods are used here: i) long-rain flood (116 events) and flash floods (12 events).

The selected flood event properties are summarized in Table 4.2. It can be inferred that the flash flood events are characterized by more intense rainfall and flow rates, given the shorter durations and larger accumulations. The standard deviations (*SDs*) of event hyetograph and hydrograph are also different between the two types of flood events, with higher values obtained for the flash floods. The above observations reveal the higher intensity and variability associated with flash floods relative to rain floods. The average values and ranges of initial soil moisture and runoff coefficient, for all the events analyzed, are also listed in the table. It is seen that although the mean of initial soil moisture is similar between the two flood types (1% higher in flash flood cases), the event-based runoff coefficients (*RC*) are quite different between rain flood and flash flood events (22% vs. 35% average *RC* with wider value range for rain vs. flash flood events).

Table 4.2. Mean and range of event properties for rain flood and flash flood.

Number of Event	Event Type	Time Series	Mean and Range of Event Properties				
			Duration (h)	Depth (mm)	SD[1] (mm/h)	Initial Soil Moisture (% saturation)	Runoff Coefficient (%)
116	Rain Flood	Rainfall	45 [9 134]	47 [7 99]	1.8 [0.4 4.7]	57 [23 92]	22 [12 34]
		Runoff	104 [34 281]	23 [3 80]	0.1 [0.0 0.6]		
12	Flash Flood	Rainfall	32 [10 69]	54 [20 106]	2.4 [1.3 5.1]	58 [36 80]	35 [18 44]
		Runoff	62 [31 123]	32 [6 69]	0.3 [0.1 0.5]		

1 Standard deviation of event time series

4.3 Methodology

4.3.1 Event matching

The start time and duration of a rainfall event varies across the different rainfall dataset, which results in also varying temporal characteristics of simulated flood hydrographs. Therefore, event-based analysis requires matching each satellite rainfall event and its associated simulated flood events with the corresponding reference rainfall and flood events. In this section, we introduce the method utilized to identify and match the 128 events from the database with their corresponding counterparts from each of the flow simulation to form the "flood event pairs" used in the error analysis. A rainfall-runoff event is considered as a combination of the basin-average rainfall and the resulting flood event. Thus, matching a rainfall-runoff event required identifying the timing of both aspects. The method is separated into two parts; firs the timing of flood events are identified and matched with the database, second rainfall events are identified for each product and third, the rainfall events from various products are matched to the corresponding flood event based on the Characteristic Point Method (CPM, Mei & Anagnostou (2015)). Inputs of the process are the timing of flood events from Zoccatelli et al. (2017), and the corresponding time series of both satellite and rain gauge-based rainfall and simulated runoff. Outputs are the start/end time of matched gauge and satellite rainfall-runoff events pairs. The following steps applied to each satellite product are:

1) The start and end hour of each flood event are identified from the simulated flow time series of all the products according to the database.
2) Identify continuous periods of nonzero rainfall, based on the basin-average rainfall time series.
3) For each product match rainfall periods from step 2) with corresponding flood events using CPM. Details of the technical steps are documented in section 3.2.3 of Mei & Anagnostou (2015). For each flood event, CPM identifies the associated rainfall period. If more than one rainfall events satisfy the conditions, they are jointed as one rainfall event and are considered as the inducing rainfall of the flood event. These rainfall and flood event pairs together form a rainfall-runoff event.

Two sample matched events derived from the above method are illustrated in Figure 4.2. As it is exhibited in the figure, the start/end time of event rainfall and runoff could be varied from different rainfall forcing. However, these differences are within relatively small extends with hydrographs having reasonable shapes. These together verify the matching technique applied in this study.

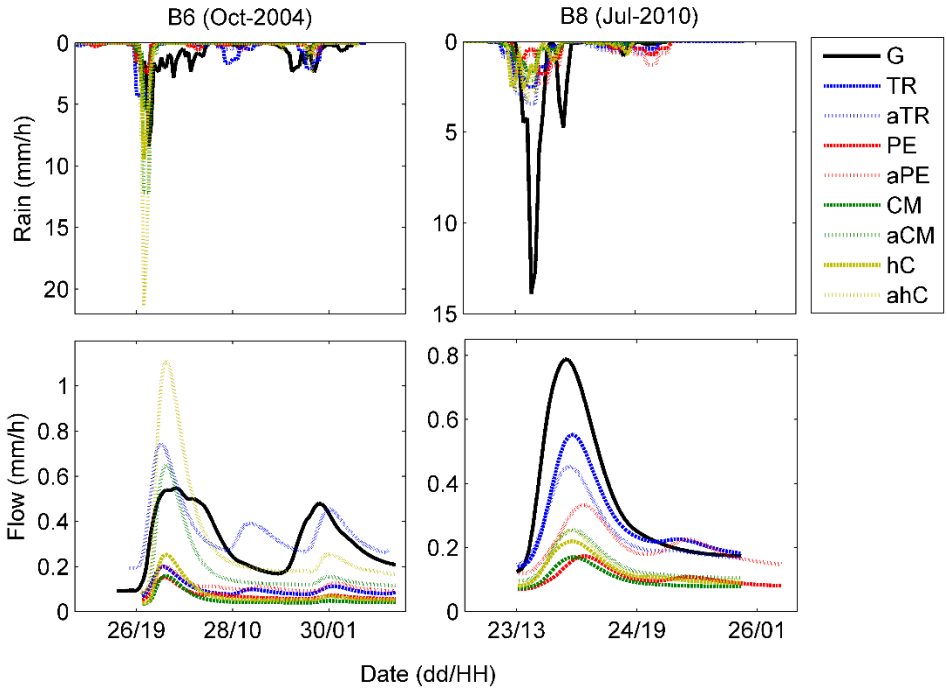

Figure 4.2. Example of two matched rainfall-runoff events for basins with ID 6 (left) and 8 (right). Basin-averaged rainfall time series (top) and simulated hydrographs (bottom) are shown for all precipitation products used.

4.3.2 Event properties

We focus our error analysis on three event properties: the event cumulative rainfall or runoff depth (V_X, in mm), the centroid of the hyetograph or hydrograph from the starting time of event (Ct_X, in h) and the spreadness of hyetograph or hydrograph (Sd_X, in h). The concept of event cumulative depth is defined as:

$$V_X = \int_{T_X} X(t)\, dt \tag{4.1}$$

where X can be properties from either the rainfall or simulated flow aspect. Thus, $X(t)$ is the precipitation or runoff time series for satellite or reference (in mm/h) and T_X is the duration of the rainfall or runoff event.

The concept of centroid is often used as a surrogate of time to peak to account for the time series dynamic. It determines the arrival of event mass center; it is the weighted average of time with respect to the temporal dynamics of rainfall (or runoff) time series:

$$Ct_X = \frac{\int_{T_X} t \cdot X(t)\, dt}{\int_{T_X} X(t)\, dt} \tag{4.2}$$

Ct_r defines the location of event mass center with respect to the temporal variability of time series.

The last event property analyzed is the spreadness (denoted as Sd_x) quantifies the temporal degree of dispersion of the event time series. It determines the variability of event time (t) with respect to the temporal dynamics of time series:

$$Sd_X = \sqrt{\frac{\int_{T_X} (t - Ct_X)^2 X(t)\, dt}{\int_{T_X} X(t)\, dt}} \tag{4.3}$$

Typically, larger Sd_x values associated with more dispersed shape of the time series around the centroid (i.e. high flow tends to locate on both the early and late phase of an event). For the same number of peak in the hydrograph (e.g. mono-modal or bi-modal) this parameter can be surrogate to the peakedness of time series.

4.3.3 Comparative analysis

Comparison between reference and satellite based rainfall/runoff events has two main objectives. First, differences in event properties (e.g. magnitude, variability etc.) are assessed to demonstrate the ability and limitations of satellite products in representing the characteristics of flood events. Second, propagation of error from rainfall-to-runoff is evaluated to understand how certain properties of error in rainfall translate into error in runoff. The error analysis is conducted based on metrics determined for the properties of "event pairs" described in the previous section. We use the Taylor diagram (Taylor, 2001) to demonstrate the

consistency between event properties calculated from the satellite products and those attained from the reference time series. The Taylor diagrams are produced for both rainfall and simulated flow. The metrics and statistics involved in the Taylor diagram are: the variance (σ^2) of satellite and gauge event time series, the centered root mean square difference (C*RMSD*) and the correlation coefficient (ρ). Forms of these three metrics (illustrated for the cumulative depth property) are:

$$\sigma_{V,G}^2 = \frac{1}{N}\sum\left[V_G(n) - \frac{1}{N}\sum V_G(n)\right]^2 \tag{4.4}$$

$$CRMSD_V = \sqrt{\frac{1}{N}\sum\left[V_S(n) - V_G(n) - \frac{1}{N}\sum[V_S(n) - V_G(n)]\right]^2} \tag{4.5}$$

$$\rho_V = \frac{\frac{1}{N}\sum\left[V_S(n) - \frac{1}{N}\sum V_S(n)\right]\left[V_G(n) - \frac{1}{N}\sum V_G(n)\right]}{\sigma_{V,S}\sigma_{V,G}} \tag{4.6}$$

where *n* and *N* stand for the event index and the total number of event and subscript *G* and *S* represent the gauge and satellite hyetograph/hydrograph respectively.

Our comparative analysis also includes the evaluation of systematic and random error determined from each event pairs. The systematic error is quantified as the mean relative error (*MRE*) of event properties between satellite and reference. The *MRE* form illustrated for the cumulative depth property is:

$$MRE_{V_X} = \frac{V_{X,S} - V_{X,G}}{V_{X,G}} \tag{4.7}$$

Analogously, MRE_{Ct} and MRE_{Sd} are similarly defined by replacing *V* with *Ct* and *Sd*, respectively. Value of *MRE* greater/smaller than 0 indicates over-/under- estimation of the reference property for an event. The random error is calculated as the centered relative root mean square difference (*CRRMSD*) determined for the time series of the "event pairs". As shown in Figure 4.2 the timing of event time series of satellite products can be slightly different from reference in terms of the beginning and ending hour. To remove the timing issues, we take the common period for satellite and reference hydrographs/hyetograph before calculating the *CRRMSD*. The *CRRMSD* is calculated based on these new time series as:

$$CRRMSD_X = \frac{\sqrt{\frac{1}{|T_X^*|}\sum\left[X_S^*(t) - X_G^*(t) - \frac{1}{|T_X^*|}\sum[X_S^*(t) - X_G^*(t)]\right]^2}}{\frac{1}{|T_X^*|}\sum X_G^*(t)} \quad (4.8)$$

where asterisk (*) represents the time series with common period T_X^*. The *CRRMSD* quantifies the random error between two time series as the smaller the value the higher degree of similarity the two time series.

To quantify the error propagation through the rainfall-runoff process, we take the absolute ratio (γ) between error metrics (*MRE* and *CRRMSD*) for the flood and rainfall event. By taking the absolute value, γ is always greater than 0, while values higher (lower) than 1 indicate amplification (dampening) of the error magnitude. We further investigate the role of event-based *RC* (as a lumped indicator of the initial condition and interaction between rainfall and the various catchment processes) on error propagation by sorting the events to three thresholds: below 40th, 40th to 75th and above 75th percentile groups of the *RC* values.

4.4 Results

As a qualitative inspection of the error pattern, we show two sample events (after completion of the matching procedure) in Figure 4.2. In the first event, the CMORPH products, particularly the gauge-adjusted ones (aCM and ahC), are overestimating the gauge rainfall. This leads also to overestimation in the simulated flow. It is worth noting from this Figure that although the 3B42V7 product is underestimating the reference rainfall, it's distinctly high initial flow condition yields overestimation of the gauge-simulated flood event (note that the initial condition for each product could be different since the simulations run continuously throughout each May – Nov period). For the rest of the satellite products, their underestimation relative to the gauge rainfall and relatively low initial flow rates resulted in strong underestimation of the reference flow simulations. For the second sample event, all the products are underestimating the gauge rainfall with similar initial flow rate. Thus, all of them are providing

underestimation of the reference flood event. This shows that the higher initial flow rate to the reference may not always yield higher cumulative flow depth (implying overestimation) to the reference due to the difference in rainfall variability and its complex interaction with the catchment processes.

4.4.1 Event Properties Error Statistics

First, we present the Taylor diagrams, which integrate the statistics introduced in Eq.(4.4) through (4.6) for the three event properties (cumulative depth, centroid and spreadness) in basin-average rainfall and simulated runoff time series. Results for cumulative rainfall and runoff depths for the two flood types are presented in Figure 4.3. As shown, the satellite products underestimate the variability of cumulative depth of the reference precipitation and simulated runoff, especially for the flash flood cases. Comparison between rain flood and flash flood events suggests that the σ^2 of cumulative depths decreases noticeably for the two 3B42 and PERSIANN products and only slightly for the CMORPH and Kalman Filter Based-CMORPH. The *CRMSD* values exhibit distinct patterns between the two flood types and between rainfall and simulated runoff parameters. Lower *CRMSD* values are shown for the runoff based event cumulative depth compared to the basin-average precipitation event parameters. Comparing the *CRMSD* of the two flood event types for 3B42 and PERSIANN shows that the flash flood events exhibit lower *CRMSD* values compared to the rain flood events on both the event rainfalls and their corresponding flow simulations; reversed trends are shown on the CMORPHs estimated cumulative rainfall depth. It is noted that the two gauge adjusted CMORPHs exhibit similar (slightly decreased) *CRMSD* values with the corresponding unadjusted counterparts. The last aspect shown on the Taylor diagram is the correlation between the *V* values of each satellite product and reference. The correlation coefficients of cumulative event flow depth are higher than the basin-averaged precipitation ones for most of the products, pointing to the fact that the inclusion of baseflow component in the cumulative depth parameter modulates the volumetric error. The ρ for the hydrograph range from 0.4 to 0.8; ρ for the hyetograph are located around 0.4. Also, similar ρ values are shown for the high-resolution Kalman Filter Based-CMORPH product compared to the original CMORPH product.

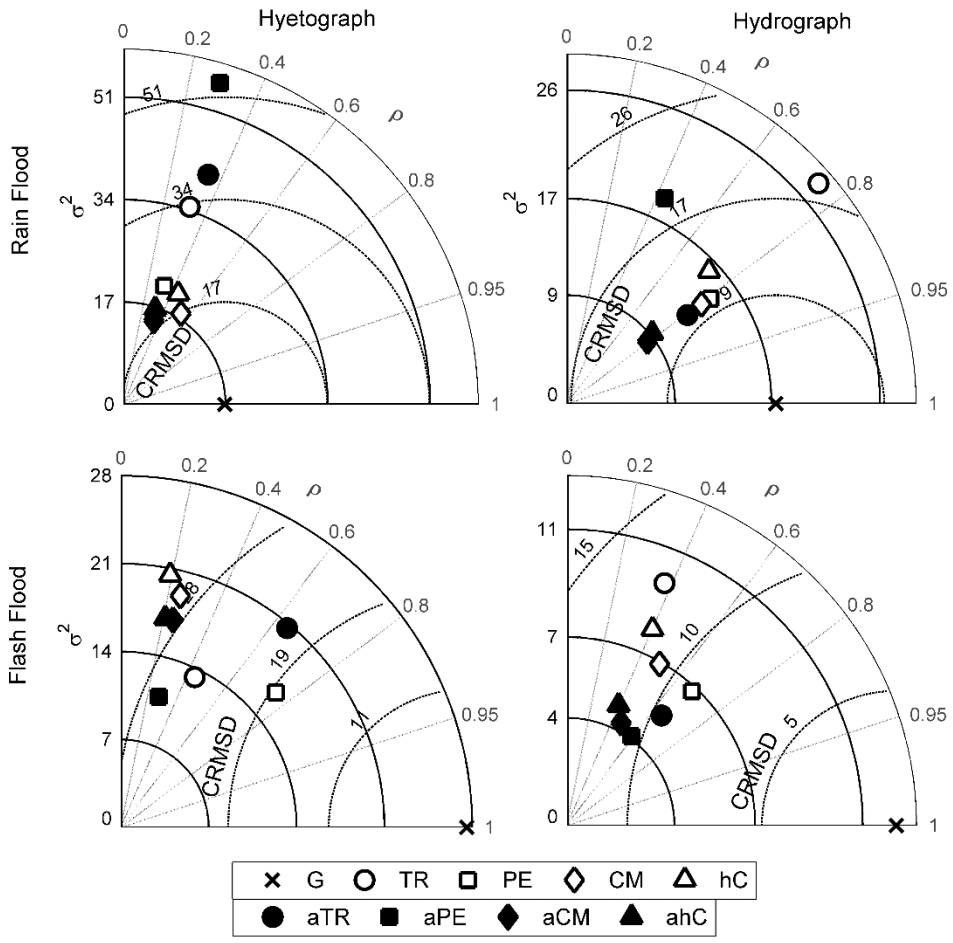

Figure 4.3. Taylor diagram of the cumulative rainfall and flow depths for different products.

Results for the event centroid parameter are illustrated by the Taylor diagram in Figure 4.4. It is shown that all the points are relatively closely distributed to each other regardless the flood types and rainfall or runoff. This is particularly seen for the rain flood hydrograph centroid cases. This means the values of σ^2, *CRMSD* and ρ are in general almost identical for the eight products and the estimations on reference flood event centroid are consistent. In other words, the effect of gauge-adjustments or spatial aggregation has little influence on the arrival of event mass center. In details, the *CRMSD* of runoff event centroids are closer to the reference compared to the rainfall ones, indicating clear dampening effect in random error of event centroid. This dampening effect can be further confirmed by the less-than-one values of $\gamma_{MRE,Ct}$ discussed in detail later in this section. The flash flood events in this case also exhibit lower *CRMSD* values contrasted to the rain flood counterparts. This is due to the shorter concentration time and duration (or

equivalently shorter in event centroid) of flash flood event than the rain flood event. Observations on the correlation coefficients reveal that the flood event centroid parameter values derived from the satellite products are characterized with high correlation (above 0.95 and 0.8 for rain flood and flash flood). The correlation coefficient is reduced in the rainfall event cases where the ρ values for rain flood and flash flood are around 0.8 and 0.6 respectively.

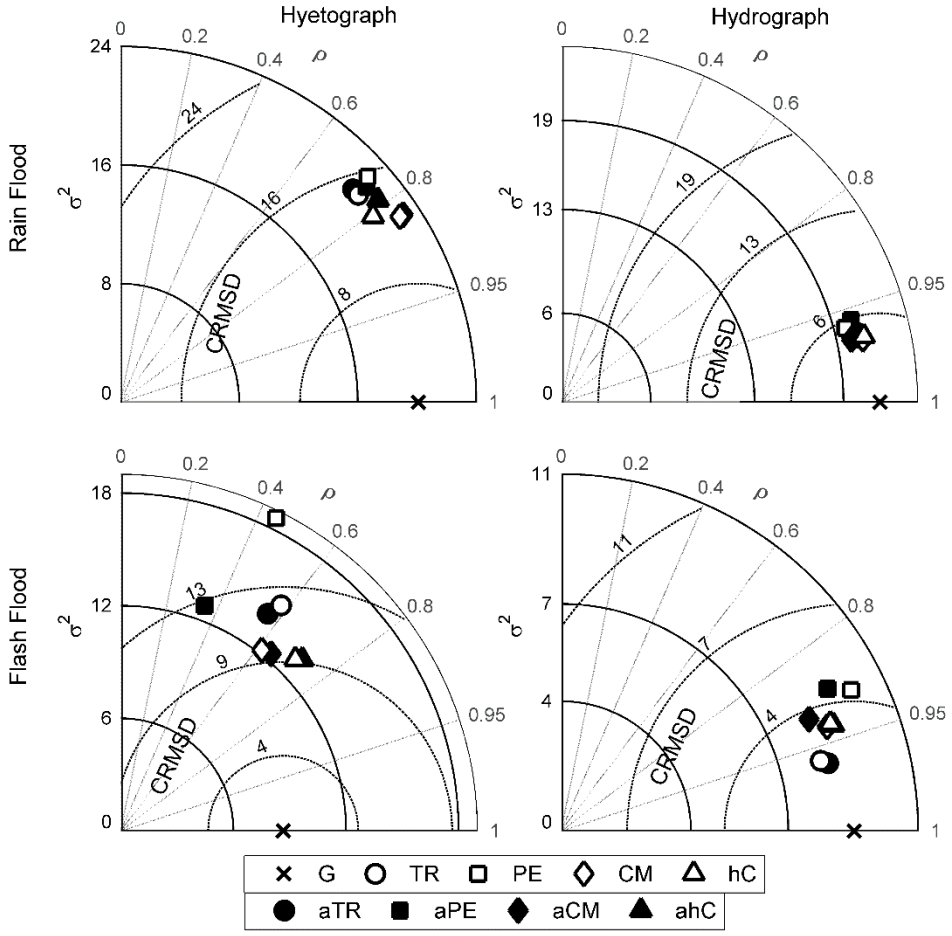

Figure 4.4. Same as in Figure 4.3, but for the event centroid.

The error metrics for spreadness are integrated in the Taylor diagrams of Figure 4.5. The variance of reference spreadness is overestimated by nearly all of the satellite products. Similar to the results of event centroid, the satellite estimations on reference time series in terms of the spreadness reveals relatively low *CRMSD*. Meanwhile, the rain flood spreadness cases share fairly similar performances among products where all the points are closely located to each other. This states the insignificant influences from gauge-

adjustment and resolution to the spreadness parameter. The *CRMSD* values of hydrograph for the two flood types show negligible change compared to the hyetograph ones implying small dampening effect in spreadness through the rainfall-runoff processes. This is also later suggested by the close-to-one median of the $\gamma_{MRE,Sd}$. A comparison from rain flood to flash flood reveals that the values of *CRMSD* are decreasing; this is because the spreadness of flash flood is smaller than the rain flood and thus results in lower degree of random error. Different from the *CRMSD*, the correlation values reveal improvements from the hyetograph to the hydrograph (from below to above 0.8 and below to above 0.4 for rain flood and flash flood).

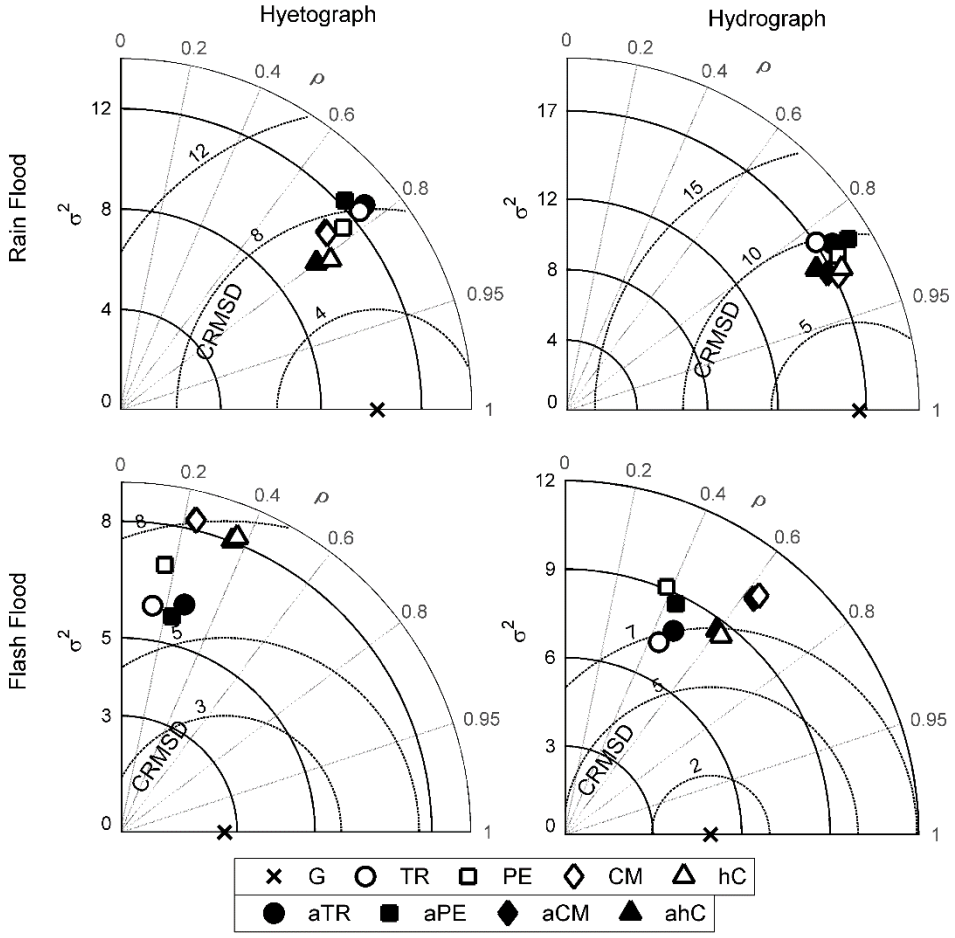

Figure 4.5. Same as in Figure 4.3, but for the spreadness.

The mean of *MRE* determined based on the three properties of the study rainfall and flow event time series are reported in Table 4.3 for each product. It is seen that *MRE* in rainfall depth is not linearly related

to those in the runoff depth indicated by fairly low *CC* values for most of the products. Results suggest that the total depth of rainfall is mostly underestimated; this leads also to underestimations for the event runoff. The *MRE* of runoff centroid and spreadness appear generally uncorrelated with the *MRE* in rainfall centroid, which suggest that differences in hyetograph are not linearly translated into differences in the shape of hydrograph. A potential explanation for this is given by the fact that hydrograph shape is controlled, apart from rainfall temporal variability, from the space-time interaction between the generated flow and flow routing (Mei, et al., 2014a; Viglione, et al., 2010b). Most of the mean *MRE* magnitudes in event rainfall centroid and spreadness are larger than the event flow ones indicating higher similarity in shape of the hydrograph compared to the corresponding hyetograph. This reveals the filtering effect of catchment which smooths the high frequent precipitation signal to low frequent flow signal (Skøien & Blöschl, 2006; Skøien, et al., 2003). We show also the mean *MRE* of peak flow as a complement to the spreadness parameter. Generally, the mean peak flow *MRE* are negative (except for the CM case) indicating underestimation in the peak flow rate. The *CC* values demonstrate the positive relationship between *MRE* in peak flow and rainfall depth (except for CM and aCM). A product-wise comparison reveals that the gauge-adjusted products show improvements in the mean *MRE* of cumulative depth contrasting to the cases of event centroid and spreadness which show no improvements. This is an expected observation since the gauge-adjustment algorithm for satellite products are monthly (i.e. the adjustment changes the cumulative volume of precipitation within the monthly period but maintains the space-time variability of precipitation fields).

Table 4.3. Mean MRE for rainfall and runoff and correlation coefficient between the biases.

Products	Cumulative Depth			Centroid			Peakedness			Peak Flow	CC[1]
	Rain	Flood	CC	Rain	Flood	CC	Rain	Flood	CC		
TR	0.22	-0.03	0.5	0.60	0.00	0.2	0.86	0.19	0.4	-0.12	0.6
aTR	0.00	-0.02	-0.0	0.60	0.52	-0.1	0.81	-0.01	0.1	-0.28	0.5
PE	-0.20	0.40	0.1	0.11	-0.04	0.1	0.49	-0.18	0.3	-0.28	0.9
aPE	-0.12	-0.30	0.3	0.08	-0.24	0.3	0.42	-0.04	-0.0	-0.01	0.7
CM	-0.45	-0.17	0.1	0.44	-0.21	0.1	0.48	-0.07	-0.3	0.13	0.1
aCM	-0.21	-0.46	0.4	0.44	-0.62	0.2	0.49	-0.36	-0.1	-0.02	0.1
hC	-0.45	0.12	0.0	0.16	-0.21	0.2	0.26	-0.34	-0.2	-0.47	0.7
ahC	-0.22	-0.03	0.1	0.14	0.13	-0.2	0.23	-0.44	0.0	-0.04	0.2

[1] Correlation coefficient between MRE of cumulative depth of rainfall and peak flow

The random error quantified by the centered relative root mean square difference (*CRRMSD*) for each event pair are visualized as boxplots in Figure 4.6 for the two food types. As it is observed from the top and bottom panels, the medians and value ranges of event rainfall *CRRMSD* are almost 10 times (4 times) of the runoff ones for the rain flood (flash flood) events. This represents a significant dampening of the random error component (in terms of the overall value and value variability) through the rainfall-runoff process. Dampening in random error through the hydrologic model is expected since the output flow signal is less dynamic relative to the rainfall forcing, which has been reported in several error propagation studies (Mei, et al., 2016a; Maggioni, et al., 2013; Vergara, et al., 2013; Nikolopoulos, et al., 2010). Comparing the two flood types reveals that the centered relative root mean square differences for both the event rainfall and runoff are closer for the flash flood cases, characterized with narrower value ranges. This could be attributed to the higher runoff coefficient condition in flash flooding which leads to a more linear behavior in error translation. The magnitudes of *CRRMSD* between the near-real-time and gauge-adjusted products are fairly similar which again could be due to the nature of gauge-adjusted algorithms as stated in the previous paragraph.

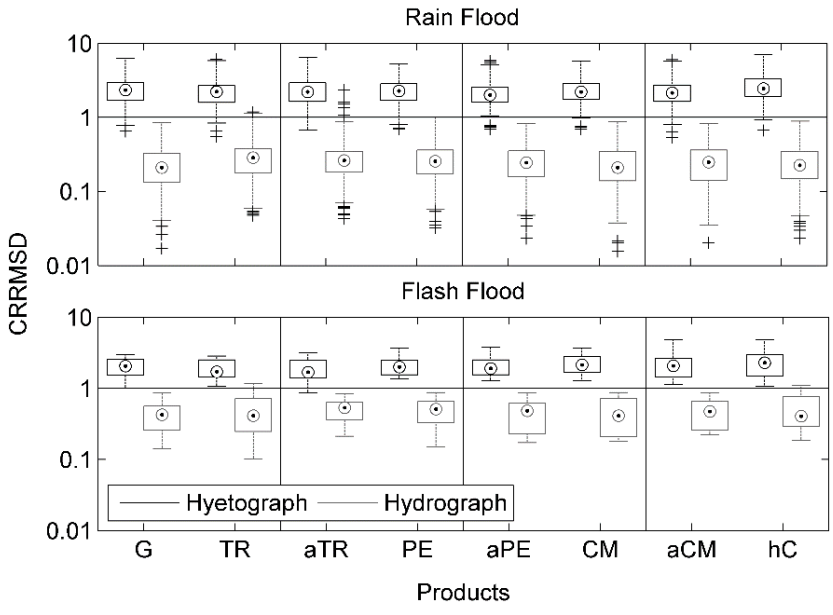

Figure 4.6. Boxplots of the centered relative root mean square difference. Cross corresponds to outlier and circle represent median.

4.4.2 Error Propagation

To further investigate the patterns of the error propagation of event properties from precipitation to runoff simulations, ratio of *MRE* between rainfall and runoff are taken (denoted as γ). The γ values for all the events and products are rendered as boxplots in Figure 4.7. The upper panel of Figure 4.7 shows the ratio of *MRE* of cumulative depth for the two flood types. It is seen that the values are mostly around 1, indicating weak dampening effect in the volumetric error when translating the event rainfall to runoff. This is consistent with the value magnitudes for mean *MRE* of rainfall and runoff exhibited in Table 4.3. The middle panel of Figure 4.7 displays the γ_{MRE} of event centroids (mostly from 0.01 to 10). Clear error buffering effect in the *MRE* of event centroid is revealed by the smaller than one $\gamma_{MRE,Ct}$ values confirming the observation from Table 4.3. This means with the various differences in arrival of rainfall event, the rainfall-runoff processes are able to mitigate these differences and give closer estimation in arrival of flood events. The event spreadness is demonstrated in the last panel with results showing again dampening effect as it is in Table 4.3 (25^{th} and 75^{th} quantiles of $\gamma_{MRE,Sd}$ are distributed within 0.1 to 1). This could be anticipated since in general the shapes of hydrograph (from different rainfall forcing) are much more alike with each other than those of the hyetograph. The gauge-adjustment is concluded to have limited effect on the error in time series shape given the almost identical $\gamma_{MRE,Ct}$ and $\gamma_{MRE,Sd}$ between the near-real-time products and their corresponding gauge-adjusted counterparts. This is also explained by the same reason that gauge adjustment is not able to change the space-time dynamic of rainfall at event scales.

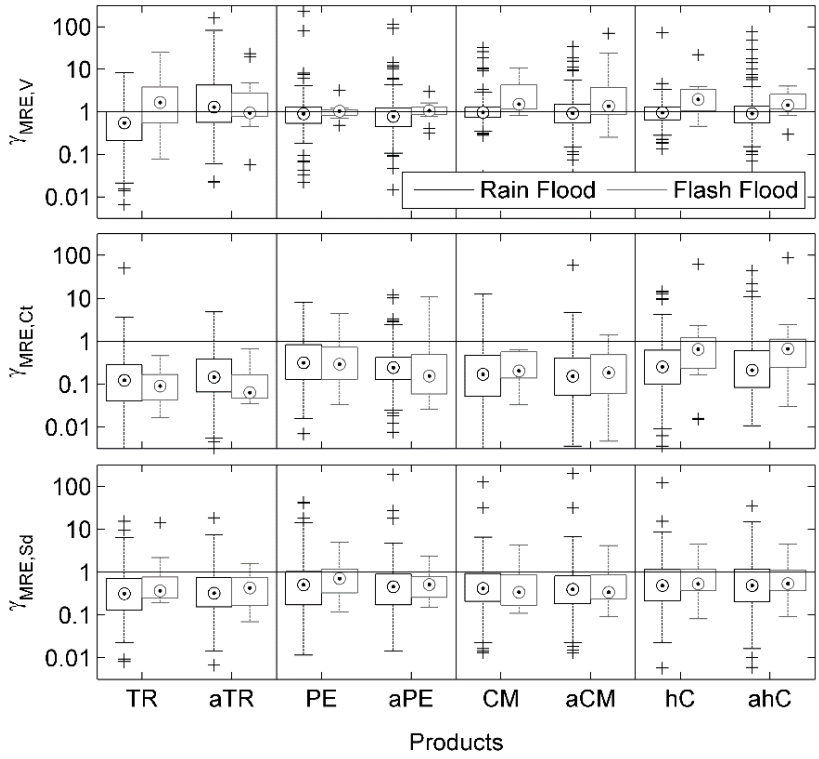

Figure 4.7. Ratio of mean relative error for the a) depth, b) centroid and c) spreadness property. Cross corresponds to outlier and circle represent median.

Similar to the *MRE*, the error propagation of *CRRMSD* is quantified by the γ_{CRRMSD} values shown in Figure 4.8. The *CRRMSD* ratio patterns are not very distinctive between products. The upper panel representing the two flood types further confirms the random error dampening effect (revealed in Figure 4.6) by giving γ_{CRRMSD} values lower than 1. The figure also demonstrates that the differences in random error dampening for the two flood types are not the same. The *CRRMSD* ratios of rain flood range from 0.05 to 0.2 for most of the event pairs (in terms of the 25th and 75th quantiles) while the flash flood counterparts are noticeably higher, distributing mostly at 0.1 to 0.4. This is ascribed to the stronger linear precipitation to runoff error translation for the flash flood events (due to the higher *RC*). The role of *RC* on the random error propagation is visualized in the lower panel of Figure 4.8. The boxplots indicate increase in the γ_{CRRMSD} values with the event-based runoff coefficients but decrease in their value ranges, indicating a positive relationship between *RC* and the degree of linearity (Nikolopoulos, et al., 2013; 2010). Values of

γ_{CRRMSD} for both gauge-adjusted and near-real-time products are almost identical because gauge adjustment changes the overall magnitude rather than the space-time organization of precipitation.

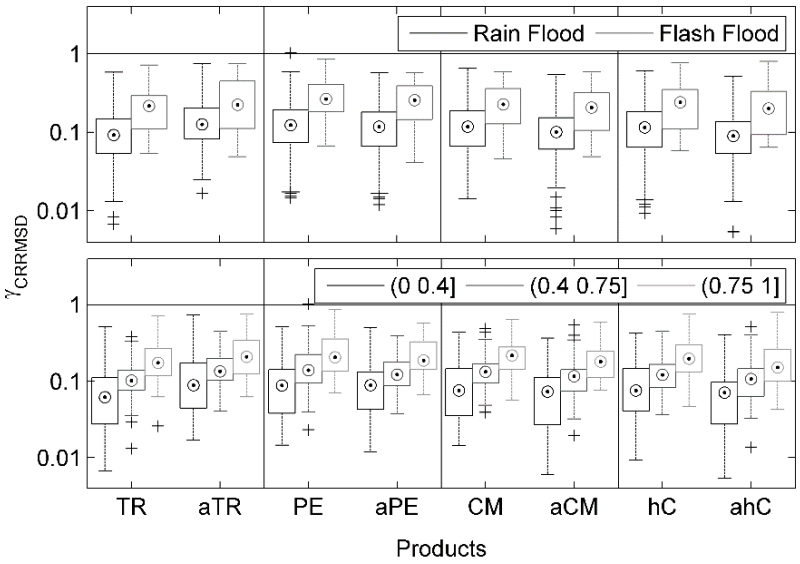

Figure 4.8. Ratio of centered relative root mean square difference sorted according to a) flood type and b) runoff coefficient. Cross corresponds to outlier and circle represent median.

4.5 Discussion

Overall, results from this study show that the satellite derived cumulative depth deviates significantly from the gauge-based one while the satellite performance in estimating the centroid and spreadness is generally better (both in terms of rainfall and simulated runoff). Specifically, lower degree of random error (*CRMSD*) with higher temporal correlation (ρ) is found in the estimates from the hydrograph cases for the three event properties parameters. It is also noted that the gauge adjustment to the satellite products and spatial aggregation yield similar degree of consistency in the event centroid and spreadness parameters described by the Taylor diagram statistics.

The systematic error in terms of *MRE* revealed mostly underestimation in the cumulative depth parameter. The *MRE* magnitudes for the shape parameters (centroid and spreadness) exhibited more

pronounced significance for the hyetograph relative to the simulated runoff due to the dampening of error from rainfall-to-runoff. Systematic error of the cumulative depth and shape parameters in rainfall is uncorrelated with error in runoff depth. This is due to the fact that volume and shape of flood hydrograph is controlled not only by the volume and shape of hyetograph but also by the space-time structure of runoff generation and routing. The magnitude of random error quantified by CRRMSD is found to be higher in the hyetograph. Also, rain flood events exhibited higher CRRMSD magnitudes than the flash flood events. Gauge-adjustment in satellite products yielded improvement in the systematic error of cumulative depth, but the systematic error of shape parameters as well as the random error component remained unaffected.

Investigation of the propagation of precipitation error to runoff reveals a clear dampening effect in the *MRE* of the centroid and spreadness parameters, but not in the cumulative depth. The error propagation ratio of cumulative depth for most of the products is fairly close to one. These findings indicate that discrepancies in hyetograph shape can be smoothed out by the rainfall-runoff process at catchment scale, which acts as space-time filter (Skøien & Blöschl, 2006). However, underestimation of rainfall volume remains a main issue in capturing flood magnitude. Finally, examination of the error propagation dependence on flood type and runoff coefficient showed a clear dependence to both factors. Specifically, higher degree of linearity in error propagation is associated with flash flood events and events with higher runoff coefficients.

4.6 Conclusions

In this work, an event-based analysis of satellite rainfall estimation error and its propagation in streamflow simulations is conducted for a number of flood events over mountainous basins in the Eastern Italian Alps. Conclusions are summarized relative to two main aspects that include the error statistics of rainfall/runoff properties (cumulative depth, centroid, spreadness) and the propagation of error with reference to these properties. For the first aspect, it is concluded that compared to the volumetric parameter, the shape-related parameters of rainfall and simulated runoff are better captured by the satellite indicated

by lower random error and higher correlation in the Taylor diagram. Comparisons between error statistics of parameters for different products also suggest that the gauge-adjustments have effects on the volumetric parameter but not on the shape-related parameters.

For the error propagation aspect, systematic error of the shape-related parameters and random error show on average a general decrease from rainfall to runoff but this does not hold for the error in volumetric parameter, which maintains a γ value close to 1. Results also reveal that higher linearity in error propagation is shown for events with higher runoff coefficient.

We recognize that results from this analysis can mainly represent satellite applications over mountainous basins with hydroclimatic and geomorphologic characteristics similar to the Alpine environment. Besides, this study was conducted based on a relatively limited number of flood events, particularly for the flash flood event type given that the occurrence frequency of this flood event type is comparatively low. However, the results of our study highlight current challenges in using satellite-based precipitation for modeling flood response over complex topography. We believe that our findings will offer the end users (e.g. hydrologic agencies, civil protection etc.) important indications on the associated sources and magnitude of uncertainty in satellite-based flood prediction, which can serve as guidance for a number of flood risk operations and decision-making. Future studies should evaluate the potential of the newly available high-resolution (0.1°/hourly) Integrated Multi-satellitE Retrievals for GPM (IMERG) product by including also the snowmelt-driven floods, which although available in the flooding database were excluded from this study. Lastly, even though this study did not demonstrate a particular benefit from using the high-resolution CMORPH product, other higher resolution products such as the PERSIANN-CCS (0.04°/hourly), GSMaP (0.1°/hourly) and the newly available IMERG should be examined to further understand the potential impact of product resolution in the error properties of satellite precipitation driven runoff simulations.

Chapter 5 A Synthesis of Space-time Variability in Multi-Component Flood Response

5.1 Introduction

Catchment flood response or, in a more general sense, the water balance at basin scale, is controlled by a range of hydrological processes with each of them contributing a different level of spatiotemporal variability (e.g. precipitation, surface runoff, infiltration, routing, etc.) (Zoccatelli, et al., 2015; Palleiro, et al., 2014; Rodríguez-Blanco, et al., 2012; Merz & Blöschl, 2009; Skøien & Blöschl, 2006; Skøien, et al., 2003). Many of these studies have investigated how these processes are linked with the catchment flood response and what the relative importance of each of these processes is in controlling the properties of flood being generated. For example, it has been argued that only a portion of space-time characteristics of the flood response process will emerge to control the dynamics of a flood hydrograph due to the catchment dampening effect (Skøien & Blöschl, 2006; Smith, et al., 2004; Skøien, et al., 2003), and this dampening effect varies dynamically according to the hydrogeological properties of the catchment and features of the triggering storm, implying a shift of relative importance of processes in catchment flood response under different flood regimes (Mei, et al., 2014a; Volpi, et al., 2012; Mejía & Moglen, 2010; Sangati, et al., 2009; Smith, et al., 2005; 2002; Sivapalan, et al., 2004). The answers to these questions are intimately related to the development of a comprehensive framework that can generalize the estimation of streamflow spatiotemporal variability by a synthesis of various catchment processes under different hydro-meteorological and geomorphological controls (Blöschl, 2006).

Describing catchment flood response based on a set of spatiotemporal variables in storm response (i.e. rainfall, runoff generation, and routing) has been established and utilized since the late 90s (Zoccatelli, et al., 2015; 2011; Mei, et al., 2014a; Mejía & Moglen, 2010; Viglione, et al., 2010a; Smith, et al., 2005; Woods & Sivapalan, 1999). The essence of such an analytical framework is to diagnose the relative importance of rainfall space-time processes that influence the runoff generation (i.e. cumulative flow

volume, hydrograph timing and shape). The first work that synthesized the space-time variables into a holistic analytical framework is that of Woods & Sivapalan (1999). That framework used the "stationary rainfall" assumption, which can be interpreted as no movement of rainfall over the catchment. This assumption is strong, but it is considered reasonable only for short-duration or orographic-enhanced storms, which have relatively fixed spatial patterns over time. This framework assumption was applied in subsequent studies by Mejía & Moglen (2010) and Zoccatelli et al. (2010). Specifically, Zoccatelli et al. (2010) investigated the influence introduced by neglecting the spatial information of rainfall distribution in flow generation. Their study showed a larger delay in the arrival of a hydrograph mass center as rainfall mass center tends to be located closer to the headwater of the basin. Mejía & Moglen (2010) investigated the flood response to the distribution of impervious surface by partitioning rainfall excess generation to pervious and impervous areas of a catchment. The study concluded that the impervousness pattern is important when it is collocated with the mass center of rainfall.

Viglione et al. (2010a) generalized the Woods & Sivapalan (1999) framework by relaxing the "stationary rainfall" assumption. Their framework has terms to describe the relative movement of rainfall to the other variables. Viglione et al. (2010b) utilized their generalized framework to study the relative importance among rainfall space-time processes in controlling runoff generation for different types of flood. The study pointed out that the space and time covariance are important in runoff generation for short-duration rainfall events due to their highly localized feature; the spatial covariance is irrelevant for long-duration rainfall events since the rainfall field tends to be uniformly distributed over the catchment. Zoccatelli et al. (2011) derived the spatial moment of catchment rainfall and catchment scale storm velocity under the constant runoff coefficient assumption. The results indicate that the closer the rainfall mass center is to the catchment outlet the earlier the arrival of the hydrograph mass center is. This aspect was also revealed in Mei et al. (2014a) that examined 164 (mostly moderate) flood events. The study further concluded that the shape of rainfall and its movement are relatively insensitive in shaping the event hydrograph mainly because of the unsaturated rainfall excess. Nikolopoulos et al. (2014) paid particular

attention to the catchment scale storm velocity and were able to demonstrate the scale dependency and rainfall intensity dependency to storm magnitude.

The Viglione et al. (2010a) analytical framework (hereafter referred to as V2010) is relevant to only one rainfall excess (event flow) component. In this sense, the different runoff generation processes associated with vertical heterogeneous catchment layers are lumped together into a single flood response (Viglione, et al., 2010b; Woods & Sivapalan, 1999). Numerous experimental studies, though, have demonstrated that catchment flood response can be identified as multiple components originating from different catchment layers and associated with different flow paths (Gonzales, et al., 2009; Liu, et al., 2004; Weiler, et al., 2003). This is also prescribed in distributed hydrologic model where rainfall excess is often partitioned into different linear reservoirs representing different routing mechanisms (Wang, et al., 2011; Blöschl, et al., 2008; Koren, et al., 2004). Thus, we see the necessity of further generalizing V2010 to represent multi-component flood responses. The analytical framework presented in this paper is visualized in Figure 5.1. Catchment rainfall forcing is converted to more than one rainfall excess component associated with various surface and subsurface layers. These rainfall excess components are subjected to different flow paths and routing schemes. The output hydrograph is a combination of hydrographs from the different components. A point to note is that our discretization of streamflow is still within the context of event flow and is not extended to the very slow response (e.g. baseflow). To sum up, our expanded framework introduces parallel channels to represent the different components of catchment flood response. This new capability relative to V2010 and other previous frameworks can support studies to help us understand which space-time process is the most dominant for a component of catchment response and how the contributions of different rainfall excess components are changing across disparate hydrologic regimes (e.g. basin scales, rainfall duration, and space-time distribution, etc.).

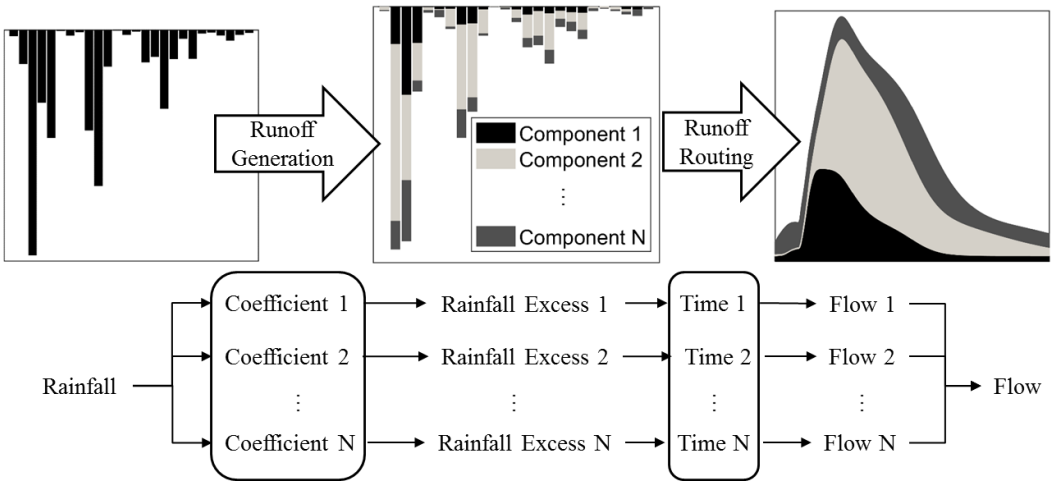

Figure 5.1. Schematic of the Analytical Framework.

We illustrate the multi-component flood response framework based on a two-component assumption consistent with a distributed hydrologic model structure. The illustration is built based on a relatively large number of rainfall-runoff events from three catchments in the Tar River basin in North Carolina. The paper is organized as follows. In Section 5.2, the study basin and data used in the study are described. Section 5.3 illustrates the experimental design with the hydrologic model. The analytical framework equations together with the demonstrations are presented in Section 5.4. Tests to understand the framework sensitivity to flood characteristics are provided in section 5.5. Conclusions (including limitation and future works) are discussed in section 5.6.

5.2 Study Area and Dataset

5.2.1 Tar River Basin and Hydrometeorology Data

We conducted our analysis over three nested catchments (namely Swift, Fishing and Tar) in the Tar River basin, a low elevation basin located in North Carolina (maximum elevation is 220 m above sea level). The study catchment areas are 426 km2, 1374 km^2, and 2406 km^2, characterized by mild-slopes (mean slope at 0.90%, 0.81%, and 0.83%, respectively). Prevailing climate of the area is humid subtropical causing

annual precipitation and runoff around 1100 mm and 250 mm, respectively. The reader is referred to Mei & Anagnostou (2015) and Mei et al. (2014a) for details on the hydrology of the study area.

The Stage IV radar-based multi-sensor precipitation estimates from the National Center for Environmental Prediction is used as our reference rainfall (STIV hereafter). The product is mosaicked from the Regional Multi-sensor Precipitation Analysis (RMPA) produced by the National Weather Service River Forecast Centers and benefits from some manual quality control process (Lin & Mitchell, 2005). The RMPA includes rain rates from merged operational radar estimates (150 Doppler Next Generation Weather Radar) and 5500 hourly rain gauge measurements. The STIV data is hourly and available at approximately 4 km spatial resolution. The data used in this study has been spatially interpolated to 1 km by the bilinear method. Another atmospheric forcing dataset used in this study is the potential evapotranspiration (PET) available from the North American Regional Reanalysis (NARR) at 3-hourly and 32 km resolution (Mesinger, et al., 2006). The NARR PET product accounts for evaporation from the soil, transpiration from the vegetation canopy, evaporation of dew and frost or canopy-intercepted precipitation, and snow sublimation. We also used hourly flow rates that were aggregated from the 15-min flow rate records available from the United States Geology Survey (USGS) for the three study catchments.

5.2.2 Rainfall-runoff Event Selection

The study rainfall-runoff events are extracted from the observation datasets using the Characteristic Point Method (CPM) introduced in Mei & Anagnostou (2015). The advantages of CPM are its parsimonious data requirement (basin area and time series of rainfall and flow) and automatic extraction of events based on time series features. Event runoff and rainfall periods are identified from the long-term continuous time series of observed flow and rainfall records. Rainfall periods satisfying the following conditions are associated with each of the flood periods:

- rainfall period(s) occurring before the flood period but within the time of concentration of the basin;
- rainfall period(s) located on the rising lib of the flood period;

- rainfall period(s) occurring prior to the end of the flood period by a time length equal to the time of concentration.

All of the rainfall periods associated with the same flood period are integrated as one rainfall event and are considered as the inducing rainfall of the flood. Each of the rainfall and flood pairs forms a rainfall-runoff event. The CPM is applied on the USGS streamflow observations and catchment-average STIV rainfall data for the three study catchments. The method identified nearly 300 flood events from the study period and these events were further filtered according to the hydrologic model performance as described in section 5.3.2.

5.3 Hydrologic Model and Experiment

5.3.1 Distributed Hydrologic Model

The Coupled Routing and Excess STorage (CREST) model version 2.1 is used for the hydrologic simulations in our study (Shen & Hong, 2015). CREST is a fully distributed rainfall-runoff model designed to simulate flow discharges over watersheds at global scale. CREST integrates a water balance model for the vertical fluxes with a horizontal routing model for the surface and subsurface runoff (Shen, et al., 2016; Wang, et al., 2011). The water balance model considers four processes—canopy interception, infiltration, evapotranspiration (ET), and runoff generation. The infiltration rate is calculated based on the variable infiltration curve developed in the Xinanjiang Model (Zhao, 1992). For each grid-cell, the actual ET (AET) is determined in terms of water and energy budget using precipitation, soil water availability and PET. In the runoff generation process, CREST separates rainfall excess into two components, the surface and subsurface runoff modeled by two linear reservoirs—the overland and interflow reservoirs. In the routing process, the sub-grid routing inhomogeneity is accounted for by employing these two runoff components. The model version used in this study implements the fully distributed linear reservoir routing method that overcomes the severe underestimation of flow in previous versions (Shen, et al., 2016). The parameter

optimization algorithm adapted in CREST is the shuffled complex evolution (SCE-UA) developed by Duan et al. (1992).

5.3.2 Experimental Design

As a first step, the model is set up over the three study catchments with 1 km spatial resolution. The geomorphologic and hydrologic variables (i.e. flow direction, flow accumulation, slope, and stream channel) of the catchment areas are generated from the Digital Elevation Model data; the STIV precipitation and NARR PET product force the model to compute the through precipitation, actual evapotranspiration, infiltration capacity, soil water content, and rainfall excess. We keep the model setting relatively simple by "turning off" the canopy interception, meaning that the process is conceptualized by a multiplier of the precipitation data, which is optimized by a calibration process. In addition, the fraction of impervious surface in this study is represented by an imperviousness parameter that was optimized through model calibration. The model was calibrated in the three catchments with respect to the observed hourly flow rate from 2004 to 2006 (year 2002 to 2003 is used as the spinning period). The Nash-Sutcliff coefficient (*NSCE*) of the flow simulations in the Swift, Fishing, and Tar catchments determined at hourly scale are 0.69, 0.62, and 0.66, respectively, indicating reasonable performance of the model over the study catchments (Moriasi, et al., 2007).

Rainfall-runoff events from the 2003 to 2012 period with duration shorter than 500 hours are identified from the continuous flow simulations during the time periods provided by the CPM. The mean error (*ME*), correlation coefficient (*CC*), and *NSCE* are calculated with respect to the observed flow rate for each event and these error metrics are ranked in ascending order (consider only the magnitude when ranking *ME*). Flood events of *ME* higher than the 95^{th} percentile and *CC* and *NSCE* lower than their respective 5^{th} percentile were discarded from the analysis to keep our results representative in the context of hydrologic simulation. These selection criteria resulted in 180 events (62, 57, and 61 events, respectively, for the smallest to largest catchments) with overall relative centered root mean square error equaling to 42.0%, 43.0% and 34.4%, respectively. Two pilot events used in the framework demonstrations are exhibited in

Figure 5.2. They are characterized by high *CC* and low relative *CRMS* values with respect to the observed flow time series. The *CC* for the two events are above 0.94 and 0.82 with relative *CRMS* at about 50% (Swift catchment for event 2 is an exception with *CRMS* at about 100%). The first is an intermittent event that lasted for 93 hours in June 2006; the second one is a 66-hour long event in November 2009. Mean rain rates (in mm/h) for the three catchments are 1.33, 0.87, 1.31 for the first event and 1.34, 1.22, 1.59 for the second event. It is noted that the concentration time increases as function of drainage area. The rainfall mass that triggered the June 2006 event is distributed around the outlet while the November 2009 event is spatially bimodal.

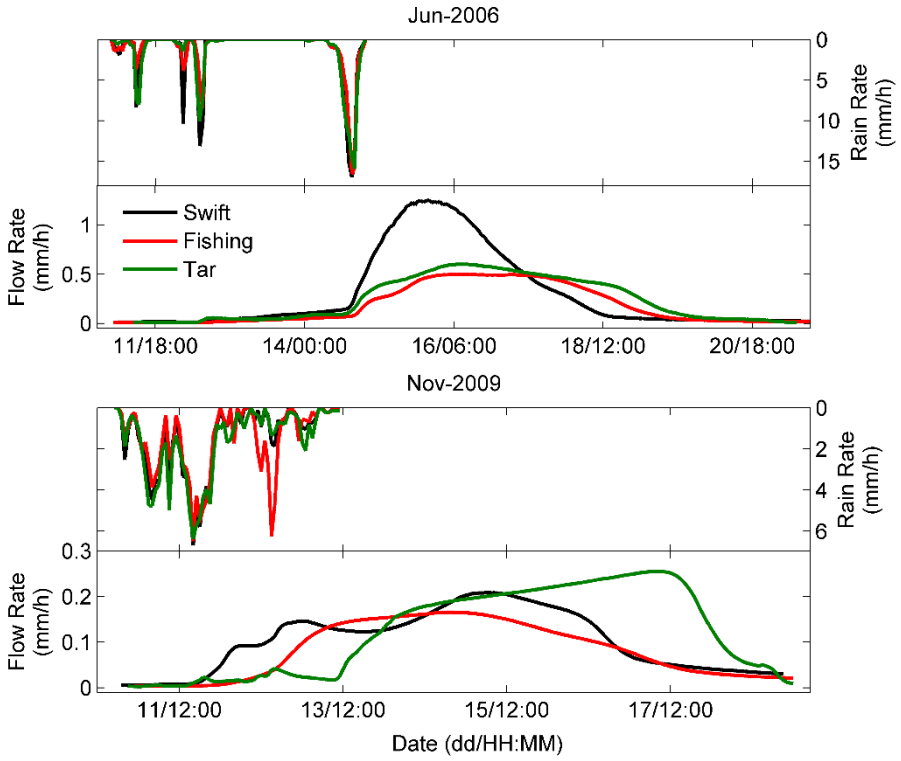

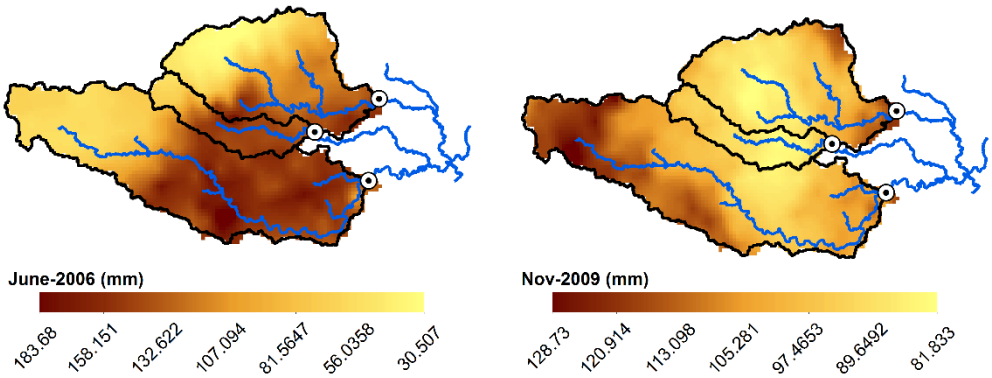

Figure 5.2. Event rainfall map and time series of rainfall and runoff for the two representative events.

Our last step is to remove the influences of non-zero initial condition of each event in the continuous simulations. For each event period, we run CREST by setting both rainfall and PET data to zero so as to output the "baseflow hydrograph". This "baseflow hydrograph" gives or mimics the recession of flow with the initial condition over the event time period. The event flow hydrographs are subtracted by the baseflow hydrographs and the new event flow hydrographs are obtained for the subsequent analysis.

5.4 Analytical Framework of Catchment Response

The V2010 analytical framework quantifies the effects of spatiotemporal variability of rainfall, runoff generation, and routing on a basin's flood response. The follow-up application by Viglione et al. (2010b) isolated the event flow component from baseflow, simulated using the Kamp model, and demonstrated the magnitudes of terms of catchment space-time processes represented in V2010. In our study, we extend the V2010 framework with the consideration that event flow consists of multiple components from the vertical layers of catchment (Figure 5.1). We illustrate the new framework using a two-component (surface and subsurface) flow generation process, consistent with the overland and interflow reservoir of CREST. Similar to V2010, our analytical framework estimates catchment response by three quantities: a) the amount of rainfall excess, b) the mean catchment response time, and c) the variance of catchment response time. These three quantities are proxies of the corresponding flood characteristics, namely, a) the cumulative

event flow volume, b) the hydrograph centroid, and c) the spreadness of hydrograph. A three-stage framework structure that decomposes the catchment response to rainfall excess generation, hillslope routing and channel routing is adopted (Zoccatelli, et al., 2015; Viglione, et al., 2010a; 2010b; Woods & Sivapalan, 1999). Specifically, we focus on deriving the analytical framework equations under the multi-component scenario described in sections 5.4.2 and 5.4.3. The variables used in the framework (rainfall, runoff coefficient, rainfall excess generation time, hillslope routing time and channel routing time) are attained from the CREST model parameters and are described in section 5.4.1.

5.4.1 Analytical Framework Variables

The analytical framework has three input variables—the rainfall, the runoff coefficient, and the runoff routing time. The rainfall variable for the framework refers to the net amount of through-rainfall and its partition in surface and subsurface runoff. Through-rainfall, $P(a,t)$, for the analytical framework is determined in this study as:

$$P(a,t) = C_I P'(a,t) - E_a(a,t) \tag{5.1}$$

where $P'(a,t)$ and $E_a(a,t)$ are actual precipitation (STIV precipitation) and evapotranspiration rates (calculated by CREST in this study). Indexes a and t stand for the location and time dimensions. C_I is the multiplier that conceptualizes the canopy.

Most distributed hydrologic models separate the rainfall excess into two components—the surface and the subsurface rainfall excess—and route them by two parallel flow paths with different speeds and outflow rates. Namely, the flood response for catchment surface and subsurface are associated with different generations and routing mechanisms characterized by different runoff coefficients and runoff routing time. The surface process is intimately related to the fraction of impervious surface over the basin where the through-rainfall is converted to rainfall excess, which can be represented as a uniform parameter, I_M, optimized through the hydrologic model calibration. Thus, the surface runoff coefficient, $W_2(a,t)$, is represented in the proposed framework by the imperviousness parameter, I_M. Values of I_M for the three catchments (from small to large) are 13.1%, 10.9%, and 11.3%. On the other hand, the amount of runoff

generated from the subsurface is positively correlated to the soil wetness based on the variable infiltration curve adopted by CREST. Thus, the subsurface runoff coefficient, $W_1(a,t)$, is estimated as:

$$W_1(a,t) = \frac{SM(a,t)}{W_M} \tag{5.2}$$

where $SM(a,t)$ is the volumetric soil moisture (one of the model outputs), and W_M is the maximum water capacity calibrated from the model. Overall, W_M increases from the smallest to the largest basin (values are 106, 198 and 249 mm).

The runoff routing consists of sub-grid scale and grid-to-grid routing in most distributed hydrologic models. To CREST, the sub-grid scale routing is represented by the surface and interflow reservoirs with different parameters, k_S and k_I, fixed at space and time. k_S and k_I represent the percentages of storage converted to runoff. Therefore, the delay in flood response due to for example the interflow reservoir is:

$$t_{h,1} = -ln(k_I) \tag{5.3}$$

The delay in time due to the surface reservoir, $t_{h,2}$, is similarly calculated by replacing k_I with k_S. Values of $t_{h,2}$ and $t_{h,1}$ for the study catchments are about 5.5 and 1 hour.

The grid-to-grid routing process is modeled by a spatially distributed concentration time. The concept of concentration time is a measurement of the time consumption for rainfall excess to flow from the current grid to the next downstream grid. The stream network travelling time of water from a given grid-cell is calculated as the summation of all the concentration time along its flow path to the basin outlet. Therefore, the network routing time, for example the interflow, is written as:

$$\theta_{n,1}(a) = \sum_{L_n(a)} \frac{l(a)}{K_X(a)s(a)^\beta} \tag{5.4}$$

where $l(a)$, $s(a)$ and $K_X(a)$ are the length of flow path from a grid to its adjacent downstream grid, the slope and the runoff velocity coefficient at that grid, respectively; $L_n(a)$ represents the space of flow path from a grid-cell to the catchment outlet; β is the flow speed exponent. The network routing time for surface flow, $\theta_{n,2}(a)$, is proportional to the subsurface one distinguished by dividing Eq.(5.4) with a constant α_n:

$$\frac{\theta_{n,2}(a)}{\theta_{n,1}(a)} = \alpha_n \tag{5.5}$$

Values of α_n is smaller than one (0.31, 0.63 and 0.67 for the study catchments) since the travel time for surface runoff should be larger than that of the subsurface one. Magnitudes of the spatially variable network routing time for the surface and subsurface processes are illustrated in Figure 5.3. The figure shows that network routing time increases going upstream. The Tar catchment (the largest one) is characterized by the widest value range compared to the other two sub-basins. The Swift catchment shows distinctively lower overall values for the surface network routing time ($\theta_{n,2}$) due to its low α value (0.3 compared to above 0.6 for the other two). This is expected given that model parameters of the three catchments are independently calibrated.

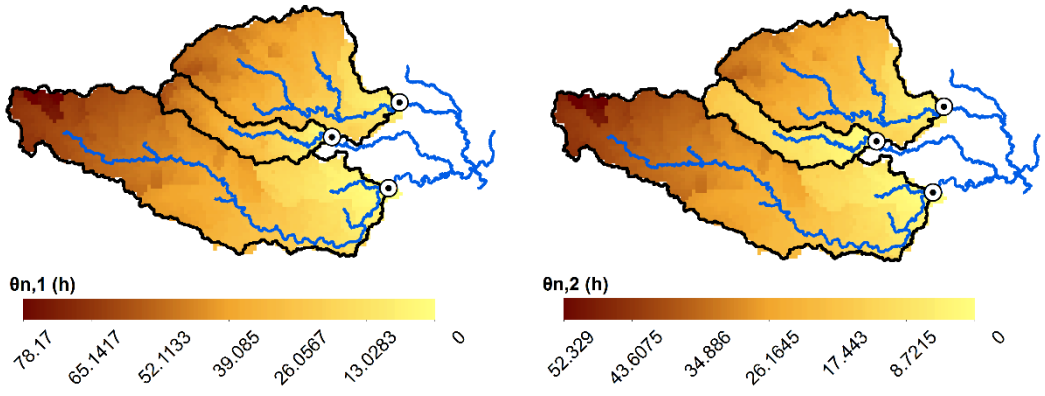

Figure 5.3. Runoff routing time for the study basins.

5.4.2 Generation of Rainfall Excess

The generation of rainfall excess at location and time *(a,t)* is calculated as:

$$R_i = PW_i \tag{5.6}$$

where R_i, P and W_i are the space-time variable rainfall excess, precipitation, and runoff coefficient field. Index *i* indicates different rainfall excess components generated from the different vertical layers of surface and subsurface. In this study we used two layers (*i = 1 & 2*) to denote the subsurface and surface rainfall excess, respectively. The total rainfall excess is the summation of all the rainfall excess components:

$$R = P\sum_{i=1}^{N} W_i \tag{5.7}$$

Note that the sum of all W_i is the total runoff coefficient W. To calculate the instantaneous basin-average rainfall excess, we take the spatial expectation of Eq.(5.7):

$$[R]_a = [P]_a \sum_{i=1}^{N} [W_i]_a + \left\{P, \sum_{i=1}^{N} W_i\right\}_a \tag{5.8}$$

where $[\ ]_a$ and $\{\ \}_a$ stand for the expectation and covariance (variance if the variables are the same) operator applied over the catchment area. The distributed storm-average rainfall excess is given by taking the temporal expectation of Eq.(5.7):

$$[R]_t = [P]_t \sum_{i=1}^{N} [W_i]_t + \left\{P, \sum_{i=1}^{N} W_i\right\}_t \tag{5.9}$$

The first term in Eq.(5.8)/(5.9) is the product between spatial or temporal average rainfall and runoff coefficient, while the second term quantifies the spatial or temporal variability between rainfall and runoff coefficient at every time step/catchment grid.

Figure 5.4 and Figure 5.5 show the magnitudes of the different terms of Eq.(5.8) and (5.9), respectively. Note that since the surface runoff coefficient W_2 is estimated as a space-time constant, the space and time covariance term between W_2 and P (i.e. $\{P,W_2\}_a$ and $\{P,W_2\}_t$) are 0 and are not shown. It is noted from Figure 5.4 that the catchment-average rainfall excess $[R]_a$ is strongly correlated to the catchment-average rainfall ($[P]_a$ shown in Figure 5.2) mainly because of the spatial covariance term $\{P,W_1\}_a$ that is irrelevant to $[R]_a$. This low magnitude of $\{P,W_1\}_a$ indicates that rainfall and runoff coefficients are not collocated in space for the two pilot events. Meanwhile, the relative importance between $[P]_a[W_1]_a$ and $[P]_a[W_2]_a$ changes dynamically throughout the event where $[P]_a[W_1]_a$ and $[P]_a[W_2]_a$ are comparable during the early phase but $[P]_a[W_1]_a$ overwhelms in the mature and decaying phase of the event. This is attributed to the dynamics of $[W_1]_a$ and $[W_2]_a$ during the event as shown by the differences between $[W_1]_a$ and $[W_2]_a$ on the top two panels of Figure 5.6. During the evolution of the event $[W_1]_a$-$[W_2]_a$ start negative and change to positive, reflecting the increase in subsurface runoff coefficient $[W_1]_a$ due to the increase in wetness condition of the catchment. This dynamic change in $[W_1]_a$ and $[W_2]_a$ also demonstrates why the surface

rainfall excess component is the quick response from the model. In addition, the differences between $[W_1]_a$ and $[W_2]_a$ of the Swift catchment are noticeably larger than the other two catchments in Figure 5.6; this could be attributed to the lower maximum water capacity of the Swift catchment compared to the other two.

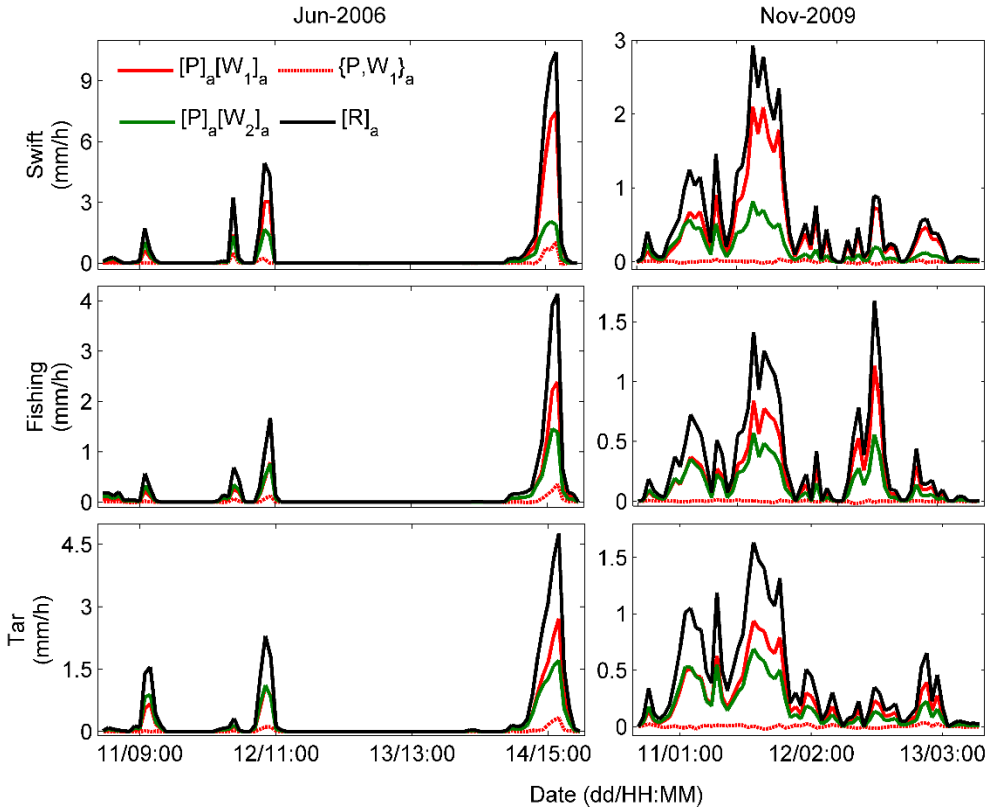

Figure 5.4. Time series showing the spatial averaged terms in Eq.(5.8) for the different rainfall excess components of the two representative events.

Figure 5.5 illustrates the temporal aggregated maps for terms in Eq.(5.9). The products between temporal average rainfall and runoff coefficient (i.e. $[P]_t[W_1]_t$ & $[P]_t[W_2]_t$) account for the major contribution of the storm-average rainfall excess. The product term $[P]_t[W_1]_t$ is generally larger than $[P]_t[W_2]_t$ because $[W_1]_t$ is larger than $[W_2]_t$ as shown in the bottom two panels of Figure 5.6. This is exemplified for the Swift catchment due to its lower maximum water capacity. The temporal covariance between rainfall and subsurface runoff coefficient, $\{P,W_1\}_t$, is higher for the June 2006 event that exhibits more distinct rainfall bursts; and for the Swift catchment where W_1 is more sensitive to rainfall dynamics.

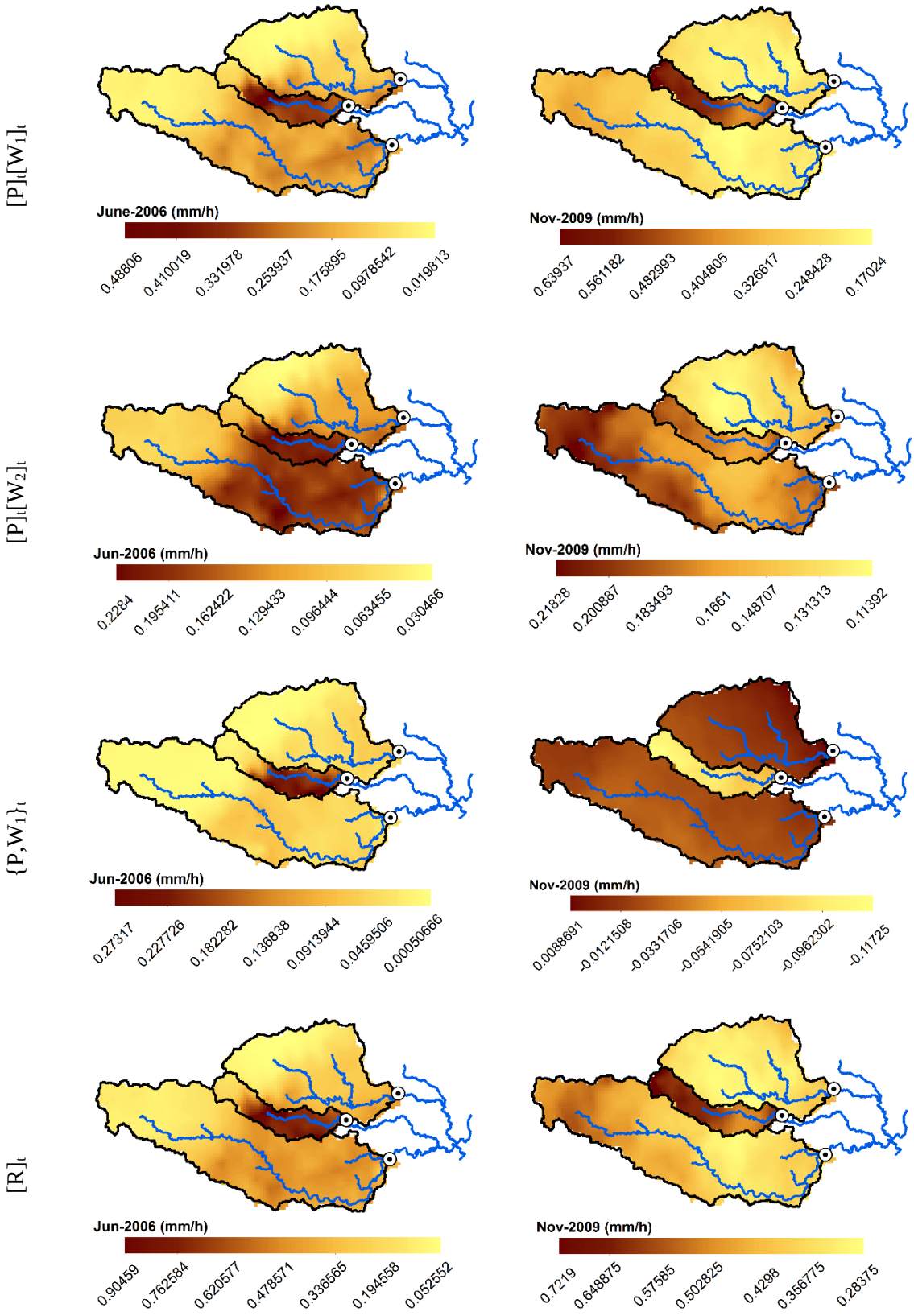

Figure 5.5. Same as Figure 5.4 but for temporal averaged terms in Eq.(5.9).

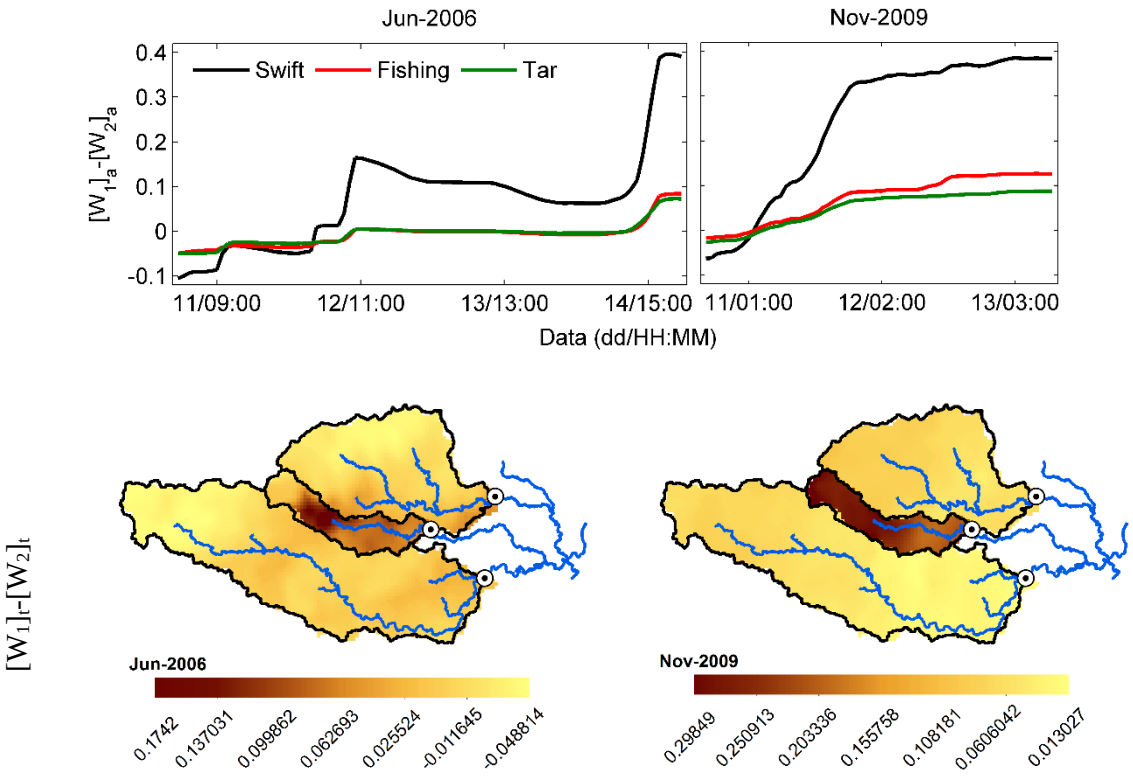

Figure 5.6. Differences between catchment-average and storm-average runoff coefficient.

The temporal or spatial integration of Eq.(5.8)/(5.9) yields the catchment-average storm rainfall excess, $[R]_{at}$ (see Appendix I for details):

$$[R]_{at} = \underbrace{[P]_{at}\sum_{i=1}^{N}[W_i]_{at}}_{R1} + \underbrace{\left\{[P]_a, \sum_{i=1}^{N}[W_i]_a\right\}_t}_{R2} + \underbrace{\left\{[P]_t, \sum_{i=1}^{N}[W_i]_t\right\}_a}_{R3} + \underbrace{\left[\left\{(P-[P]_t), \sum_{i=1}^{N}(W_i-[W_i]_t)\right\}_a\right]_t}_{R4} \tag{5.10}$$

where $[\ ]_{at}$ is the space-time aggregation on the catchment area and event period. This equation indicates that the amount of total catchment-average storm rainfall excess is the sum of catchment-average storm rainfall excess from all components. Term *R1* represents the sum of product between the catchment-average storm rainfall and runoff coefficient for all components. Term *R2*/*R3* is the sum of temporal/spatial covariance between the catchment-/storm-average rainfall and runoff coefficient. *R4* is the sum of temporal covariance between spatial variation of precipitation and runoff coefficient. Moreover, V2010 has shown

that the effect of storm movement can be isolated as $R4\text{-}R2\cdot R3/R1$. This movement effect is also studied later.

The magnitudes of terms in Eq.(5.10) along with the movement effect, *MV*, for the study events are illustrated in Figure 5.7 with statistics summarized in Table 5.1 (the two sample events are highlighted in the figure). Note that the *R2*, *R3*, *R4*, and *MV* for the surface component are zero due to the space-time constant surface runoff coefficient and thus are not shown. A term-wised comparison shows clearly that *R1* is the most dominant contributor to $[R]_{at}$. The figure and table reveal that the spatial and temporal correlation between rainfall and runoff coefficients is almost negligible. This is consistent with the previous studies which show generally low magnitudes of the *R2*, *R3*, and *R4* but high R_1 (Viglione, et al., 2010b; Mejía & Moglen, 2010). The relatively low magnitudes of term $\{P,W_1\}_a$ and $\{P,W_1\}_t$ in Figure 5.4 and Figure 5.5 also agree with this observation. The fairly low magnitudes of space and time covariance lead to insignificant movement effect (mean at 10^{-3} mm/h from Table 5.1). Investigation on *R1* (the most significant term) shows a decrease in magnitude with basin scale. This dampening effect has different reasons for the two rainfall excess components. For the surface component, the diminishing in magnitude with increase in scale is a result of the decrease in catchment-average rainfall given that W_2 is constant among catchments. For the subsurface process, this is due to both the decrease in runoff coefficient and catchment-average rainfall. Moreover, Table 5.1 reveals that the subsurface component generally outperforms the surface one in contribution to *R1*. Yet this magnitude differences are diminishing from the smallest to the largest catchment since the gap between W_1 and W_2 is narrowing.

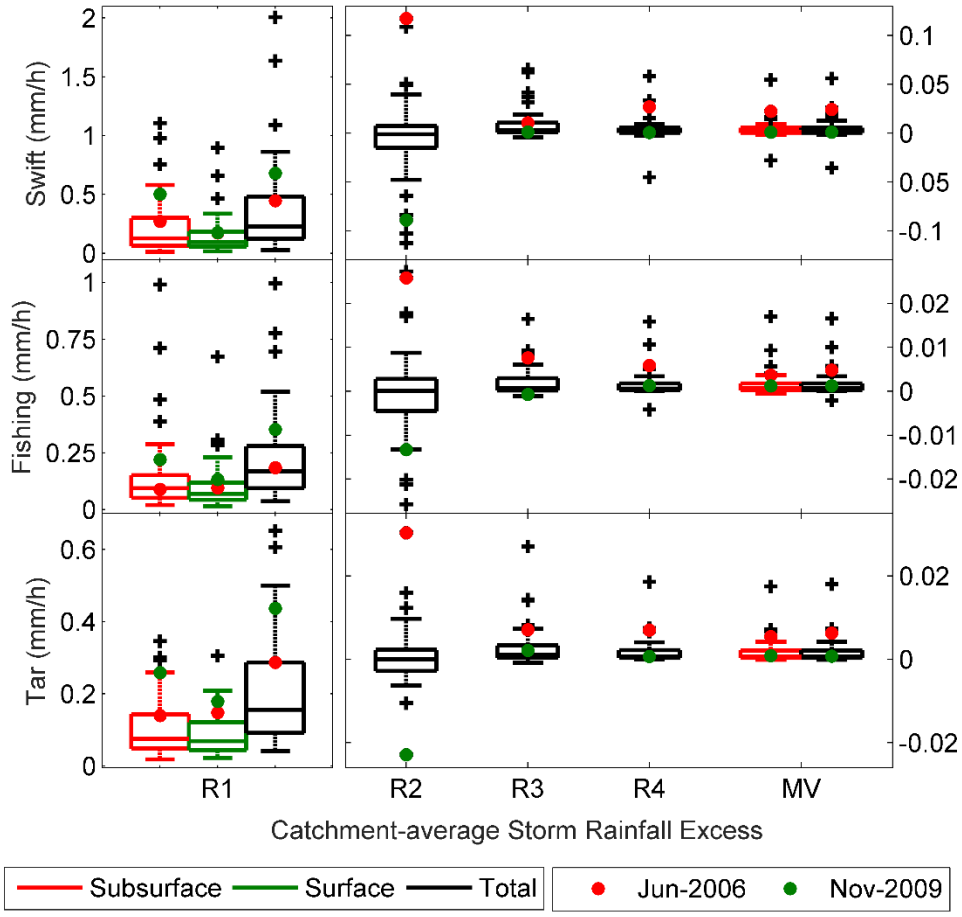

Figure 5.7. Boxplot showing the spatiotemporal averaged terms in Eq.(5.10) for all events from the study basins.

Table 5.1. Mean magnitudes of terms in Eq.(5.10) in mm/h.

Terms	Swift			Fishing			Tar		
	Sub-surface	Surface	Total	Sub-surface	Surface	Total	Sub-surface	Surface	Total
R1	0.212	0.149	**0.361**	0.138	0.100	**0.239**	0.103	0.090	**0.193**
R2	-0.005	\	-0.005	-0.001	\	-0.001	0.000	\	0.000
R3	0.011	\	0.011	0.005	\	0.005	0.004	\	0.004
R4	0.004	\	0.004	0.001	\	0.001	0.002	\	0.002
$[R]_{at}$	***0.222***	0.149	0.371	***0.144***	0.100	0.244	***0.108***	0.090	0.198
MV	0.004	\	0.004	0.001	\	0.001	0.002	\	0.002

5.4.3 Catchment Response Time

The catchment response is conceptualized by three stages—rainfall on the catchment and a portion of it turning into rainfall excess; then the rainfall excess is routed to the closest entrance of channel and subsequently to the catchment outlet (Zoccatelli, et al., 2015; Viglione, et al., 2010a; 2010b; Woods & Sivapalan, 1999). These stages are associated with their own "holding times" which are treated as random variables (Rodríguez-Iturbe & Valdés, 1979). The catchment response time is the sum of these holding times and thus is also a random variable. It measures the time needed from the beginning of a storm to a drop of rainwater exiting the catchment outlet, whose probability distribution function (PDF) for the *i*-th rainfall excess component, f_{Ri}, is

$$f_{R_i} = \frac{R_i}{[R_i]_{at}} \tag{5.11}$$

Note that f_{Ri} is a space-time variable. Thus, the PDF for total rainfall excess, f_R, can be written as:

$$f_R = \sum_i^N \psi_i f_{R_i} \tag{5.12}$$

where ψ_i is the rainfall excess ratio defined as the ratio of catchment-average storm rainfall excess for a component to that for the total rainfall excess:

$$\psi_i = \frac{[R_i]_{at}}{[R]_{at}} \tag{5.13}$$

Sum of ψ_i goes up to 1 by definition. Eq.(5.12) shows that the PDF of catchment response time is a convex combination for each PDF of the rainfall excess component.

5.4.3.1 Expectation of Catchment Response Time

For the three-stage analytical framework in this study, the expectation of catchment response time $E(\Phi)$ can be decomposed to the expectation of holding time of the three stages:

$$E(\Phi) = \underbrace{E(T_r)}_{Stage1} + \underbrace{E(T_h)}_{Stage2} + \underbrace{E(T_n)}_{Stage3} \tag{5.14}$$

where T_r, T_h and T_n correspond to the rainfall excess generation time, hillslope and channel routing time. The rainfall excess generation time is represented by the instantaneous time, T. Thus, the expected rainfall excess generation time, $E_i(T_{r,i})$, for any component is provided as (see Appendix II):

$$E_i(T_{r,i}) = \frac{|T_P|}{2} + \frac{\{T, [R_i]_a\}_t}{[R_i]_{at}} \tag{5.15}$$

where $|T_P|$ is the duration of the rainfall event. $E_i(T_{r,i})$ is a measurement of the temporal mass center of rainfall excess. If the rainfall mass is symmetric with respect to its mid-point, the half-duration is sufficient to describe the expectation of rainfall excess generation. Following the distribution function of Eq.(5.12), we derived the expected rainfall excess generation time for total rainfall excess $E(T_r)$ as (see Appendix III for derivation):

$$E(T_r) = \sum_i^N \psi_i E_i(T_{r,i}) \tag{5.16}$$

Eq.(5.16) indicates that the temporal mass center of total rainfall excess is a linear combination (or the expectation) of the mass centers of all the other rainfall excess components with respect to the rainfall excess ratio. The equation also implies that the larger the magnitude of a component, the greater impact it has on the timing of the total rainfall excess. Substituting Eqs.(5.13) and (5.15) into Eq.(5.16), we have,

$$E(T_r) = \underbrace{\frac{|T_P|}{2}}_{E1} + \underbrace{\frac{\left\{T, \sum_i^N [R_i]_a\right\}_t}{[R]_{at}}}_{E2} \tag{5.17}$$

E1 refers to the event half-duration and *E2* is the expectation of time distance from the event midpoint to the temporal mass center of catchment-average rainfall excess.

The magnitudes of terms in Eq.(5.17) are illustrated in Figure 5.8 (left panel) and summarized in Table 5.2 (first three rows). At a first glance, the expectation of rainfall excess generation time is increasing with the basin area due to the increase in event duration. The magnitude of the half-duration is of more relevance to $E(T_r)$, while the temporal covariance term can be an important contributor for a portion of events. This means that rainfall excess is not symmetric with respect to the event's mid-point. *E2* of the surface component is higher than the subsurface counterpart in magnitude. This is interpreted to mean that the

surface rainfall excess preserves the temporal dynamics of catchment-average rainfall due to the constant runoff coefficient. On the other hand, for the subsurface component, the temporal characteristics of rainfall have been dampened through its interaction with runoff coefficients. This leads to a more symmetrically distributed time series based on the mid-point. Besides, Table 5.2 implies that the temporal locations of rainfall excess mass center appear earlier than the event's mid-point by rendering negative mean values of *E2*. Lastly, we observe that the *E2* term of the June 2006 event is characterized by a larger value (20 hours) than the other events (less than 7 hours). This can be interpreted by its increasing trend in rain rate with time exhibited in the time series of Figure 5.2.

The delay in flood response due to the hillslope routing for a rainfall excess component is modeled by a constant response time $\theta_{h,i}$ because the hillslope routing process represents only the routing of water within a grid cell. If this response time is later mimicked by the linear reservoir adopted by the hydrologic model of this study, the expectation of hillslope routing time is (refer to Appendix II):

$$E_i(T_{h,i}) = t_{h,i} \tag{5.18}$$

This means that the delay in flood response caused by the hillslope routing for a rainfall excess component is fixed for any location within the basin. The hillslope routing time for the total rainfall excess is modeled by θ_h, which is assumed analytically as a function of all $\theta_{h,i}$:

$$\theta_h = \sum_i^N \psi_i \theta_{h,i} \tag{5.19}$$

Eq.(5.19) indicates that θ_h is a linear combination of $\theta_{h,i}$ with respect to the weight or rainfall excess where component with larger weight exerts higher degree of control on the total hillslope routing time. It also ensures that θ_h is always taking value within the range of all $\theta_{h,i}$. Since $\theta_{h,i}$ is a constant, the ratio between each two $\theta_{h,i}$ is also a constant:

$$\alpha_{h,i} = \frac{\theta_{h,i}}{\theta_{h,1}} \tag{5.20}$$

Under the two-component scenario of this study, $\alpha_{h,1}$ is always 1 and $\alpha_{h,2}$ is the ratio between the surface and subsurface hillslope response time (i.e. $t_{h,2}/t_{h,1}$). Based on Eqs.(5.19) & (5.20), we may write:

$$\theta_h = \xi_{h,i}\theta_{h,i} \tag{5.21}$$

where

$$\xi_{h,i} = \frac{1}{\alpha_{h,i}}\sum_i^N \psi_i \alpha_{h,i} \tag{5.22}$$

$\xi_{h,i}$ is the ratio between the weighted average of $\alpha_{h,i}$ (with respect to ψ_i) and $\alpha_{h,i}$. It is a measure of disparity in hillslope routing time from a rainfall excess component to the total one. It accounts for the relative importance of rainfall excess and hillslope effects as the inclusion of ψ_i and $\alpha_{h,i}$. With Eq.(5.21), $E(T_h)$ is derived as (Appendix III):

$$E(T_h) = \sum_i^N \psi_i \xi_{h,i} E_i\left(T_{h,i}\right) \tag{5.23}$$

Mathematically, Eq.(5.23) indicates that $E(T_h)$ is the expectation of $\xi_{h,i}E_i(T_{h,i})$, but not $E_i(T_{h,i})$, with respect to ψ_i. Substituting Eqs.(5.18) and (5.21) into Eq.(5.23), $E(T_h)$ can be written as (Appendix III):

$$E(T_h) = \underbrace{\xi_{h,i}t_{h,i}}_{E3} \tag{5.24}$$

Eq.(5.24) has only one term, *E3*, quantifying the mean of hillslope routing time. The absence of a covariance term as it is shown in the case of $E(T_r)$ is because the parameter for the linear reservoir is a constant.

The magnitudes of $E(T_h)$ is exhibited in the right panel of Figure 5.8 with the mean statistics shown in Table 5.2. Values of $E(T_h)$ for the three catchments are similar at around 3 hour for the total rainfall excess. The surface hillslope routing time is larger than the subsurface one and the relative importance for the subsurface hillslope routing time is increasing from the smallest to the largest basin. Overall, $E(T_h)$ accounts for a very small portion of $E(\Phi)$ because the overland and interflow reservoirs in CREST represent only the sub-grid scale routing.

Holding time for the third stage is determined as the spatial distributed network routing time $\theta_{n,i}$. Thus, the expectation of the channel routing time, $E_i(T_{n,i})$, for a rainfall excess component is derived as (Appendix II):

$$E_i(T_{n,i}) = [\theta_{n,i}]_a + \frac{\{\theta_{n,i}, [R_i]_t\}_a}{[R_i]_{at}} \tag{5.25}$$

The first term stands for the catchment-average channel routing time and the second term quantifies the delay in response due to spatial covariance between channel routing time and storm-average rainfall excess. Analogously, we describe the relationship between $E_i(T_{n,i})$ and $E(T_n)$. The channel routing time for the total rainfall excess is modeled by a spatial distributed variable, θ_n, which is assumed again as a linear combination of all $\theta_{n,i}$ with respect to ψ_i:

$$\theta_n = \sum_i^N \psi_i \theta_{n,i} \tag{5.26}$$

This analytical formulation ensures that θ_n neither goes beyond nor below the slowest and quickest responses. Also, we again assume that the ratio between each two $\theta_{n,i}$ is a space-time constant:

$$\alpha_{n,i} = \frac{\theta_{n,i}}{\theta_{n,1}} \tag{5.27}$$

This is consistent with the modeling structure of CREST as shown in Eq.(5.5). Based on Eq.(5.27), $\alpha_{n,1}$ is always 1 and $\alpha_{n,2}$ is the α_n in Eq.(5.5). From Eqs. (5.26) & (5.27), we may further write:

$$\theta_n = \xi_{n,i} \theta_{n,i} \tag{5.28}$$

where

$$\xi_{n,i} = \frac{1}{\alpha_{n,i}} \sum_i^N \psi_i \alpha_{n,i} \tag{5.29}$$

Similarly, $\xi_{n,i}$ is the ratio between the weighted average of $\alpha_{n,i}$ by ψ_i and $\alpha_{n,i}$. It measures the disparity in channel routing time from a rainfall excess component to the total one. It quantifies the effects from rainfall excess and channel routing as the inclusion of ψ_i and $\alpha_{n,i}$. With Eq.(5.28), the expectation of T_n is derived as (see Appendix III):

$$E(T_n) = \sum_i^N \psi_i \xi_{n,i} E_i(T_{n,i}) \tag{5.30}$$

Eq.(5.30) indicates that $E(T_n)$ is the expectation of $\xi_i E_i(T_{n,i})$ with respect to ψ_i. It also implies that the combination of $E_i(T_{n,i})$ to form $E(T_n)$ takes into consider effects from both the rainfall excess and geomorphologic aspects. Substituting Eq.(5.25) into Eq.(5.30), $E(T_n)$ can be written as:

$$E(T_n) = \underbrace{\xi_{n,i}\left[\theta_{n,i}\right]_a}_{E4} + \underbrace{\frac{\xi_{n,i}\left\{\theta_{n,i}, \sum_i^N [R_i]_t\right\}_a}{[R]_{at}}}_{E5} \tag{5.31}$$

E4 is the catchment-average channel routing time for the total rainfall excess (i.e. $[\theta_n]_{at}$, if one put $\xi_{n,i}$ into $[\theta_{n,i}]_a$). *E5* is the expected distance from the geomorphologic center of catchment to the centroid of storm-average rainfall excess

The right panel of Figure 5.8 shows the magnitude of terms from Eq.(5.31) for all events with the mean magnitude reported in the middle three rows of Table 5.2. As expected, the expected channel routing time, $E(T_n)$, increases according to catchment drainage area, which is mainly attributed to the elongation in flow path (i.e. increases in *E4*). The spatial covariance term (*E5*) is low, indicating that the contours of rainfall excess are not followed by the contours of isochrones for channel routing (Volpi, et al., 2012; Viglione, et al., 2010b; Sangati, et al., 2009; Woods & Sivapalan, 1999). This is anticipated given the low elevation and mild-slope topographic setups of the study region causing no orographic pattern in rainfall excess. Component-wisely speaking, the subsurface routing is taking longer time than the surface one as shown in Figure 5.3. Under the relationship specified by Eq.(5.30), values of the $E(T_n)$ is in between $E(T_{n,1})$ and $E(T_{n,2})$ of the subsurface and surface component. We also observe from the figure that $E(T_{n,1})$ and $E(T_{n,2})$ are getting closer to $E(T_n)$ with the increase of the drainage area. This reflects the trend of change in mean values of $\xi_{n,i}$ where $\xi_{n,1}$ and $\xi_{n,2}$ are getting closer from Swift to Tar given that ψ_1 and ψ_2 remain relatively unchanged. The June 2006 event is an example showing that the subsurface process is characterized by negative spatial covariance (*E5* is about -4 hours for all catchments). This is explained by its outlet concentrated cumulative rainfall (Figure 5.2). Moreover, comparing $E(T_r)$, $E(T_h)$, $E(T_n)$ and $E(\Phi)$ in Table 5.2, we note that the delay in catchment response is increasing with drainage area; contribution to $E(\Phi)$ from the rainfall excess generation stage and the runoff routing stage (a combination of hillslope and

channel routing stage) are comparable in magnitude, with $E(T_r)$ been mostly slightly larger than the sum of $E(T_h)$ and $E(T_n)$.

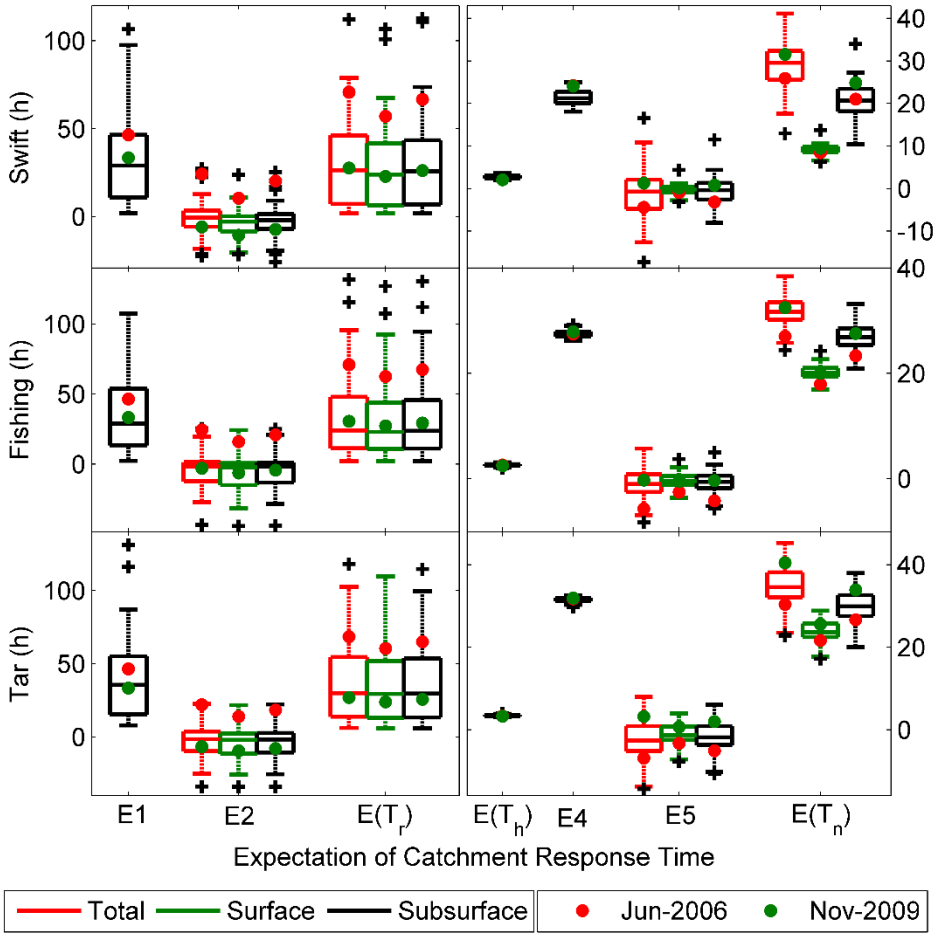

Figure 5.8. Same as Figure 5.7 but for Eqs.(5.17), (5.24) & (5.31).

Table 5.2. Same as in Table 5.1 but for Eqs.(5.17), (5.24) & (5.31).

Term	Swift			Fishing			Tar		
	Sub-surface	Surface	Total	Sub-surface	Surface	Total	Sub-surface	Surface	Total
E1	32	32	32	37	37	37	40	40	40
E2	-0.78	-4.5	-2.3	-4.1	-6.2	-5.0	-2.0	-4.1	-3.0
$E(T_r)$	32	28	**30**	33	31	**32**	38	36	**37**
$E(T_h)$	0.60	5.6	2.8	0.68	5.3	2.6	1.4	5.7	3.4
E4	30	9.4	21	33	20	27	37	25	32
E5	-1.2	-0.22	-0.64	-1.0	-0.37	-0.68	-2.6	-1.2	-1.8

$E(T_n)$	29	9.2	21	32	20	27	35	24	30
ψ	0.57	0.43	\	0.57	0.43	\	0.54	0.46	\
ξ_h	4.59	0.49	\	3.86	0.50	\	2.37	0.60	\
ξ_n	0.70	2.27	\	0.84	1.34	\	0.85	1.27	\
$E(\Phi)$	***61***	43	53	***66***	57	62	***74***	65	70

5.4.3.2 Variance of Catchment Response Time

In the three-stage analytical framework, the variance of catchment response time is contributed by the variances introduced from the holding time of each of the stages and the covariance between holding time of any two stages. Thus, we write:

$$var(\Phi) = \underbrace{var(T_r)}_{Stage1} + \underbrace{var(T_h)}_{Stage2} + \underbrace{var(T_n)}_{Stage3} + \underbrace{2cov(T_r, T_h)}_{Stage\ 1\ \&\ 2} + \underbrace{2cov(T_r, T_n)}_{Stage\ 1\ \&\ 3} + \underbrace{2cov(T_h, T_n)}_{Stage\ 2\ \&\ 3} \quad (5.32)$$

For stage 1, the variance of delay in rainfall excess generation for a rainfall excess component is provided as (see Appendix IV):

$$var_i(T_{r,i}) = \frac{|T_P|^2}{12} + \frac{\{T^2, [R_i]_a\}_t - |T_P|\{T, [R_i]_a\}_t - \frac{(\{T, [R_i]_a\}_t)^2}{[R_i]_{at}}}{[R_i]_{at}} \quad (5.33)$$

$var_i(T_r)$ represents the variance of instantaneous time with respect to the temporal distribution of rainfall excess; the second term takes null for temporal uniform rainfall excess or rainfall excess concentrated purely on the event mid-point.

For total rainfall excess, the variance of delay in rainfall excess generation, $var(T_r)$, is correlated with $var_i(T_{r,i})$ as (see Appendix V for derivations):

$$var(T_r) = \sum_i^N \psi_i var_i(T_{r,i}) + \sum_i^N \psi_i \left[E_i(T_{r,i}) - E(T_r)\right]^2 \quad (5.34)$$

The first term is clearly the expectation of variance from all the other components. It signifies that the larger the rainfall excess component, the stronger the control in dispersion of the total rainfall excess. The second term quantifies the variability of $E_i(T_{r,i})$ that arises since variance is not a linear operator. It measures the

mean difference in the temporal mass center between each of the component to the total rainfall excess. The first and the second term account for the intra- and inter-component variability. Substituting in Eqs.(5.15), (5.17), & (5.33) to Eq.(5.34), a complete form is given as:

$$var(T_r) = \underbrace{\frac{|T_P|^2}{12}}_{v1} + \underbrace{\frac{\{T^2, \sum_i^N [R_i]_a\}_t - |T_P|\{T, \sum_i^N [R_i]_a\}_t - \frac{\sum_i^N (\{T, [R_i]_a\}_t)^2}{[R_i]_{at}}}{[R]_{at}}}_{v2} + \underbrace{\sum_i^N \psi_i \left(\frac{\{T, [R_i]_a\}_t}{[R_i]_{at}} - \frac{\{T, \sum_i^N [R_i]_a\}_t}{[R]_{at}} \right)^2}_{LT_r} \quad (5.35)$$

Term *v1* stands for the variance in time generated by a temporal invariant catchment-average rainfall excess. Term *v2* represents component-wised mean of additional variance caused by the temporal variation in catchment-average rainfall excess. The last term is named LT_r and represents the mean square of "time lag" (between each component to the total) in rainfall excess generation.

Results for Eq.(5.35) are illustrated in the left panel of Figure 5.9 and the first four rows of Table 5.3. The major source of $var(T_r)$ is the variance of event duration (*v1*). However, the additional variance caused by the temporal interaction between rainfall excess and time (*v2*) is not negligible. This states that the distributions of rainfall excess of the events are not uniform in time (Viglione, et al., 2010b; Woods & Sivapalan, 1999). Additionally, event time series of the two rainfall excess components are equally dispersed during the event period given the fairly close $var_i(T_{r,i})$ values (only the Swift case shows medium difference). This is exemplified by Figure 5.4 where the shapes of time series for the two components are quite close in the Fishing and Tar case but a bit more deviated in the Swift. Besides, by comparing the time series of the two test events we can see that the June 2006 event is characterized by multiple peak rainfall values, while the November 2009 is closer to a single-peak event. This general differences in shapes are well described by the positive and negative sign of term *v2* for the first and second event. Results from the figure and table also suggest that the magnitude of "time lag" term (LT_r) is irrelevant. A better visualization of reason is provided by the sample events time series in Figure 5.4. Most of the temporal variability of

rainfall is preserved in the time series as we can see from the shapes of $[P]_a[W_1]_a$ and $[P]_a[W_2]_a$. Inspection on $var(T_r)$ reveals that although the magnitudes of *v1*, *v2* and LT_r show no scale-dependency, their combination, $var(T_r)$, is increasing with drainage area.

The variance of hillslope routing time with respect to the variability of rainfall excess is derived as (Appendix IV):

$$var_i(T_{h,i}) = t_{h,i}^2 \tag{5.36}$$

Only one term presents in Eq.(5.36) because $\theta_{h,i}$ is again a constant.

We may derive the variance of hillslope routing time for the total flow, $var(T_h)$, as (see Appendix V):

$$var(T_h) = \sum_i^N \psi_i \xi_{h,i}^2 var_i(T_{h,i}) \tag{5.37}$$

Eq.(5.37) has only one term accounts for the intra-component variability of hillslope routing. This term is a linear combination of $\xi_{h,i}^2 var_i(T_{h,i})$; it highlights the combined effect from rainfall excess distribution and hillslope. Using Eqs.(5.21) and (5.36), Eq. (5.37) may be further written as:

$$var(T_h) = \underbrace{\xi_{h,i}^2 t_{h,i}^2}_{v3} \tag{5.38}$$

Term *v3* quantifies the variance in time as if the hillslope routing time is uncorrelated with the rainfall excess.

Values of $var(T_h)$ are plotted in the middle panel of Figure 5.9 with mean values reported in Table 5.3. The results demonstrate that the contribution to $var(\Phi)$ from $var(T_h)$ is almost negligible. This is expected since the linear reservoir model adopted in CREST to implement the hillslope process represents only the sub-grid scale routing. The mean values of $var(T_h)$ are generally closer to those of the subsurface component, implying the larger controls from subsurface rainfall excess due to its higher magnitudes.

For the channel routing stage, we derive the variance of channel routing time for any rainfall excess component, $var_i(T_{n,i})$, as (refer to Appendix IV):

$$var_i(T_{n,i}) = \{\theta_{n,i}\}_a + \frac{\{\theta_{n,i}^2, [R_i]_t\}_a - 2[\theta_{n,i}]_a\{\theta_{n,i}, [R_i]_t\}_a - \frac{\left(\{\theta_{n,i}, [R_i]_t\}_a\right)^2}{[R_i]_{at}}}{[R_i]_{at}} \quad (5.39)$$

The first term is the spatial variance of the channel routing time. The second one accounts for the additional variance introduced by the interaction between time average rainfall excess and the channel routing time. If the rainfall excess is spatially uniform or concentrated on the isochrones representing the mean channel routing time (i.e. $[\theta_n]_a$), the second term vanishes.

We may derive the variance of delay in channel routing for the total flow, $var(T_n)$, as (see Appendix V):

$$var(T_n) = \sum_i^N \psi_i \xi_{n,i}^2 var_i(T_{n,i}) + \sum_i^N \psi_i \left[\xi_{n,i} E_i(T_{n,i}) - E(T_n)\right]^2 \quad (5.40)$$

$var(T_n)$ is consisted by two terms accounting for the intra- and inter-component variability of channel routing. The intra-component variability is quantified as the linear combination of $\xi_{n,i}^2 var_i(\theta_{n,i})$, highlighting the combined effect from rainfall excess variability and channel routing. The second term is the variance of $\xi_{n,i} E_i(T_{n,i})$; it quantifies the squared mean distance in spatial mass center with respect to the channel network between all components to the total. $var(T_n)$ may be rewritten as:

$$var(T_n) = \underbrace{\xi_{n,i}^2\{\theta_{n,i}\}_a}_{v4} + \underbrace{\frac{\xi_{n,i}^2\{\theta_{n,i}^2, \sum_i^N [R_i]_t\}_a - 2\xi_{n,i}^2[\theta_{n,i}]_a\{\theta_{n,i}, \sum_i^N [R_i]_t\}_a - \frac{\sum_i^N \xi_{n,i}^2\left(\{\theta_{n,i}, [R_i]_t\}_a\right)^2}{[R_i]_{at}}}{[R]_{at}}}_{v5} + \underbrace{\sum_i^N \psi_i \xi_{n,i}^2 \left(\frac{\{\theta_{n,i}, [R_i]_t\}_a}{[R_i]_{at}} - \frac{\{\theta_{n,i}, \sum_i^N [R_i]_t\}_a}{[R]_{at}}\right)^2}_{LT_n} \quad (5.41)$$

Term *v5* represents the variance in time generated by a spatial invariant storm-average rainfall excess. Term *v6* is the mean of additional variance caused by the spatial variation in storm-average rainfall excess. The

term LT_n represents the mean of "time lag" in channel routing between rainfall excess components to the total.

The magnitudes of terms in Eq.(5.41) are plotted in the middle panel of Figure 5.9 with mean statistics listed in Table 5.3 (from the row of *v4* to *var*(T_n)). Results suggest that *v4* is the main contributor of *var*(T_n) compared to the additional spatial variance (*v5*). *v5* is positively skewed as shown in the figure with negative mean, indicating that the event rainfall excess tends to be concentrated by the catchment (i.e. spatially unimodal pattern) (Mei, et al., 2014a; Zoccatelli, et al., 2011). *v5* is low in magnitude because, again, there is little spatial correlation between the location of isochrones for network routing and the rainfall excess under the study area's topographic setups. Component-wised comparison reveals that the variance of delay in channel routing of the surface rainfall excess are smaller than the subsurface one. This is ascribed to the larger magnitude of $\theta_{n,1}$ and $[R_1]_{at}$ than $\theta_{n,2}$ and $[R_2]_{at}$. Besides, results suggest negligible "time lag" term (LT_n) in contribution to the total variance of network routing, meaning that the spatial mass center of rainfall excess for the two rainfall excess components are fairly close to the total one. This is an expected result because of the highly similar spatial pattern of rainfall excess and network routing for the two components. Observations of the two sample events demonstrate that *v5* for the November 2009 event is closer to null (for instance *v5* of the Tar catchment is 4 h^2 compared to 50 h^2 of the June 2006 event). This is substantiated by the generally more uniformly distributed rainfall excess pattern of the November event ($[R]_t$ in Figure 5.5). Moreover, we compare the values of *var*(T_h), *var*(T_n), *var*(T_r) and *var*(Φ) from the results. Values of *var*(Φ) are increasing with the basin drainage areas, referring the higher degree of smoothing for larger basin scales. *var*(T_r) dominates *var*(Φ) where the mean of *var*(T_r) are at least more than 3 times of the mean of *var*(T_h) plus *var*(T_n).

There are three covariance terms in Eq.(5.32) , quantifying the covariance between holding times of any two stages. In this study, we focus on *cov*(T_r,T_n) because *cov*(T_r,T_h) and *cov*(T_h,T_n) are essentially zero (Appendix VI). The covariance between holding times of stage 1 and 3 is often interpreted as an indicator of "movement of storm", resulting from the relaxation of "stationary rainfall" assumption. The so-called

"movement of storm" is not just the geographic movement, it also accounts for the change in space-time dynamic of rainfall excess with respect to the channel network during the storm period (Zoccatelli, et al., 2015; 2011; Mei, et al., 2014a; Nikolopoulos, et al., 2014). For any component of rainfall excess, $cov_i(T_{r,i},T_{n,i})$ is written as (refer to Appendix VI for details):

$$cov_i\left(T_{r,i},T_{n,i}\right)=\frac{\left\{T,\left\{\theta_{n,i},R_i\right\}_a\right\}_t}{[R_i]_{at}}-\frac{\{T,[R_i]_a\}_t\left\{\theta_{n,i},[R_i]_t\right\}_a}{[R_i]_{at}^2} \tag{5.42}$$

This term is the additional variance generated from the correlation in runoff generation and channel routing. Positive and negative covariance are interpreted as the centroid of rainfall excess moving towards the catchment portion with longer or shorter channel routing time (near periphery or outlet) as the event evolves. Therefore, an upstream (downstream) movement leads to addition (subtraction) of variance in catchment response.

The covariance term in our multi-component assumption may be written as (see Appendix VII):

$$cov(T_r,T_n)=\sum_i^N\psi_i\xi_{n,i}cov_i\left(T_{r,i},T_{n,i}\right)+\sum_i^N\psi_i\left[E_i\left(T_{r,i}\right)\xi_{n,i}E_i\left(T_{n,i}\right)-E(T_r)E(T_n)\right] \tag{5.43}$$

The covariance operator also results in two terms where the first one is a combination of covariance between $T_{r,i}$ and $T_{n,i}$ with respect to $\xi_{n,i}\psi_i$; it measures the coevolution of all rainfall excess components over catchment and event period. The second term is the covariance between $E_i(T_{r,i})$ and $\xi_{n,i}E_i(\theta_{n,i})$; positive or negative value of the second term implies that rainfall excess components with temporal mass centers distance from the early phase of event are located closer to the catchment portion with larger or smaller routing time (catchment periphery or outlet). Based on this interpretation, the inter-component covariance should be very small in most of the cases happening in the nature; this is because there is no restriction that a rainfall excess component with time center further away from the event mid-point should be centered over isochrones with longer routing time or vice versa. Combining Eqs.(5.42) & (5.43), $cov(T_r,T_n)$ may be further written as:

$$cov(T_r, T_n) = \underbrace{\frac{\sum_i^N \xi_{n,i}\left(\left\{T, \left\{\theta_{n,i}, R_i\right\}_a\right\}_t - \frac{\{T, [R_i]_a\}_t \left\{\theta_{n,i}, [R_i]_t\right\}_a}{[R_i]_{at}}\right)}{[R]_{at}}}_{c} + \underbrace{\sum_i^N \psi_i \xi_{n,i}\left(\frac{\{T, [R_i]_a\}_t \{\theta_n, [R_i]_t\}_a}{[R_i]_{at}^2} - \frac{\left\{T, \sum_i^N [R_i]_a\right\}_t \left\{\theta_{n,i}, \sum_i^N [R_i]_t\right\}_a}{[R]_{at}^2}\right)}_{LT_rT_n} \tag{5.44}$$

Magnitudes of terms in Eq.(5.44) for the surface and subsurface component and the total are rendered in the right panel of Figure 5.9 with mean of terms reported in Table 5.3. Note that the magnitudes of terms have been multiplied by 2 given the mass conservation in Eq.(5.32). Values of the covariance terms are almost symmetrically distributed at zero and slightly positively skewed. This observation indicates that there is no clear tendency for the storm movement. This is again explained by the fact that there is no preferred spatial pattern of rainfall over the study region with negligible orographic enhancement. The LT_rT_n term reveals an insignificant effect from the inter-component covariance between the temporal and spatial mass center of rainfall excess. This result supports our first guess on the magnitude of LT_rT_n. Due to the low LT_rT_n, $cov(T_r,T_n)$ is mainly manipulated by c. Inspection on magnitudes of the two rainfall excess components demonstrates that the correlation between T_r and T_n for the subsurface one is higher. Meanwhile, we observe an increase of $cov(T_r,T_n)$ magnitude from the Swift to the Tar catchment, consisting of the positive scale dependency in magnitude of storm movement concluded in Mei et al. (2014a) over the same area. In all, the movement effect of rainfall excess in variance of catchment response is relatively insignificant in the study region.

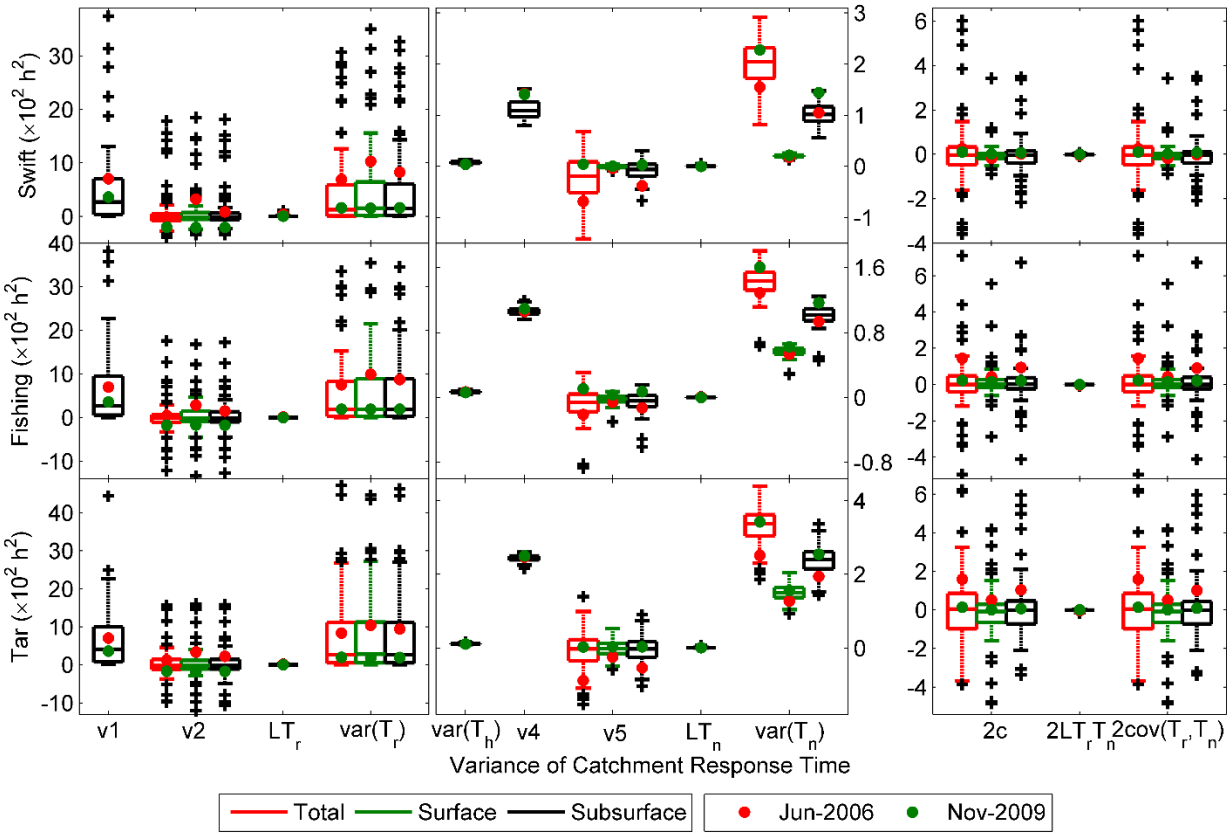

Figure 5.9. Same as Figure 5.7 but for Eqs.(5.35), (5.38), (5.41) & (5.44).

Table 5.3. Same as in Table 5.1 but for Eqs.(5.35), (5.38), (5.41) & (5.44).

Term	Swift			Fishing			Tar		
	Sub-surface	Surface	Total	Sub-surface	Surface	Total	Sub-surface	Surface	Total
v1	536	536	536	766	766	766	740	740	740
v2	73	103	86	22	25	24	60	60	61
LT_r	\	\	7.6	\	\	2.4	\	\	2.5
$var(T_r)$	609	638	**629**	788	791	**792**	800	800	**803**
$var(T_h)$	0.36	32	7.8	0.47	28	7.0	2.1	32	12
v3	223	21	112	150	59	106	340	152	244
v4	-22	-0.96	-8.8	-7.7	-2.6	-5.1	-10	-3.4	-6.7
LT_n	\	\	0.65	\	\	0.18	\	\	0.58
$var(T_n)$	201	20	103	142	56	101	330	149	238
c	57	0.07	24	28	14	21	-57	-30	-42
LT_rT_n	\	\	-0.59	\	\	-0.56	\	\	-0.82

$cov(T_r,T_n)$	57	0.07	24	28	14	20	-57	-30	-43
var(Φ)	867	***691***	764	958	***889***	921	1075	***952***	1010

5.5 Role of the Analytical Framework on Flood Characteristics

The rainfall and catchment surface properties are intimately related with the generation of flood. Specifically, the analytical framework quantities, $[R]_{at}$, $E(\Phi)$, and $var(\Phi)$, are correlated with the cumulative volume (V), centroid (C), and spreadness (S) of event flow time series, respectively (Volpi, et al., 2012; Mejía & Moglen, 2010; Viglione, et al., 2010a; 2010b; Sangati, et al., 2009). To address the question of how sensitive the framework quantities are to the flood characteristics, we conducted sensitivity tests with respect to the flow simulations and observations in this section. The V, C, and S, which quantify the catchment flood response are defined as:

$$V = \int_{T_F} Q(t)\, dt \tag{5.45}$$

$$C = \frac{\int_{T_F} t \cdot Q(t)\, dt}{\int_{T_F} Q(t)\, dt} \tag{5.46}$$

$$S = \sqrt{\frac{\int_{T_F} (t-C)^2 Q(t)\, dt}{\int_{T_F} Q(t)\, dt}} \tag{5.47}$$

where $Q(t)$ is either the simulated or observed event flow time series; T_F correspond to the flood event period. V reflects the magnitude of cumulative flow of a flood event while C and S are related to the shape of flood event hydrograph. Specifically, C is the temporal location of mass center of the hydrograph which can be used to surrogate the time to peak (for single peak hydrographs); S represents the temporal degree of dispersion with respect to C; typically for a unimodal event the larger S indicates less concentrated peak for the hydrograph.

Results of the sensitivity tests with respect to simulations and observations are illustrated in Figure 5.10 and Table 5.4. Overall, the catchment-average cumulative rainfall excess ($[R]_{at}|T_P|$) shows relatively high consistency with the cumulative flow volume derived by the model simulations (upper left panel), especially for the Fishing and Tar catchments where the mean of mean error (*ME*) are within 1 mm for the events. For the Swift cases, a slight overestimation of *V* by merely 3 mm (in terms of mean *ME*) is observed. Table 5.4 also provides the centered root mean square (*CRMS*) as an indicator of the random error in estimating *V*. Magnitudes of *CRMS* are fairly small within 1.6 mm, considering that these are produced based on cumulative volume. A comparison between *ME* and *CRMS* gives more insights on the performance of the analytical framework. Random error is the main error source for the Fishing and Tar cases, while in the Swift, systematic overestimation is more dominated. On the other hand, comparisons between the framework $[R]_{at}|T_P|$ and *V* derived from the observed flow shows significant reduction in linearity of the relationship (upper right panel of Figure 5.10). This is also reflected by the higher *CRMS* values in Table 5.4 (*CRMS* of *V* compared to the observations are at least 3 mm larger than those compared with the model simulations). *ME* with respect to the observed *V* for the Fishing and Tar catchments are still relatively low (lower than the *CRMS* of *V*) while the Swift case is characterized by 5.4 mm of *ME*. In all, the analytical framework provides reliable estimation on the cumulative volume, especially when compared to the model simulations, given the low magnitudes of *ME* and *CRMS*. The sensitivity of framework predicted cumulative volume shows noticeable drop from comparing with the model simulations to the observed flow.

The middle panel of Figure 5.10 demonstrates the correlation between expectation of catchment response time and centroid of flood event. Both of the sensitivity tests against the flow simulations and observations show that $E(\Phi)$ are positively correlated with *C* but with apparent underestimations. For the simulation-based sensitivity test, the systematic underestimation on event centroid is about 32 hours for events from the smallest basin and increases to 36 hours for events from the largest basin. The random components of error are within 23% of the systematic one in magnitude. Results of the observation-based

sensitivity test indicates lower systematic error by the analytical framework but, as expected, higher degree of random error (*ME* are about 80% of the simulated-based tests but *CRMS* are twice as those). This signifies that the main issue in estimation of *C* is the systematic underestimation from the analytical framework. This underestimation lies in the simplified structure of the analytical framework compared to a distributed hydrologic model in both land surface and routing processes. In the land surface process during the early phase of the event, precipitation is principally used to fill the water capacity of catchment under the infiltration excess; after a certain time period, flow rate rises rapidly with the existence of precipitation because of the saturation excess process. This can be visualized by the sample events time series in Figure 5.2. Consequently, the inclusion of precipitations before the functioning of saturation excess advances the temporal mass center of rainfall, leading to underestimation of the mass center location. Furthermore, in the analytical framework a water parcel is approximated traveling at a constant speed once it enters the basin while the linear reservoir routing scheme of CREST only discharges a portion of the water amount from the total storage in a given grid cell, which in turn, increases the equivalent travelling time. Given that the hydrologic simulations provide reasonable performance with respect to the observed flow, systematic underestimation by $E(\Phi)$ to the observations-derived *C* is also seen.

The spreadness is compared to the standard deviation of the catchment response time (square root of variance of the catchment response time) in the last panel of Figure 5.10. Systematic underestimation is still the major source of error in the estimation for the simulation-based tests. Its magnitudes are about -12 hours and the magnitudes decrease with increasing spreadness. *ME* of the observed-based sensitivity tests also reveal systematic underestimation but to lesser significance against the simulation-based ones. The random error reaches similar magnitudes of systematic error (above 9 hours) due to the increase in nonlinearity of the $\sqrt{var(\Phi)}$-*to*-*S* relationship. The underestimation in *S* is also originated from the differences in structure of a distributed hydrologic model and the framework. During the early phase of event, the infiltration excess is the dominant mechanism for runoff generation. Under such a condition, the flow rate rises gradually and the hydrograph tends to be smooth, implying high spreadness. One can take

the November 2009 event as an example; instead of having one rapid rising, the Swift catchment hydrograph has two rising limbs due to the switch in rainfall excess generation mechanism. This bi-modal shape introduces larger spreadness compared to a unimodal rising shape. A similar argument regarding the influence of infiltration excess on runoff generation has been reviewed in Mei et al. (2014). Their study argues that the low sensitivity between shape error of rainfall and simulated runoff shown for the events is because most of the events from the Tar region do not have a bank-full condition. On the other hand, the equivalent travel time in the channel routing is underestimated, and this underestimation is increasing with the length of water path given that θ_n represents a cumulative sum along water path (Eq.(5.4)). This leads to underestimation in the variability of travelling time of CREST by the framework. To sum up, the analytical framework works better in predicting the spreadness of hydrograph compared to the centroid. Mean values of *ME* for *S* are approximately 34% of the *C* case. Meanwhile, we observe relatively low values of the mean *CRMS* for both the *S* and *C* estimation for the catchments (around 6 hours).

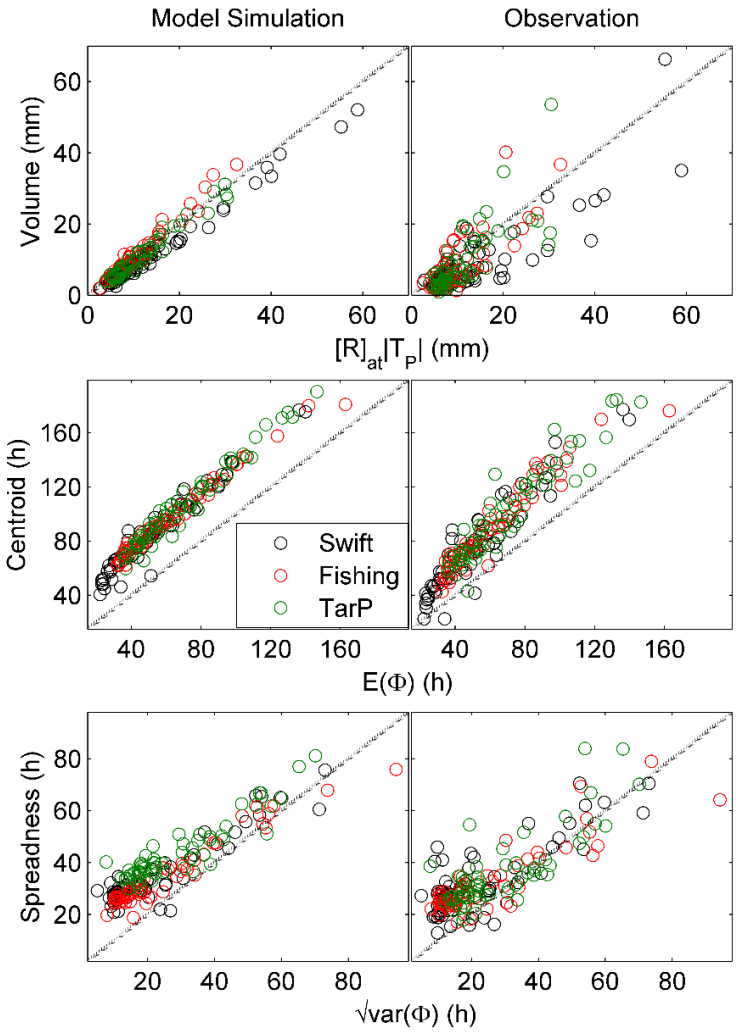

Figure 5.10. Scatterplots of the analytical framework outputs vs. hydrograph properties.

Table 5.4. Statistics of the sensitivity tests.

Reference Type	Basin	Mean Error			Centered Root Mean Square		
		V (mm)	C (h)	S (h)	V (mm)	C (h)	S (h)
Model Simulation	Swift	2.9	-32.4	-12.4	1.6	7.6	6.5
	Fishing	-0.6	-34.4	-9.8	1.6	3.8	6.3
	Tar	0.6	-36.3	-15.0	1.3	6.6	6.4
Observation	Swift	5.4	-24.1	-9.9	6.2	13.5	9.8
	Fishing	1.5	-28.6	-7.2	4.8	10.5	9.1
	Tar	1.7	-31.0	-7.3	5.7	12.5	9.0

5.6 Conclusions

We presented an expansion of V2010 hydrologic analytical framework under the consideration of multiple components in catchment flood response. To demonstrate the framework in this study we fixed the flow generation components to two (surface and subsurface), and used a distributed hydrological model (CREST) to provide the necessary framework parameters and event flow hydrographs. We demonstrated the framework based on a large number of flood events that occurred between 2003 and 2012 over three sub-catchments of the Tar River basin. Two of the flood events were used for a detailed demonstration of the framework. Sensitivity tests were rendered to investigate the correlation between framework and flood characteristics. The findings from this study are summarized below.

For the aspect of rainfall excess generation, we showed that the amount of rainfall excess generation is inverse proportional to catchment size. The most significant contribution came from the product term between space-time aggregated rainfall and runoff coefficients, while spatial and temporal correlation and movement effects were not significant. In addition, it was shown that the subsurface component outperformed the surface component of runoff in the contribution to rainfall excess generation, but this difference diminished in larger catchments.

The expectation of catchment response time was also investigated. We found that the total rainfall excess generation time is a linear combination of the expected generation times of all rainfall excess components weighted by their rainfall excess ratio. The total hillslope (channel) routing time is also a combination of routing times of all rainfall excess components weighted according to their rainfall excess ratio. Results show that both rainfall excess generation and runoff routing (hillslope plus channel) stages are important to the timing of the catchment response. The length of the rainfall event and the magnitude of the channel routing time play a significant role in controlling the timing of the hydrograph. Delay in response due to the spatial and temporal correlation term is low. The total catchment response time was shown to be closer to the subsurface rainfall excess one, indicating a higher degree of influence, which

agrees with the higher rainfall excess ratio for the subsurface component. However, the value gap between components is narrowing from small to large catchment area.

For the variance of catchment response time, our findings showed that the total variance in rainfall excess generation comes from two parts—the linear combination of all components variance and the variance of expected rainfall excess generation time for components. These two parts account for the intra- and inter-component variability, respectively. The total variance in delay due to the hillslope (channel) routing stage is consisted of two parts—a combination of variances from all the other components and the variance of expected runoff routing time with the participation of the hydrologic and geomorphologic related coefficients. Note that the second part for hillslope routing is zero since the hillslope routing time is fixed at the space and time dimensions. Analogously, the covariance between holding times of the stage 1 and 3 also consists of two parts—the expectation of component covariance and the covariance between expectations of rainfall excess generation and channel routing. Results revealed that variance of the rainfall excess generation stage is of higher importance than those of the hillslope and channel routing stage. For stage 1, the variance from rainfall duration was more important than the additional variance from temporal interactions between rainfall excess and time. For stage 3, the spatial variance of channel routing time outperformed the additional variance that rose from the spatial interaction between rainfall excess and channel routing. The covariance between holding times of stage 1 and 3 was also found to be irrelevant. Additionally, variance of the surface component was closer to the total variance, indicating a higher degree of influence. Furthermore, the inter-component variability was negligible compared to the intra-component variability.

Results from the sensitivity analysis revealed that the framework is characterized by relatively low random errors in estimating the flood characteristics. The random errors were larger in the observations-based sensitivity tests compared to the simulation-based ones. A slight overestimation was found in the Swift catchment on the estimation of cumulative flow volume. Systematic underestimation in event centroid and spreadness were notable, especially for the timing issue, which demonstrates an increasing trend with

catchment scale. Moreover, for the simulation-based sensitivity tests, the underestimation of spreadness was reduced with the increase in magnitude of spreadness.

From the herein analytical framework results, we showed that magnitudes of the new "time lag" terms are low. We believe this is not a general finding because the surface runoff coefficient and hillslope routing time was represented by a constant imperviousness ratio (I_M) for this study and the channel routing times for the two components had the same spatial pattern (differed merely in magnitude by the constant α_n). Also, the "time lag" term for hillslope routing was vanished due to the use of constant linear reservoir parameters (k_I and k_S). Future studies will need to replace the constant imperviousness ratio by a spatially distributed variable to mimic the spatial variability of the very fast flood response of a catchment. Besides, we suggest using spatially varied k_I, k_S and $\alpha_{n,i}$ to better represent the differences in routing among excess rainfall components. This is particularly useful in analyzing the flood response of urbanized catchments where the distribution of excess rainfall into different vertical soil layers is quite different between the highly impervious urban areas (e.g. roads, rooftops, parking lots, etc.) and the more pervious suburban or rural areas of the basin (Mejía, et al., 2015; Mejía & Moglen, 2010; Smith, et al., 2002). We believe the "time lag" terms could be important for flood response of the urbanized catchment and our new framework can serve as a diagnostic tool to verify the significance of these terms.

We acknowledge certain limitations of our analytical framework study. The framework variables and flow simulation are dependent on the distributed hydrologic model devised in this study (e.g. vegetation interception, imperviousness areas, linear reservoir parameter, coefficient α, etc.). Since the retrievals of framework variables are based on the model structure and parameterization, the way a variable is calculated could vary across models, while in certain models such an explicit parameter may not be available. An alternative path to circumventing this issue is to apply directly observed data for the calculation of the analytical framework variables. For instance, the vegetation interception can be estimated from the leaf area index data (Xiao, et al., 2014); database of the impervious area are provided in certain data rich locations (Homer, et al., 2015); the spatial patterns of runoff coefficients could be retrieved in highly gauged

catchments or from satellite-derived soil moisture fields at global scale (Massari, et al., 2014; Dhakal, et al., 2012; Penna, et al., 2011; Merz & Blöschl, 2009); and the parameters related to runoff routing could be estimated based on the geomorphologic properties of catchments (Shen, et al., 2017).

Chapter 6 Quantifying the Error Propagation of Satellite Precipitation by a Hydrologic Analytical Framework

6.1 Introduction

The evaluation of satellite precipitation in hydrological simulation provides information on the potential sources of error from precipitation and how these error sources are propagated to the error of flow simulation. Such information can help facilitate a number of flood risk applications, such as reservoir operation and timely emergency response. Many past studies have focused on the assessment of the error propagation of satellite precipitation products through the rainfall-runoff process. A common finding has been that the properties of error propagation (magnification vs. dampening and linear vs. nonlinear) vary with different factors. For instance, a wetter flood-event initial condition (e.g. soil moisture, runoff coefficient, etc.) results in error propagation that behaves more linearly (Mei, et al., 2016b; Shah & Mishra, 2016; Nikolopoulos, et al., 2011); larger basins are often observed to be more tolerant of random error in precipitation estimation (Mei, et al., 2016b; Vergara, et al., 2013). Other factors, such as regional climate pattern, land cover types, seasonality, and the choice of hydrological model or modeling complexity, also affect the error propagation properties (Kim, et al., 2016; Gebregiorgis & Hossain, 2013; Xue, et al., 2013; Gebregiorgis, et al., 2012; Beighley, et al., 2011).

Researchers previously have proposed and developed an analytical framework for estimating flood characteristics by synthesizing various space-time processes of catchments (Mei, et al., 2016c; Viglione, et al., 2010a; Woods & Sivapalan, 1999). The framework estimates three flood event properties (that is, cumulative volume, centroid, and dispersion) by the generation of rainfall excess and the expectation and variance, respectively, of catchment response time. These three framework quantities are formulated into terms containing the space and time information on rainfall, runoff generation, and routing. Thus, the framework has been used as a diagnostic tool to assess the relative importance of these space and time terms to catchment response, generally finding that the space-time information on runoff generation and routing

is important for short-duration events occurring over small basins with the impact of orographic effects (Mei, et al., 2016c; Viglione, et al., 2010b).

The framework has also been utilized to understand the effect of neglecting the spatial information on rainfall in runoff generation. Zoccatelli et al. (2011) proposed the concept of spatial moment of catchment rainfall, built upon the framework. They assessed the difference in timing of hydrographs if the spatial information of rainfall is neglected (lumped rain) and found that the timing of event-based hydrographs is sensitive to the location of the rainfall mass center over the catchment. Following a similar methodology, others have investigated the effects of the second-order moment of catchment rainfall and catchment-scale storm velocity on runoff generation (Mei, et al., 2014a; Nikolopoulos, et al., 2014). Nikolopoulos et al. (2014) compared the variability of flood event hydrographs generated from rainfall fields without a spatial pattern and those with a fixed spatial pattern to hydrographs derived from the original rainfall field. Their results highlight the important role of spatial information in shaping the variability of flood event hydrographs. Among these studies, the analytical framework has been used as a tool to formulate the differences in the space-time characteristics of rainfall, with the corresponding flow simulations.

To the same end, we are inspired to use the hydrological analytical framework to link the error in satellite precipitation characteristics with the error in flow simulations driven by the satellite precipitation products. This allows us to view and investigate, from a novel angle, the error propagation process of the products in hydrological simulations. Specifically, the strengths of the framework allow us to decompose the error in satellite precipitation estimation and runoff generation into different terms representing the precipitation and catchment space-time characteristics. This offers information on the relative importance of those error terms with respect to contribution to error in satellite-derived flow simulations, providing an understanding of the level of space and time complexity required to model the error propagation process at the scale of catchment and event. We believe this approach is beneficial for the developers and end users of the satellite precipitation products and the hydrological models. On the one hand, it can guide the selection of an optimal spatiotemporal resolution (a tradeoff between the space and time variability of

observations) for satellite precipitation products, based on the available measurements from different satellite sensors. On the other hand, the end users can choose the optimal space and time complexity of hydrological modeling with minimal loss in accuracy for particular basins and events.

In this paper we introduce the integration of the hydrological analytical framework for the assessment of the propagation of satellite precipitation error. The paper is structured as follows: in section 6.2, we describe our error modeling framework by first giving reviews of the hydrological analytical framework (section 6.2.1) and then introducing its use to model the error propagation of satellite precipitation (section 6.2.2). Section 6.3 describes the datasets and the hydrological model for the implementation and parameterization of the error modeling framework. Section 6.4 presents the results regarding the volumetric bias and the bias in hydrodynamics. Last, we present our conclusions, together with limitations and future directions of this study, in section 6.5.

6.2 Error Modeling Framework

6.2.1 Catchment Flood Response

Researchers have proposed a hydrological analytical framework to conceptualize the catchment flood response process in three stages (Viglione, et al., 2010a; Woods & Sivapalan, 1999). In stage 1, rain falls on the catchment surface and is converted to rainfall excess. A parsimonious runoff generation function (that is, a runoff coefficient) is adopted to conceptualize the complex space-time interactions of precipitation in runoff generation. The rainfall excess generated from the first stage is subjected to two subsequent routing stages, namely hillslope and channel routing, which refer to the processes by which the rainfall excess is routed from the place it was generated to the entrance of the channel network and then to the catchment outlet. Each of the stages is associated with a "holding time," treated as a random variable (Rodríguez-Iturbe & Valdés, 1979). The framework focuses on three quantities: the amount of rainfall

excess and the expectation and variance of catchment response time. These are used to estimate the cumulative volume, the centroid, and the dispersion of the event flow hydrograph.

The amount of rainfall excess, $[R]_{at}$ in mm/h, is the intensity of excess rainwater generated during the storm event period over the catchment area. It is written as

$$[R]_{at} = \underbrace{[P]_{at}[W]_{at}}_{R1} + \underbrace{\{[P]_a, [W]_a\}_t}_{R2} + \underbrace{\{[P]_t, [W]_t\}_a}_{R3} + \underbrace{[\{P - [P]_t, W - [W]_t\}_a]_t}_{R4} \tag{6.1}$$

where P, W, and R are, respectively, the space-time variable precipitation, runoff coefficient, and rainfall excess; $[\ ]$ and $\{\ \}$ with subscript a and/or t stand for the expectation and covariance (variance if the variables are the same) operators applied to the dimensions of catchment area and/or storm period. The definitions of *R1*, *R2*, *R3*, and *R4* are listed in Table 6.1. The cumulative amount of rainfall excess (the product of $[R]_{at}$ and the duration of storm, $|T_P|$) is used to estimate the cumulative volume of the event flow hydrograph (V in mm), defined as

$$V = \int_{T_F} Q(t)\, dt \tag{6.2}$$

where $Q(t)$ is the event flow hydrograph and T_F is the period of flow event.

The catchment response time is a random variable composed of the runoff generation time, the hillslope routing time, and the channel routing time. Thus, the expectation of catchment response time, $E(\Phi)$, is the summation of the expectation of holding times of these three stages,

$$E(\Phi) = \underbrace{E(T_r)}_{Stage\ 1} + \underbrace{E(T_h)}_{Stage\ 2} + \underbrace{E(T_n)}_{Stage\ 3} \tag{6.3}$$

where Φ, T_r, T_h, and T_n are variables representing the holding times of catchment response, runoff generation, and the hillslope and channel routing processes. T_r is modeled by the instantaneous time (T), which follows a uniform distribution of the storm period (Viglione, et al., 2010a; Woods & Sivapalan, 1999). T_h is represented by a linear reservoir response time, θ_h, which is a space-time constant (Mei, et al., 2016c). T_n is modeled by a spatially distributed network routing time, θ_n, retrieved based on the hydrological model (see Eq.(6.26) in section 6.3.3). Therefore, the expectation of holding times may be written as

$$E(T_r) = \underbrace{\frac{|T_P|}{2}}_{E1} + \underbrace{\frac{\{T, [R]_a\}_t}{[R]_{at}}}_{E2} \tag{6.4}$$

$$E(T_h) = \underbrace{t_h}_{E3} \tag{6.5}$$

$$E(T_n) = \underbrace{[\theta_n]_a}_{E4} + \underbrace{\frac{\{\theta_n, [R]_t\}_a}{[R]_{at}}}_{E5} \tag{6.6}$$

where t_h is the linear reservoir parameter defined by Eq.(6.25) in section 6.3.3. The definition of each term is given in Table 6.1. The expectation of catchment response time is an estimator of the centroid of event flow hydrograph (*C* in h). *C* is calculated as the instantaneous time weighted by the flow rate:

$$C = \frac{\int_{T_F} t \cdot Q(t)\, dt}{\int_{T_F} Q(t)\, dt} \tag{6.7}$$

C is a measure of time from the beginning of the flow event to the mass center of the event; it can be used as a surrogate for the concept of time to peak for a mono-modal flow event.

The variance of catchment response time, *var(Φ)* in h^2, for the three-stage framework is contributed by the variance of the holding times from the stages and the covariance between the holding times of any two stages:

$$var(\Phi) = \underbrace{var(T_r)}_{Stage\ 1} + \underbrace{var(T_h)}_{Stage\ 2} + \underbrace{var(T_n)}_{Stage\ 3} + \underbrace{2cov(T_r, T_h)}_{Stage\ 1\ \&\ 2} + \underbrace{2cov(T_h, T_n)}_{Stage\ 2\ \&\ 3} + \underbrace{2cov(T_n, T_r)}_{Stage\ 3\ \&\ 1} \tag{6.8}$$

The three variance terms of the equation may be written as:

$$var(T_r) = \underbrace{\frac{|T_P|^2}{12}}_{v1} + \underbrace{\left(\frac{\{T^2, [R]_a\}_t}{[R]_{at}} - \frac{|T_P|\{T, [R]_a\}_t}{[R]_{at}} - \frac{\{T, [R]_a\}_t^2}{[R]_{at}^2}\right)}_{v2} \tag{6.9}$$

$$var(T_h) = \underbrace{t_h^2}_{v3} \tag{6.10}$$

$$var(T_n) = \underbrace{\{\theta_n\}_a}_{v4} + \underbrace{\left(\frac{\{\theta_n^2,[R]_t\}_a}{[R]_{at}} - \frac{2[\theta_n]_a\{\theta_n,[R]_t\}_a}{[R]_{at}} - \frac{\{\theta_n,[R]_t\}_a^2}{[R]_{at}^2}\right)}_{v5} \tag{6.11}$$

Refer to Table 6.1 for the meanings of these terms. Three covariance terms also appear in Eq.(6.8) accounting for the covariance between the holding times of any two stages. Since T_h is represented by a constant θ_h in space and time, $cov(T_r,T_h)$ and $cov(T_n,T_h)$ are zero. The only covariance term remaining is $cov(T_r,T_n)$, which is often interpreted as the movement of storm (Zoccatelli, et al., 2015; 2011). It may be written as

$$cov(T_r,T_n) = \underbrace{\frac{\{T,\{\theta_n,R\}_a\}_t}{[R]_{at}} - \frac{\{T,[R]_a\}_t\{\theta_n,[R]_t\}_a}{[R]_{at}^2}}_{c} \tag{6.12}$$

The square root of the variance of catchment response time is used to estimate the dispersion of event flow hydrograph (S in h). S is defined as the square root of the second moment of time with respect to flow rate:

$$S = \sqrt{\frac{\int_{T_F}(t-C)^2Q(t)\,dt}{\int_{T_F}Q(t)\,dt}} \tag{6.13}$$

S reflects the distribution of mass with respect to the mass center of flow. For example, a flow event with most of its mass located around the mass center (that is, a flow event with a sharp peak) takes small S; a flow event with its mass located farther away from the mass center (that is, a flow event with peaks located at its beginning and end) is characterized by large S.

Table 6.1. Meanings of quantities in the hydrologic analytical framework.

Term	Meaning
R1	Product between spatiotemporal-average rainfall and runoff coefficient
R2	Temporal covariance between the catchment-average rainfall and runoff coefficient
R3	Spatial covariance between storm-average rainfall and runoff coefficient
R4	Temporal correlation between spatial variation of precipitation and runoff coefficient
$[R]_{at}$	Amount of rainfall excess
E1	Midpoint of the rainfall event
E2	Time distance from the event midpoint to the temporal mass center of catchment-average rainfall excess
$E(T_r)$	Expectation of rainfall excess generation time

E3	Expectation of the linear reservoir response time
$E(T_h)$	Expectation of hillslope routing time
E4	Spatial mean of the network routing time
E5	Distance from the geomorphologic center of catchment to the spatial mass center of the storm-average rainfall excess
$E(T_n)$	Expectation of channel routing time
$E(\Phi)$	Expectation of catchment response time
v1	Variance in time generated by a temporal invariant catchment-average rainfall excess
v2	Additional variance causes by the temporal variation in catchment-average rainfall excess
$var(T_r)$	Variance of rainfall excess generation time
v3	Variance of the linear reservoir response time
$var(T_h)$	Variance of hillslope routing time
v4	Spatial variance of the network routing time
v5	Additional variance causes by the spatial variation in storm-average rainfall excess with respect to the network routing time
$var(T_n)$	Variance of channel routing time
c	Time evolution of rainfall excess over the catchment network
$cov(T_r,T_n)$	Covariance between rainfall excess generation time and channel routing time
$var(\Phi)$	Variance of catchment response time

6.2.2 Error in Catchment Flood Response

A scheme for how to use the hydrological analytical framework in a satellite precipitation error propagation study is shown in Figure 6.1. The property pairs (satellite versus reference) of catchment flood response, namely $[R]_{at}$, $E(\Phi)$, and $var(\Phi)$, are calculated based on the analytical framework (the sign "^" represents the satellite-derived properties). Then the discrepancies among these property pairs are defined by the differences, that is, $\Delta[R]_{at}$, $\Delta E(\Phi)$, and $\Delta var(\Phi)$ in Figure 6.1. To test the sensitivity of the analytical error modeling framework, $\Delta[R]_{at}$, $\Delta E(\Phi)$, and $\Delta var(\Phi)$ are compared with the error in cumulative volume, centroid, and dispersion (ε_V, ε_C, and ε_S) of a flood event hydrograph, based on the simulations from a numerical model (described later in section 6.3). Given the additive relationships of the terms in Eqs.(6.1), (6.3) and (6.8) to the properties, the error in properties of catchment flood response are decomposed into terms quantifying the different space-time interactions among rainfall, runoff generation and routing. The error in amount of rainfall excess, $\Delta[R]_{at}$, may be written as

$$\Delta[R]_{at} = \underbrace{\hat{R}1 - R1}_{\Delta R1} + \underbrace{\hat{R}2 - R2}_{\Delta R2} + \underbrace{\hat{R}3 - R3}_{\Delta R3} + \underbrace{\hat{R}4 - R4}_{\Delta R4} \tag{6.14}$$

where the terms with/without a "^" are derived based on the satellite/reference precipitation.

Four error components exist in Eq.(6.14). *ΔR1* represents the difference in satellite precipitation product's spatiotemporal-average precipitation and runoff coefficient. It is a quantification of the systematic error in runoff generation derived between the satellite and reference rainfall. *ΔR2* and *ΔR3* represent the differences in temporal and spatial covariance between the spatial- and temporal-average precipitation and runoff coefficient, respectively. *ΔR4* stands for the difference in temporal correlation between the spatial variation of precipitation and the runoff coefficient. The terms *ΔR2*, *ΔR3* and *ΔR4* represent the correlation in space and time patterns between the runoff generations from different rainfall fields. Eq.(6.14) indicates that the difference in amount of rainfall excess can be decomposed into terms representing the lumped (*ΔR1*), temporal (*ΔR2*), spatial (*ΔR3*), and spatiotemporal (*ΔR4*) information. This means that if only the space-time aggregated estimate of rainfall is available for the two rainfall fields, the total difference in amount of rainfall excess is *ΔR1*. If the available information is at the level of time series/spatial maps, then the total difference is a sum of *ΔR1* and *ΔR2*/*ΔR3*.

The error in expectation of catchment response time, *ΔE(Φ)*, is contributed from the runoff generation stage, the hillslope routing stage, and the channel routing stage. Therefore, *ΔE(Φ)* is the sum of error from the three stages:

$$\Delta E(\Phi) = \underbrace{E\left(\widehat{T_r}\right) - E(T_r)}_{\Delta E(T_r)} + \underbrace{E\left(\widehat{T_h}\right) - E(T_h)}_{\Delta E(T_h)} + \underbrace{E\left(\widehat{T_n}\right) - E(T_n)}_{\Delta E(T_n)} \tag{6.15}$$

Given the additive relationship of $E(T_r)$, $E(T_h)$, and $E(T_n)$ to $E(\Phi)$, we can rewrite Eq.(6.15) as following:

$$\Delta E(\Phi) = \underbrace{\hat{E}2 - E2}_{\Delta E2} + \underbrace{\hat{E}3 - E3}_{\Delta E3} + \underbrace{\hat{E}4 - E4}_{\Delta E4} + \underbrace{\hat{E}5 - E5}_{\Delta E5} \tag{6.16}$$

Note that no *ΔE1* term appears in the equation because the satellite- and reference-suggested rainfall event pairs are always taking the same event period, and the subtraction between the two *E1*—the half-length of events—is always zero.

ΔE(Φ) can be decomposed into four error terms from the equation. *ΔE2* represents the difference in temporal covariance between catchment-average rainfall excess and time. *ΔE3* and *ΔE4* are the differences in mean of hillslope response time and network routing time, respectively. These two terms together represent the error in mean runoff routing time between runoff generated by the two rainfall fields. *ΔE5* is the difference in spatial covariance between storm-average rainfall excess and runoff routing time. Eq.(6.16) dictates that the error in expectation of catchment response time can be categorized as the lumped (*ΔE3* and *ΔE4*), temporal (*ΔE2*), and spatial (*ΔE5*) information of the difference. Analogously, with knowledge only of the means of the variables—the cumulative amount of runoff generated during the event period and the mean values of hillslope response and network routing time—*ΔE(Φ)* equals *ΔE3* plus *ΔE4*. With the temporal distribution of rainfall, *ΔE(Φ)* returns to the sum of *ΔE2*, *ΔE3*, and *ΔE4*. The available information on spatial pattern of rainfall and runoff routing times results in a total error equal to *ΔE3* plus *ΔE4* plus *ΔE5*.

The error in variance of catchment response time, *Δvar(Φ)*, comes from four aspects, since any covariance term between T_h and another holding time is zero. They are the differences in variance arising from the rainfall excess generation stage and the runoff routing stage and the covariance between these two stages. Thus,

$$\Delta var(\Phi) = \underbrace{var(\widehat{T_r}) - var(T_r)}_{\Delta var(T_r)} + \underbrace{var(\widehat{T_h}) - var(T_h)}_{\Delta var(T_h)} + \underbrace{var(\widehat{T_n}) - var(T_n)}_{\Delta var(T_n)} + 2\underbrace{\left(cov(\widehat{T_r}, \widehat{T_n}) - cov(T_r, T_n)\right)}_{\Delta cov(T_r, T_n)} \tag{6.17}$$

Each of the term in Eq.(6.17) may be further expressed using Eqs.(6.9), (6.10), (6.11), and (6.12):

$$\Delta var(\Phi) = \underbrace{\hat{v}2 - v2}_{\Delta v2} + \underbrace{\hat{v}3 - v3}_{\Delta v3} + \underbrace{\hat{v}4 - v4}_{\Delta v4} + \underbrace{\hat{v}5 - v5}_{\Delta v5} + 2\underbrace{(\hat{c} - c)}_{\Delta c} \tag{6.18}$$

Again, there is no *Δv1* term because, for any event, the difference of *v1* derived between the satellite and reference rainfall event pair is always zero.

$\Delta var(\Phi)$ is described by five error terms. $\Delta v2$ stands for the difference in additional variance caused by the temporal variation in catchment-average rainfall excess. $\Delta v3/\Delta v4$ represents the difference in variance of hillslope response time and channel routing time. $\Delta v5$ is the difference in additional variance caused by the spatial variation in storm-average rainfall excess. Δc is the difference in covariance between the rainfall excess generation time and channel routing time. It can also be interpreted as the difference in motion of runoff generations over the catchment (Zoccatelli, et al., 2015; 2011; Nikolopoulos, et al., 2014). Therefore, the difference in variance of catchment response time is separated into terms standing for the lumped ($\Delta v3$ and $\Delta v4$), temporal ($\Delta v2$), spatial ($\Delta v5$), and spatiotemporal ($2\Delta c$) information. $\Delta var(\Phi)$ equals $\Delta v3$ plus $\Delta v4$ if the rainfall fields are uniformly distributed in space and time. The availability of rainfall as a time series results in a total difference of variation equal to $\Delta v2$ plus $\Delta v3$ and $\Delta v4$. The information on distributed spatial rainfall patterns returns a total error as the sum of $\Delta v3$, $\Delta v4$, and $\Delta v5$.

The three error quantities in catchment flood response—$\Delta[R]_{at}$, $\Delta E(\Phi)$, and $\Delta var(\Phi)$—are used to estimate the error in flood event properties (that is, ε_V, ε_C, and ε_S). ε_V, ε_C, and ε_S are similarly determined by the differences between V, C, and S derived from the satellite-driven flow simulations to those from reference precipitation. Thus, ε_V, ε_C, and ε_S are defined as

$$\varepsilon_V = \hat{V} - V \tag{6.19}$$

$$\varepsilon_C = \hat{C} - C \tag{6.20}$$

$$\varepsilon_S = \hat{S} - S \tag{6.21}$$

where $\hat{V}$ (V), $\hat{C}$ (C), and $\hat{S}$ (S) are derived from the satellite- (reference-) driven flow simulations. The term ε_V is the error in cumulative volume of flow and is estimated by $|T_P|\Delta[R]_{at}$. ε_C is the error in flood event centroid, estimated by $\Delta E(\Phi)$; it can be used as a surrogate for the error in time to peak for events with one peak. ε_S is the error in dispersion of the flood event hydrograph; it is a measure of difference in degree of dispersion between the hydrographs. The square root of $\Delta var(\Phi)$ is used to estimate ε_S.

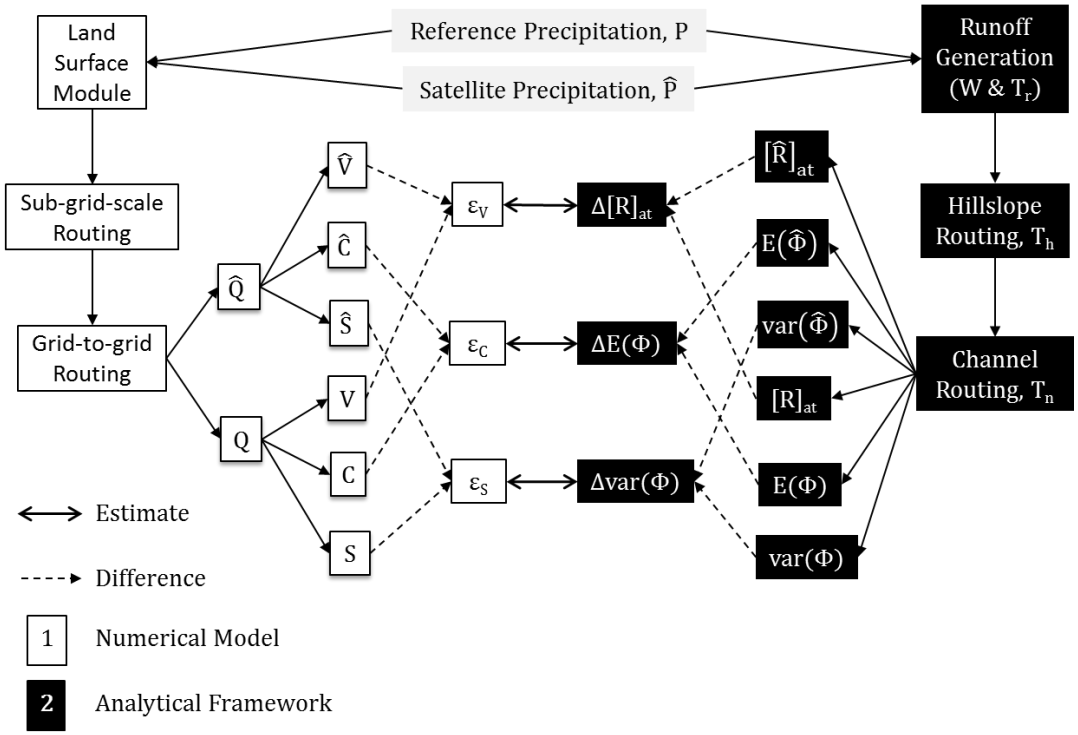

Figure 6.1. Scatterplots of the analytical framework outputs vs. hydrograph properties.

6.3 Implementation of the Framework

The implementation of the analytical error modeling framework requires five parameters, rainfall (P), runoff coefficient (W), runoff generation time (T_r), hillslope routing time (T_h), and channel routing time (T_n). These parameters can be retrieved from the input data and hydrological model. This section describes the integrations of a radar-based precipitation product (considered the reference) and twelve different satellite precipitation products with a hydrological model for the flow simulations of three catchments (section 6.3.1 and 6.3.2). Section 6.3.3 introduces the use of the hydrological model to retrieve parameters for the framework.

6.3.1 Hydrologic Model Setup

The Coupled Routing and Excess Storage (CREST) distributed hydrological model version 2.1 is used in this study (Shen, et al., 2016; Wang, et al., 2011). CREST consists of a land surface module and a runoff

routing module. The land surface module takes into account four processes of precipitation interaction with land surface and vegetation—canopy interception, infiltration, evapotranspiration (ET), and runoff generation. Canopy interception can be estimated using the leaf area index data or, conveniently, by putting a multiplier in front of the precipitation data. The infiltration rate is calculated based on the variable infiltration curve originally contained in the Xin'anjiang Model (Zhao, 1992) and the actual ET (AET) is determined in terms of water and energy budget using precipitation, soil water availability, and PET. For runoff generation, rainfall excess is separated into two components—the surface and subsurface runoff, modeled by the overland and interflow reservoirs, respectively. The runoff routing process of CREST is consisted by the subgrid scale and grid-to-grid routing. The subgrid scale routing is modeled by the overland and interflow reservoirs, and the grid-to-grid routing is implemented by a spatially distributed concentration time.

The model has been set up over three nested catchments (Swift, Fishing and Tar) of the Tar River basin in North Carolina, USA, with area equal to 426 km^2, 1374 km^2 and 2406 km^2 (Figure 6.2). The study area is a suitable site for testing the new analytical error modeling framework because precipitation occurring over the catchments is not subjected to significant orographic effects and is in the form of liquid throughout the entire year, due to the area's geomorphology and climate. We adopted in our study the same modeling setup as described by Mei et al. (2016c). Specifically, we generated the catchment areas from the Digital Elevation Model (DEM) data, and the spatiotemporal resolution of the model was 1 km and hourly. We used the Stage IV (STIV) radar-based multisensory precipitation estimates (Lin & Mitchell, 2005) and the PET data available from the North American Regional Reanalysis (NARR) (Mesinger, et al., 2006) as input meteorological forcing datasets. Space-time resolution for the STIV precipitation and NARR PET products were 4 km hourly and 32 km 3-hourly, respectively. To keep the modeling relatively simple, the vegetation interception process was conceptualized by a constant multiplier applied to the precipitation fields; the percentage of impervious surface and the hillslope response time of the catchment were modeled by constants, which we optimized through model calibration. We calibrated CREST with respect to the hourly

flow rate from United States Geological Survey (USGS) for the period 2004–6, with 2002–3 for model spin up. Results suggested reasonable model performance, with hourly Nash-Sutcliff coefficient efficiency (*NSCE*) equal to 0.69, 0.62, and 0.66 for Swift, Fishing, and Tar, respectively.

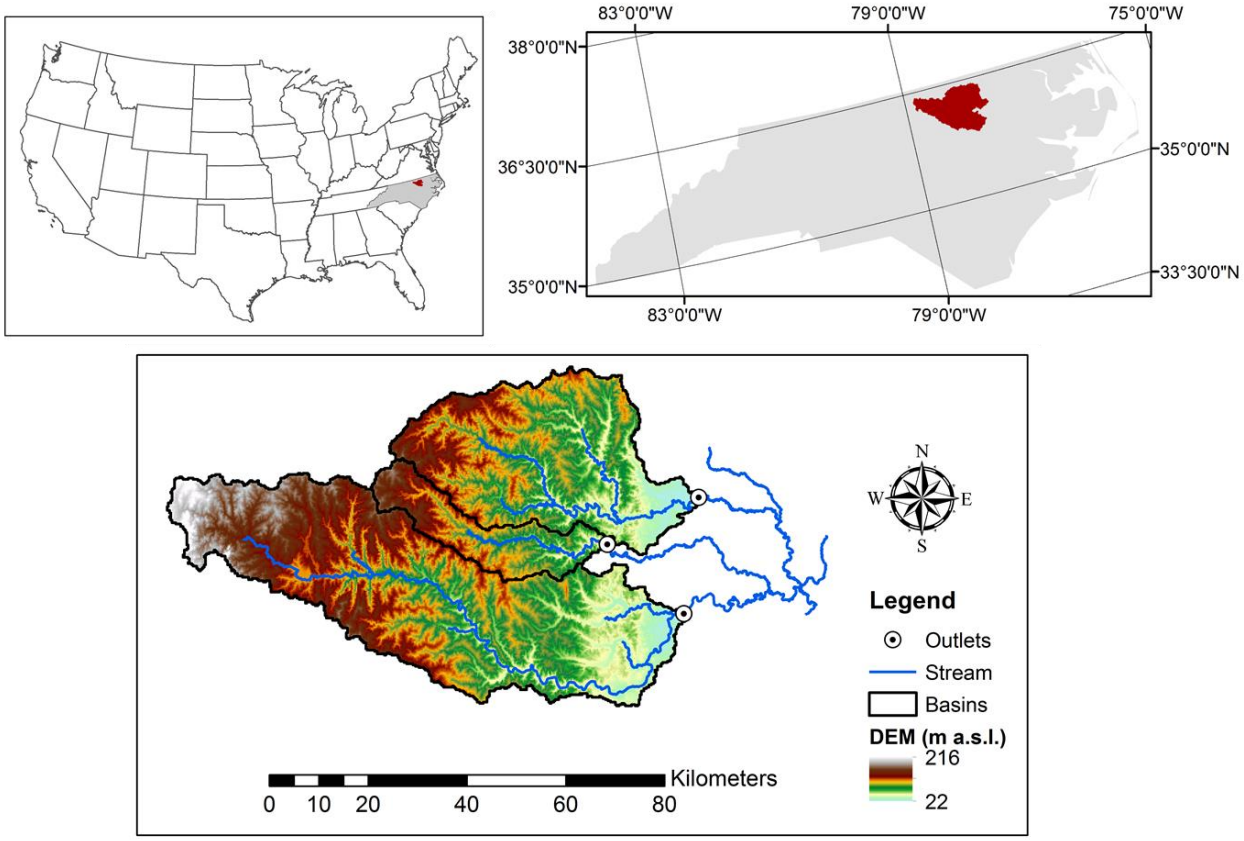

Figure 6.2. Geolocation and elevation of the study area.

Mei et al. (2016c) selected 180 rainfall-runoff events over the catchments from 2003–12, based on the performance of the hydrological simulations. In this study, we utilized events of the inventory from 2003 to 2010, which is the overlapping period of the twelve satellite products. The results in 160 rainfall-runoff events were 55, 50, and 55, respectively, from the Swift, Fishing, and Tar basins. The STIV-based simulations of these events were used as reference simulations. We evaluated these event-based flow simulations with respect to the observed flow events in terms of the relative error of the three hydrographical properties (V, C, and S, defined in Eqs.(6.2), (6.7) & (6.13)). Taking the cumulative volume as an example, relative error is defined as

$$RE_V = \frac{V - V_o}{V_o} \tag{6.22}$$

where V_o is the cumulative volume parameter calculated from an observed flow events. Table 6.2 lists the mean and standard deviation (SD) of RE_V, RE_C and RE_S based on the event population. As the table shows, the means and SDs of RE_C and RE_S were of low magnitude. This indicates the timing and shape of the radar-derived hydrographs were in good agreement with the observed flow event hydrographs. The means of RE_V for the basins were also low (11% for Swift and Fishing and 4.5% for Tar), but exhibited large SDs, indicating some of the cases had over- or underestimation up to 50% and -30%, respectively. Overall, the radar-based simulations provided reliable estimates on the event flow hydrographs.

Table 6.2. Error in hydrograph properties between radar-driven event flow simulations and observed flow events.

Basin	RE_V (%)		RE_C (%)		RE_S (%)	
	mean	SD	mean	SD	mean	SD
Swift	11.7	39.7	-0.1	7.3	-5.4	7.9
Fishing	11.5	39.2	-0.4	6.9	-6.5	7.5
Tar	4.5	40.6	-0.6	6.9	-6.3	8.2

6.3.2 Satellite Precipitation Products

This study evaluated twelve quasi-global satellite precipitation products. The first three were the 3B42 products from the Tropical Rainfall Measuring Mission Multi-Satellite Precipitation Analysis. The 3B42 products are available in real time (T), in adjustment from the climatological correction algorithm (T_{cca}), and in post processing using gauge adjustment (T_g) (Huffman, et al., 2010; 2007). These three 3-hourly products are in 0.25° spatial resolution.

Another three products evaluated were the Precipitation Estimation from Remotely Sensed Information using Artificial Neural Networks (PERSIANN) product (Sorooshian, et al., 2000), the PERSIANN Cloud Classification System product (Hong, et al., 2004) and gauge-adjusted version of PERSIANN (Huffman,

et al., 2009; Adler, et al., 2003). These three products are abbreviated as P, P_{ccs} and P_g, respectively. Product P and its gauge-adjusted version, P_g, are in 0.25°/3-hourly resolution, while the P_{ccs} is 0.04°/hourly.

Also used were the National Oceanic and Atmospheric Administration Climate Prediction Center morphing technique (CMORPH) product available at resolutions of 0.25°/3-hourly and 0.072°/hourly, abbreviated as C and HC, respectively (Joyce, et al., 2004). The gauge-corrected versions of these two products (Xie, et al., 2011), denoted as C_g and HC_g, were also included.

Finally, we considered the Global Satellite Mapping of Precipitation (GSMaP) version 5 Microwave-IR Combined product and the Motion Vector Kalman Filter GSMaP (Ushio, et al., 2009) and its gauge adjusted counterpart (Mega, et al., 2014), abbreviated as G and G_g, respectively. The two GSMaP products are hourly and in 0.1° spatial resolution.

We used the twelve satellite precipitation products to drive CREST for flow simulations of the 160 rainfall-runoff events, with the optimum parameters calibrated for the STIV precipitation. For each event, we forced the simulation of each satellite product to take the same initial condition outputted by the STIV simulation. This ensured the same initial condition for each of the event pairs simulated by the different products.

6.3.3 Framework Parameters

The five framework parameters were the precipitation (P), runoff coefficient (W), runoff generation time (T_r), hillslope routing time (T_h), and channel routing time (T_n). The rainfall excess generation time, T_r, was the instantaneous time within the encapsulated period of the rainfall event provided by the 160 extracted rainfall-runoff events. The precipitation parameter was the through-rainfall, defined as the net amount of precipitation that reaches the catchment surface and participates in the runoff generation process. Thus, P was calculated by removing the vegetation intercepted rainfall and the AET (Mei, et al., 2016c):

$$P = C_I P_o - E_a \tag{6.23}$$

where P_o is the actual precipitation magnitudes; C_I is a scalar to conceptualize vegetation interception; and E_a is the AET rates calculated by CREST.

We converted through-rainfall into surface and subsurface rainfall excess components, entering a surface and an interflow reservoir that we subjected to fast and relatively slow response. The surface process was intimately related to the fraction of impervious surface over the basin where the through-rainfall was converted to rainfall excess. We conveniently treated this as a uniform parameter, I_M, optimized through model calibration. For the subsurface process, the amount of runoff being generated was positively correlated to the soil wetness, *SM*, based on the variable infiltration curve adopted by CREST. Based on mass conservation, the total runoff coefficient is a summation of these component-wise runoff coefficients (Mei, et al., 2016c):

$$W = I_M + \frac{SM}{W_M} \tag{6.24}$$

where *SM* is the space-time variant soil moisture (mm). Scalar I_M and W_M are the imperviousness and maximum water storage (mm) parameter optimized by the hydrologic model.

The runoff routing process of CREST is comprised by the subgrid-scale and grid-to-grid routing. The subgrid-scale routing is modeled by a surface and an interflow linear reservoir for the surface and subsurface rainfall excess, respectively. Mei et al. (2016c) show a method for calculating an equivalent linear reservoir for the total rainfall excess by combining the two reservoir parameters based on the weights of catchment-average storm rainfall excess,

$$t_h = \psi_S \, ln(k_S^{-1}) + \psi_I \, ln(k_I^{-1}) \tag{6.25}$$

where k_S and k_I are the linear reservoir discharge parameters for the surface and interflow reservoir. The natural log of the reciprocal of these parameters is the response times of the linear reservoirs. Parameters ψ_S and ψ_I are the weights of catchment-average storm rainfall excess, defined as the cumulative amount of a rainfall excess component over the amount of total rainfall excess. That means the sum of ψ_S and ψ_I goes to 1. Eq.(6.25) states that the hillslope response time for the total rainfall excess is a linear combination of

response time of the components. Under this definition, t_h is bounded by the range between the two response times.

The grid-to-grid routing for the surface and subsurface rainfall excess are separated by different concentration times, measuring the time consumptions for the rainfall excess components to flow from the current grid to the next downstream grid. For each component, a sum of concentration times along the flow paths for the grid cells yields the network routing time. To calculate the equivalent network routing time for the total rainfall excess, the same method is adopted to linearly combine the component network travel time (Mei, et al., 2016c):

$$\theta_n = \psi_S \sum_L \frac{l}{K_X s^\beta} + \frac{\psi_I}{\alpha} \sum_L \frac{l}{K_X s^\beta} \tag{6.26}$$

where l, s and K_X are the length of the flow path from a grid to its adjacent downstream grid, the slope, and the runoff velocity coefficient at that grid, respectively; L represents the space of the flow path from a grid-cell to the catchment outlet; β is the flow speed exponent; and α (smaller than 1) is a coefficient to distinguish the network routing time for the surface and subsurface rainfall excess component. By dividing α, the network routing time for the subsurface component (the second term) is always larger than the surface one. Eq.(6.26) ensures θ_n does not go above/below the quickest/slowest responses.

6.4 Results

6.4.1 Error in Amount of Rainfall

To attain overall understandings of the discrepancies between each of the satellite precipitation product and the STIV reference rainfall data, the error in rainfall intensity normalized with the reference-derived rainfall intensity, $\Delta[P]_{at}/[P]_{at}$, for all of the rainfall-runoff events over the three basins are plotted in Figure 6.3. Basin-wise speaking, it can be seen that the patterns of $\Delta[P]_{at}/[P]_{at}$ distributions are fairly similar. Overall, most of the satellite precipitation products tend to underestimate the cumulative rainfall depth of

the events, especially the near-real-time products. The gauge-adjusted products show median of error much closer to zero for all the basins. The higher resolution CMORPH and PERSIANN are characterized by median slightly closer to zero compared to their coarser resolution counterparts. Among all the 0.25°/3-hourly products, the gauge-adjusted CMORPH and GSMaP are characterized by medians of $\Delta[P]_{at}/[P]_{at}$ closer to zero than the others. For the near-real-time TMPA products, the climate correction algorithm is able to reduce the error in the estimation of event rainfall intensity from the real-time 3B42.

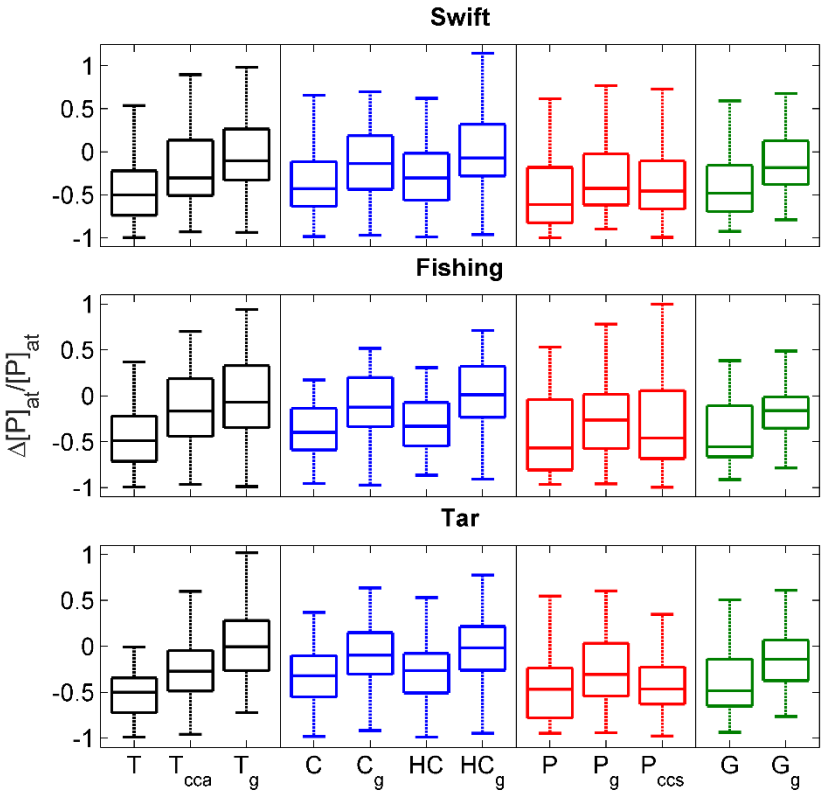

Figure 6.3. Error in cumulative volume of event rainfall for all the basin scales and products.

6.4.2 Error in Amount of Rainfall Excess

The error in amount of rainfall excess is normalized with respect to the radar rainfall-derived rainfall excess and the quantity $\Delta[R]_{at}/[R]_{at}$, as illustrated in Figure 6.4. The distributions of $\Delta[R]_{at}/[R]_{at}$ share quite similar patterns with those of $\Delta[P]_{at}/[P]_{at}$ in Figure 6.3. Most of the satellite product–driven flow simulations underestimate the STIV-driven ones, with negative medians of the $\Delta[R]_{at}/[R]_{at}$ quantity.

$\Delta[R]_{at}/[R]_{at}$ derived from the gauge-adjusted products are characterized by medians closer to zero than the corresponding near-real-time ones. The magnitude of $\Delta[R]_{at}/[R]_{at}$ derived from the gauge-adjusted 3B42 is the smallest among the gauge-adjusted products. Among all the near-real-time products, the T_{cca} product outperforms the others with regard to the relative error in amount of rainfall excess for the three basins. The high resolution products (HC, HC_g, and P_{ccs}) outperform the corresponding coarse resolution ones (C, C_g, and P) in terms of the medians of $\Delta[R]_{at}/[R]_{at}$. Altogether, these observations demonstrate the importance of higher resolution estimates and the inclusion of gauge-adjustment to the accuracy of satellite-driven flow simulations.

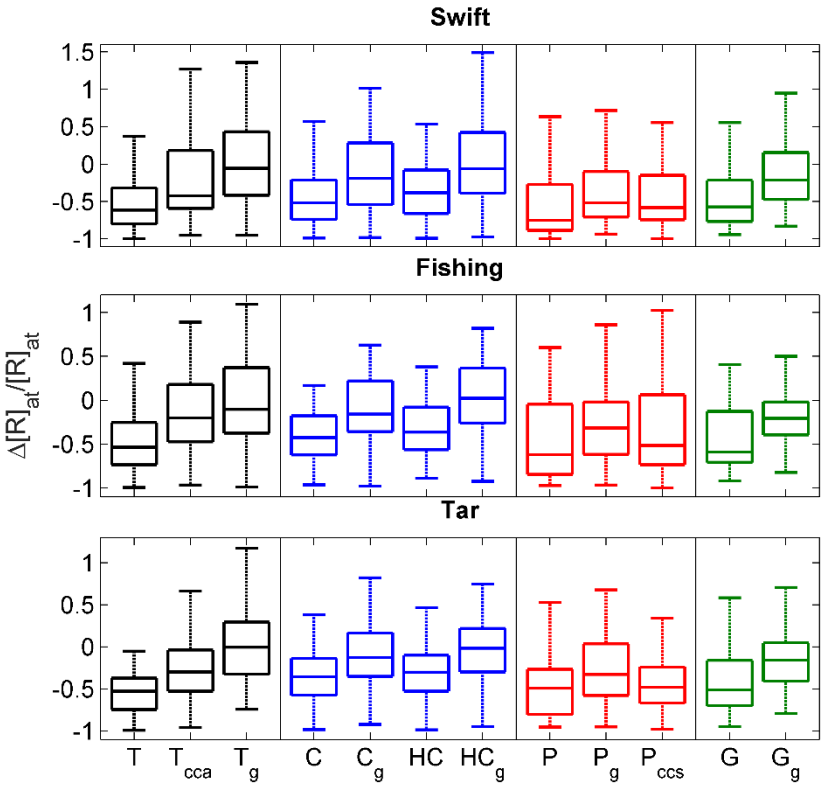

Figure 6.4. Same as in Figure 6.3 but for the amount of rainfall excess.

To provide an understanding of the distribution of total error in the different space-time catchment flood response processes, we illustrate the magnitudes of the terms in Eq.(6.14), using the HC_g product as an example in Figure 6.5 (the error distribution of rainfall excess generation for the other products are provided in Figure S1 of the supplemental material). Note that the terms in Eq.(6.14) have been normalized

by $[R]_{at}$, derived from the radar rainfall, to provide the relative magnitudes. Underestimation of the amount of rainfall excess prevails for most of the events, as indicated by the negative medians for nearly all of the terms. The figure also shows $\Delta R1$ is the main contributor to the total error in amount of rainfall excess, indicated by the widest value ranges for all basins. This is to be anticipated, since $R1$ is the main contributor to $[R]_{at}$ under the smooth topographical setup of the study area, as demonstrated by Mei et al. (2016c). The value ranges of $\Delta R2$ also demonstrate that the error in temporal information is more significant than the errors in spatial ($\Delta R3$) and space-time information ($\Delta R4$). Overall, the systematic component of error outweighs the error in the space-time covariance and movement in the smooth topography of the study area. A basin-wise comparison indicates the variations of the error terms are generally highest for the smallest basin and narrowest for the largest one. This is explained by the decrease in magnitude of the respective rainfall excess components (terms $R1$, $R2$, $R3$, and $R4$), as the increase in basin areas points to the dampening effect of basin area on the magnitudes and variability of precipitation (Mei, et al., 2016c). Another observation on the basin scale is that the magnitudes of $\Delta R2$, $\Delta R3$, and $\Delta R4$ are closest to $\Delta R1$ for the smallest basin and farthest away for the largest. This implies a decrease in the relative importance of the space and time information with the increase in basin area.

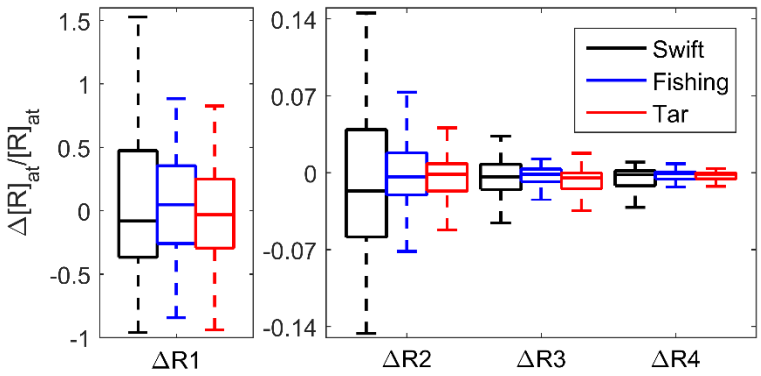

Figure 6.5. Magnitudes of error terms in Eq.(6.14) derived from the HC_g product.

6.4.3 Error in Expectation of Catchment Response Time

The error in expectation of catchment response time (normalized by the radar-derived expected catchment response time) for the twelve satellite precipitation products is plotted in Figure 6.6. Overall, the distributions of $\Delta E(\Phi)/E(\Phi)$ for all the products are symmetrical with respect to zero, indicating no preferences for either advance or delay in arrival of the flow event mass center estimated by the products. The gauge-adjusted GSMaP product is characterized by medians of $\Delta E(\Phi)/E(\Phi)$ closest to zero and the narrowest value ranges of all the products. This implies the G_g product provides generally the most consistent estimates on timing of the flow events. By comparing values of $\Delta E(\Phi)/E(\Phi)$ derived by the gauge-adjusted products and high resolution products, we concluded that the benefits of finer space-time resolution and inclusion of rain gauge information are not obvious. Mei et al. (2016b) similarly conclude that the gauge-adjusted products cannot adjust properties related to the shape of the hydrograph. In addition, comparison of $\Delta E(\Phi)/E(\Phi)$ for the three basins reveals the variability of $\Delta E(\Phi)/E(\Phi)$, decreasing from the smallest to the largest basin. This is again attributed to the dampening effect of rainfall excess.

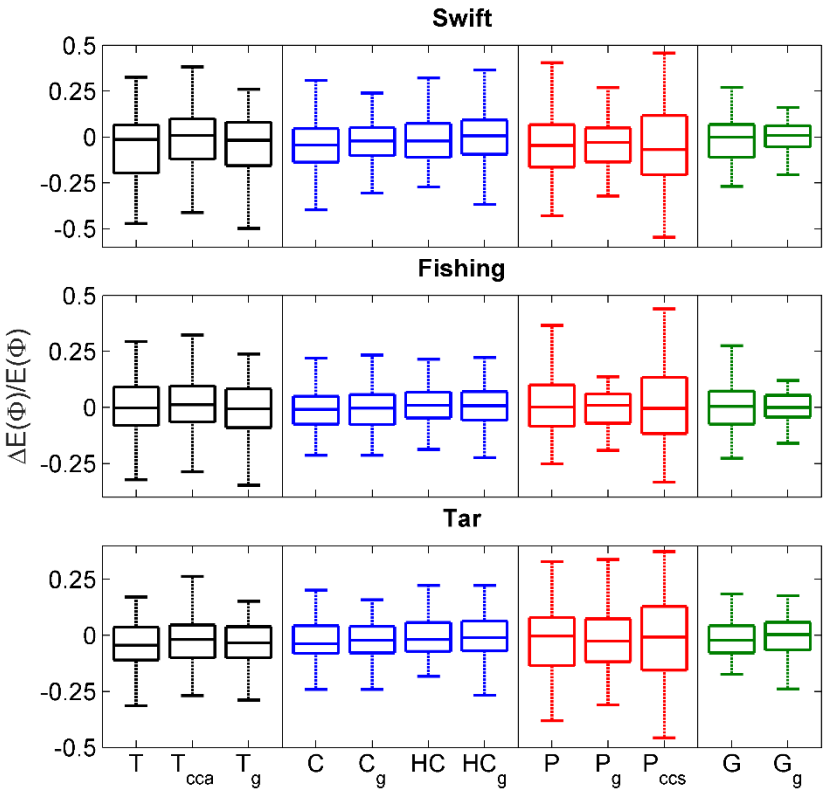

Figure 6.6. Same as in Figure 6.3 but for the expectation of catchment response time.

A focus evaluation on magnitudes of the normalized error terms in Eq.(6.16) for the HC_g product is rendered in Figure 6.7. Note that *ΔE1* (not shown) is always zero, and, thus, $\Delta E(T_r)$ is contributed by *ΔE2* solely, and $\Delta E(T_h)$ is the same as *ΔE3*. The distributions of error in the different space-time terms for the rest of the products are provided in Figure S2 of the supplemental materials, which shows the medians of the terms very close to zero, consistent with the observations from Figure 6.6. A comparison of $\Delta E(T_r)$, $\Delta E(T_h)$, and $\Delta E(T_n)$ indicates that the contribution to the error in expectation of catchment response time from the rainfall excess generation stage is larger than that from the two runoff routing stages. The error in expectation of hillslope routing time is low in magnitude because of the space-time constant hillslope response time, θ_h, employed in this study. In all, the errors in temporal (*ΔE2*) and spatial covariance (*ΔE5*), especially temporal, are the main contributors to $\Delta E(\Phi)$; the errors in mean of hillslope response time (*ΔE3*) and channel routing time (*ΔE4*) are secondary. No clear basin-scale dependencies are illustrated for the magnitude of either $\Delta E(T_r)$ or $\Delta E(T_n)$, except for *ΔE3* and *ΔE4*.

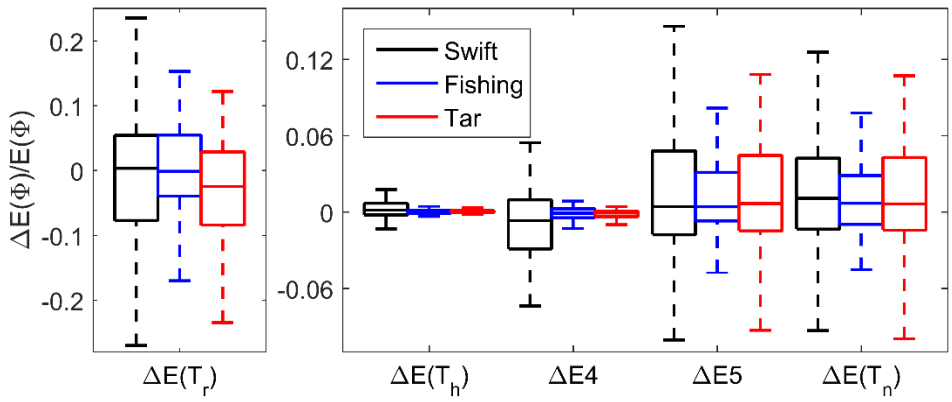

Figure 6.7. Same as in Figure 6.5 but for the expectation of catchment response time.

6.4.4 Error in Variance of Catchment Response Time

The normalized error in variance of catchment response time, $\Delta var(\Phi)/var(\Phi)$, is evaluated in Figure 6.8. The satellite-derived $var(\Phi)$ slightly underestimates the radar-derived, as indicated by the negative medians. Since $var(\Phi)$ is a measure of dispersion of the hydrograph, this observation implies the reference

flow time series are less peaked than the satellite-derived ones. The HC_g and G_g products generally outperform the others in estimating the variance of catchment response time. In the case of the Swift catchment, nearly all the gauge-adjusted products are characterized by medians of $\Delta var(\Phi)/var(\Phi)$ closer to zero. But this is less pronounced for the other two catchments. This again refers to the relatively weak effects exerted by satellite precipitation gauge adjustment on the shape of the hydrograph (Mei, et al., 2016b). The benefit of higher resolution is not clear in terms of estimating the shape of hydrograph in comparisons of the high resolution products with their coarser resolution counterparts.

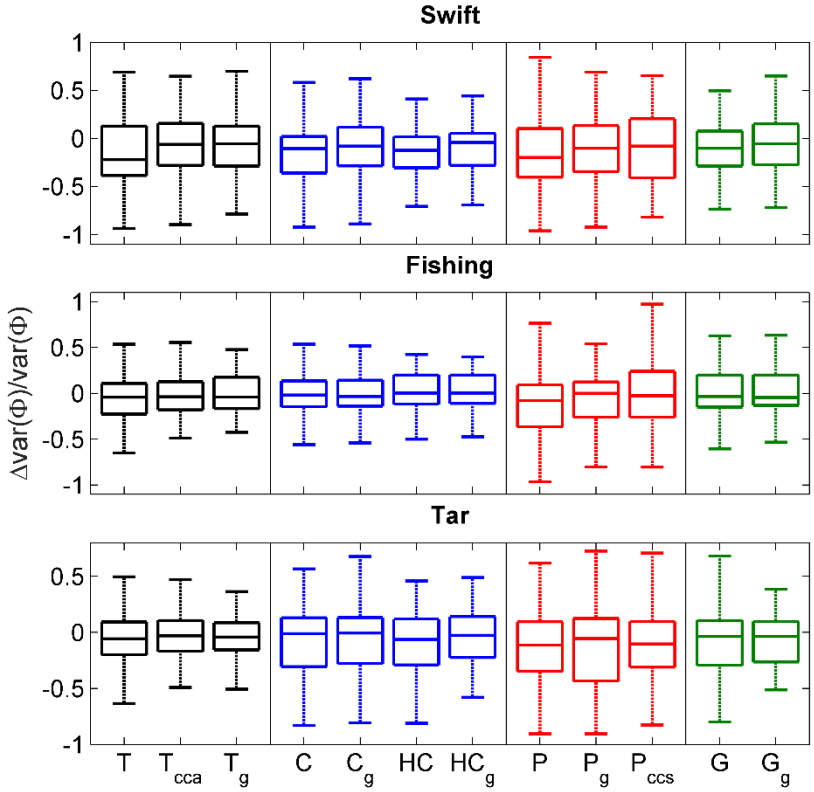

Figure 6.8. Same as in Figure 6.3 but for the variance of catchment response time.

The magnitudes of the different error terms in Eq.(6.18) derived from the HC_g product are illustrated as boxplots in Figure 6.9 (results for the other products are provided in Figure S3 of the supplemental material). Note that $\Delta v1$ is not shown because it is always zero, and, therefore, $\Delta var(T_r)$ equals $\Delta v2$; $\Delta v3$ is $\Delta var(T_h)$. Overall, patterns of the distribution of the terms suggest no obvious basin-scale dependency. Value ranges of $\Delta var(T_r)$ are about five times and two times those of $\Delta var(T_n)$ and $\Delta cov(T_r,T_n)$, respectively,

pointing to the fact that most of the error in shape of the hydrograph is contributed by the rainfall excess generation stage. It is interesting to note that the movement of rainfall excess with respect to the catchment channel network accounts for a considerable amount of error contribution. Magnitudes for $\Delta var(T_h)$ are nearly negligible because of the constant hillslope response time. To sum up, these observations indicate $\Delta var(\Phi)$ is mainly caused by the error in temporal variations of rainfall excess ($\Delta v2$ and Δc), while contributions from the spatial variations ($\Delta v3$, $\Delta v4$, and $\Delta v5$) are less relevant. The relatively low contribution from spatial information is again ascribed to the smooth topographical setup of the study area (Mei, et al., 2016c).

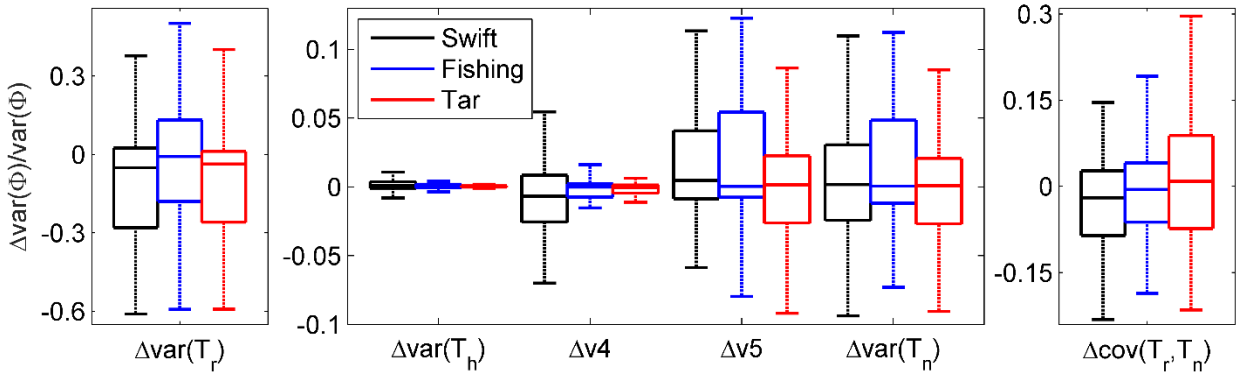

Figure 6.9. Same as in Figure 6.5 but for the variance of catchment response time.

6.4.5 Sensitivity to Error in Hydrograph Properties

The three error quantities calculated by the framework, $\Delta[R]_{at}$, $\Delta E(\Phi)$, and $\Delta var(\Phi)$, are used to estimate the error in hydrograph properties for tests of sensitivity. Figure 6.10 renders scatter plots between the normalized errors for the different types of satellite precipitation products, with corresponding statistics reported in Table 6.3. The twelve satellite products are grouped by the involvement of gauge information and resolution (equal to or less than 0.25°). Overall, the different types of products do not show distinguished clusters on the three properties and basin scales.

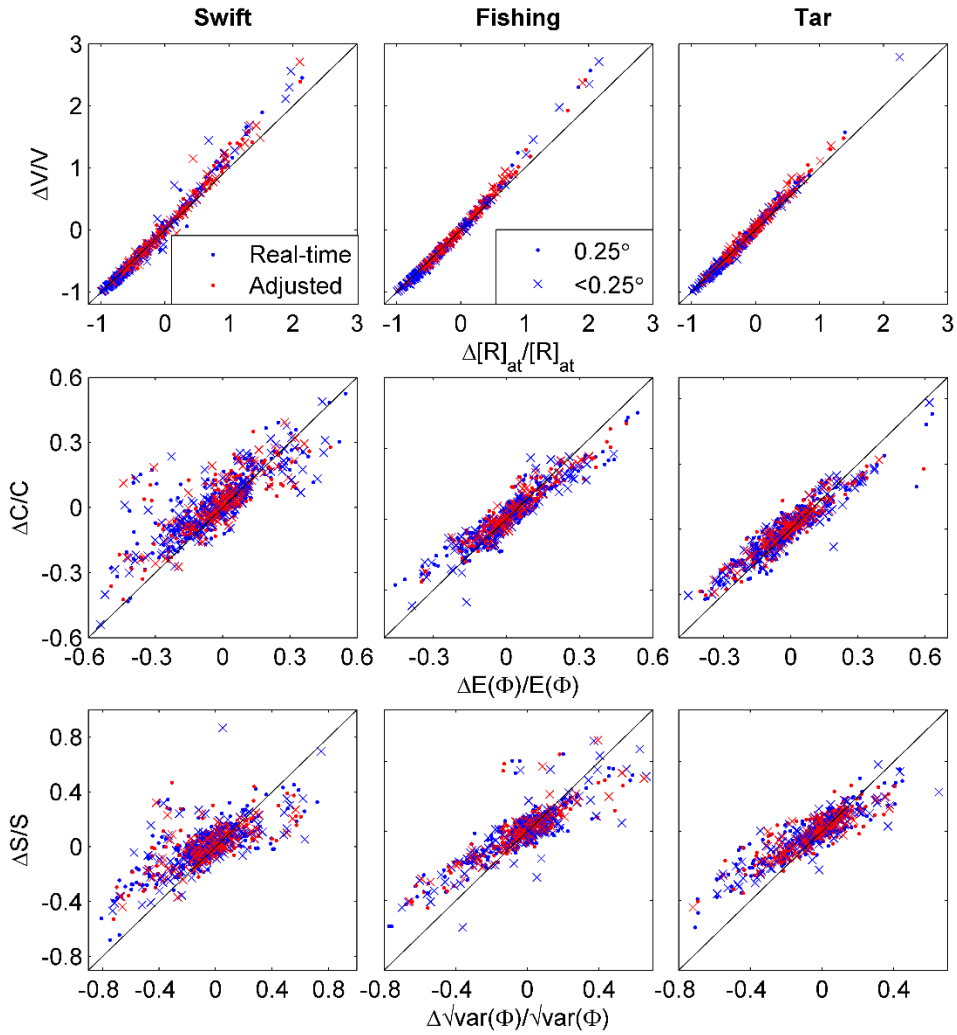

Figure 6.10. Sensitivity tests of the framework derived error quantities vs. the error in hydrograph properties.

Table 6.3. Sensitivity of the error in catchment flood response and the error in hydrograph properties.

Error Quantity	Product Type	ME (%)			CRMS (%)		
		Swift	Fishing	Tar	Swift	Fishing	Tar
Volume	Real-time/0.25°	-0.4	-0.1	-0.1	8.2	8.4	4.1
	Adjusted/0.25°	-2.3	-1.4	-2.2	8.8	7.1	5.6
	Real-time/<0.25°	-1.6	0.5	0.1	16.6	8.2	6.0
	Adjusted/<0.25°	-3.5	-1.7	-2.6	12.0	7.2	5.7
Centroid	Real-time/0.25°	-5.1	-0.7	-1.2	10.7	6.1	5.9
	Adjusted/0.25°	-3.7	-0.9	-1.6	10.5	4.9	5.6
	Real-time/<0.25°	-4.3	-0.2	-0.8	10.7	6.4	5.7

	Adjusted/<0.25°	-3.4	-1.0	-1.2	9.9	4.1	4.3
Dispersion	Real-time/0.25°	-7.6	-3.8	-4.1	17.7	11.6	10.1
	Adjusted/0.25°	-6.1	-3.1	-4.0	17.4	11.2	10.2
	Real-time/<0.25°	-6.8	-1.6	-3.4	17.9	12.0	10.4
	Adjusted/<0.25°	-4.9	-1.7	-3.1	15.4	10.0	8.4

The first row of Figure 6.10 shows a fairly strong linear relationship following the one-to-one line between the normalized error in amount of rainfall excess, $\Delta[R]_{at}/[R]_{at}$, and that of the cumulative flow volume, $\Delta V/V$. This is confirmed by the low magnitudes of mean error (*ME*, less than 4%) and the centered root mean square (*CRMS*, less than 17%) shown in Table 6.3. The table also reveals that the framework error quantity $\Delta[R]_{at}$ slightly underestimates ΔV calculated from the hydrological model; the random component of error outweighs the systematic one by more than two times. The gauge-adjusted and high resolution products demonstrate higher magnitudes of systematic error in estimating $\Delta V/V$. The random error of the $\Delta V/V$ estimations produce lower values for the gauge-adjusted products and lower values for the high resolution ones. Together, these observations indicate that the framework-derived $\Delta[R]_{at}$ is more sensitive to numerical model–derived ΔV when using the unadjusted coarse resolution products (T, T_{cca}, C, P) as input rainfall. Basin-wise comparison shows the magnitudes of *CRMS* decreasing with basin scale.

The correlation between normalized error in expectation of catchment response time and normalized error in hydrograph centroid is illustrated in the second row of Figure 6.10. The systematic and random error metrics (*ME* and *CRMS*) are listed in Table 6.3 for the three basins. Overall, the correlation is obviously lower than that of rainfall excess, but it still follows the one-to-one line. The Fishing and Tar basin cases show higher correlation than the Swift basin, confirmed by the lower *ME* and *CRMS* in the table. Values of *ME* are all negative, indicating underestimations of ΔC by $\Delta E(\Phi)$; the magnitudes of *ME* are lower than those of *CRMS*, indicating that the random error is the main source of uncertainty in the estimation of ΔC. Product-wise, the high resolution and gauge-adjusted products are characterized by smaller values of *ME* and *CRMS* in most of the cases. This means $\Delta E(\Phi)$ is more sensitive to ΔC for HC_g and G_g products.

The last row of Figure 6.10 and Table 6.3 illustrate the sensitivity test on $\Delta\sqrt{var(\Phi)}/\sqrt{var(\Phi)}$ to $\Delta S/S$. The plots show correlation but deviate from the one-to-one line. The linear relationship is more pronounced for the cases of the Fishing and Tar basins, as revealed by the lower magnitudes of *ME* and *CRMS* in the table. Values of *ME* are all negative, with smaller magnitudes than those of *CRMS*. This implies ΔS is underestimated by $\Delta\sqrt{var(\Phi)}$, and the random component of error is the main issue for the estimations. Investigation of the effect of gauge adjustment and product resolution reveals the products with gauge adjustment and with resolutions higher than 0.25° are characterized by lower magnitudes of *ME* and *CRMS*. This suggests better estimation of ΔS by $\Delta\sqrt{var(\Phi)}$ in the HC_g and G_g cases.

6.5 Conclusions

In this study, we presented the use of a hydrologic analytical framework to access the error propagation process of satellite precipitation through the rainfall-runoff translation. This allows to decompose the error in hydrograph properties into terms representing the different space-time interactions among rainfall, runoff generation and routing. Specifically, by using the framework the error in three hydrograph properties (that is, cumulative volume, centroid, and dispersion of the hydrograph) are estimated by the error in three corresponding framework quantities (i.e. amount of rainfall excess, and expectation and variance of catchment response time). Error in the three framework quantities are broken into terms reflecting the error related to the mean, the spatial and temporal variation and the movement of rainfall/rainfall excess. The framework is implemented by the simulations of 160 rainfall-runoff events derived from a distributed hydrologic model driven by twelve satellite precipitation products and the STIV radar-based product as reference.

We found that the satellite precipitation products underestimate the amount of rainfall and rainfall excess, with magnitudes decreasing from the smallest to the largest basin. The gauge-adjusted and high-resolution products yield lower degree of error than the corresponding near-real-time and coarse resolution ones. The error in mean magnitudes of rainfall and runoff coefficient is the main contributor to the total

error in the amount of rainfall excess. Error related to the temporal and spatial correlation between rainfall and runoff coefficient and the movement of rainfall are of secondary importance. The variability of these error terms diminishes with the increase in basin scale, while terms related to the time and space correlation are more important in the smaller basin cases.

The magnitudes of error in expectation of catchment response time is low and no preference of either delay or advance in detection of event centroid is found. Gauge adjustment and high resolution reveal no clear effects on the estimation of event timing. Additionally, the error arising from the rainfall excess generation stage and the runoff routing stage (hillslope plus channel routing) share comparable magnitudes. Error due to the differences in temporal and spatial correlation of rainfall excess and the holding times maintain significant contributions to the total error in expectation of catchment response time. Error in mean values of hillslope and channel routing time is relatively minor in the context of total contributions.

The satellite-derived variance of catchment response time slightly underestimates the reference-derived one. The gauge-adjusted products are not always characterized by lower degrees of discrepancy. Same goes to the high resolution products. The rainfall excess generation stage contributes a larger amount of error to the variance of catchment response time than the runoff routing stage and the movement of rainfall excess. The error terms related to the temporal variation of rainfall excess and the movement are the significant contributors to the total error in variance, while the term of the spatial variation is weaker.

Results of the sensitivity tests suggest strong correlation for the estimations on the three hydrograph properties, especially for the rainfall excess amount vs. cumulative flow volume estimation, which follows the one-to-one relationship. Slight systematic underestimation is common to the estimations on the hydrograph properties, while the random components of error outweigh the systematic components in terms of magnitude. Product-wise speaking, the systematic and random error of the rainfall excess-to-flow volume estimation are in lower magnitude for the cases of the unadjusted coarse resolution products. For the other two sensitivity tests on the shape-related parameters, the cases of adjustment and high resolution products yield higher degree of consistencies. For the three basin scales, the lowest systematic (random) error are retrieved from the estimations for the Fishing (Tar) basin.

We acknowledge certain limitations of the implementation of the hydrologic analytical framework, as well as its use in analyzing the error propagation of precipitation in this study. Our results revealed that the systematic error in magnitudes of rainfall and runoff generation is the main contributor to the error in amount of rainfall excess, while the error due to the space and time correlation and movement are secondary. This finding may not be generalizable to other hydrological regimes, given that the rainfall-runoff events of this study ranged between moderate to high flows with no orographic effects on the triggering storm. We believe the error in spatial and temporal variation of rainfall, runoff generation and routing could be more important for flash flood–scale events and catchments, with clear orographic effects on precipitation. In fact, our results indicate that the weights of the space and time correlation increases as the basin scale decreases. Future studies should involve more basin scales and categorization by flood types. This can help demonstrate the changes in relative importance of the different error terms as responses to the spatial and temporal scales.

The error propagation analysis in this study is built upon a hydrological analytical framework, sharing common variables—runoff coefficient and runoff routing time—that require the use of a distributed hydrological model to derive (Mei, et al., 2016c). This means the calculation of these variables could vary across models, or be unavailable in certain models. To circumvent this issue, we suggest use of independent information, such as that obtained from remote sensing, to retrieve the variables. For instance, runoff coefficient may be retrieved solely based on the soil moisture stage (Massari, et al., 2014; Penna, et al., 2011), which gives a different form of the current Eq.(6.14):

$$\Delta[R]_{at} = \underbrace{\Delta[P]_{at}[W]_{at}}_{\Delta\hat{R}1} + \underbrace{\{\Delta[P]_a, [W]_a\}_t}_{\Delta\hat{R}2} + \underbrace{\{\Delta[P]_t, [W]_t\}_a}_{\Delta\hat{R}3} + \underbrace{[\{\Delta P - \Delta[P]_t, W - [W]_t\}_a]_t}_{\Delta\hat{R}4} \quad (6.27)$$

Compared to Eq.(6.14), Eq.(6.27) excludes the error in runoff coefficient because the derivation of runoff coefficient is no longer based on rainfall. This allows revealing the effects of error in space-time dynamic of rainfall fields. Alternatively, the runoff routing-related parameters could be estimated based on the geomorphologic properties of catchments (Shen, et al., 2017). In this case, the hillslope and channel routing time for different rainfall fields are the same, with the current Eq.(6.16) and (6.18) reduced to simpler forms:

$$\Delta E(\Phi) = \underbrace{\hat{E}2 - E2}_{\Delta E2} + \underbrace{\hat{E}5 - E5}_{\Delta E5} \tag{6.28}$$

$$\Delta var(\Phi) = \underbrace{\hat{v}2 - v2}_{\Delta v2} + \underbrace{\hat{v}5 - v5}_{\Delta v5} + \underbrace{\hat{c} - c}_{\Delta c} \tag{6.29}$$

The error in mean and variance of the hillslope and channel routing time (that is, *ΔE3*, *ΔE4*, *Δv3* and *Δv4*) are vanished because the holding times for hillslope and channel routing are not related to the different rainfall excess any more. Future studies could investigate those aspects based on data from different hydro-climatic regimes.

Chapter 7 Conclusions and Future Research

7.1 Conclusions

In this study, I provided assessments on the hydrologic potential of different satellite precipitation products over two study areas, namely the Upper Adige river basin and Tar River basin, representing distinct geomorphology and climate conditions. To investigate factors that affect the accuracy of the satellite products, a direct comparison to the ground-truth precipitation over the mountainous Upper Adige river basin was rendered in Chapter 2. Long-term and event-based error propagation studies using a numerical hydrologic model were conducted in Chapter 3 and Chapter 4 to reveal the properties of error translation through the rainfall-to-runoff process over the same area. In addition, a hydrologic analytical framework was proposed in Chapter 5 and was later applied to study the error propagation of satellite precipitation in Chapter 6. Advantage of using the analytical framework to study error propagation is it can decompose the error in hydrograph properties into different error terms related to the space-time interactions among rainfall, runoff generation and routing. Demonstration studies for the analytical framework were conducted on flood events occurred over the Tar River basin.

7.1.1 Numerical Investigation of Satellite Precipitation Error Propagation

Error in satellite precipitation estimation was propagated to the flow simulations through the rainfall-to-runoff processes. Properties of the error and its propagation depend on a range of factors, including the severity of rainfall and flow rate, the basin scale and elevation, the properties of event, the seasonality and the precipitation estimation algorithm. The principal conclusions from the numerical investigation presented in this work can be summarized as follows:

- The systematic error in satellite precipitation products and their corresponding flow simulations reveal higher degree of underestimation for the extreme rain and flow rates and basins with lower mean elevations over the mountainous Eastern Alps region.

- The random component of error and correlation coefficient in precipitation and flow estimations indicate higher degree of consistencies (smaller mean magnitudes and lower degree of variability) for the warm season (May – Aug) and medium to large-scale (greater than 1000 km^2) estimations.
- The PERSIANN and CMORPH products tend to underestimate rainfall and flow rate over the mountainous basins while the TMPA products show slight overestimations.
- The random error in the event-based hyetograph and hydrograph of the rain flood are characterized by higher magnitudes than those of the flash flood. The random error dampening effect tends to be more linear for the flash flood events, which are characterized by higher runoff coefficient than the rain flood.
- The shape-related parameters (mass center and degree of dispersion) of the event rainfall and flow are better captured by the satellite products compared to the volume of rainfall and flow. The error in shape-related parameters are dampened through the rainfall-to-runoff processes while the error in volumetric parameter remains unchanged.
- The gauge-adjustments introduced to the different satellite products can reduce the volumetric error but have few advantages in estimations of the shape-related parameters and cannot reduce the random error in rainfall and flow simulations.

7.1.2 Assessing the Error Propagation by a Hydrologic Analytical Framework

A hydrologic analytical framework was developed to quantify the catchment flood response processes and subsequently used to analyze the error propagation of satellite precipitation products. Findings revealed the relative importance of the different space-time processes in terms of their contribution to the properties of flood response and the error in flood response. Main findings are summarized as:

- Among the different space-time processes, main contributor to the runoff generation is the net magnitudes of rainfall and runoff coefficient, while the space-time variation and movement effects of rainfall are insignificant. The subsurface runoff component is the main contributor to the total runoff in the Tar River basin.

- Delay due to the runoff generation and routing stages are equally important. The duration of storm and net magnitude of routing times are the main contributors to the delay in flood response. The total catchment response time is closer to the response time of the subsurface runoff component, but the difference in response time between the two components is narrowing from small to large catchment area.
- The shape (degree of dispersion) of the event flow hydrograph is controlled mainly by the duration of storm and variance of the runoff routing times. Contributions from the space-time variation and movement of the runoff generation are insignificant. The inter-component variability is negligible compared to the intra-component variability in controlling the shape of the hydrograph.
- The simulation-based sensitivity tests suggest that the framework is characterized by relatively low random errors in estimating the flood characteristics while the systematic underestimation in event centroid and spreadness parameters are notable. The observations-based sensitivity tests are characterized by larger random errors compared to the simulation-based ones.
- Error in mean magnitudes of rainfall and runoff coefficient is the main sources of error in runoff generation, while error related to the temporal and spatial variation and movement of rainfall are of minor importance. As the basin scale increases, magnitudes of all the error terms and the relative importance of terms related to the space-time variation decrease.
- The error in hydrograph timing is low and is neither under- nor overestimated by the satellite precipitation. The runoff generation stage and routing stage are comparable in terms of error contributions. The error terms related to the space-time interactions of runoff generation and holding times are significant contributors to the timing error of the hydrograph.
- Slight underestimations on the degree of dispersion are revealed for the satellite precipitation products. Error in the estimations of hydrograph shape is mainly originating from the runoff generation stage. The difference in temporal variation of runoff generation and the movement of its mass center are the major sources of error in hydrograph shape estimations.

- Gauge-adjusted and high resolution products yield higher degree of consistency on the runoff generation estimation, but show no improvements on the estimations of the timing and shape related parameters.
- Results of the sensitivity tests suggest strong correlation for the estimations of the three hydrograph properties with the random error outweigh the systematic ones.

7.2 Future Research

The numerical investigations of satellite-precipitation error-propagation were conducted at a mountainous area (in the Eastern Italian Alps) exhibiting perennial snow cover and the occurrence of mixed-phase precipitation. This introduced some degree of biases to the TRMM-era satellite precipitation products since none of them has explicit estimations on the solid-phase precipitation. Future investigations should focus on the integration of new satellite precipitation products from the GPM-era. Such example is the IMERG product (Huffman, et al. 2015) available since the launch of GPM satellite on February 2014. This novel algorithm is expected to overcome some issues in precipitation estimation encountered in the TRMM-era precipitation products (e.g. coverage of sensors, quantification of snow) that will provide estimations with higher accuracy at finer resolution, which could potentially advance flood-modeling applications worldwide. In addition, we recognize the limited sample (in terms of number and flood types) of flood events and study areas investigated. Future research should focus on evaluating the use of satellite precipitation in flood modeling based on more comprehensive flood event records, representing wider ranges of flood typology of different hydro-climatic and geomorphologic regime.

The hydrologic analytical framework proposed in this study separate the event flow into a fast and a relative slow response component representing the heterogeneity of the vertical layers of catchment. Future studies should draw on the strengths of this framework to investigate the flood response of urbanized catchments. This provides an analytical way to assess the correlation between the degree of urbanization and the rapidness of flood response. In addition, the implementation of the hydrologic analytical framework requires the strengths of numerical hydrologic models to derive the variables (i.e. rainfall, runoff coefficient

and runoff routing time), which may lead to model-specific results on catchment flood response. The applications of these variables estimated from independent sources (e.g. in-situ measurements, remote sensing, reanalysis data) can potentially circumvent the model-dependent issue and develop the framework into an analytical model for event flow simulation. This is extremely beneficial since the use of an analytical model can reduce the computational workload compared to the traditional numerical models.

Appendix

I. Catchment-average storm rainfall excess

The catchment-average storm rainfall excess is calculated by integrating either $[R]_a$ over the storm period or $[R]_t$ over the catchment area. This means

$$[R]_{at} = \begin{cases} \frac{1}{|T_P|}\int_{T_P} [R]_a\, dt = [P]_{at}\sum_{i=1}^{N}[W_i]_{at} + \left\{[P]_a, \sum_{i=1}^{N}[W_i]_a\right\}_t + \left[\left\{P, \sum_{i=1}^{N} W_i\right\}_a\right]_t \\ \frac{1}{|A|}\int_{A} [R]_t\, da = [P]_{at}\sum_{i=1}^{N}[W_i]_{at} + \left\{[P]_t, \sum_{i=1}^{N}[W_i]_t\right\}_a + \left[\left\{P, \sum_{i=1}^{N} W_i\right\}_t\right]_a \end{cases}$$

The last term of the second equation can be rewritten as

$$\left[\left\{P, \sum_{i=1}^{N} W_i\right\}_t\right]_a = \frac{1}{|A|}\int_A \frac{1}{|T_P|}\int_{T_P} (P - [P]_t)\left(\sum_{i=1}^{N} W_i - \sum_{i=1}^{N}[W_i]_t\right) dt\, da$$

where

$$P^* = P - [P]_t \quad \& \quad W^* = \sum_{i=1}^{N} W_i - \sum_{i=1}^{N}[W_i]_t$$

the equation becomes

$$\frac{1}{|A|}\int_A \frac{1}{|T_P|}\int_{T_P} P^*W^*\, dt\, da = \frac{1}{|T_P|}\int_{T_P}\frac{1}{|A|}\int_A P^*W^*\, da\, dt = [[P^*W^*]_a]_t$$

The second term of the first $[R]_{at}$ equation can be rewritten as

$$\left\{[P]_a, \sum_{i=1}^{N}[W_i]_a\right\}_t = \frac{1}{|T_P|}\int_{T_P}\left[\frac{1}{|A|}\int_A (P - [P]_t)\, da\right]\left[\frac{1}{|A|}\int_A \left(\sum_{i=1}^{N} W_i - \sum_{i=1}^{N}[W_i]_t\right) da\right] dt$$

$$= \frac{1}{|T_P|}\int_{T_P}\left(\frac{1}{|A|}\int_A P^*\, dt\right)\left(\frac{1}{|A|}\int_A W^*\, dt\right) da = [[P^*]_a[W^*]_a]_t$$

Note that

$$[[P^*W^*]_a]_t - [[P^*]_a[W^*]_a]_t = [[P^*W^*]_a - [P^*]_a[W^*]_a]_t = [\{P^*, W^*\}_a]_t$$

Therefore

$$\left[\left\{P, \sum_{i=1}^{N} W_i\right\}_a\right]_t - \left\{[P]_t, \sum_{i=1}^{N}[W_i]_t\right\}_a = \left[\left\{(P - [P]_t), \sum_{i=1}^{N}(W_i - [W_i]_t)\right\}_a\right]_t$$

Replacing $\left[\left\{P, \sum_{i=1}^{N} W_i\right\}_a\right]_t$ in the first equation of $[R]_{at}$, Eq.(5.10) is attained.

II. Expectation of holding times for a component

The rainfall excess generation time is modeled by the instantaneous time, T. T is a variable in time and follows a uniform distribution over the event period T_P. Therefore,

$$E_i(T_{r,i}) = \frac{1}{|T_P|}\int_{T_P}\frac{1}{|A|}\int_A (T \cdot f_{R_i}) da\, dt = \frac{1}{|T_P|}\int_{T_P}\frac{1}{|A|}\int_A \frac{T \cdot R_i}{[R_i]_{at}} da\, dt = \frac{1}{|T_P|}\int_{T_P}\frac{T \cdot [R_i]_a}{[R_i]_{at}} dt$$

$$= [T]_t + \frac{\{T, [R_i]_a\}_t}{[R_i]_{at}}$$

Since T follows a uniform distribution on T_P, the solution of $[T]_t$ is:

$$[T]_t = \int_{T_P} T \cdot f_{T_P}\, dT = \int_{T_P}\frac{T}{|T_P|} dT = \frac{|T_P|}{2}$$

The hillslope routing time is modeled by the response time, $\theta_{h,i}$, treated as a constant in space and time. Thus, write

$$E_i(T_{h,i}) = \frac{1}{|T_P|}\int_{T_P}\frac{1}{|A|}\int_A (\theta_{h,i} f_{R_i})da\,dt = \frac{1}{|T_P|}\int_{T_P}\frac{1}{|A|}\int_A \frac{\theta_{h,i}R_i}{[R_i]_{at}}da\,dt = [\theta_{h,i}]_{at}$$

Since $\theta_{h,i}$ is implemented by the response time of a linear reservoir, the solution of $[\theta_{h,i}]_{at}$ is given as:

$$[\theta_{h,i}]_{at} = \int_0^\infty \theta_{h,i} f_{t_{h,i}}\, d\theta_{h,i} = \int_0^\infty \frac{\theta_{h,i}}{t_{h,i}} e^{-\frac{\theta_{h,i}}{t_{h,i}}}\, d\theta_{h,i} = t_{h,i}$$

The channel routing time is modeled by a spatial variable network routing time, $\theta_{n,i}$, write

$$E_i(T_{n,i}) = \frac{1}{|T_P|}\int_{T_P}\frac{1}{|A|}\int_A (\theta_{n,i} f_{R_i})da\,dt = \frac{1}{|T_P|}\int_{T_P}\frac{1}{|A|}\int_A \frac{\theta_{n,i}R_i}{[R_i]_{at}}da\,dt = \frac{1}{|A|}\int_A \frac{\theta_{n,i}[R_i]_t}{[R_i]_{at}}da$$
$$= [\theta_{n,i}]_a + \frac{\{\theta_{n,i}, [R_i]_t\}_a}{[R_i]_{at}}$$

III. Expectation of holding times for the total rainfall excess

The total rainfall excess generation time is also represented by T. Thus, write

$$E(T_r) = \frac{1}{|T_P|}\int_{T_P}\frac{1}{|A|}\int_A (T \cdot f_R)\,da\,dt = \frac{1}{|T_P|}\int_{T_P}\frac{1}{|A|}\int_A \left(T \cdot \sum_i^N \psi_i f_{R_i}\right)da\,dt$$
$$= \sum_i^N \psi_i \frac{1}{|T_P|}\int_{T_P}\frac{1}{|A|}\int_A \frac{T \cdot R_i}{[R_i]_{at}}da\,dt = \sum_i^N \psi_i E_i(T_{r,i})$$

The hillslope routing time for the total flow is modeled by θ_h which is a function of $\theta_{h,i}$ (Eq.(5.21)). Write

$$E(T_h) = \frac{1}{|T_P|}\int_{T_P}\frac{1}{|A|}\int_A (\theta_h f_R)\,da\,dt = \frac{1}{|T_P|}\int_{T_P}\frac{1}{|A|}\int_A \left(\theta_h \sum_i^N \psi_i f_{R_i}\right)da\,dt$$
$$= \frac{1}{|T_P|}\int_{T_P}\frac{1}{|A|}\int_A \left(\sum_i^N \xi_{h,i}\theta_{h,i}\psi_i \frac{R_i}{[R_i]_{at}}\right)da\,dt = \sum_i^N \psi_i \xi_{h,i}\frac{1}{|T_P|}\int_{T_P}\frac{1}{|A|}\int_A \frac{\theta_{h,i}R_i}{[R_i]_{at}}da\,dt$$
$$= \sum_i^N \psi_i \xi_{h,i} E_i(T_{h,i})$$

For the case of channel routing time, replace $\theta_{h,i}$ by $\theta_{n,i}$, θ_h by θ_n and $\xi_{h,i}$ by $\xi_{n,i}$ in the equation, yield

$$E(T_n) = \sum_i^N \psi_i \xi_{n,i} E_i(T_{n,i})$$

IV. Variance of holding times for a component

For the variance of holding time, we first define $E_i(T_{r,i}^2)$, $E_i(T_{h,i}^2)$ and $E_i(T_{n,i}^2)$ as

$$E_i(T_{r,i}^2) = \frac{1}{|T_P|}\int_{T_P}\frac{1}{|A|}\int_A (T^2 f_{R_i})da\,dt = \frac{1}{|T_P|}\int_{T_P}\frac{1}{|A|}\int_A \frac{T^2 R_i}{[R_i]_{at}}da\,dt = [T^2]_t + \frac{\{T^2, [R_i]_a\}_t}{[R_i]_{at}}$$

$$E_i(T_{h,i}^2) = \frac{1}{|T_P|}\int_{T_P}\frac{1}{|A|}\int_A (\theta_{h,i}^2 f_{R_i})da\,dt = \frac{1}{|T_P|}\int_{T_P}\frac{1}{|A|}\int_A \frac{\theta_{h,i}^2 R_i}{[R_i]_{at}}da\,dt = [\theta_{h,i}^2]_{at}$$

$$E_i(T_{n,i}^2) = \frac{1}{|T_P|}\int_{T_P}\frac{1}{|A|}\int_A (\theta_{n,i}^2 f_{R_i})da\,dt = \frac{1}{|T_P|}\int_{T_P}\frac{1}{|A|}\int_A \frac{\theta_{n,i}^2 R_i}{[R_i]_{at}}da\,dt = [\theta_{n,i}^2]_a + \frac{\{\theta_{n,i}^2, [R_i]_t\}_a}{[R_i]_{at}}$$

The solution for $[T^2]$ and $[\theta_{h,i}^2]$ are provided as:

$$[T^2]_t = \int_{T_P} T^2 f_{T_P}\, dT = \int_{T_P} \frac{T^2}{|T_P|} dT = \frac{|T_P|^2}{3}$$

$$\left[\theta_{h,i}^2\right]_{at} = \int_0^\infty \theta_{h,i}^2 f_{t_{h,i}}\, d\theta_{h,i} = \int_0^\infty \frac{\theta_{h,i}^2}{t_{h,i}} e^{-\frac{\theta_{h,i}}{t_{h,i}}}\, d\theta_{h,i} = t_{h,i}^2$$

The variance of holding times for component *i* is then calculated as

$$var_i(T_{r,i}) = E_i(T_{r,i}^2) - \left[E_i(T_{r,i})\right]^2 = \frac{|T_P|^2}{12} + \frac{\{T^2, [R_i]_a\}_t - |T_P|\{T, [R_i]_a\}_t}{[R_i]_{at}} - \left(\frac{\{T, [R_i]_a\}_t}{[R_i]_{at}}\right)^2$$

$$var_i(T_{h,i}) = E_i(T_{h,i}^2) - \left[E_i(T_{h,i})\right]^2 = \theta_{h,i}^2$$

$$var_i(T_{n,i}) = E_i(T_{n,i}^2) - \left[E_i(T_{n,i})\right]^2 = \{\theta_{n,i}\}_a + \frac{\{\theta_{n,i}^2, [R_i]_t\}_a - 2[\theta_{n,i}]_a\{\theta_{n,i}, [R_i]_t\}_a}{[R_i]_{at}} - \left(\frac{\{\theta_{n,i}, [R_i]_t\}_a}{[R_i]_{at}}\right)^2$$

V. Variance of holding times for the total rainfall excess

For the case of *var(T_r)*, it is trivia to show

$$E(T_r^2) = \sum_i^N \psi_i E_i(T_{r,i}^2)$$

Thus

$$\begin{aligned} var(T_r) &= E(T_r^2) - [E(T_r)]^2 = \sum_i^N \psi_i E_i(T_{r,i}^2) - [E(T_r)]^2 \\ &= \sum_i^N \psi_i E_i(T_{r,i}^2) - \sum_i^N \psi_i \left[E_i(T_{r,i})\right]^2 + \sum_i^N \psi_i \left[E_i(T_{r,i})\right]^2 - 2[E(T_r)]^2 + [E(T_r)]^2 \\ &= \sum_i^N \psi_i \left\{E_i(T_{r,i}^2) - \left[E_i(T_{r,i})\right]^2\right\} + \sum_i^N \psi_i \left\{\left[E_i(T_{r,i})\right]^2 - 2E_i(T_{r,i})E(T_r) + [E(T_r)]^2\right\} \\ &= \sum_i^N \psi_i var_i(T_{r,i}) + \sum_i^N \psi_i \left[E_i(T_{r,i}) - E(T_r)\right]^2 \end{aligned}$$

For *var(T_h)*, we know the following

$$E(T_h^2) = \sum_i^N \psi_i \xi_i^2 E_i(T_{h,i}^2)$$

Use the property of variance, write

$$\begin{aligned} var(T_h) &= E(T_h^2) - [E(T_h)]^2 = \sum_i^N \psi_i \xi_{h,i}^2 E_i(T_{h,i}^2) - [E(T_h)]^2 \\ &= \sum_i^N \psi_i \xi_{h,i}^2 E_i(T_{h,i}^2) - \sum_i^N \psi_i \xi_{h,i}^2 \left[E_i(T_{h,i})\right]^2 + \sum_i^N \psi_i \xi_{h,i}^2 \left[E_i(T_{h,i})\right]^2 - 2[E(T_h)]^2 + [E(T_h)]^2 \\ &= \sum_i^N \psi_i \xi_{h,i}^2 \left\{E_i(T_{h,i}^2) - \left[E_i(T_{h,i})\right]^2\right\} + \sum_i^N \psi_i \left\{\left[\xi_{h,i} E_i(T_{h,i})\right]^2 - 2\xi_{h,i} E_i(T_{h,i})[E(T_h)] + [E(T_h)]^2\right\} \\ &= \sum_i^N \psi_i \xi_{h,i}^2 var_i(T_{h,i}) + \sum_i^N \psi_i \left[\xi_{h,i} E_i(T_{h,i}) - E(T_h)\right]^2 \end{aligned}$$

Note that $\xi_{h,i}\theta_{h,i}$ is θ_h and therefore the second term is zero.

Using a similar procedure, we can write for *var(T_n)* the following

$$var(T_n) = \sum_i^N \psi_i \xi_{n,i}^2 var_i(T_{n,i}) + \sum_i^N \psi_i \left[\xi_{n,i} E_i(T_{n,i}) - E(T_n)\right]^2$$

VI. Covariance between holding routing times for a component

The covariance between holding times of any two stages are calculated by finding the expectation of products of holding times as the first step. So, write

$$E_i(T_{r,i}T_{h,i}) = \frac{1}{|T_P|}\int_{T_P}\frac{1}{|A|}\int_A (T\theta_{h,i}f_{R_i})da\,dt = [T]_t\left[\theta_{h,i}\right]_{at} + \frac{\left[\theta_{h,i}\right]_{at}\{T,[R_i]_a\}_t}{[R_i]_{at}}$$

$$E_i(T_{r,i}T_{n,i}) = \frac{1}{|T_P|}\int_{T_P}\frac{1}{|A|}\int_A (T\theta_{n,i}f_{R_i})da\,dt$$

$$= [T]_t\left[\theta_{n,i}\right]_a + \frac{\left[\theta_{n,i}\right]_a\{T,[R_i]_a\}_t}{[R_i]_{at}} + \frac{[T]_t\{\theta_{n,i},[R_i]_t\}_a}{[R_i]_{at}} + \frac{\left\{T,\{\theta_{n,i},R_i\}_a\right\}_t}{[R_i]_{at}}$$

$$E_i(T_{h,i}T_{n,i}) = \frac{1}{|T_P|}\int_{T_P}\frac{1}{|A|}\int_A (\theta_{h,i}\theta_{n,i}f_{R_i})da\,dt = \left[\theta_{h,i}\right]_{at}\left[\theta_{n,i}\right]_a + \frac{\left[\theta_{h,i}\right]_{at}\left\{\left[\theta_{n,i}\right]_a,[R_i]_a\right\}_t}{[R_i]_{at}}$$

Subtract $E_i(T_{r,i}T_{h,i})$, $E_i(T_{r,i}T_{n,i})$ and $E_i(T_{h,i}T_{n,i})$ correspondingly by $E_i(T_{r,i})E_i(T_{h,i})$, $E_i(T_{r,i})E_i(T_{n,i})$ and $E_i(T_{h,i})E_i(T_{n,i})$, one can see that the covariance between the hillslope routing time and any other one goes to zero. The covariance between rainfall excess generation time and channel routing time is then written as:

$$cov_i(T_{r,i},T_{n,i}) = E_i(T_{r,i}T_{n,i}) - E_i(T_{r,i})E_i(T_{n,i}) = \frac{\left\{T,\{\theta_{n,i},R_i\}_a\right\}_t}{[R_i]_{at}} - \frac{\{T,[R_i]_a\}_t\{\theta_{n,i},[R_i]_t\}_a}{[R_i]_{at}^2}$$

VII. Covariance between holding times for the total rainfall excess

For the case of $cov(T_r,T_n)$, it is trivial to show

$$E(T_rT_n) = \sum_i^N \psi_i\xi_{n,i}E_i(T_{r,i}T_{n,i})$$

Write

$$cov(T_r,T_n) = E(T_rT_n) - E(T_r)E(T_n) = \sum_i^N \psi_i\xi_{n,i}E_i(T_{r,i}T_{n,i}) - E(T_r)E(T_n)$$

$$= \sum_i^N \psi_i\xi_{n,i}E_i(T_{r,i}T_{n,i}) - \sum_i^N \psi_iE_i(T_{r,i})\xi_{n,i}E_i(T_{n,i}) + \sum_i^N \psi_iE_i(T_{r,i})\xi_{n,i}E_i(T_{n,i}) - E(T_r)E(T_n)$$

$$= \sum_i^N \psi_i\xi_{n,i}cov_i(T_{r,i},T_{n,i}) + \sum_i^N \psi_i\left[E_i(T_{r,i})\xi_{n,i}E_i(T_{n,i}) - E(T_r)E(T_n)\right]$$

Reference

Adler, R. F., Huffman, G. J., Chang, A., Ferraro, R., Xie, P.-P., Janowiak, J., . . . Nelkin, E. (2003). The Version-2 Global Precipitation Climatology Project (GPCP) Monthly Precipitation Analysis (1979–Present). *J. Hydrometeor., 4*(6), 1147-1167. doi:10.1175/1525-7541(2003)004<1147:TVGPCP>2.0.CO;2

AghaKouchak, A., Behrangi, A., Sorooshian, S., Hsu, K., & Amitai, E. (2011). Evaluation of Satellite-retrieved Extreme Precipitation Rates across the Central United States. *J. Geophys. Res., 116*, D02115. doi:10.1029/2010JD014741

Ali, A., Amani, A., & Lebel, T. (2005). Rainfall Estimation in the Sahel. Part II: Evaluation of Rain Gauge Networks in the CILSS Countries and Objective Intercomparison of Rainfall Products. *J. Appl. Meteor., 44*(11), 1707-1722. doi:10.1175/JAM2305.1

Anagnostou, E. N. (2004). Overview of Overland Satellite Rainfall Estimation for Hydro-Meteorological Applications. *Surv. Geophys., 25*(5-6), 511-537. doi:10.1007/s10712-004-5724-6

Anagnostou, E. N., Maggioni, V., Nikolopoulos, E. I., Meskele, T., Hossain, F., & Papadopoulos, A. (2010). Benchmarking High-Resolution Global Satellite Rainfall Products to Radar and Rain-gauge Rainfall Estimates. *IEEE Trans. Geosci. Remote Sens., 48*(4), 1667-1683. doi:10.1109/TGRS.2009.2034736

Arkin, P. A., & Ardanuy, P. E. (1989). Estimating Climatic-Scale Precipitation from Space: A Review. *J. Climate, 2*(11), 1229-1238. doi:10.1175/1520-0442(1989)002<1229:ECSPFS>2.0.CO;2

Artan, G., Gadain, H., Smith, J. L., Asante, K., Bandaragoda, C. J., & Verdin, J. P. (2007). Adequacy of Satellite Derived Rainfall Data for Stream Flow Modeling. *Nat. Hazards, 43*(2), 167-185. doi:10.1007/s11069-007-9121-6

Beighley, R. E., Ray, R. L., He, Y., Lee, H., Schaller, L., Andreadis, K. M., . . . Shum, C. K. (2011). Comparing satellite derived precipitation datasets using the Hillslope River Routing (HRR) model in the Congo River Basin. *Hydrol. Process., 25*(20), 3216-3229. doi:10.1002/hyp.8045

Berne, A., & Krajewski, W. F. (2013). Radar for Hydrology: Unfulfilled Promise or Unrecognized Potential? *Adv. Water Resour., 51*, 357-366. doi:10.1016/j.advwatres.2012.05.005

Bitew, M. M., & Gebremichael, M. (2011). Assessment of Satellite Rainfall Products for Streamflow Simulation in Medium Watersheds of the Ethiopian Highlands. *Hydrol. Earth Syst. Sci., 15*(4), 1147-1155. doi:10.5194/hess-15-1147-2011

Bitew, M. M., Gebremichael, M., Ghebremichael, L. T., & Bayissa, Y. A. (2011). Evaluation of High-resolution Satellite Rainfall Products through Streamflow Simulation in a Hydrological Modeling of a Small Mountainous Watershed in Ethiopia. *J. Hydrometeor., 13*(1), 338-350. doi:10.1175/2011JHM1292.1

Blöschl, G. (2006). Chap 1. In *On the Fundamentals of Hydrological Sciences.* John Wiley & Sons, Ltd. doi:10.1002/0470848944.hsa001a

Blöschl, G., Reszler, C., & Komma, J. (2008). A spatially distributed flash flood forecasting model. *Environ. Modell. Softw., 23*(4), 464-478. doi:10.1016/j.envsoft.2007.06.010

Borga, M., Anagnostou, E. N., Blöschl, G., & Creutin, J. -D. (2010). Flash Floods: Observations and Analysis of Hydrometeorological Controls. *J. Hydrol., 394*(1-2), 1-3. doi:http://dx.doi.org/10.1016/j.jhydrol.2010.07.048

Borga, M., Nikolopoulos, E. I., Davide, Z., & Francesco, M. (2014). *Extension of Adige River Flood Forecasting System for debris flow forecasting, simulation of glacial hydrology and artificial reservoir*

storage accounting. University of Padova, Alto Adige, Autonomous Province of Bolzano. Retrieved from http://webcache.googleusercontent.com/search?q=cache:ZDL1lB2SSv0J:www.provinz.bz.it/zivilschutz/service/veroeffentlichungen.asp%3Fsomepubl_action%3D300%26somepubl_image_id%3D349342+&cd=1&hl=it&ct=clnk&gl=it

Carpenter, T. M., & Georgakakos, K. P. (2006). Intercomparison of Lumped versus Distributed Hydrologic Model Ensemble Simulations on Operational Forecast Scales. *J. Hydrol., 329*(1-2), 174-185. doi:10.1016/j.jhydrol.2006.02.013

Cazorzi, F., & Dalla Fontana, G. (1996). Snowmelt Modelling by Combining Air Temperature and a Distributed Radiation Index. *J. Hydrol., 181*(1-4), 169-187. doi:10.1016/0022-1694(95)02913-3

Ciach, G. J., Krajewski, W. F., & Villarini, G. (2007). Product-Error-Driven Uncertainty Model for Probabilistic Quantitative Precipitation Estimation with NEXRAD Data. *J. Hydrometeor., 8*(6), 13325-1347. doi:doi: 10.1175/2007JHM814.1

Creutin, J.-D., & Borga, M. (2003). Radar Hydrology Modifies the Monitoring of Flash-flood Hazard. *Hydrol. Process., 17*(7), 1453-1456. doi:10.1002/hyp.5122

Cunge, J. A. (1969). On The Subject Of A Flood Propagation Computation Method (Musklngum Method). *J. Hydraul. Res., 7*(2), 205-230. doi:10.1080/00221686909500264

Cunha, L. K., Mandapaka, P. V., Krajewski, W. F., Mantilla, R., & Bradley, A. A. (2012). Impact of Radar-rainfall Error Structure on Estimated Flood Magnitude across Scales: An Investigation Based on a Parsimonious Distributed Hydrological Model. *Water Resour. Res., 48*(10), W10515. doi:10.1029/2012WR012138

Delrieu, G., Bonnifait, L., Kirstetter, P.-E., & Boudevillain, B. (2014). Dependence of radar quantitative precipitation estimation error on the rain intensity in the Cévennes region, France. *Hydrolog. Sci. J., 59*(7), 1308-1319. doi:10.1080/02626667.2013.827337

Dhakal, N., Fang, X., Cleveland, T. G., Thompson, D. B., Asquith, W. H., & Marzen, L. J. (2012). Estimation of Volumetric Runoff Coefficients for Texas Watersheds Using Land-Use and Rainfall-Runoff Data. *J. Irrig. Drain Eng., 138*(1), 43-54. doi:10.1061/(ASCE)IR.1943-4774.0000368

Dinku, T., Ceccato, P., Grover-Kopec, E., Lemma, M., Connor, S. J., & Ropelewski, C. F. (2007). Validation of Satellite Rainfall Products over East Africa's Complex Topography. *Int. J. Remote Sens., 28*(7), 1503-1526. doi:10.1080/01431160600954688

Duan, Q., Sorooshian, S., & Gupta, V. (1992). Effective and efficient global optimization for conceptual rainfall-runoff models. *Water Resour. Res., 28*(4), 1015-1031. doi:10.1029/91WR02985

Ebert, E. E., Janowiak, J. E., & Kidd, C. (2007). Comparison of Near-real-time Precipitation Estimates from Satellite Observations and Numerical Models. *Bull. Amer. Meteor. Soc., 88*(1), 47-64. doi:10.1175/BAMS-88-1-47

Falck, A. S., Maggioni, V., Tomasella, J., Vila, D. A., & Diniz, F. L. (2015). Propagation of satellite precipitation uncertainties through a distributed hydrologic model: A case study in the Tocantins–Araguaia basin in Brazil. *J. Hydrol., 527*, 943-957. doi:10.1016/j.jhydrol.2015.05.042

Fleming, K., Awange, J., Kuhn, M., & Featherstone, W. (2011). Evaluating the TRMM 3B42 Monthely Precipitation Product Using Gridded Rain-gauge Data over Australia. *Aust. Meteorol. Ocean. J., 61*, 171-184.

Frei, C., & Schär, C. (1998). A Precipitation Climatology of the Alps from High-resolution Rain-gauge Observations. *Int. J. Climatol., 18*(8), 873-900. doi:10.1002/(SICI)1097-0088(19980630)18:8<873::AID-JOC255>3.0.CO;2-9

Gebregiorgis, A. S., & Hossain, F. (2013). Understanding the Dependence of Satellite Rainfall Uncertainty on Topography and Climate for Hydrologic Model Simulation. *IEEE T. Geosci. Remote, 51*(1), 704-718. doi:10.1109/TGRS.2012.2196282

Gebregiorgis, A. S., Tian, Y., Peters-Lidard, C. D., & Hossain, F. (2012). Tracing hydrologic model simulation error as a function of satellite rainfall estimation bias components and land use and land cover conditions. *Water Resour. Res., 48*(11), W11509. doi:10.1029/2011WR011643

Germann, U., Galli, G., Boscacci, M., & Bolliger, M. (2006). Radar Precipitation Measurement in a Mountainous Region. *Q.J.R. Meteorol. Soc., 132*(618), 1669-1692. doi:10.1256/qj.05.190

Gonzales, A. L., Nonner, J., Heijkers, J., & Uhlenbrook, S. (2009). Comparison of different base flow separation methods in a lowland catchment. *Hydrol. Earth Sys. Sci., 13*(11), 2055-2068. doi:10.5194/hess-13-2055-2009

Gourley, J. J., Hong, Y., Flamig, Z. L., Wang, J., Vergara, H., & Anagnostou, E. N. (2011). Hydrologic Evaluation of Rainfall Estimates from Radar, Satellite, Gauge, and Combinations on Ft. Cobb Basin, Oklahoma. *J. Hydrometeor., 12*(5), 973-988. doi:10.1175/2011JHM1287.1

Grimes, D. I., & Diop, M. (2003). Satellite-based Rainfall Estimation for River Flow Forecasting in Africa. I: Rainfall Estimates and Hydrological Forecasts. *Hydrolog. Sci. J., 48*(4), 567-584. doi:10.1623/hysj.48.4.567.51410

Guetter, A. K., Georgakakos, K. P., & Tsonis, A. A. (1996). Hydrologic Applications of Satellite Data: 2. Flow Simulation and Soil Water Estimates. *J. Geophys. Res., 101*(D21), 26527-26538. doi:10.1029/96JD01655

Guo, H., Chen, S., Bao, A., Behrangi, A., Hong, Y., Ndayisaba, F., . . . Stepanian, P. M. (2016). Early Assessment of Integrated Multi-satellite Retrievals for Global Precipitation Measurement over China. *Atmos. Res., 176-177*, 121-133. doi:10.1016/j.atmosres.2016.02.020

Habib, E., Haile, A. T., Sazib, N., Zhang, Y., & Rientjes, T. (2014). Effect of bias correction of satellite-rainfall estimates on runoff simulations at the source of the Upper Blue Nile. *Remote Sens., 6*(7), 6688-6708. doi:10.3390/rs6076688

Hargreaves, G. H., & Samani, Z. A. (1982). Estimating potential evapotranspiration. *J. Irr. Drain. Div., 108*(3), 225-230.

Homer, C., Dewitz, J., Yang, L., Jin, S., Danielson, P., Xian, G., . . . Megown, K. (2015). Completion of the 2011 National Land Cover Database for the Conterminous United States – Representing a Decade of Land Cover Change Information. *Photogramm. Eng. Rem. S., 81*(5), 345-354. doi:10.1016/S0099-1112(15)30100-2

Hong, Y., Hsu, K.-L., Sorooshian, S., & Gao, X. (2004). Precipitation Estimation from Remotely Sensed Imagery Using an Artificial Neural Network Cloud Classification System. *J. Appl. Meteor., 43*(12), 1834-1853. doi:10.1175/JAM2173.1

Hossain, F., & Anagnostou, E. N. (2004). Assessment of current passive-microwave- and infrared-based satellite rainfall remote sensing for flood prediction. *J. Geophys. Res., 109*(D7), D07102. doi:10.1029/2003JD003986

Hsu, K.-l., Gao, X., Sorooshian, S., & Gupta, H. V. (1997). Precipitation Estimation from Remotely Sensed Information Using Artificial Neural Networks. *J. Appl. Meteor., 36*(9), 1176-1190. doi:10.1175/1520-0450(1997)036<1176:PEFRSI>2.0.CO;2

Huffman, G. J., Adler, R. F., Bolvin, D. T., & Gu, G. (2009). Improving the global precipitation record: GPCP Version 2.1. *Geophys. Res. Lett., 36*(17), L17808. doi:10.1029/2009GL040000

Huffman, G. J., Adler, R. F., Bolvin, D. T., & Nelkin, E. J. (2010). The TRMM Multi-Satellite Precipitation Analysis (TMPA). In M. Gebremichael, & F. Hossain (Eds.), *Satellite Rainfall Applications for Surface Hydrology* (pp. 3-22). New York: Springer Netherlands. doi:10.1007/978-90-481-2915-7_1

Huffman, G. J., Bolvin, D. T., Braithwaite, D., Kuolin, H., Joyce, R., Kidd, C., . . . Xie, P. (2015). *NASA Global Precipitation Measurement (GPM) Integrated Multi-satellitE Retrievals for GPM (IMERG).* Greenbelt: NASA. Retrieved from http://pmm.nasa.gov/sites/default/files/document_files/IMERG_ATBD_V4.5.pdf

Huffman, G. J., Bolvin, D. T., Nelkin, E. J., Wolff, D. B., Adler, R. F., Fu, G., . . . Stocker, E. F. (2007). The TRMM Multisatellite Precipitation Analysis (TMPA): Quasi-Global, Multiyear, Combined-Sensor Precipitation Estimates at Fine Scales. *J. Hydrometeor., 8*(1), 38-55. doi:10.1175/JHM560.1

Jiang, S., Ren, L., Hong, Y., Yong, B., Yang, X., Yuan, F., & Ma, M. (2012). Comprehensive evaluation of multi-satellite precipitation products with a dense rain gauge network and optimally merging their simulated hydrological flows using the Bayesian model averaging method. *J. Hydrol., 452-453*(0), 213-225. doi:10.1016/j.jhydrol.2012.05.055

Joyce, R. J., & Xie, P. (2011). Kalman Filter–Based CMORPH. *J. Hydrometeor., 12*(6), 1547-1563. doi:10.1175/JHM-D-11-022.1

Joyce, R. J., Janowiak, J. E., Arkin, P. A., & Xie, P. (2004). CMORPH: A Method that Produces Global Precipitation Estimates from Passive Microwave and Infrared Data at High Spatial and Temporal Resolution. *J. Hydrometeor., 5*(3), 487-503. doi:10.1175/1525-7541(2004)005<0487:CAMTPG>2.0.CO;2

Kidd, C., Kniveton, D. R., Todd, M. C., & Bellerby, T. J. (2003). Satellite Rainfall Estimation Using Combined Passive Microwave and Infrared Algorithms. *J. Hydrometeor., 4*(6), 1088-1104. doi:10.1175/1525-7541(2003)004<1088:SREUCP>2.0.CO;2

Kim, J. P., Jung, I. W., Park, K. W., Yoon, S. K., & Lee, D. (2016). Hydrological Utility and Uncertainty of Multi-Satellite Precipitation Products in the Mountainous Region of South Korea. *Remote Sens., 8*(7), 608. doi:10.3390/rs8070608

Kirstetter, P.-E., Gourley, J. J., Hong, Y., Zhang, J., Moazamigoodarzi, S., Langston, C., & Arthur, A. (2015). Probabilistic precipitation rate estimates with ground-based radar networks. *Water Resour. Res., 51*(3), 1422-1442. doi:10.1002/2014WR015672

Koren, V., Reed, M., Zhang, Z., & Seo, D.-J. (2004). Hydrology laboratory research modeling system (HL-RMS) of the US national weather service. *J. Hydrol., 291*(3-4), 297-318. doi:10.1016/j.jhydrol.2003.12.039

Li, L., Hong, Y., Wang, J., Adler, R. F., Policelli, F. S., Habib, S., . . . Okello, L. (2009). Evaluation of the real-time TRMM-based multi-satellite precipitation analysis for an operational flood prediction system in Nzoia Basin, Lake Victoria, Africa. *Nat. Hazards, 50*(1), 109-123. doi:10.1007/s11069-008-9324-5

Li, X.-H., Zhang, Q., & Xu, C.-Y. (2012). Suitability of the TRMM satellite rainfalls in driving a distributed hydrological model for water balance computations in Xinjiang catchment, Poyang lake basin. *J. Hydrol., 426-427*(0), 28-38. doi:10.1016/j.jhydrol.2012.01.013

Lin, Y., & Mitchell, K. E. (2005). 1.2 the NCEP stage II/IV hourly precipitation analyses: Development and applications. San Diego, CA, USA: 19th Conf. Hydrology, American Meteorological Society. Retrieved from http://citeseerx.ist.psu.edu/viewdoc/download?doi=10.1.1.182.2080&rep=rep1&type=pdf

Liu, F., Williams, M. W., & Caine, N. (2004). Source waters and flow paths in an alpine catchment, Colorado Front Range, United States. *Water Resour. Res., 40*(9), W09401. doi:10.1029/2004WR003076

Maggioni, V., Vergara, H. J., Anagnostou, E. N., Gourley, J. J., Hong, Y., & Stampoulis, D. (2013). Investigating the Applicability of Error Correction Ensembles of Satellite Rainfall Products in River Flow Simulations. *J. Hydrometeor, 14*(4), 1194-1211. doi:10.1175/JHM-D-12-074.1

Marchi, L., Borga, M., Preciso, E., & Gaume, É. (2010). Characterisation of selected extreme flash floods in Europe and implications for flood risk management. *J. Hydrol., 394*(1-2), 118-133. doi:10.1016/j.jhydrol.2010.07.017

Massari, C., Brocca, L., Barbetta, S., Papathanasiou, C., Mimikou, M., & Moramarco, T. (2014). Using globally available soil moisture indicators for flood modelling in Mediterranean catchments. *Hydrol. Earth Syst. Sci., 18*(2), 839-853. doi:10.5194/hess-18-839-2014

Mega, T., Ushio, T., Kubota, T., Kachi, M., Aonashi, K., & Shige, S. (2014). Gauge adjusted global satellite mapping of precipitation (GSMaP_Gauge). *General Assembly and Scientific Symposium (URSI GASS), 2014 XXXIth URSI*, (pp. 1-4). Beijing. doi:10.1109/URSIGASS.2014.6929683

Mei, Y., & Anagnostou, E. N. (2015). A Hydrograph Separation Method Based on Information from Rainfall and Runoff Records. *J. Hydrol., 523*, 636-649. doi:10.1016/j.jhydrol.2015.01.083

Mei, Y., Anagnostou, E. N., Nikolopoulos, E. I., & Borga, M. (2014b). Error Analysis of Satellite Rainfall Products in Mountainous Basins. *J. Hydrometeorol., 15*(5), 1778-1793. doi:10.1175/JHM-D-13-0194.1

Mei, Y., Anagnostou, E. N., Nikolopoulos, E. I., & Borga, M. (2015). Reply to "Comments on 'Error Analysis of Satellite Precipitation Products in Mountainous Basins'". *J. Hydrometeor., 16*(3), 1445-1446. doi:10.1175/JHM-D-15-0022.1

Mei, Y., Anagnostou, E. N., Stampoulis, D., Nikolopoulos, E. I., Borga, M., & Vegara, H. J. (2014a). Rainfall Organization Control on the Flood Response of Mild-slope Basins. *J. Hydrol., 510*, 565-577. doi:10.1016/j.jhydrol.2013.12.013

Mei, Y., Nikolopoulos, E. I., Anagnostou, E. N., & Borga, M. (2016a). Evaluating Satellite Precipitation Error Propagation in Runoff Simulations of Mountainous Basins. *J. Hydrometeor., 17*(5), 1407-1423. doi:10.1175/JHM-D-15-0081.1

Mei, Y., Nikolopoulos, E. I., Anagnostou, E. N., Zoccatelli, D., & Borga, M. (2016b). Error Analysis of Satellite Precipitation-Driven Modeling of Flood Events in Complex Alpine Terrain. *Remote Sens., 8*(4), 293. doi:10.3390/rs8040293

Mei, Y., Shen, X., & Anagnstou, E. N. (2016c). A Synthesis of Space-time Variability in Multi-component Flood Response. *Hydrol. Earth Syst. Sci. Discuss., 2016*, 1-36. doi:10.5194/hess-2016-255

Mejía, A. I., & Moglen, G. E. (2010). Spatial distribution of imperviousness and the space-time variability of rainfall, runoff generation, and routing. *Water Resour. Res., 46*(7), W07509. doi:10.1029/2009WR008568

Mejía, A., Rossel, F., Gironás, J., & Jovanovic, T. (2015). Anthropogenic controls from urban growth on flow regimes. *Adv. Water Resour., 84*, 125-135. doi:10.1016/j.advwatres.2015.08.010

Merz, R., & Blöschl, G. (2003). A process typology of regional floods. *Water Resour. Res., 39*(12), 1340. doi:10.1029/2002WR001952

Merz, R., & Blöschl, G. (2009). A regional analysis of event runoff coefficients with respect to climate and catchment characteristics in Austria. *Water Resour. Res., 45*(1), W01405. doi:10.1029/2008WR007163

Mesinger, F., DiMego, G., Kalnay, E., Mitchell, K., Shafran, P. C., Ebisuzaki, W., . . . and Shi, W. (2006). North American Regional Reanalysis. *Bulletin of the American Meteorological Society, 87*(3), 343-360. doi:10.1175/BAMS-87-3-343

Michaelides, S., Levizzani, V., Anagnostou, E. N., Bauer, P., Kasparis, T., & Lane, J. E. (2009). Precipitation science: measurement, remote sensing, climatology and modelling EGU08 Precipitation European Geosciences Union General Assembly. *Atmos. Res., 94*(4), 512-533. doi:http://dx.doi.org/10.1016/j.atmosres.2009.08.017

Mishra, A. K. (2012). Application of Merged Precipitation Estimation Technique to Study Intense Rainfall Events over India and Associated Oceanic Region. *Atmos. Clim. Sci., 2*(2), 222-229. doi:10.4236/acs.2012.22023

Moore, R. J. (1985). The probability-distributed principle and runoff production at point and basin scales. *Hydrolog. Sci. J., 30*(2), 273-297.

Moore, R. J. (2007). The PDM rainfall-runoff model. *Hydrol. Earth Syst. Sci., 11*(1), 483-499. doi:10.5194/hess-11-483-2007

Moriasi, D. N., Arnold, J. G., Van Liew, M. W., Bingner, R. L., Harmel, R. D., & Veith, T. L. (2007). Model Evaluation Guidelines for Systematic Quantification of Accuracy in Watershed Simulations. *Trans. ASABE, 50*(3), 885−900. doi:10.13031/2013.23153

Nash, J. E., & Sutcliffe, J. V. (1970). River flow forecasting through conceptual models part I — A discussion of principles. *J. Hydrol., 10*(3), 282-290. doi:10.1016/0022-1694(70)90255-6

Nikolopoulos, E. I., Anagnostou, E. N., & Borga, M. (2013). Using High-resolution Satellite Rainfall Products to Simulate a Major Flash Flood Event in Northern Italy. *J. Hydrometeorol., 14*(1), 171-185. doi:10.1175/JHM-D-12-09.1

Nikolopoulos, E. I., Anagnostou, E. N., Borga, M., Vivoni, E. R., & Papadopoulos, A. (2011). Sensitivity of a mountain basin flash flood to initial wetness condition and rainfall variability. *J. Hydrol., 402*(3-4), 165-178. doi:10.1016/j.jhydrol.2010.12.020

Nikolopoulos, E. I., Anagnostou, E. N., Hossain, F., Gebremichael, M., & Borga, M. (2010). Understanding the Scale Relationships of Uncertainty Propagation of Satellite Rainfall through a Distributed Hydrologic Model. *J. Hydrometeor., 11*(2), 520-532. doi:10.1175/2009JHM1169.1

Nikolopoulos, E. I., Borga, M., Creutin, J. D., & Marra, F. (2015). Estimation of debris flow triggering rainfall: Influence of rain gauge density and interpolation methods. *Geomorphology, 243*, 40-50. doi:10.1016/j.geomorph.2015.04.028

Nikolopoulos, E., Borga, M., Zoccatelli, D., & Anagnostou, E. (2014). Catchment scale storm velocity: Quantification, scale dependence and effect on flood response. *Hydrol. Sci. J., 59*(7), 1363-1376. doi:10.1080/02626667.2014.923889

Norbiato, D., Borga, M., & Dinale, R. (2009b). Flash flood warning in ungauged basins by use of the flash flood guidance and model-based runoff thresholds. *Met. Apps., 16*(1), 65-75. doi:10.1002/met.126

Norbiato, D., Borga, M., Degli Esposti, S., Gaume, E., & Anquetin, S. (2008). Flash flood warning based on rainfall thresholds and soil moisture conditions: An assessment for gauged and ungauged basins. *J. Hydrol., 362*(3-4), 274-290. doi:10.1016/j.jhydrol.2008.08.023

Norbiato, D., Borga, M., Merz, R., Blöschl, G., & Carton, A. (2009a). Controls on Event Runoff Coefficients in the Eastern Italian Alps. *J. Hydrol., 375*(3-4), 312-325. doi:10.1016/j.jhydrol.2009.06.044

Palleiro, L., Rodríguez-Blanco, M. L., Taboada-Castro, M. M., & Taboada-Castro, M. T. (2014). Hydrological response of a humid agroforestry catchment at different time scales. *Hydrol. Process., 28*(4), 1677-1688. doi:10.1002/hyp.9714

Pan, M., Li, H., & Wood, E. (2010). Assessing the skill of satellite-based precipitation estimates in hydrologic applications. *Water Resour. Res., 46*(9), W09535. doi:10.1029/2009WR008290

Parajka, J., Kohnová, S., Bálint, G., Marbuc, M., Borga, M., Claps, P., . . . Blöschl, G. (2010). Seasonal characteristics of flood regimes across the Alpine–Carpathian range. *J. Hydrol., 394*(1-2), 78-89. doi:10.1016/j.jhydrol.2010.05.015

Penna, D., Tromp-van Meerveld, H. J., Gobbi, A., Borga, M., & Dalla Fontana, G. (2011). The influence of soil moisture on threshold runoff generation processes in an alpine headwater catchment. *Hydrol. Earth Syst. Sci., 15*(3), 689-702. doi:10.5194/hess-15-689-2011

Petty, G. W., & Krajewski, W. F. (1996). Satellite Estimation of Precipitation over Land. *Hydrolog. Sci. J., 41*(4), 433-451. doi:10.1080/02626669609491519

Piccolo, F., & Chirico, G. B. (2005). Sampling errors in rainfall measurements by weather radar. *Adv. Geosci., 2*, 151-155. doi:10.5194/adgeo-2-151-2005

Prakash, S., Mitra, A. K., Aghakouchak, A., Liu, Z., Norouzi, H., & Pai, D. (2016). A Preliminary Assessment of GPM-based Multi-satellite Precipitation Estimates over a Monsoon Dominated Region. *J. Hydrol.* doi:10.1016/j.jhydrol.2016.01.029

Prat, O. P., & Nelson, B. R. (2015). Evaluation of precipitation estimates over CONUS derived from satellite, radar, and rain gauge data sets at daily to annual scales (2002–2012). *Hydrol. Earth Syst. Sci., 19*(4), 2037-2056. doi:10.5194/hess-19-2037-2015

Rodríguez-Blanco, M. L., Taboada-Castro, M. M., & Taboada-Castro, M. T. (2012). Rainfall–runoff response and event-based runoff coefficients in a humid area (northwest Spain). *Hydrolog. Sci. J., 57*(3), 445-459. doi:10.1080/02626667.2012.666351

Rodríguez-Iturbe, I., & Valdés, J. B. (1979). The geomorphologic structure of hydrologic response. *Water Resour. Res., 15*(6), 1409-1420. doi:10.1029/WR015i006p01409

Sangati, M., Borga, M., Rabuffetti, D., & Bechini, R. (2009). Influence of rainfall and soil properties spatial aggregation on extreme flash flood response modelling: An evaluation based on the Sesia river basin, North Western Italy. *Adv. Water Resour., 32*(7), 1090-1106. doi:10.1016/j.advwatres.2008.12.007

Sapiano, M. R., & Arkin, P. A. (2009). An Intercomparison and Validation of High-Resolution Satellite Precipitation Estimates with 3-Hourly Gauge Data. *J. Hydrometeorol., 10*(1), 149-166. doi:doi: 10.1175/2008JHM1052.1

Schneebeli, M., Nicholas, D., Lehning, M., & Berne, A. (2013). High-Resolution Vertical Profiles of X-Band Polarimetric Radar Observables during Snowfall in the Swiss Alps. *J. Appl. Meteor. Climatol., 52*(2), 378-394. doi:10.1175/JAMC-D-12-015.1

Scofield, R. A., & Kuligowski, R. J. (2003). Status and Outlook of Operational Satellite Precipitation Algorithms for Extreme-Precipitation Events. *Weather Forecast., 18*(6), 1037-1051. doi:10.1175/1520-0434(2003)018<1037:SAOOOS>2.0.CO;2

Seyyedi, H., Anagnostou, E. N., Beighley, E., & McCollum, J. (2015). Hydrologic Evaluation of Satellite and Reanalysis Precipitation Datasets over a Mid-Latitude Basin. *Atmos. Res., 164-165*, 37-48. doi:10.1016/j.atmosres.2015.03.019

Shah, H. L., & Mishra, V. (2016). Uncertainty and Bias in Satellite-Based Precipitation Estimates over Indian Subcontinental Basins: Implications for Real-Time Streamflow Simulation and Flood Prediction. *J. Hydrometeor., 17*(2), 615-636. doi:10.1175/JHM-D-15-0115.1

Sharif, H. O., Ogden, F. L., Krajewski, W. F., & Xue, M. (2002). Numerical simulations of radar rainfall error propagation. *Water Resour. Res., 38*(8), 1-14. doi:10.1029/2001WR000525

Shen, X., & Hong, Y. (2015, Oct 28). *The coupled routing and excess storage (CREST).* Retrieved Oct 28, 2015, from Hydrometeorology and Remote Sensing Laboratory: http://hydro.ou.edu/wp-content/uploads/2013/02/CREST-User-Manual-v2.1.0_Matlab.pdf

Shen, X., Emmanouil, A. N., Mei, Y., & Hong, Y. (2017). A global distributed basin morphometric dataset (In press). *Sci. Data*.

Shen, X., Hong, Y., Zhang, K., & Hao, Z. (2016). Refining a Distributed Linear Reservoir Routing Method to Improve Performance of the CREST Model. *J. Hydrol. Eng.*, 04016061. doi:10.1061/(ASCE)HE.1943-5584.0001442

Siddique-E-Akbor, A. H., Hossain, F., Sikder, S., Shum, C. K., Tseng, S., Yi, Y., . . . Limaye, A. (2014). Satellite Precipitation Data–Driven Hydrological Modeling for Water Resources Management in the Ganges, Brahmaputra, and Meghna Basins. *Earth Interact., 18*(17), 1-25. doi:10.1175/EI-D-14-0017.1

Sivapalan, M., Blöschl, G., Merz, R., & Gutknecht, D. (2004). Linking flood frequency to long-term water balance: Incorporating effects of seasonality. *Water Resour. Res., 41*(6), W06012. doi:10.1029/2004WR003439

Skøien, J. O., & Blöschl, G. (2006). Catchments as space-time filters – a joint spatio-temporal geostatistical analysis of runoff and precipitation. *Hydrol. Earth Syst. Sci., 10*(5), 645-662. doi:10.5194/hess-10-645-2006

Skøien, J. O., Blöschl, G., & Western, A. W. (2003). Characteristic space scales and timescales in hydrology. *Water Resour. Res., 39*(10), 1304,19. doi:10.1029/2002WR001736

Smith, J. A., Baeck, M. L., Meierdiercks, K. L., Nelson, P. A., Miller, A. J., & Holland, E. J. (2005). Field studies of the storm event hydrologic response in an urbanizing watershed. *Water Resour. Res., 41*(10), W10413, 15. doi:10.1029/2004WR003712

Smith, J. A., Baeck, M. L., Morrison, J. E., Turner-Gillespie, D. F., & Bates, P. D. (2002). The Regional Hydrology of Extreme Floods in an Urbanizing Drainage Basin. *J. Hydrometeor., 3*(3), 267-282. doi:10.1175/1525-7541(2002)003<0267:TRHOEF>2.0.CO;2

Smith, M. B., Koren, V. I., Zhang, Z., Reed, S. M., Pan, J.-J., & Moreda, F. (2004). Runoff response to spatial variability in precipitation: an analysis of observed data. *J. Hydrol., 298*(1-4), 267-286. doi:10.1016/j.jhydrol.2004.03.039

Sorooshian, S., Hsu, K.-L., Gao, X., Gupta, H. V., Imam, B., & Braithwaite, D. (2000). Evaluation of PERSIANN System Satellite–Based Estimates of Tropical Rainfall. *Bull. Amer. Meteor. Soc., 81*(9), 2035-2046. doi:10.1175/1520-0477(2000)081<2035:EOPSSE>2.3.CO;2

Stampoulis, D., & Anagnostou, E. N. (2011). Evaluation of Global Satellite Rainfall Products over Continental Europe. *J. Hydrometeorol., 13*(2), 588-603. doi:10.1175/JHM-D-11-086.1

Steele, J. M. (2004). *The Cauchy-Schwarz Master Class: An Introduction to the Art of Mathematical Inequalities* (illustrated, reprint ed.). Cambridge University Press. Retrieved from http://books.google.com/books?id=7GDyRMrlgDsC

Su, F., Hong, Y., & Lettenmaier, D. P. (2008). Evaluation of TRMM Multisatellite Precipitation Analysis (TMPA) and Its Utility in Hydrologic Prediction in the La Plata Basin. *J. Hydrometeor., 9*(4), 622-640. doi:10.1175/2007JHM944.1

Tang, G., Zeng, Z., Long, D., Guo, X., Yong, B., Zhang, W., & Hong, Y. (2016). Statistical and Hydrological Comparisons between TRMM and GPM Level-3 Products over a Midlatitude Basin: Is Day-1 IMERG a Good Successor for TMPA 3B42V7? *J. Hydrometeor, 17*(1), 121-137. doi:10.1175/JHM-D-15-0059.1

Taylor, K. E. (2001). Summarizing multiple aspects of model performance in a single diagram. *J. Geophys. Res., 106*(D7), 7183-7192. doi:10.1029/2000JD900719

Thiemig, V., Rojas, R., Zambrano-Bigiarini, M., & De Roo, A. (2013). Hydrological evaluation of satellite-based rainfall estimates over the Volta and Baro-Akobo Basin. *J. Hydrol., 499*(0), 324-338. doi:10.1016/j.jhydrol.2013.07.012

Tian, Y., Peters-Lidard, C. D., Eylander, J. B., Joyce, R. J., Huffman, G. J., Adler, R. F., . . . Zeng, J. (2009). Component analysis of errors in satellite-based precipitation estimates. *J. Geophys. Res., 114*(D24), D24101. doi:10.1029/2009JD011949

Tobin, K. J., & Bennett, M. E. (2009). Using SWAT to Model Streamflow in Two River Basins With Ground and Satellite Precipitation Data1. *J. Am. Water Resour. As., 45*(1), 253-271. doi:10.1111/j.1752-1688.2008.00276.x

Tong, K., Su, F., Yang, D., & Hao, Z. (2014). Evaluation of satellite precipitation retrievals and their potential utilities in hydrologic modeling over the Tibetan Plateau. *J. Hydrol., 519, Part A*(0), 423-437. doi:10.1016/j.jhydrol.2014.07.044

Tsintikidis, D., Georgakakos, K. P., Artan, G. A., & Tsonis, A. A. (1999). A feasibility study on mean areal rainfall estimation and hydrologic response in the Blue Nile region using METEOSAT images. *J. Hydrol., 221*(3-4), 97-116. doi:10.1016/S0022-1694(99)00071-2

Ushio, T., Sasashige, K., Kubota, T., Shige, S., Okamoto, K., Aonashi, K., . . . Kawasaki, Z.-I. (2009). A Kalman Filter Approach to the Global Satellite Mapping of Precipitation (GSMaP) from Combined Passive Microwave and Infrared Radiometric Data. *J. Meteor. Soc. Japan, 87A*, 137-151. doi:10.2151/jmsj.87A.137

Vergara, H. J., Hong, Y., Gourley, J. J., Anagnostou, E. N., maggioni, V., Stampoulis, D., & Kirstetter, P.-E. (2013). Effects of Resolution of Satellite-Based Rainfall Estimates on Hydrologic Modeling Skill at Different Scales. *J. Hydrometeor., 15*(2), 593-613. doi:10.1175/JHM-D-12-0113.1

Viglione, A., Chirico, G. B., Komma, J., Woods, R., Borga, M., & Blöschl, G. (2010b). Quantifying space-time dynamics of flood event types. *J. Hydrol., 394*(1-2), 213-229. doi:10.1016/j.jhydrol.2010.05.041

Viglione, A., Chirico, G. B., Woods, R., & Blöschl, G. (2010a). Generalised synthesis of space–time variability in flood response: An analytical framework. *J. Hydrol., 394*(1-2), 198-212. doi:10.1016/j.jhydrol.2010.05.047

Volpi, E., Di Lazzaro, M., & Fiori, A. (2012). A simplified framework for assessing the impact of rainfall spatial variability on the hydrologic response. *Adv. Water Resour., 46*, 1-10. doi:10.1016/j.advwatres.2012.04.011

Wang, J., Hong, Y., Li, L., Gourley, J. J., Khan, S. I., Yilmaz, K. K., . . . Okello, L. (2011). The coupled routing and excess storage (CREST) distributed hydrological model. *Hydrolog. Sci. J., 56*(1), 84-98. doi:10.1080/02626667.2010.543087

Weiler, M., McGlynn, B. L., McGuire, K. J., & McDonnell, J. J. (2003). How does rainfall become runoff? A combined tracer and runoff transfer function approach. *Water Resour. Res., 39*(11), 1315. doi:10.1029/2003WR002331

Wilk, J., Kniveton, D., Andersson, L., Layberry, R., Todd, M. C., Hughes, D., . . . Vanderpost, C. (2006). Estimating rainfall and water balance over the Okavango River Basin for hydrological applications. *J. Hydrol., 331*(1-2), 18-29. doi:10.1016/j.jhydrol.2006.04.049

Woods, R. A., & Sivapalan, M. (1999). A synthesis of space-time variability in storm response: Rainfall, runoff generation, and routing. *Water Resour. Res., 35*(8), 2469-2485. doi:10.1029/1999WR900014

Wu, H., Adler, R. F., Hong, Y., Tian, Y., & Policelli, F. (2012). Evaluation of Global Flood Detection Using Satellite-Based Rainfall and a Hydrologic Model. *J. Hydrometeor., 13*(4), 1268-1284. doi:10.1175/JHM-D-11-087.1

Xiao, Z., Liang, S., Wang, J., Chen, P., Yin, X., Zhang, L., & Song, J. (2014). Use of General Regression Neural Networks for Generating the GLASS Leaf Area Index Product From Time-Series MODIS Surface Reflectance. *IEEE T. Geosci. Remote, 52*(1), 209-223.

Xie, P., Yoo, S.-H., Joyce, R. J., & Yarosh, Y. (2011). Bias-Corrected CMORPH: A 13-Year Analysis of High-Resolution Global Precipitation. *EGU General Assembly 2011 Geophysical Research Abstracts. 13.* EGU. Retrieved from http://meetingorganizer.copernicus.org/EGU2011/EGU2011-1809.pdf

Xue, X., Hong, Y., Limaye, A. S., Gourley, J. J., Huffman, G. J., Khan, S., . . . Chen, S. (2013). Statistical and hydrological evaluation of TRMM-based Multi-satellite Precipitation Analysis over the Wangchu Basin of Bhutan: Are the latest satellite precipitation products 3B42V7 ready for use in ungauged basins? *J. Hydrol., 499*, 91-99. doi:10.1016/j.jhydrol.2013.06.042

Yilmaz, K. K., Adler, R. F., Tian, Y., Hong, Y., & Pierce, H. F. (2010). Evaluation of a satellite-based global flood monitoring system. *Int. J. Remote Sens., 31*(14), 3763-3782. doi:10.1080/01431161.2010.483489

Yilmaz, K. K., Hogue, T. S., Hsu, K.-l., Sorooshian, S., Gupta, H. V., & Wagener, T. (2005). Intercomparison of Rain Gauge, Radar, and Satellite-Based Precipitation Estimates with Emphasis on Hydrologic Forecasting. *J. Hydrometeor., 6*(4), 497-517. doi:10.1175/JHM431.1

Yong, B., Hong, Y., Ren, L.-L., Gourley, J. J., Huffman, G. J., Chen, X., . . . Khan, S. I. (2012). Assessment of evolving TRMM-based multisatellite real-time precipitation estimation methods and their impacts on hydrologic prediction in a high latitude basin. *J. Geophys. Res., 117*(D9), D09108. doi:10.1029/2011JD017069

Yong, B., Liu, D., Gourley, J. J., Tian, Y., Huffman, G. J., Ren, L.-L., & Hong, Y. (2014). Global view of real-time TRMM Multi-satellite Precipitation Analysis: implication to its successor Global Precipitation Measurement mission. *Bull. Amer. Meteor. Soc.* doi:10.1175/BAMS-D-14-00017.1

Yong, B., Ren, L., Hong, Y., Gourley, J. J., Tian, Y., Huffman, G. J., . . . Wen, Y. (2013). First evaluation of the climatological calibration algorithm in the real-time TMPA precipitation estimates over two basins at high and low latitudes. *Water Resour. Res., 49*(5), 2461-2472. doi:10.1002/wrcr.20246

Yong, B., Ren, L.-L., Hong, Y., Wang, J.-H., Gourley, J. J., Jiang, S.-H., . . . Wang, W. (2010). Hydrologic Evaluation of Multisatellite Precipitation Analysis Standard Precipitation Products in Basins beyond Its Inclined Latitude Band: A Case Study in Laohahe Basin, China. *Water Resour. Res., 46*(7), W07542. doi:10.1029/2009WR008965

Zahumenský, I. (2010). *Guidelines on Quality Control Procedures for Data from Automatic Weather Stations.* World Meteorological Organization, Geneva, Switzerland. Retrieved from https://www.wmo.int/pages/prog/www/IMOP/meetings/Surface/ET-STMT1_Geneva2004/Doc6.1(2).pdf

Zhang, X., Anagnostou, E. N., & Vergara, H. (2016). Hydrologic Evaluation of NWP-Adjusted CMORPH Estimates of Hurricane-Induced Precipitation in the Southern Appalachians. *J. Hydrometeor., 17*(4), 1087-1099. doi:10.1175/JHM-D-15-0088.1

Zhang, Y., Seo, D.-J., Habib, E., & McCollum, J. (2015). Differences in Scale-dependent, Climatological Variation of Mean Areal Precipitation Based on Satellite and Radar-gauge Observations. *J. Hydrol., 522*, 35-48. doi:10.1016/j.jhydrol.2014.11.077

Zhao, R.-J. (1992). The Xinanjiang model applied in China. *J. Hydrol., 135*(1), 371-381. doi:10.1016/0022-1694(92)90096-E

Zhu, D., Peng, D. Z., & Cluckie, I. D. (2013). Statistical analysis of error propagation from radar rainfall to hydrological models. *Hydrol. Earth Syst. Sci., 17*(4), 1445-1453. doi:10.5194/hess-17-1445-2013

Zoccatelli, D., Borga, M., Chirico, G., & Nikolopoulos, E. I. (2015). The relative role of hillslope and river network routing in the hydrologic response to spatially variable rainfall fields. *J. Hydrol., 531, Part 2*, 349-359. doi:10.1016/j.jhydrol.2015.08.014

Zoccatelli, D., Borga, M., Viglione, A., Chirico, G. B., & Blöschl, G. (2011). Spatial moments of catchment rainfall: rainfall spatial organisation, basin morphology, and flood response. *Hydrol. Earth Syst. Sci., 8*(3), 5811-5847. doi:10.5194/hessd-8-5811-2011

Zoccatelli, D., Borga, M., Zannon, F., Antonescu, B., & Stancalie, G. (2010). Which rainfall spatial information for flash flood response modelling? A numerical investigation based on data from the Carpathian range, Romania. *J. Hydrol., 394*(1-2), 148-161. doi:10.1016/j.jhydrol.2010.07.019

Zoccatelli, D., Parajka, J., Gaál, L., Blöschl, G., & Borga, M. (2017). A process flood typology along an Alpine transect: analysis based on observations and modelling approaches (Submitted). *J. Hydrol.*

Zulkafli, Z., Buytaert, W., Onof, C., Manz, B., Tarnavsky, E., Lavado, W., & Guyot, J.-L. (2014). A Comparative Performance Analysis of TRMM 3B42 (TMPA) Versions 6 and 7 for Hydrological Applications over Andean-Amazon River Basins. *J. Hydrometeor., 15*(2), 581-592. doi:10.1175/JHM-D-13-094.1